# The Effects of Laser Ablation Coating Removal on the Fatigue Performance of a High Strength Structural Steel

---

A Dissertation

Presented to

the faculty of the School of Engineering and Applied Science

University of Virginia

---

in partial fulfillment

of the requirements for the degree

Doctor of Philosophy

by

Md Shamsujjoha

December

2017

APPROVAL SHEET

The dissertation

is submitted in partial fulfillment of the requirements

for the degree of

Doctor of Philosophy

shamsujjoha

AUTHOR

The dissertation has been read and approved by the examining committee:

Sean R. Agnew

Advisor

James M. Fitz-Gerald

James T. Burns

Leonid V. Zhigilei

Matthew B. Panzer

Stephen R. Sharp

Accepted for the School of Engineering and Applied Science:

Craig H. Benson, Dean, School of Engineering and Applied Science

December

2017

## Abstract

Laser removal of protective coatings from naval vessels and bridge structural members is a promising alternative to traditional paint stripping methods such as abrasive blasting due to significant advantages in paint-layer selection, spatial control, and flexibility (reduced need for containment and hazardous waste clean-up). However, in order to substitute laser ablation coating removal (LACR) for legacy paint stripping methods, the laser-interaction effects on the morphological and mechanical properties of the underlying steel substrate have to be assessed. The main objective of this study is to determine the effect of LACR on the surface condition and mechanical properties (esp. fatigue) of high strength structural steel, obtained from two different lots having distinctive microstructures. Both materials were abrasive blasted (typical control condition prior to coating), using two different blasting protocols, i.e., laboratory controlled conditions of low-pressure (690 kPa, small particle size basting) versus typical industrial practice involving high-pressure (827 kPa, large particle size blasting). The results obtained from this study advance the knowledge and understanding of the process in a quantitative manner, enabling interested parties to assess the efficacy of LACR on low carbon structural steels.

The study showed that the LACR process was effective in the removal of a typical epoxy-based coating from the steel substrate. The efficiency of the coating removal depends on the laser processing parameters. However, multiple passes were required for complete removal of coatings on the order of 250 μm in thickness. At this thickness, a coating removal rate of 1.8 $m^2$/hr was measured using a 7.6 cm laser scan width. The appearance of the underlying

substrate surface is clearly changed at the microscopic level. However, conventional surface roughness (profile) measurements using stylus profilometry (or 3D optical microscope) indicate no statistically significant change in the roughness. Pneumatic Adhesion Tensile Testing Instrument (PATTI) studies performed on samples repainted after LACR confirm equivalent, or superior, performance to the abrasive blasted and painted samples.

Pull-pull fatigue testing of the samples revealed that the condition of the starting surface has a major impact on the fatigue performance after LACR. When low-pressure laboratory scale abrasive blasting is employed, the fatigue strength is unchanged by LACR. When industrial, high-pressure abrasive blasting is performed prior to LACR, the fatigue strength showed a knock down of 12%. SEM observations of the surface and cross-section of abrasive blasted samples showed a high density of particles embedded in the near surface regions. Multiple, hard particle impacts during abrasive blasting produce beneficial compressive residual stresses (measured using depth-resolved X-ray diffraction methods), as well as surface defects such roughness, embedded particles, micro-cracks, etc. The laser treatment process results in surface melting and resolidification, which leads to changes in the surface residual stress state, i.e., the beneficial compressive residual stress is replaced by potentially harmful tensile residual stress state at the surface.

SEM observations of the fatigue fracture surface illustrate that, in cases where fatigue life remained unchanged by LACR, fatigue cracks initiated from the valleys of the surface profile in both abrasive blasted and LACR treated conditions. However, for the cases where the fatigue life decreased after LACR treatment, fatigue cracks tended to initiate at embedded abrasive

media (~73% of the time). Even though this embedded media was present, it only sometimes (~25% of the time) served as the primary initiation site, prior to LACR treatment. Local residual stresses and geometrical stress concentrations of the impact-induced surface defects are shown to be the two root causes that result in such discrepancy in fatigue performances after LACR treatment.

Elastic stress concentration factor estimation using both an analytical function based on roughness parameters and finite element analysis (FEA) using real surface profiles obtained from SEM cross-sectional images revealed that $k_{t,max}$ (associated with the surface) decreases after LACR processing, due to surface smoothing. The counterbalancing effects of detrimental tensile residual stress and beneficial smoothing of the surface result in similar fatigue lives, in the cases where no embedded particles were observed. On the other hand, $k_t$ associated with embedded particles remains the same after LACR.

Finally, FEA was performed on the samples containing embedded particles to evaluate their local residual distributions. FEA results show that the residual stress in the proximity of the particles is typically highly compressive for the abrasive blasted surface conditions. Upon subsequent laser treatment, the local residual stress field relaxes. Depending on the size and depth of the particle, it can even undergo complete relaxation. Monotonic elastoplastic simulations were carried out to evaluate how the combined effects of the high value of $k_t$ and changes in residual stress state alter the local stress fields under tensile load. The results suggest that the preferred site for crack initiation will switch from the surface to the embedded particles following LACR, in agreement with observation. Thus, the high stress concentration

associated with sharp, embedded particles combined with alterations in the residual stress state provides an explanation for the transition in fatigue behavior.

## Dedication

**To my late father, Md Abul Kashem.**

## Acknowledgement

I would like to express my sincere gratitude to Prof. Sean Agnew for his encouragement, insightful guidance as my supervisor. I feel he is the best advisor that anyone can have and feel truly blessed to have him as my advisor.

Special thanks goes to Prof. James M. Fitz-Gerald for providing guidance, support and listen to me and answered all my questions what may have seemed very silly. I have learned a lot from all the conversations that I had with him.

I would also like to thank the members of my thesis committee: Prof. James Burns, Prof. Leonid Zhigilei, Prof. Matthew Panzer, and Dr. Stephen Sharp for their valuable inputs on my research.

I would like to thank Chris Calhoun, Jishnu Bhattacharyya, Fulin Wang, Robert Klein, Jay Einhorn, Jasmine Keene, and Daniel Malta from the Agnew research group.

Last and most important of all, I would like to thank my family, especially my Mom, daughter, wife, brother, and sisters for their love, support, and encouragement.

# Contents

## List of Figures

# List of Tables

# Chapter 1: Introduction

Heavy-duty coatings have been widely used to protect naval vessels, aircraft frames, structural bridges, etc. from the surface damage, erosion loss, corrosion, etc. However, components are maintained by periodically removing and replacing worn and aged coatings from the substrates they are designed to protect. In addition, coatings are also removed from localized regions for the purpose of inspection or repair. The traditional coating removal methods that are employed for these purposes include grit blasting, waterjet blasting, power/hand sanding, needle gunning, hand scraping and chemical stripping. Although these are proven methods, they all have their own disadvantages. For example, the use of power tools (e.g. needle gun or grinder) for coating removal is taxing upon the worker and can lead to injuries of the eyes, hands, and forearms. The chemical stripping process is typically conducted with the use of methylene chloride, which contains volatile organic compounds and hazardous air pollutants, both of which are targeted for elimination by environmental regulations. Abrasive blasting coating removal results in large quantities of solid waste subjected to high disposal costs as well as scrutiny under environmental regulations [1-3]. Because of these concerns, aerospace, shipbuilding and transportation sectors are currently involved in the identification of safe, efficient, and more environmentally friendly methods of coating removal. Laser ablation has been identified as a promising technology for removing paint without generating secondary waste to supplement the existing coating removal methods.

## 1.1 Laser ablation coating removal

Laser ablation is the ejection of material from the surface as a result of intense laser irradiation. Laser-material interaction, more generally, is a complex process as several phenomena contribute at the same time. Laser interactions with polymeric materials have been studied extensively in the past decades because of its importance in laser paint stripping [4-6]. During coating removal, a laser distributes thousands of laser pulses per second onto the target surface. The paint absorbs most of the laser energy and ablates by photochemical, photo-thermal, or combination of two types of processes. Photochemical processes are dominant for the lasers operating at ultraviolet (UV) regime, since these are energetic enough to cause molecular dissociation. On the other hand, infrared (IR) lasers are only energetic enough to cause excitation of molecular vibrational modes that cause raise in the localized temperature.

As the temperature rises beyond a threshold value, paint ablates by thermal phenomena such as selective vaporization [4]. If the laser pulse is very intense and short, i.e., higher power density, it raises temperature of the most materials above their vaporized temperature. The hot vapor becomes partially ionized and begins to strongly absorb the subsequent laser pulse energy by forming a plasma at the paint surface. This high temperature plasma can heat the underlying paints by thermal conduction. As the plasma heated further with incoming laser pulses, it expands a high velocity producing extremely high localized pressures on the coating surface [5-7]. The mechanical stress thus generated can rupture and fragment the coating and eject it from the substrate. The relevant mechanical stresses can be the thermo-elastic stress emerging due to thermal expansion or can be caused the by the increase of volume due to the

production of low-molecular products in both photo-thermal and photochemical reactions [8]. In conclusion, laser ablation coating removal is a complex process and the actual mechanism depends on the thermal properties of the paints as well as the laser processing condition (wavelength of the laser, laser intensity, pulse duration etc.). Quite often both thermal and non-thermal mechanisms are activated. Such mixed-mode processes are known as photo-physical processes [4]. Based upon the infrared (1064 nm) laser and epoxy-based paint examined in this study, LACR from steel substrates is most likely dominated by thermal processes. The efficiencies discussed below are empirical and not based on the mechanistic calculation.

The main parameters that describe the ablation process are the ablation rate, defined as the layer thickness removed per pulse *h*, at a given laser fluence *F*, the threshold fluence $F_{th}$, which is defined as the minimum laser fluence at the onset of ablation for a given wavelength. These parameters are related as [9, 10]:

$$h = \frac{1}{\alpha_{eff}} ln\left(\frac{F}{F_{th}}\right)$$

where $\alpha_{eff}$ is the effective absorption coefficient of a material for a given wavelength. Profilometric measurements, as determined by optical interferometry, mechanical stylus, or atomic force microscopy, are typically used to calculate the ablation rate [10].

Based on the various experimental results, the dependence of the ablation depth on the laser fluence can be illustrated schematically as shown in Figure 1:1. The dependence can be divided into three regions: i) low fluence, ii) intermediate fluence, and iii) high fluence [4]. In low

fluence regime, selective vaporization, paint combustion etc. are the primary ablation mechanism. An incubation period before the paint ablation can be observed. The ablation threshold is normally defined from this range. The threshold fluence for the initiation of paint ablation can be estimated theoretically by [11]:

$$F_{th} = \frac{\rho(H + C_p \Delta T)}{\alpha_{eff}(1 - R)}$$

where $C_p \Delta T$ is the stored energy, $\rho$ is the density, $H$ is the heat of vaporization and $R$ is the reflectivity of the paint.

The slope of the ablation depth vs. fluence curve increases with increasing fluence in the intermediate fluence range, which is typical for shorter pulse duration (< μs), due to more efficient decomposition of the polymers within this regime. The slope is relatively shallower in the high fluence region because of the screening of the laser radiation by solid, liquid and gaseous ablation products and the laser produced plasma [10]. The LACR process under investigation is in the high fluence regime, where rate depends only weakly on fluence.

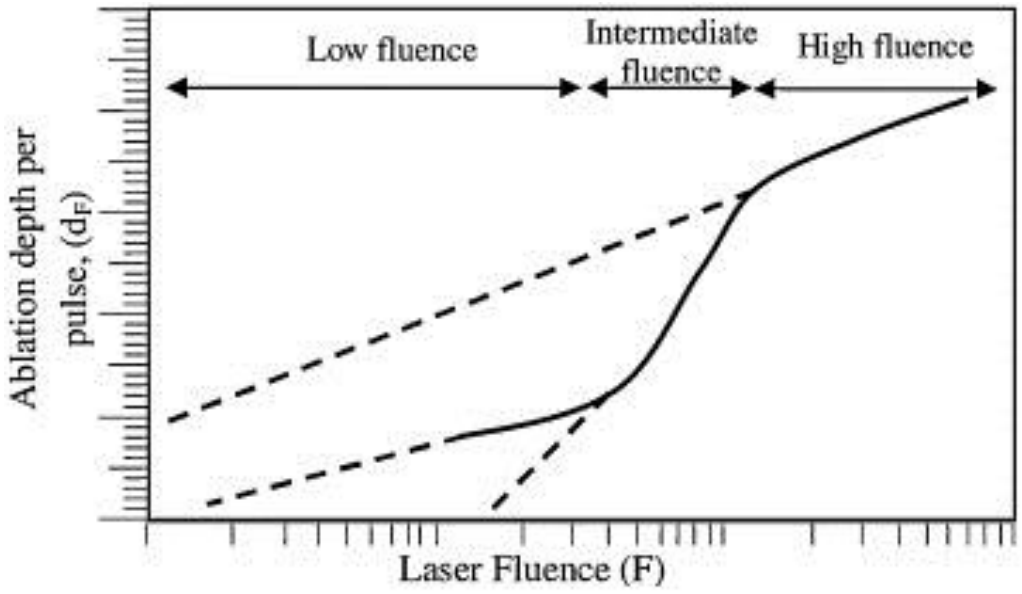


**Figure 1:1: Schematic of the effects of laser fluence on ablation depth, which are typically observed for polymeric materials [4].**

The ablation rate of epoxy-based polymer coatings from steel substrate was investigated. In addition to laser intensity (fluence), pulse duration, pulse repetition rate, and laser sweep speed (which refer to the rate at which the sample was translated under the laser beam) are also important factors that affects the ablation rate. One way that this manifests is through the concept of pluse overlap. Obviously, as the pulse duration and repetition rate increase, the opportunity for pulse overlap also increases. On the other hand, as the sweep speed increases, pulse overlap tends to decrease. The effect of each of these parameters on efficiency is explored empirically over a range of conditions accessible to the equipment employed, as detailed in the next chapter.

As an example, consider the case of a pulse frequency of 24 kHZ, pulse duration of 83 ns, scan rate of 110 Hz and sweep speed of 25.4 mm/s. Under these conditions, which were employed

in many of the LACR trials in this study, 4 laser passes were required to completely remove a ~250 µm thick coating for this laser processing parameters. It is also important to note that an overlap ratio of 30% and 50%, respectively, in the scanning and sweeping directions is obtained under these conditions. This means that a given spot in the material experiences 16 laser pulses during the course of de-coating, which gives an average ablation rate of ~15 µm per pulse, though the actual amount of ablation per pulse may vary as the coating is removed.

It is expected that some fraction of the laser radiation will be transmitted through the paint when the optical penetration depth ($\delta = \alpha_{eff}^{-1}$) of the laser is higher than the remaining paint thickness. Thus, interaction between laser and underlying substrate will take place, even prior to complete coating removal. Under such conditions, and depending on the thermal properties of the underlying materials and the intensity of the laser beam, the underlying substrate may undergo transformation hardening, shock hardening, glazing, melting etc. [12-15].

The absorption of laser beam in paint along depth (y) can be given by the following equation:

$$I(y) = I_0(1 - R)\alpha_{eff}\exp(-\alpha_{eff}y)$$

Here $R$ is the reflectivity, $\alpha_{eff}$ is the absorption coefficient, and $I$ is the laser intensity. A typical value of the absorption coefficient of the epoxy-based polymers is 200 $cm^{-1}$ at 1064 nm wavelength, which means laser beam of wavelength 1064 nm will be absorbed within ~50 µm thick paint layer [16]. As the paint thickness decreases below this optical penetration depth before the last laser pulses complete removal of paint (recall that about ~15 µm is removed per pulse), a significant portion of laser energy will be absorbed by the underlying material, and the

laser-material interaction will raise the temperature. One implication of this is that underlying material can undergo thermal damage even before the ablation of the final layer of paint (e.g. the primer) during closed-loop application [17].

Strong evidence of surface melting of the underlying steel substrate will be presented throughout the remainder of this study. This was true for cases when the laser was rastered on the bare steel without paint (laser surface modification) as well as during LACR treatments. The rise in the surface temperature $T_0$ can be calculated using the following formula [18]

$$T_0 = \frac{2I}{k}(1-R)\sqrt{Dt}\sqrt{\frac{1}{\pi}}$$

where *I* is the incident laser intensity (on the steel substrate), *k* is the thermal conductivity and *D* is the thermal diffusivity of the material. Using the laser parameters discussed above and the thermal properties of steel, it can be shown that the underlying steel material can undergo melting even if it absorbs only a small fraction (~0.3) of laser energy employed in the present LACR system.

Now the question arises, can the steel melt prior to removal of the paint, i.e. after the incident intensity is attenuated by some residual paint? The answer is yes, because it is certainly possible for $I/I_o$ ~ 0.3 when the coating is intermediate to 15 and 50 µm. As such, it is curious that melting of the underlying steel was never observed for cases where some portion of the coating was still intact. Therefore, in instances where the laser light penetrates the coating with sufficient intensity to melt the steel, the energy absorbed by the coating (through photo-

physical processes and thermal conduction from the steel) must also be sufficient to simultaneously ablate that remaining portion of the coating.

In any case, it is important to investigate the potential modification of the surface region of the underlying steel, by the LACR process. As such, the rest of the thesis will document an exploration of the possible modifications of the near surface microstructure, roughness, stress state, and/or hardness as well as their potential influence on the fatigue life of the underlying steel substrate.

## 1.2 Fatigue life assessment

Fatigue is the most common failure mode of materials under service. It is the process of progressive damage accumulation in engineering components subjected to repeat cyclic loading. The fatigue failure process can be divided into several stages [19]:

i) Initial cyclic damage (cyclic hardening or softening);

ii) Initiation of microscopic flaws;

iii) Coalescence of the microscopic flaws to form a major growing defect;

iv) Macroscopic propagation of such flaws (macro-crack growth); and

v) Final catastrophic failure.

All these stages are very interesting from the materials science point of view, but in engineering terms, the first three stages are grouped into the single process called “macrocrack initiation”, implying the formation of “engineering-size” detectable crack. Obviously, detectable crack size is not a clear term and it depends on the non-destructive technique methods employed during

inspection, but generally it is the order of millimeter or tens of millimeter [20]. Thus, the total fatigue life ($N_{total}$) can be calculated as the sum of the number of cycles required to initiate a macro-crack ($N_i$) plus those required to propagate the crack up to final fracture ($N_p$), i.e., $N_{total} = N_i + N_p$.

The knowledge of the crack initiation life and the propagation life is critical for fatigue-limited design and fatigue life prediction. Traditionally, life assessment methodologies can be distinguished as either total life or damage tolerant in nature. Phenomenological, continuum mechanics-based total life approaches characterize damage evolution, crack nucleation and crack growth stages of fatigue life as one parameter, the number of cycles to failure, $N_f$. Damage tolerant (fracture mechanics-based) approaches, on the other hand, consider the cycles taken for the growth of an initial defect to a critical size as a function of a crack tip driving parameter, such as stress intensity factor (SIF) range, $\Delta K$.

### 1.2.1 Fatigue crack initiation

Fatigue crack initiation life is usually predicted by classical local strain at a notch tip. The local strains at the notch tip can be obtained by using the Neuber [21] approach, the Glinka model [22] or directly from the finite element (FE) model. The Neuber model is based on the following hyperbolic relationship:

$$K_t^2 = K_\sigma . K_\varepsilon$$

where $K_t$ is the geometrical stress intensity factor, $K_\varepsilon$ is the local strain concentration factor (the ratio of the local to remote strain) and $K_\sigma$ is the local stress concentration factor (the ratio of the local to remote stress). For cyclic loading the equation can be written as:

$$\frac{(K_t \Delta\sigma_\infty)^2}{2E} = \Delta\sigma . \Delta\epsilon$$

where $\Delta\sigma_\infty$is the applied stress, $\Delta\sigma$ and $\Delta\epsilon$ is the local stress and strain amplitude at the notch tip. According to Glinka's approach, the local strains and stresses should represent energy equivalence as compared to the remote loading conditions, this lead to the following expression:

$$\frac{(K_t \Delta\sigma_\infty)^2}{2E} = \frac{\Delta\sigma^2}{4E} + \frac{\Delta\sigma}{n^{'}+1}\left(\frac{\Delta\sigma}{2K^{'}}\right)^{\frac{1}{n^{'}}}$$

To determine the local strains, either the Neuber or Glinka expression can then be coupled with a cyclic stress-strain response model (e.g. Ramberg-Osgood constitutive equation):

$$\frac{\Delta\varepsilon}{2} = \frac{\Delta\sigma}{2E} + \left(\frac{\Delta\sigma}{2K^{'}}\right)^{\frac{1}{n^{'}}}$$

The local strain amplitude can then be used to determine the fatigue life using the strain life relationship of the form:

$$\frac{\Delta\varepsilon}{2} = \frac{\sigma_f^{'}}{2E} N_i^b + \varepsilon_f^{'} N_i^c$$

where $\sigma_f^{'}$,is the fatigue strength coefficient, *b* is the fatigue strength exponent, $\varepsilon_f^{'}$ is the fatigue ductility exponent, *c* is the fatigue ductility exponent and $N_i$ is the number of cycles to crack initiate. Finally, this equation can be modified to incorporate the effect of mean stress ($\sigma_m$) by using the Smith, Watson and Topper (SWT) correction parameter [23]:

$$\frac{\Delta\varepsilon}{2}\sigma_{max} = \frac{(\sigma_f^{'})^2}{2E} N_i^{2b} + \sigma_f^{'}\varepsilon_f^{'} N_i^{b+c}$$

Other mean stress correction methods such as Walker, Morrow, Goodman can also be used for this purpose [23].

### 1.2.2 Fatigue crack propagation

In general, fatigue crack growth rate can be written as:

$$\frac{da}{dN} = f(\Delta K, R)$$

where $\frac{da}{dN}$ is the crack growth per cycle, $\Delta K = K_{max} - K_{min}$ is the stress intensity range, and $R = \frac{K_{min}}{K_{max}}$ is the so-called R ratio or load ratio. The number of cycles to failure for a component with an initial flow of length of $a_0$ is then found by integration:

$$N_f = \int_{a_0}^{a_f} \frac{da}{f(\Delta K, R)}$$

where $a_f$ is the critical crack length chosen to denote failure. Paris was the first to relate to *da/dN* to the $\Delta K$ [24, 25]:

$$\frac{da}{dN} = C(\Delta K)^m$$

where *C* and *m* are the materials parameter.

Figure 1:2 shows an example of a fatigue crack growth curve. It can be shown from the figure that the crack growth rate deviates from the log-linear relation in the above equation at low (Region I) and high (Region III) $\Delta K$. Therefore, the Paris relation is only used in Region II, which is also known as Paris regime. This region is corresponds to the stable macroscopic crack growth. Microstructure and mean stress have less influence on fatigue crack growth behavior in this region, as compared to Regions I or III. The unstable crack growth in Region III is influenced

by the fracture toughness $K_c$ and is usually ignored in fatigue life prediction since the number of cycles corresponds to this region is insignificant compared to the total fatigue life. Region I describes the condition when the size of the near tip plastic zone is smaller than the grain dimensions for both long cracks with low applied stresses in the near threshold regime ($K_{th}$) and short crack just after initiation. Crack growth rates in this regime are very sensitive to microstructure, load ratio, and environment.

However, Elber [26] proposed that crack growth rate prediction should be based on the effective stress intensity factor range $\Delta K_{eff}$ rather than $\Delta K$. Elber considers that as a crack propagates, crack closure occurs as a result of plastically deformed material left in the path taken by the crack. This material is referred to as the plastic wake. The plastic wake enables the crack to close before the minimum load is reached, and Elber reasoned that the stress intensity factor at the crack tip does not change while the crack is closed even when the applied load is changing. The value of K when the crack is first fully opened is defined as $K_o$ and the reduced range of $K$ due to closure is given by:

$$\Delta K_{eff} = K_{max} - K_o, \text{ if } K_o > K_{min}$$

$$\Delta K_{eff} = K_{max} - K_o, \text{ if } K_o \leq K_{min}$$

The conversion from $\Delta K$ to $\Delta K_{eff}$, based on the calculation of the stress intensity value corresponding to the opening stress ($K_o$), is fairly complex and usually, finite element model is usually used to make these determinations.

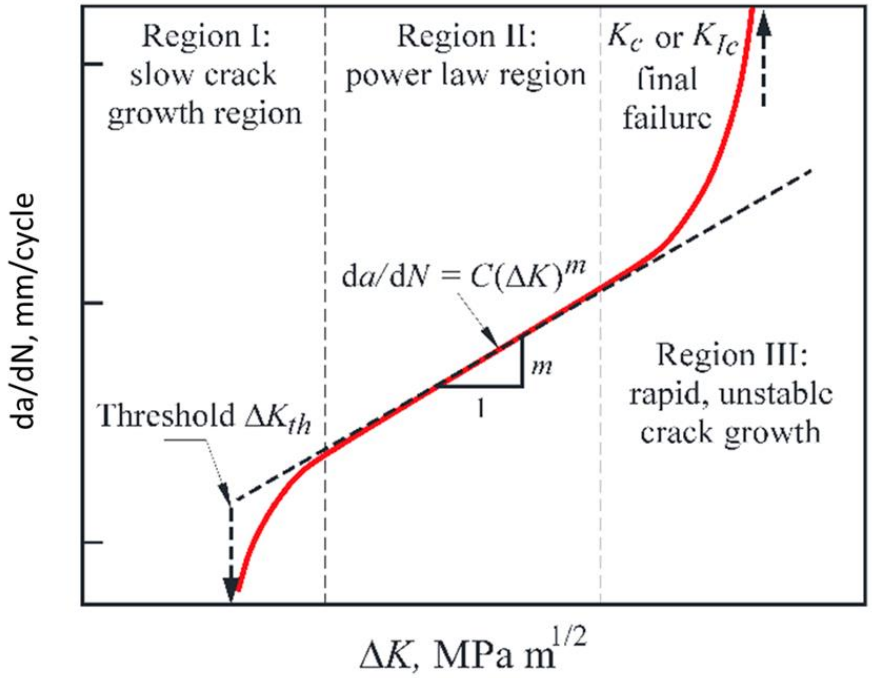


**Figure 1:2: Schematic illustrations of different regimes of fatigue crack propagation [27].**

### 1.2.3 Surface modification effects on fatigue life

It is known that surface conditions have a major impact on the fatigue performance of the materials, especially the initiation life. Three parameters are typically used to describe the surface conditions [28]: i) geometrical parameter (surface roughness), ii) mechanical parameter (residual stress) and iii) metallurgical parameter (microstructure).

The surface roughness acts like small notches and introduces local stress concentrations in the surface where fatigue crack may initiate. Li et al. [29]suggested that the stress concentration factor ($K_t$) caused by surface roughness can be described as:

$$K_t = 1 + 2.1\left(\frac{R_t}{S_m}\right)$$

where $R_t$ is the mean to peak valley height, $S_m$ is the spacing of adjacent peaks. However, it has been pointed out that the stress concentration is significantly affected by the bluntness of the notch. According to the Neuber [30], the stress concentration associated with roughness and hence the fatigue performance depends on the notch depth (related to $R_z$) and notch root radius rather than average roughness value ($R_a$).

$$K_t = 1 + n\sqrt{\lambda\frac{R_z}{\rho}}$$

where *n* represents the stress state (*n=1* for shear and *n=2* tension loading). Arola-Ramulu [31] proposed a modification of the Neuber rule. In their calculation, they incorporated standard roughness parameters ($R_a$, average roughness, $R_y$, *peak-to-valley height*, and $R_z$, *ten-point roughness)* and valley radii.

$$K_t = 1 + n\left(\frac{R_a}{\rho}\right)\left(\frac{R_y}{R_z}\right)$$

Any mechanical, e.g., shot peening, machining etc., or thermal, e.g., laser surface melting, heat treatment and quenching, etc. processing can introduce residual stress in the surface. Compressive residual stresses are known to have beneficial while the tensile residual known to detrimental effects on the component fatigue life. Residual surface stresses show the same general influence as the mean stress on loading. For example, the compressive residual stress is

summed with the applied stress range and the resultant reduction in the mean stress is considered in fatigue life analysis. A thorough consideration of the effect of residual stress on fatigue has been made for in published work [32] for shot peening samples, where compressive stresses are induced in the surface layer to improve fatigue life. Fatigue crack initiation at the locations of peak tensile residual stresses below the surface has been reported in literature for this type of surface processing samples.

For the fatigue crack propagation analysis, the superposition technique is often used to assess the effects of a known residual stress field on the crack propagation. This involves calculation of stress intensity factor for external loading $(K)_L$ and for pre-existing residual stress field $(K)_R$ [33-35].

$$K_{max} = (K_{max})_L + (K)_R$$

$$K_{min} = (K_{min})_L + (K)_R$$

$$\Delta K = K_{max} - K_{min} = (K_{max})_L - (K_{min})_L$$

$$R = \frac{K_{min}}{K_{max}}$$

This shows that stress intensity factor range $\Delta K$ is independent of the residual stress and only the stress ratio *R* is affected. The stress intensity factor for the initial residual stress $(K)_L$ then can be calculated using a weight function method. As such, the stress intensity factor is:

$$(K)_R = \int_0^a \sigma(x).m(x,a)dx$$

## 1.3 Motivation

Over the last decade, industries like aerospace, shipbuilding, transportation have been trying to implement LACR in their production application. Because of this, a number of research has been conducted in this field with the aim to evaluate the effectiveness of this technology for paint removal, in terms of cleanliness and removal rate, with the examination of the effects of laser parameters, like laser power density, to achieve a high degree of cleanliness with a good paint removal rate. However, a very little attention has been paid to the consequence of the laser paint stripping on the damage of the underlying substrate. Thus, the focus of this study to understand the effects of the laser paint stripping on the modifications of the surface morphology, near surface microstructure, stress state and their consequences on the mechanical properties, i.e., hardness, fatigue of the underlying steel substrate. An emphasize is placed to understand the effects of surface conditions prior to LACR treatment, i.e., abrasive blasting, on the performance of the LACR treated samples. It is also the aim of the study to compare the performance of the LACR treated samples with the abrasive blasted samples, a well-established coating removal method.

In addition to fatigue, surface roughness also effects the residual stress measurement using XRD and this study seek to theoretically evaluate these influences. Finally, a special attention is paid to understand the complicated interaction of the stress concentration of the surface defects and residual stress results from the surface treatment on the fatigue performance.

## 1.4 Thesis outline

This dissertation is prepared using a manuscript format. Five papers are composed to describe the research results, discussions and conclusions based on the research goals, as described in previous section. They are provided here with minor modification to provide a consistent style.

**Chapter 2** explores the effectiveness of LACR as a paint removal method and its impact on the substrate material, i.e., modifications of surface morphology, roughness, and microstructure, and suitability of affected substrate for subsequent coating application. (This work was published in the journal *Surface and Coating Technology (2015)* [36].)

**Chapter 3** presents the tension-tension fatigue test results obtained from the LACR treated and abrasive blasted samples. Residual stress distributions generated from each surface treatment are also provided in this chapter. Finally, the influence of the surface roughness and residual stress on the fatigue performance is analyzed. (This work was also published in the journal *Surface and Coating Technology (2015)* [37].)

**Chapter 4** describes the effects of variations in initial microstructure and prior abrasive blasting parameters on the fatigue performance of another lot of high strength steel after LACR. It introduces a new method to calculate the elastic stress concentration factor from the SEM cross-sectional images using FEA. (Prepared for publication in the *International Journal of Fatigue.*)

**Chapter 5** presents a theoretical approach to examine the influence of periodic surface profiles on the stress measured by the x-ray diffraction method. An inhomogeneous stress distribution

due to surface roughness is modeled using finite element simulation. (This paper was submitted to the International Journal of Applied Crystallography.)

**Chapter 6** expands the FE model presented in Chapter 4 to include residual stress and embedded particle effects. A simple algorithm is presented the incorporated the residual stress in FEA model. Elastic-plastic finite element analysis is conducted to evaluate the combined effects of stress concentration and residual stress effects on fatigue crack initiation. (Together with Chapter 4, it is contemplated to submit the results described in this chapter for publication to the International Journal of Fatigue.)

**Chapter 7** provides a summary and conclusions from this work, and suggests potential avenues for future work.

Finally, another example of the laser-material interaction, namely that which occurs laser powder bed additive manufacturing of stainless steel was also investigated during the same time frame as this dissertation work. Because this additional study is not directly related to the main theme of the thesis, it is presented in the Appendix.

## References

[1] K. Wolf, R. Krinker, J. Ermalovich," Institute for Research and Technical Assistance, California (2009).

[2] E.D. Oller, Naval application of laser ablation paint removal technology, in: U.S. Navy Corrosion Conference, Norfolk, VA June 2011.

[3] G. A. Mongelli, Portable Handheld Laser Small Area Supplemental Coatings Removal

System Final Report, Headquarters Air Force Materiel Command Depot Modernization and Logistics Environmental Office (2005).

[4] Y. K. Madhukar, S. Mullick, A. K. Nath, *Appl. Surf. Sci.*, 286(2013) 192–205.

[5] P. Fitzsimons, Department of Engineering. Diss. University of Liverpool (2012).

[6] R. E. Litchfield, Institute of Polymer Technology and Materials Engineering. Loughborough University (2004).

[7] N. Arnold, N. Bityurin, *Appl. Phys. A,* 68(1999) 615–625.

[8] G. Paltauf, P. E. Dyer, *Chem. Rev.*, 103(2003) 487–518.

[9] R. Srinivasan, B. Braren, I. B. M. Thomas, *J. Polym. Sci. Polym. Chem. Ed.*, 22 (1984) 2601–2609.

[10] T. Lippert, UV Laser Ablation of Polymers: From Structuring to Thin Film Deposition, *Laser-Surface Interact. New Mater. Prod.*, *ed.* A. Miotello and P.M. Ossi, Springer, Berlin (2009) 141–175.

[11] J. E. Andrew, P. E. Dyer, D. Forster, P. H. Key, *Appl. Phys. Lett.*, 43(1983) 717–719.

[12] J. P. Nemeth, M. L. Kligenberg, J. J. Valencia, G. A. Price, T. P. Blair, "Naval aplication of laser ablation paint removal," Navy Metalworking Center, Johnstown, PA 15904-1935, 2010.

[13] S. N. Aqida, Department of Mechanical and Manufacturiang Engineering. Diss. Dublin City Universtiy (2011).

[14] G. X. Chen, T. J. Kwee, K. P. Tan, Y. S. Choo, M. H. Hong, *Appl. Phys. A Mater. Sci. Process.*, 101(2010) 249–253.

[15] S. Marimuthu, A. M. Kamara, H. K. Sezer, L. Li, and G. K. L. Ng, *Comput. Mater. Sci.*, 88(2014) 131–138.

[16] M. Dubois, F. Enguehard, L. Bertrand, M. Choquet* and J. P. Monchalin, *Le Journal de Physique IV* 4.C7 (1994): C7-377.

[17] R. L. Cargill, Closed-Loop Laser Ablation for Navy Maintenance Applications, General Lasertronics Corporation, ASNE Symposium (2011).

[18] J. H. Bechtel, J. of Appl. Phys. 46 (1975), 1585-1593.

[19] S. Suresh, R. O. Ritchie, *Int. Met. Rev.*, 29(1984) 445–475.

[20] R. J. H. Wanhill, L. Schra, Short cracks and durability analysis of the Fokker 100 wing/fuselage structure, *NLR TP 90336 L, National Aerospace Laboratory, NLR* (1990).

[21] H. Neuber, *J. Appl. Mech.*, 28(1961) 544–550.

[22] G. Glinka, *Eng. Fract. Mech.*, 22(1985) 839–854.

[23] N. E. Dowling, *2nd SAE Bras. Int. Conf. Fatigue*, Sao Paulo, Brasil, ˜ SAE Paper No. 2004-01-2227, SAE (2004).

[24] P. C. Paris, M. . Gomez, W. Anderson, *Trend Eng.*, 13(1961) 9–14.

[25] P. Paris, F. Erdogan, *J. Basic Eng.*, 85(1963) 528-534.

[26] E. Wolf, *Engineering Fracture Mechanics*, 2(1970) 37–45.

[27] R. R. Ambriz, D. Jaramillo, *Light Metal Alloys Applications*, InTech (2014).

[28] M. Suraratchai, J. Limido, C. Mabru, R. Chieragatti, *Int. J. Fatigue*, 30 (2008) 2119–2126.

[29] J. K. Li, M. Yao, D. Wang, R. Z. Wang, *Fatigue Fract. Eng. Mater. Struct.*, 15(1992) 1271–1279.

[30] H. Neuber, Theory of notch stresses: principles for exact stress calculation, Edward Bros, Ann Arbor, MI (1946) .

[31] D. Arola, C. L. Williams, *Int. J. Fatigue*, 24(2002) 923–930.

[32] P. J. Withers, *Reports Prog. Phys.*, 70(2007) 2211–2264.

[33] J. E. LaRue, S. R. Daniewicz, *Int. J. Fatigue*, 29(2007) 508–515.

[34] M. Dorman, M. B. Toparli, N. Smyth, A. Cini, M. E. Fitzpatrick, P. E. Irving, *Mater. Sci. Eng. A*, 548(2012) 142–151.

[35] M. Achintha, D. Nowell, D. Fufari, E. E. Sackett, M. R. Bache, *Int. J. Fatigue*, 62(2014) 171–179.

[36] M. Shamsujjoha, S. R. Agnew, M. A. Melia, J. R. Brooks, T. J. Tyler, J. M. Fitz-Gerald, *Surf. Coatings Technol.*, 281(2015), 193–205.

[37] M. Shamsujjoha, S. R. Agnew, J. R. Brooks, T. J. Tyler, J. M. Fitz-Gerald, *Surf. Coatings Technol.*, 281(2015), 206-214.

# Chapter 2: Effects of Laser Ablation Coating Removal (LACR) on a Steel Substrate: Part 1: surface profile, microstructure, hardness, and adhesion


## Abstract

The effects of laser ablation coating removal (LACR) from a high strength shipbuilding steel have been assessed. The LACR process was shown to be effective for the removal of a typical epoxy based coating. However, multiple passes were required to remove the coating, with an increased number of passes required at higher sweep speeds. Scanning electron microscope (SEM) imaging of the surface and cross-sections reveals that the underlying metal substrate is melted and re-solidified during LACR. The appearance of the surface is clearly changed at the microscopic level. However, conventional surface roughness (profile) measurements indicate no statistically significant change in the roughness, using conventional metrics such as average roughness, Ra. Finally, studies performed on samples repainted after LACR confirm equivalent, or superior, adhesion as compared to the abrasive blasted and painted samples.


## 2.1 Introduction

During both in-depot and underway maintenance and repair operations, the removal of protective coatings from naval vessels is a time consuming and often hazardous operation. For large-scale ship components (sections, compartments, decking etc.), this has been traditionally accomplished through various abrasive blasting methods. However, in specific instances, only a small percentage of a component may require repair. Repair of small sections via abrasive blasting can lead to contamination of the entire component and adjacent regions. Besides,

conventional blasting methods generate copious amounts of secondary waste that can be expensive to dispose. The use of power tools (e.g. needle gun or grinder) for coating removal is taxing upon the worker, and can lead to injuries of the eyes, hands, and forearms. A self-contained, spatially controlled, coating removal technique which is both friendly to the environment and the worker is sought for such "niche" operations.

Over the last 25 years, pulsed and continuous laser sources have been increasingly used in commercial applications related to surface modification (alloy chemistry, roughness, cladding, cleanliness, hardness, and local microstructure) [1-6]. Laser ablation coating removal (LACR) has already been successfully applied on aircraft structures [7-9]. Due to this past success, some research work has focused on the study of the feasibility of LACR on marine structures [10, 11].

Prior laser paint stripping studies [7, 10-13] have indicated that they can: a) lower the environmental impact of the paint stripping process, e.g. relative to the use of solvents and b) offer a cost-effective alternative to conventional grit blasting and solvent-based approaches for niche applications. Another attractive feature of photon-based surface modification is the ability to selectively modify surface layers of bulk samples, eliminating associated detrimental consequences of bulk modification. However, in the case of coating removal, there are concerns regarding the impact of even near-surface damage on overall component performance. Notably, prior field applications on fixed wing aircraft and rotorcraft have involved stripping paint down to primer. The current application would require stripping paint and primer to bare metal [7].

Prior studies have already highlighted the key metallurgical and engineering issues that must be investigated:

a) Reduction in surface roughness (profile) has emerged as a major concern, since it could detrimentally affect subsequent coating adhesion and prevent meeting recoating specifications.

b) Melting of the near surface is common, irrespective of the base metal. This raises questions about the detailed chemistry, metallurgical phase content, stress state of the re-solidified metal, and the heat affected zone (HAZ).

c) Quantification of cleanliness after LACR remains an open question. Two specific issues of concern are the possible re-deposition of particulates and alloying of coating constituents within the bulk alloy composition at the near surface region.

These metallurgical issues could have a major impact on the quality, lifetime, and overall performance attributes of the component and new surface coating to be applied. The three major engineering performance concerns are:

i) adhesion of subsequent coatings, due to changes in surface roughness (addressed in the present paper).

ii) fatigue performance, due to changes in roughness or residual stress (addressed in Chapter 2 [14]), and

iii) corrosion behavior (recommended for future study).

The main objective of this paper is to evaluate the use of laser ablation as a method for coating removal and to investigate the laser interaction with the underlying metal substrate (steel). A comparative study of the effect of grit blasting and LACR on the change in surface appearances, microstructural evolution of the steel has been made. The impact on key features including roughness, hardness, and coating adhesion after repainting also has been investigated.

## 2.2 Experimental

Paint removal was done using an Adapt Laser Systems model CL1000QNd:YAG. This system delivers 1 kW average laser power while operating at the fundamental wavelength (1064 nm). Previous work by the Navy Metalworking Center (Concurrent Technologies Corp., CTC) has shown that a 1 kW Nd:YAG laser operating at the fundamental wavelength in pulsed mode is suitable [11]. The laser is diode pumped and uses a fiber optic delivery method (Figure 2:1). An integrated filter vacuum unit is equipped with laser delivery head to captures and filters the paint fumes and particles. Laser window was cleaned in between the samples as the current design is not capable of collecting all materials resulting in re-deposition on the laser focusing optic. Laser processing of all samples was conducted at the Norton Sandblasting Center (NSC) located in Chesapeake, VA. A pulse frequency of 24 kHz was employed with a pulse duration of 83 ns, while few laser processing trials were performed at 40 kHz pulse frequency and at 135 ns pulse duration. In general, a scan rate of 110 Hz was employed with a limited number of experiments performed at 50, 80, and 120 Hz. The scan rate refers to the speed at which the laser pulse is actively raster scanned within the laser head to create a 7.6 cm wide beam profile (Figure 2:2). A majority of the processing was performed at a pulse frequency of 24 kHz, pulse

duration of 83 ns and scan rate of110 Hz. The standoff distance was maintained at 32 mm for all experiments, this distance represented the focal length crossover for the optic used, and representing the highest localized fluence and defects in the beam profile. The pulse spot size is approximately 1 mm and the pulse overlap ratio in the scanning direction is about 30 %. It was calculated from the laser power, spot size, pulse duration and pulse frequency that maximum fluence for this study is 5.3 J/cm2. The laser sweep speed was varied from 6.4, 12.7, and 25.4 mm/s along with the number of laser passes, with most of the tests utilizing 1 to 10 passes. Both "manual sweep" (the operator would approximate the speed and adjust based on visual feedback) and “automated sweep" (sweep speed was controlled by a Newport ILS translation stage system) were performed for paint removal. Although both "manual sweep" and "automated sweep" were shown to be capable of effective paint removal, this study mainly focused on the “automated sweep" experiments in order to precisely determine the effect of sweep speed.

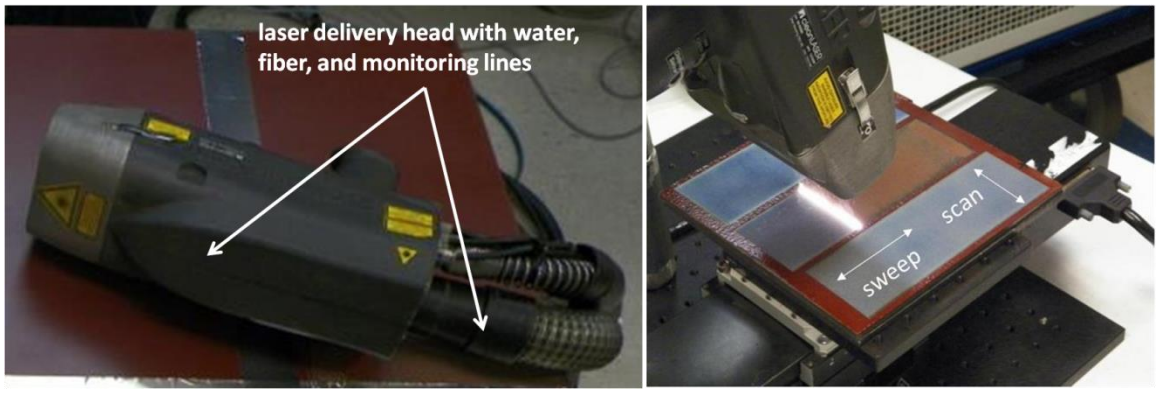


**Figure 2:1: Experimental set-up for laser processing.**

High strength shipbuilding steel [15] plate in the abrasive blasted condition was used a baseline as this is the typical condition prior to painting. Garnet of 254 to 559 µm sizes was used as abrasive blasting medium. Abrasive blasting was conducted using 12.7 mm (0.5 inch) diameter straight bore nozzle at a standoff distance of 127 mm (5 inch) and with air pressure of 621 kPa. A red epoxy paint (no primer) was applied at thicknesses of 0.25 and 0.76 mm (10 and 30 mils). Following application, the paint was air dried at ambient temperature and aged for 15 to 20 days prior to LACR. Samples for surface and cross-sectional analysis were cut from abrasive blasted and laser processed samples with conventional machining methods (band saw and slow-speed diamond saw). The cross-section samples were mounted in Konductomet™, ground using SiC paper down to 1200 grade, followed by polishing using diamond paste down to 1 µm. Finally, the cross-section samples had their microhardness evaluated and/or they were etched to reveal the microstructure using a nital solution (2% nitric acid in ethyl alcohol). Both the surfaces and cross-sections were examined using Scanning Electron Microscopy (SEM) within a JEOL 6700 cold-field emission gun instrument. Energy Dispersive X-ray Spectroscopy (EDS) was used to determine the chemistry of features of interest during SEM investigations. Energy Dispersive X-Ray Spectroscopy (EDS) was used to determine the chemistry of features of interest during SEM investigations.

The surface roughness was evaluated quantitatively using two techniques for both abrasive blasted and laser surface treated using a range of laser processing parameters.

a) Elcometer 224 Model B was used in accordance with ASTM D 4417-B and SABS772. (This is a common technique for the U.S. paint industry to assess roughness).

b) A Mitutoyo SJ-210 portable stylus profilometer with a tip radius of 7 µm was used subject to applicable standards: JIS B 0633:'01, ISO 4288:'96. The average roughness (*Ra*), root mean square roughness (*Rq*), ten-point height roughness (*Rz*) was calculated using a cutoff length of 0.8 mm and 6 mm traverse length.

Another perspective on roughness was provided by 3D optical microscopy using a HiroxTM7700.

Vickers microhardness measurements were made at various depths using a diamond pyramid indenter with an apical angle of 136°, an indentation load of 0.5 kg, and an indentation duration of 15 seconds. Rockwell hardness (scale B) measurements of the abrasive blasted, and laser processed surfaces were also carried out.

The Gardco Pneumatic Adhesion Tensile Testing Instrument (PATTI) employed in the study conforms to ASTM D4541 and D7234. The PATTI testing device was utilized to determine the pull off tensile strength of paint post-lasing as compared to that of paint applied to an abrasive blasted surface. A paint thickness of 0.25 mm was used for all samples in this portion of the study. Aluminum stubs were applied to the painted surface via high strength epoxy, which was cured for 24 hours in ambient condition. Once this high strength epoxy set, the aluminum stubs were pulled off using the PATTI tester, which gives a reading of the breaking pressure (BP). The BP can be converted to pull off tensile strength (POTS) according to the following relation:

$$POTS = \frac{(BP \times A_g) - C}{APS}$$

Where *BP* = Burst pressure (psi), $A_g$ = contact area between gasket and reaction plate = 26.2 cm2 (4.06 $in^2$) for F-4 piston, *C* = piston constant = 1.3 N (0.286 lbs) for F-4 piston, *APS* = area of pull-stub (1.3 $cm^2$). The control sample was abrasively blasted and painted. The test samples were subjected to various LACR treatments and then repainted. At each sample condition, 20 tests were performed.

## 2.3 Results and Discussions

### 2.3.1 Laser Processing

The determination of process parameters for production work is beyond the scope of the present investigation. However, two of the major process variables (sweep speed and number of laser passes) were explored during the course of this study. It was found that multiple passes were required for complete removal of paint, at all sweep speeds explored. At least 2 passes were required to remove 0.25 mm of paint at sweep speeds as low as 12.7 mm/sec. It was also observed that a larger number of passes was required to remove the paint at higher sweep speeds. However, there was too much scatter in the results to develop a strict quantitative correlation between the number of passes and sweep speeds. This is due to the fact that cleaning efficiency was also dependent upon the frequency of laser window cleaning and laser focusing condition. It was observed that, during the ablation process, a deposited film can form on the window. This reduces the energy of the transmitted beam to the sample surface. An effective coating removal rate of 290 sq. cm. per minute (~19 sq. ft. per hour) was measured at an effective sweep speed of 6.4 mm/sec using the 7.6 cm laser scan width on 0.25 mm coated samples. The effective sweep speed is the actual sweep speed/ number of passes.

### 2.3.2 Surface Characterization

The surface characterization portion of the study focused on three issues, which prior studies had raised as concerns. First, it was of interest to determine if the surface had melted. Melting is of interest because it could induce significant changes in the microstructure and the residual stress state of the material, both of which could alter the mechanical properties of the near surface region. Second, concerns about possible alteration of the surface topology (roughness) have been raised. Roughness is important for applications involving coatings since it can promote mechanical interlocking between the substrate and the coating. Lastly, possible changes in the surface chemistry were of interest since chemicals from the coating could become absorbed by the underlying substrate due to the high temperature levels encountered during laser material interactions. As a minimum, it is of interest to determine if any residue from the ablated coating remains on the surface after LACR. In order to address these concerns, the surface morphology of the paint removed surfaces was extensively examined using SEM. Surface roughness was also evaluated.

#### 2.3.2.1 Surface Morphology

Figure 2:2 shows a SEM micrograph and the 3-D schematic view of the sample surface, which was partially cleaned by 3 passes of LACR (bottom of micrograph), performed at a sweep speed of 6.4 mm/sec). From Figure 2:2, it is clear that the LACR results in a sharp interface between a painted surface (top) and partially cleaned surface. This result also emphasizes that multiple passes were required to remove as little as 0.25 mm of coating even at a low sweep speeds, which would be nearly impossible to obtain in a manual sweep mode.

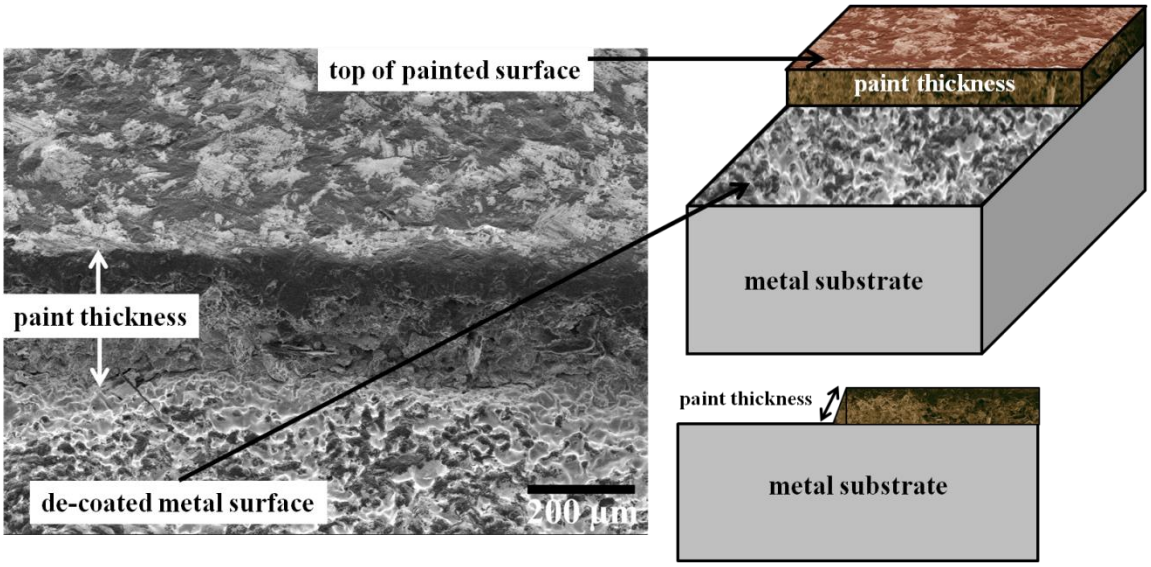


**Figure 2:2: Scanning electron micrograph of the sample surface tilted at 45° reveals the abrupt interface at the macro scale between the partially cleaned metal surface (bottom) and with the original full-thickness, un-lased paint (top). 3D and side view schematics provide an aid to the eye. (6.4 mm/sec., 3 passes).**

In order to gain better insights on the effects of LACR on the morphology of the steel substrate, laser surface modification (LSM) was performed on bare unblasted and abrasive blasted steel. Clear variations in surface morphology following LSM are shown in Figure 2:3. Figure 2:3(a) shows some fine corrosion features on the as-received steel plate prior to abrasive blasting, while Figure 2:3(b) shows the abrasive blasted sample. The abrasive blasted surfaces are tortuous, with evidence of surface cracks (see encircled region), and some micrographs show evidence of embedded abrasive blasting media. The laser processed samples in Figure 2:3(c, d) show clear evidence of laser-induced surface modification of the un-blasted and abrasive blasted surface morphology, respectively.

The morphological changes observed are consistent with laser melting and re-solidification. During melting, surface tension pulls down the peaks in the melt, the behavior of which is controlled by viscosity. This results in damped oscillation, and as oscillation damped out at the time of solidification, resulting in a smoother, flowing surface [16]. This contrast can be observed with the smooth, flowing appearance of Figure 2:3(d), relative to the tortuosity of the abrasive blasted sample shown in Figure 2:3(b) as well as small, round depressions, and dimples, which appear dark in this micrograph.

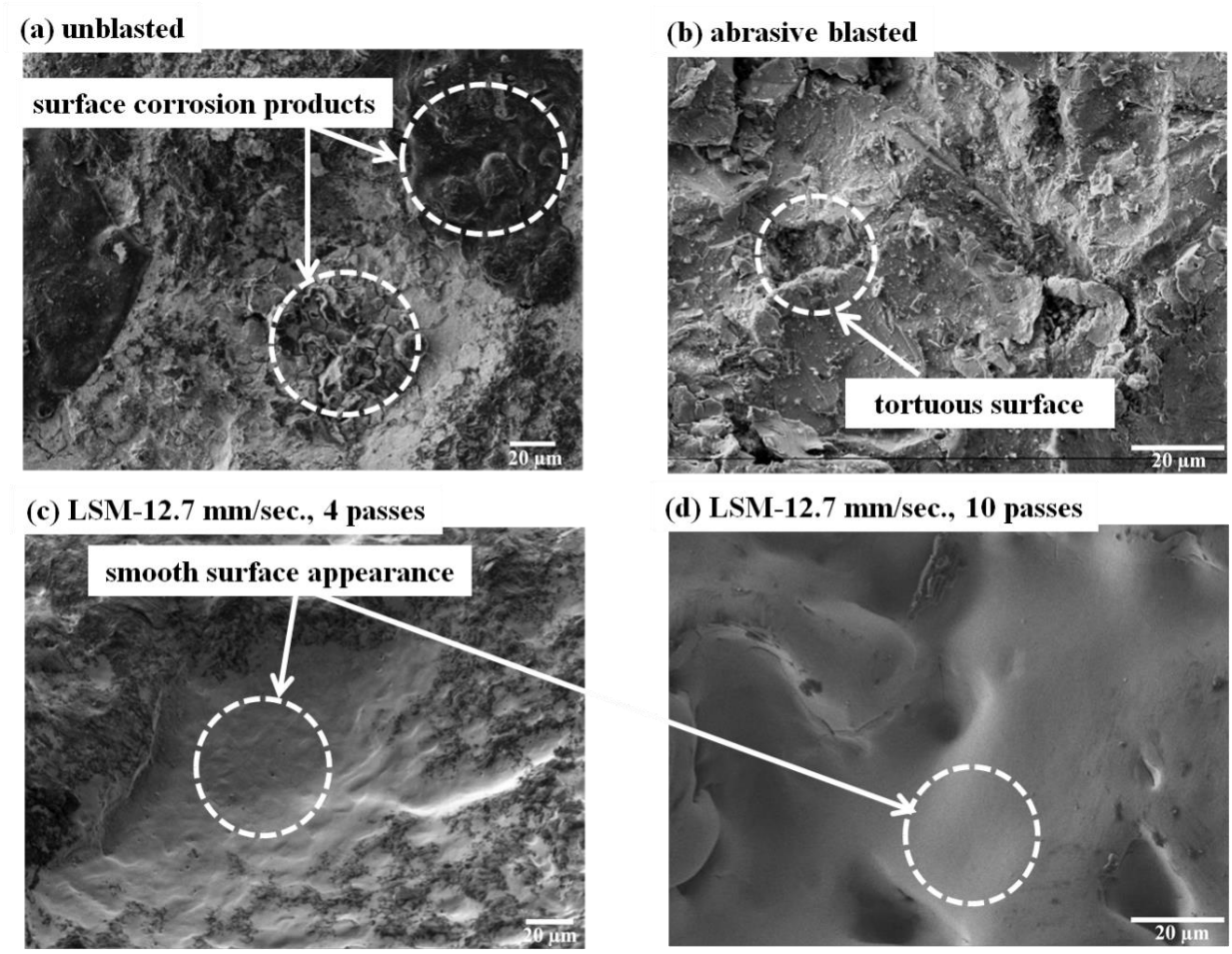


**Figure 2:3: Scanning electron micrographs of four categories: a) unblasted, b) abrasive blasted, c) unblasted and laser processed, and d) abrasive blasted and laser processed.**

Another feature of interest is the formation of "mud-cracks" following LACR, more prevalent in the valleys than along the ridges in the surface topology. Surface cracks suggest the possibility of high tensile residual stresses, greater than the strength of material, in the surface after laser treatment. These microcracks can act as nuclei for fatigue crack initiation [17]. These features were observed over a wide range of laser processed samples in this research task, and one of the more pronounced examples is shown in Figure 2:4, recorded from the surface of an

unpainted, abrasive blasted sample exposed to a single laser pass condition. It is noted that the sort of gross “mud-cracking” observed in Figure 2:4 was generally restricted to the manual, freehand scan trials, with a smaller amount observed in the controlled samples.

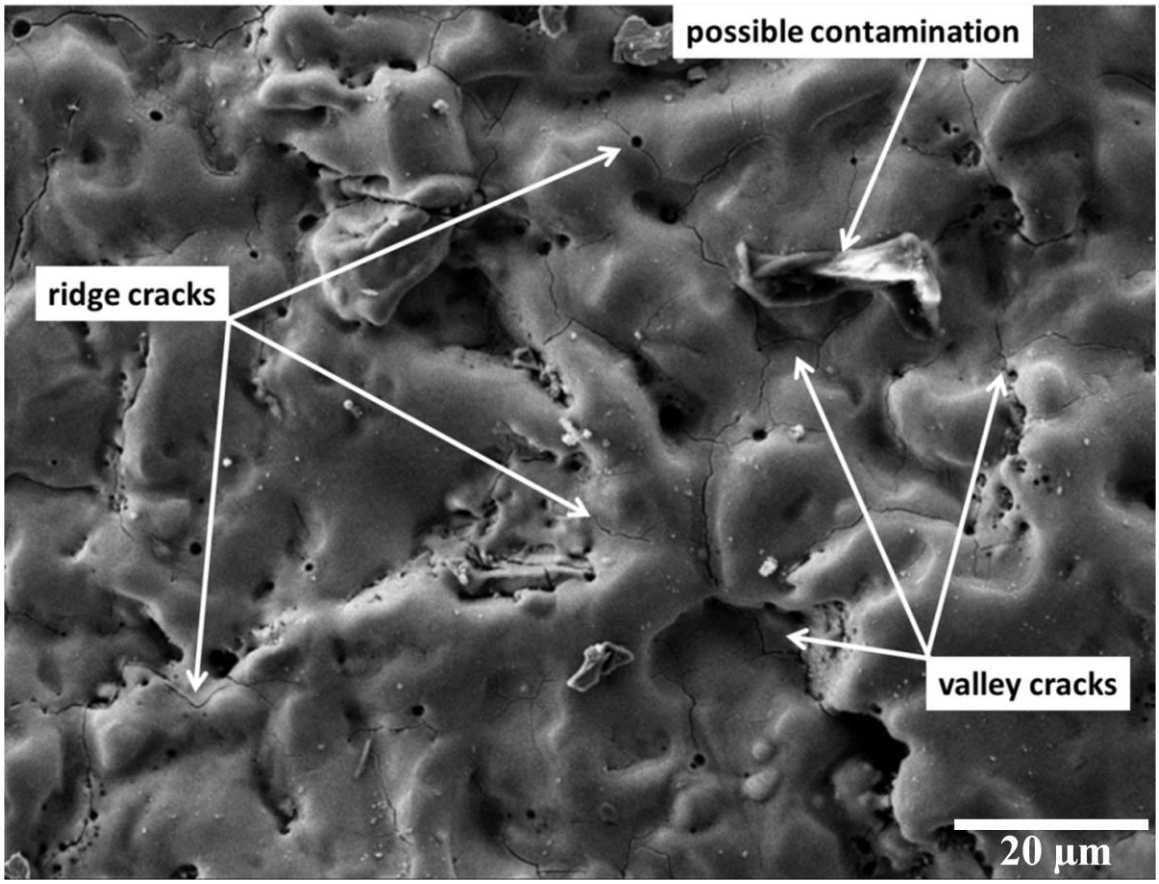


**Figure 2:4: Scanning electron micrograph of the surface showing the presence of laser-induced “mud cracks” on an abrasive blasted sample exposed to a single laser pass**.

Similar to LSM, smooth, flowing surface was observed after LACR (Figure 2:5), which confirms laser melting and re-solidification during laser paint removal. While the effects of LACR on the underlying metal surfaces are consistent throughout the range of samples examined, processing parameters do have an effect on the final surface morphology. Of the various laser

processing parameters examined, it appears that the number of passes plays the most important role. Figure 2:5 shows the effect of the number of laser passes on a sample while holding the automated sweep speed constant at 6.4 mm/sec. This sample was abrasive blasted and painted (0.25 mm) prior to laser processing. The Figure 2:5 shows that the surface appears increasingly smooth as one increases the number of passes. However, even at this low sweep speed, residual paint debris can be observed in the electron micrographs after processing 4 passes. To examine the overall chemistry of the surface, energy dispersive x-ray spectroscopy (EDS) was recorded at 15 kV at 100x magnification in field of view mode, meaning the EDS spectra is recorded from the overall scanned region or field of view in comparison to point or line profile modes. The laser processed (LACR) samples did not show an observable deviation from the baseline chemistry of the substrate alloy (within the resolution of the EDS system), which is composed mainly of Fe, Mn, Si and C (Figure 2:6).

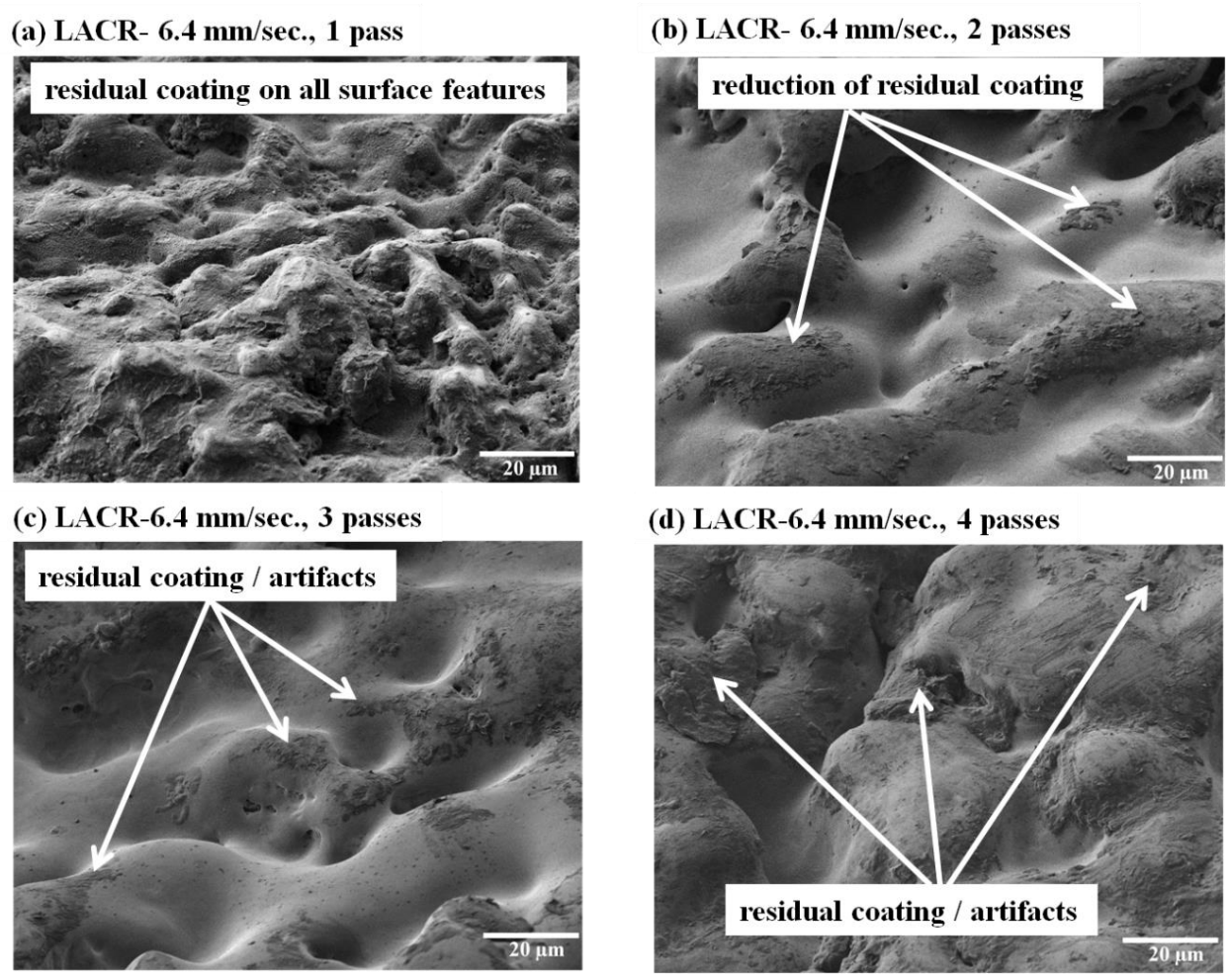


**Figure 2:5: Scanning electron micrographs of abrasive blasted / painted plates as a function of laser passes, after (a) 1 pass, (b) 2 passes, (c) 3 passes, and (d) 4 passes (all 0.25 mm painted samples) at a constant sweep speed of 6.4 mm/sec..**

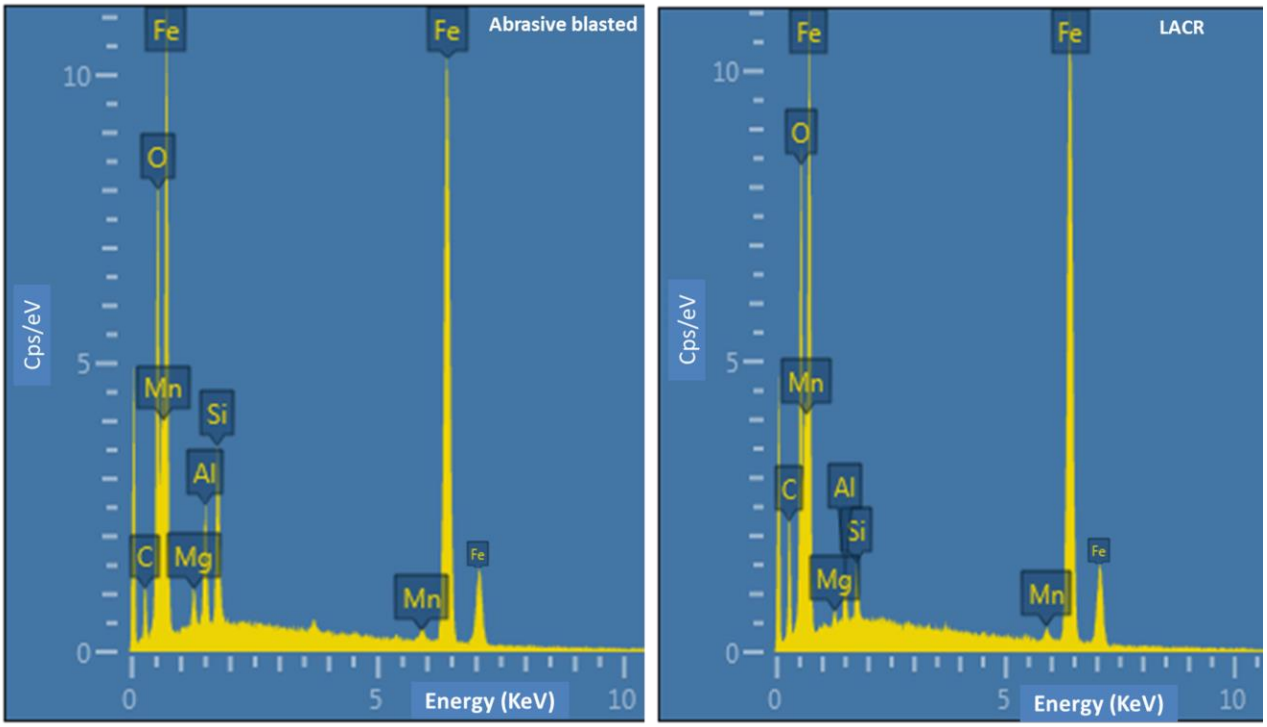


**Figure 2:6: Representative energy dispersive x-ray spectroscopy (EDS) spectrum of an abrasive blasted and LACR region. From the spectra, the base metal elements of the steel are present while no contamination consistent with the coating was detected.**

### 2.3.2.2 Roughness

The value reported from the Elcometer, as listed in Table 2.1, is the mean of the peak-to-valley height for 120-150 measurements per sample. Although the student's T-test values for the various lased conditions versus the abrasive blasted surface support the statement that individual samples did possess distinct roughness values , the actual roughness values observed are both above and below the baseline (abrasive blasted) sample. Thus, there are no obvious trends in the roughness values with laser processing conditions (i.e. more passes did not result in a quantitatively smoother surface, as characterized by the Elcometer, despite the smoother

appearance in SEM imaging.) Comparing the mean roughness of all lased samples with the abrasive blasted samples yields a high T value of 0.632. Thus, there is no statistically significant difference between the roughness of the abrasive blasted and laser surface treated samples if all the lased samples are considered collectively.

**Table 2.1: Laser conditions of samples used in Elcometer roughness study, the mean of the Elcometer readings, and the T-Test of the lased condition mean values versus the abrasive blasted condition.**

| Sample | Paint (mm) | Pulse (kHz) | Scan (Hz) | Sweep (mm/sec) | Passes | Mean (µm) | T-test of mean |
|---|---|---|---|---|---|---|---|
| Blasted | n/a | n/a | n/a | n/a | n/a | 55.97 | - |
| LACR-1 | 0.25 | 24 | 110 | 12.7 | 2 | 54.14 | 0.42 |
| LACR-2 | 0.25 | 24 | 110 | 12.7 | 7 | 50.49 | 0.02 |
| LACR-3 | 0.25 | 24 | 110 | 6.4 | 4 | 64.14 | 1.00E-03 |
| LACR-4 | 0.25 | 24 | 110 | 25.4 | 14 | 52.37 | 0.10 |
| LSM-5 | N/A | 24 | 110 | 12.7 | 1 | 52.28 | 0.08 |
| LSM-6 | N/A | 24 | 110 | 12.7 | 10 | 56.99 | 0.64 |

The Mitutoyo portable surface profilometer provided a more detailed assessment of the surface topology. Representative line traces are shown in Figure 2:7 for abrasive blasted and laser treated surfaces. From such traces, standard roughness metrics were calculated: average (Ra), root mean squared (Rq), and the 10-point average peak to valley (Rz) roughness. The collective profilometer measurements (N=10) support the Elcometer data, i.e. that samples have distinct variances in surface roughness, but laser processing has no definitive effect, or obvious trend relative to baseline abrasive blasted surface (Table 2.2). As for example, there is a slight decrease in roughness values (*Ra, Rq, Rz*) for increasing number of laser passes from 2 (LACR-1) to 7 (LACR-2), but opposite trends was observed between LSM-5 (1 pass) and LSM-7 (10 passes). It is also noted that LACR samples have slightly higher roughness value compare to abrasive blasted samples and LSM samples have lowest roughness values.

**Table 2.2: Laser conditions of samples and surface profilometer readings, *Ra*, *Rq* and *Rz* values, and T-tests of lased condition Ra, Rq and Rz values versus the abrasive blasted condition.**

| Sample | Paint (mils) | Pulse (kHz) | Scan (Hz) | Sweep (mm/sec) | Passes | $R_a$ (μm) | $R_q$ (μm) | $R_z$ (μm) | $R_a$ T-test | $R_q$ T-test | $R_z$ T-test |
|---|---|---|---|---|---|---|---|---|---|---|---|
| Blasted | n/a | n/a | n/a | n/a | n/a | 5.96 | 7.36 | 32.20 | n/a | n/a | n/a |
| LACR-1 | 0.25 | 24 | 110 | 12.7 | 2 | 6.75 | 8.24 | 35.86 | 0.05 | 0.06 | 0.02 |
| LACR-2 | 0.25 | 24 | 110 | 12.7 | 7 | 6.56 | 8.08 | 35.28 | 0.07 | 0.07 | 0.02 |
| LACR-3 | 0.25 | 24 | 110 | 25.4 | 4 | 6.44 | 7.91 | 35.20 | 0.12 | 0.11 | 0.01 |
| LACR-4 | 0.25 | 24 | 110 | 25.4 | 14 | 5.94 | 7.33 | 32.11 | 0.97 | 0.94 | 0.96 |
| LSM-5 | n/a | 24 | 110 | 12.7 | 1 | 5.56 | 6.86 | 30.44 | 0.2 | 0.14 | 0.12 |
| LSM-6 | n/a | 24 | 110 | 12.7 | 10 | 5.60 | 6.95 | 30.67 | 0.24 | 0.22 | 0.14 |
| All Lased | n/a | 24 | 110 | n/a | n/a | 6.04 | 7.44 | 32.72 | 0.50 | 0.51 | 0.24 |

The profilometry-based roughness results are somewhat surprising, given the change in the surface appearance observed with scanning electron microscopy. Furthermore, there is a distinct appearance in the details of the profilometry traces themselves (Figure 2:7). Note that the abrasive blasted sample shows a level of fine-scale roughness (especially on the peaks) that

is not apparent in the laser treated. The laser treated surface profile shows rounded features on the tops of the peaks, which are consistent with the electron micrographs. The valleys still appear somewhat sharp in the profile of the laser treated surface. However, it is suggested that is a result of the tip-radius effect.

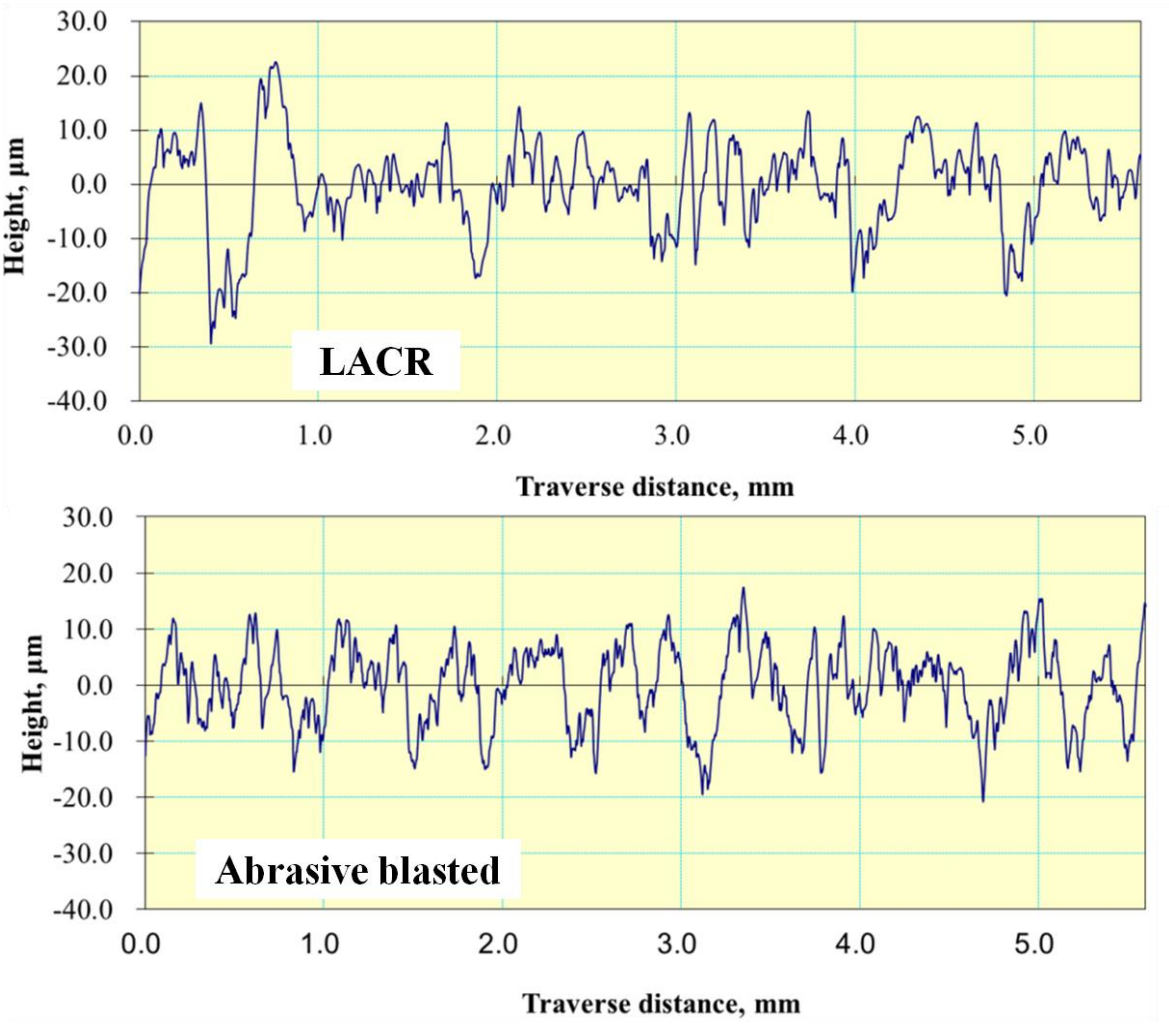


**Figure 2:7: Representative surface roughness profiles of a) LACR processed and b) abrasive blasted sample.**

The stylus based roughness measurement tends to “soften” the profile of the peaks and “sharpen” the profile of the valleys relative to the actual surface due to the finite radius of the tip. In order to minimize this systematic error, a simple profile correction method was employed, where profilometry data was corrected using the information about the position of the measured point and a rounded shape of probe with finite radius of 7 µm (verified by optical microscopy measurement [18]. The system records the position of stylus tip as it contacts the sample surface. This position equates to the center of the stylus tip. From this set of positions (x,y), the inherent challenge is to estimate where the surface contacted the tip on the outside of the sphere and have a set of positions that would fall on the sample surface (x’,y’). In order to do that, considering the positions of the two neighboring points. In the current computation, a circle was drawn around each data point to simulate the stylus tip geometry. In order to choose a point on each of these circles, the position of the neighboring circle was considered. Common tangent points are computed (P1 and P2 in Figure 2:8(a)), and it is assumed the contact point is the bisecting point of these two common tangents (shown in Figure 2:8(a)). A schematic of the corrected surface is shown Figure 2:8(b).

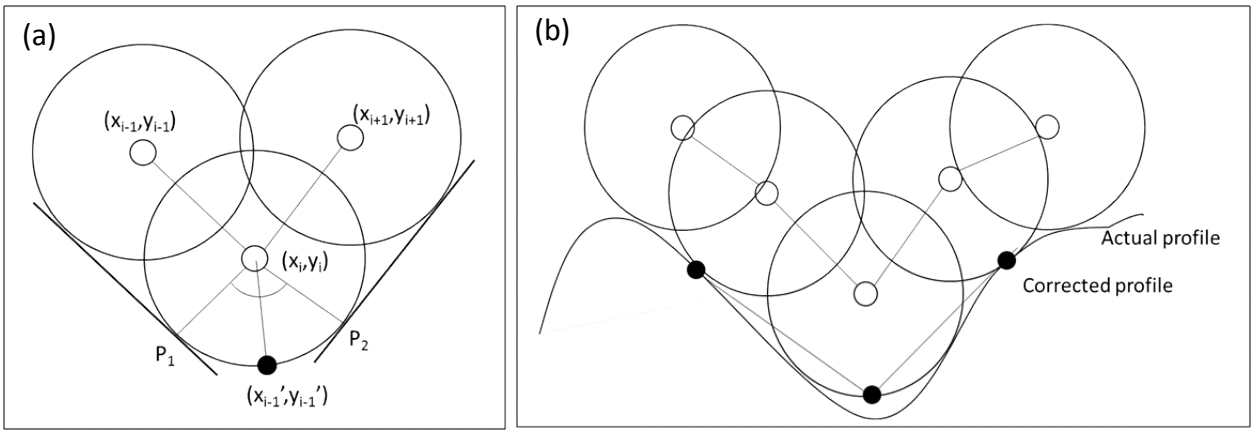


**Figure 2:8: Illustrations of (a) the construction of the common tangents and (b) the selection of the corrected positions.**

Figure 2:9 shows a sample corrected roughness profile along with the original roughness profile. It can be shown from the Figure 2:9, the adopted correction method reduces the distortion of the roughness profile, but it still potentially deviates from the actual profile due to the fact that it is not possible to measure valleys having a radius of curvature smaller than the stylus tip. Finally, roughness parameters, *Ra, Rq* were calculated from the corrected profile of both laser treated and abrasive blasted samples, as listed in Table 2.3. The results indicates that the values of Ra and Rq increased after performing the correction. However, similar to original measurement, no significant difference in roughness values between laser treated and abrasive blasted samples was observed after performing the correction.

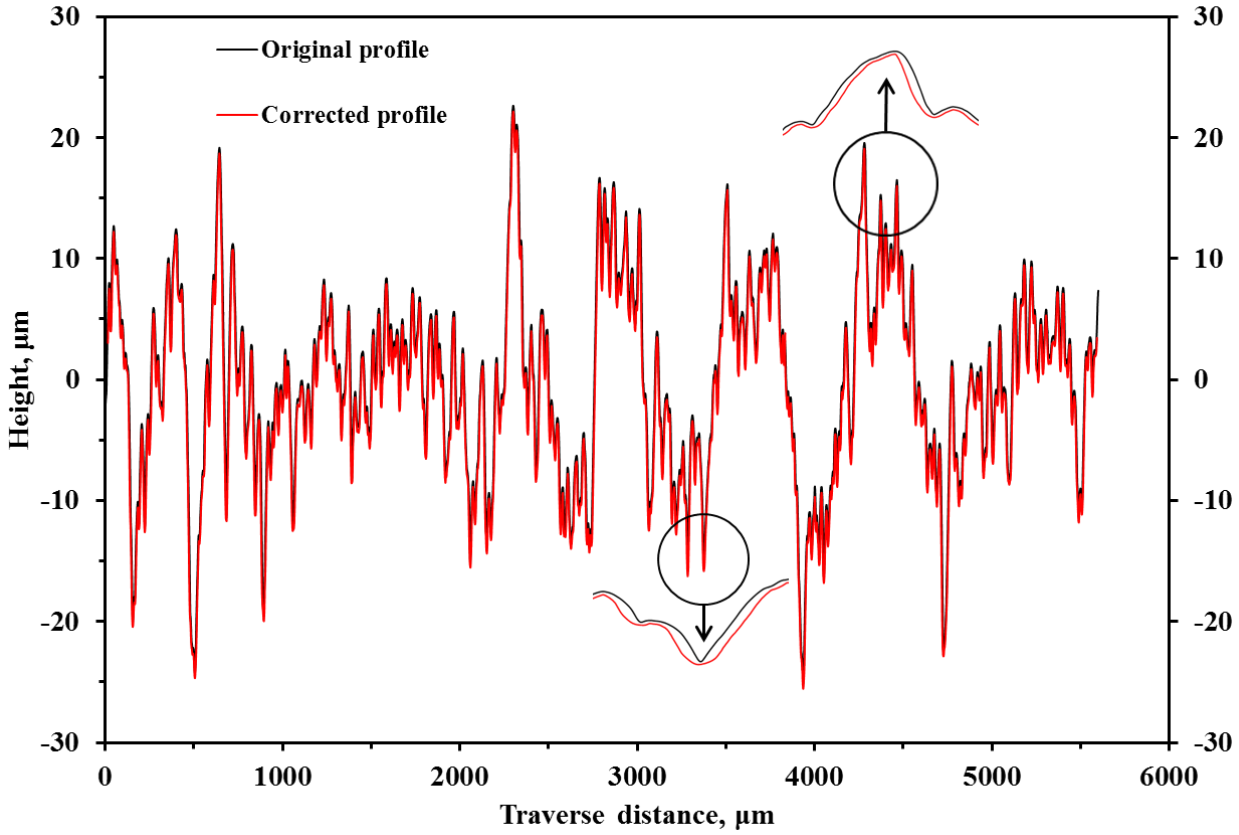


**Figure 2:9: Corrected roughness profile for tip radius r =7 µm showing peak sharpening and valley broadening after correction.**

**Table 2.3: Laser conditions of samples and Ra, Rq values of laser treated and abrasive blasted samples based upon tip-corrected stylus profilometry and optical profilometry.**

| | Laser processing parameters | | | | | Tip corrected | | Optical profilometry | |
|---|---|---|---|---|---|---|---|---|---|
| Sample | Paint (mm) | Pulse (kHz) | Scan (Hz) | Sweep (cm/s) | Passes | $R_a$ (µm) | $R_q$ (µm) | $R_a$ (µm) | $R_q$ (µm) |
| Blasted | N/A | N/A | N/A | N/A | N/A | 6.01 | 7.66 | 6.41 | 7.97 |
| LACR-1 | 0.25 | 24 | 110 | 12.7 | 2 | 6.71 | 8.42 | | |
| LACR-3 | 0.25 | 24 | 110 | 25.4 | 4 | 6.17 | 7.71 | 6.46 | 7.91 |
| LSM-6 | N/A | 24 | 110 | 12.7 | 10 | 5.46 | 7.06 | | |
| All Lased | N/A | 24 | 110 | N/A | N/A | 6.12 | 7.72 | | |

The results of the surface profile measurement using 3D optical microscopy, as shown in Figure 2:10, complement those obtained using the conventional Elcometer and profilometer. From the

Figure 2:10, it is obvious that the laser treated surface is less tortuous than the abrasive blasted surface. However, the overall scale of the roughness is similar, as it was for Elcometer and profilometer roughness measurements, as shown in Table 2.3. It is reiterated that all of the lased samples examined exhibited the appearance of having been melted and resolidified. There does not appear to be a laser processing parameter setting that would permit complete paint removal down to bare metal without some level of surface melting. It remains to be seen whether this has an adverse effect on any of the service properties of interest.

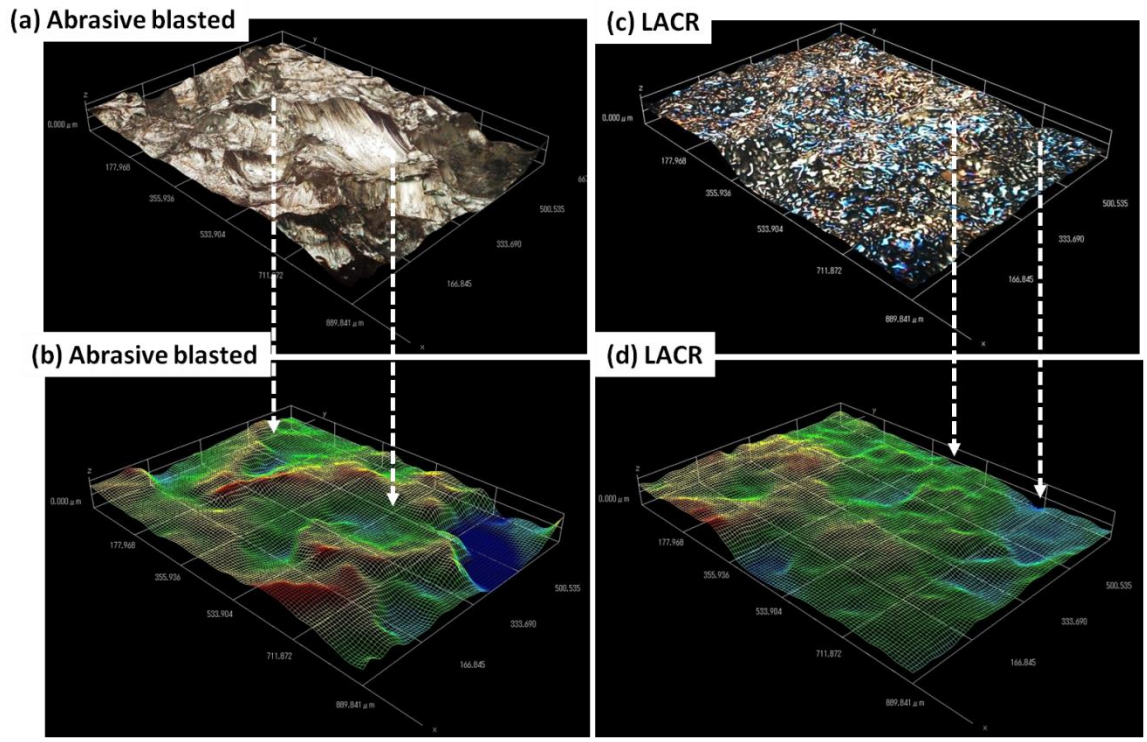


**Figure 2:10: 3D optical microscopy micrographs obtained using the HiroxTM 7700 provide another perspective on the comparison of surface profiles. Figures (a, b) are from an abrasive blasted sample while (c, d) are from a LACR sample (12.7mm/sec., 9 passes, 0.76 mm**

### 2.3.3 Microstructural Characterization

Cross-section analyses were performed to determine if there was any change to the underlying microstructure of the metal substrate after LACR. This information is useful in completing the assessment of surface melting and determining the depth of the melted region. Finally, it was of interest to determine if LACR induced any change in the mechanical properties (e.g. microhardness) relative to the baseline abrasive blasted condition as a result of the heat introduced. Microstructure of as-received grit blasted sample showed plastically deformed grain structure near the surface, as shown in Figure 2:11(a). Thickness of the deformed region is about 10 µm.

Cross-section analyses of metal substrate after LACR confirmed melting in the near surface regions with no discernible changes at greater depths. Melt depth varied between 1 to 5 µm. Figure 2:11(b) shows delineation of the laser solidified region, which is on the order of 5 µm in depth. This conclusion is based upon the fine, columnar-shaped grains, which form in the near surface region and the fact that the surface profiles of laser-processed material typically appear flowing or undulating in these cross-sectional views. They generally do not have the jagged appearance typical of the abrasive blasted material. However, the underlying material still exhibits elongated grains, deformed appearance suggesting that they have not recrystallized. This, in turn, suggests that the temperature gradient is extremely steep (hot enough to melt the near surface region, but not hot enough for long enough to significantly recrystallize the abrasive blasted material immediately below the previously melted layer). TEM analysis would be required to determine if localized recrystallization had occurred.

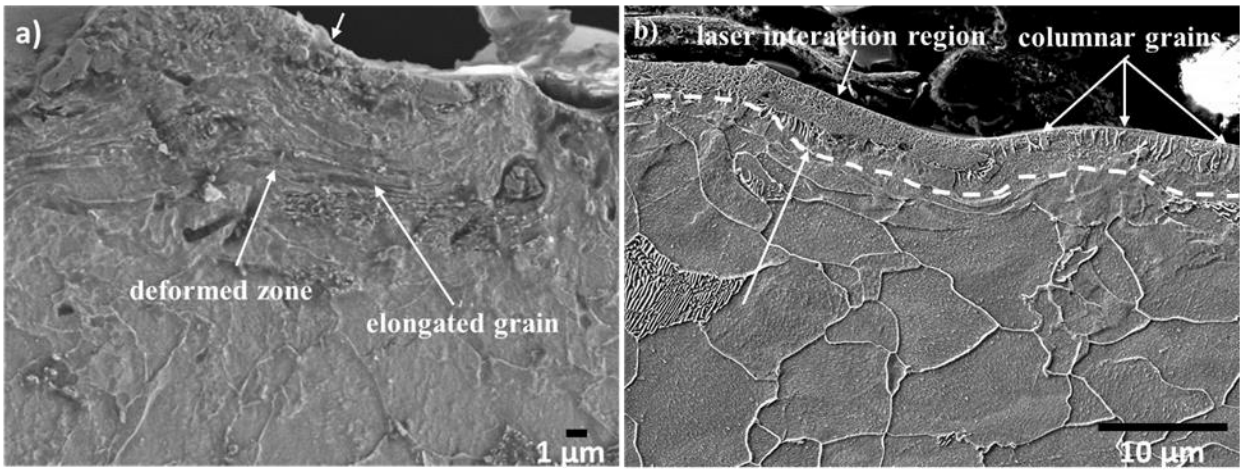


**Figure 2:11: Scanning electron micrographs of cross-section from a) abrasive blasted, and b) LACR sample (6.4 mm/sec., 4 passes, 0.25 mm paint).**

As mentioned above, the microstructure of laser melted and re-solidified layer consists of fine columnar grains, growing in the direction of the applied heat flux. Figure 2:12 shows higher magnification micrographs of a region, which has melted and re-solidified. Characteristics of a rapidly re-solidified material such as modified grain size and columnar grains are noted.

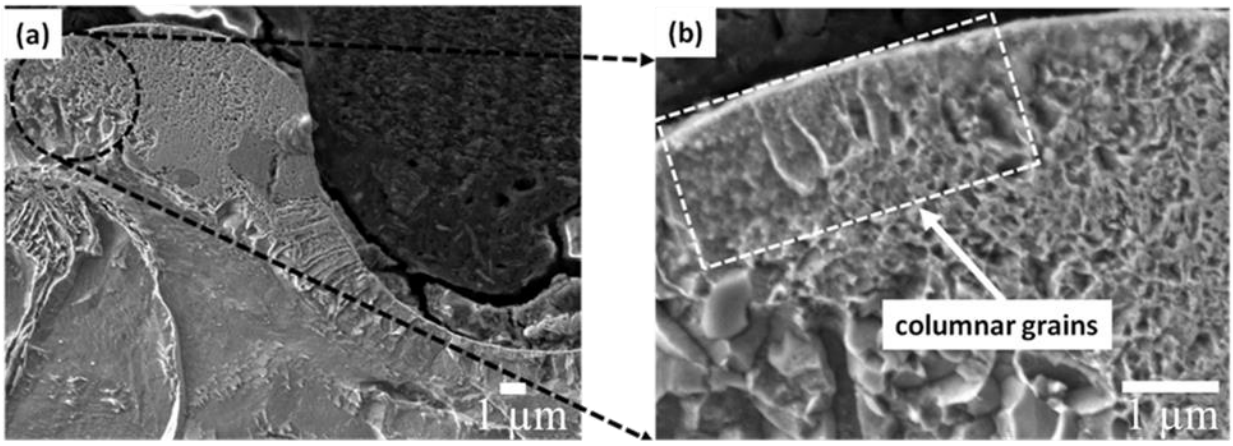


**Figure 2:12: Higher magnification scanning electron micrographs providing additional details of the columnar structures generally associated with a re-solidified microstructure of LACR process (6.4 mm/sec., 1 pass, 0.25 mm painted sample).**

### 2.3.4 Hardness

The hardness of laser treated (plate front) and abrasive blasted (plate back) surfaces of two samples were examined. At least 18 measurements were obtained from each sample surface. Averages and standard deviation of Rockwell B hardness measurements are listed in Table 2.4. The results show unequivocally that the overall surface hardness is unchanged from the originally abrasive blasted condition. Given the shallow depth (~5 µm) of the layer which is melted and resolidified and the subtle changes observed in the microstructure at larger depths, this result is not surprising. The Rockwell B indenter is large (1.588 mm), and the depth of the indentation is approximately 150 µm, for the present tests. Measurements obtained from the central region of plate cross-sections revealed that both abrasive blasted and laser-treated surfaces have hardness values that are elevated above the specimen interiors. It would be of interest to determine the hardness of the near-surface region. However, no standardized

hardness measurement technique can simultaneously poll such a shallow depth and tolerate the large surface roughness levels of the samples in this study.

**Table 2.4: Mean Rockwell B hardness values and standard deviations for laser treated and abrasive blasted surfaces.**

| Sample | Paint (mm) | Pulse (kHz) | Scan (Hz) | Sweep (mm/sec) | Passes | Mean | Standard Deviation |
|---|---|---|---|---|---|---|---|
| Abrasive blasted-1 | n/a | n/a | n/a | n/a | n/a | 85.6 | 2.2 |
| Abrasive blasted-2 | n/a | n/a | n/a | n/a | n/a | 84.5 | 3.2 |
| LACR-1 | 0.25 | 24 | 110 | 12.7 | 4 | 84.5 | 2.3 |
| LACR-2 | 0.76 | 24 | 110 | 12.7 | 9 | 85.2 | 2.3 |
| Bulk | n/a | n/a | n/a | n/a | n/a | 79.5 | 2.5 |

Vickers microhardness values from cross-sectioned samples were obtained at a depth of 70 µm from the top surface (lased), middle (bulk material), and approximately 70 µm from the bottom surface (abrasive blasted) regions of the specimen. The reason for taking the measurements at a finite depth is that the indentation has a finite size and the volume of material, which interacts with the indenter, is even larger. It is standard practice to obtain hardness data a distance no less than 2 ½ times the linear dimension of the indentation from the surface, in

order to avoid edge effects. Ten readings were taken in each region of each sample to obtain satisfactory statistics (Table 2.5). The results in Table 2.5 highlight the enhanced hardness of both the abrasive blasted and blasted/painted/LACR surface regions, as compared to the bulk. The data presented in Table 2.5 also show that different abrasive blasted samples have a slightly different hardness value. This variation in hardness value can be resulted from the variations in abrasive blasting parameters like shot velocity, impact angle etc. However, examining the effect of abrasive blasting parameters on the hardness evolution is beyond the scope of this study. Similar to the abrasive blasted surface, different laser treating conditions result in slightly different hardness values, but no obvious trend was observed. However, if all abrasive blasted and laser treated samples are considered collectively, there is no statistically significant difference between the hardness values recorded for the abrasive blasted surface and those of the blasted/painted/LACR surface, when collected from near surface region (~70 μm).

Finally, a series of microhardness measurements were performed as a function of depth from the surface of abrasive blasted samples as well as those subjected to LACR. As mentioned above, due to the size of the microhardness indentations, reliable microhardness measurements were only obtained for depths of 70 μm or more. Laser treating conditions of the samples selected for in-depth microhardness analysis are given below:

LACR-1: Abrasive blasted+0.25 mm paint, 12.7 mm/s sweep speed, 2 passes.

LACR-2: Abrasive blasted+0.25 mm paint, 12.7 mm/s sweep speed, 3 passes.

LACR-3: Abrasive blasted+0.25 mm paint, 25.4 mm/s sweep speed, 4 passes.

LSM: Abrasive blasted + no paint, 12.7 mm/s sweep speed, 10 passes.

**Table 2.5: Laser conditions of cross-sectional samples used in microhardness study, average LACR, bulk and abrasive blasted (AB) region values, and a T-test comparison.**

| Paint (mm) | Pulse (kHz) | Scan (Hz) | Sweep (mm/sec) | Passes | AVG LACR | AVG Bulk | AVG Blasted | T-test LACR-Bulk | T-test LACR-Blasted | T-test Blasted-Bulk |
|---|---|---|---|---|---|---|---|---|---|---|
| 10 | 24 | 110 | 6.4 | 1 | 200 | 165 | 194 | 2.3E-05 | 0.376 | 5.0E-05 |
| 10 | 24 | 110 | 6.4 | 2 | 208 | 170 | 190 | 1.3E-05 | 0.010 | 4.6E-05 |
| 10 | 24 | 110 | 6.4 | 3 | 199 | 163 | 186 | 2.8E-04 | 0.087 | 3.8E-09 |
| 30 | 24 | 110 | 6.4 | 4 | 195 | 163 | 212 | 4.9E-06 | 0.016 | 1.7E-06 |
| 30 | 24 | 110 | 6.4 | 5 | 190 | 174 | 201 | 3.9E-04 | 0.047 | 1.2E-04 |
| 30 | 24 | 110 | 12.7 | 8 | 202 | 172 | 200 | 3.6E-05 | 0.785 | 3.2E-05 |
| 30 | 24 | 110 | 12.7 | 9 | 201 | 172 | 198 | 1.8E-04 | 0.656 | 9.7E-06 |
| 30 | 24 | 110 | 6.4 | 5 | 227 | 166 | 199 | 1.2E-06 | 0.001 | 1.3E-09 |
| 30 | 24 | 110 | 6.4 | 5 | 220 | 162 | 206 | 1.4E-08 | 0.033 | 9.1E-07 |

Figure 2:13 presents the microhardness profiles obtained. Both the abrasive blasted and LACR surface regions, irrespective of laser processing conditions, have high hardness close to the surface and then the values gradually decrease to a depth of ~0.75 mm from the sample surface. However, changes in microhardness are more pronounced in the near surface region as compared to the deep region. Again, given the level of uncertainty, the hardness profile of the samples subjected to LACR is indistinguishable from that of the baseline abrasive blasted material. Perhaps nanoindentation on cross-sectioned samples would reveal a change induced by LACR. However, the present study does show that the depth of the affected region is less than 70 µm. This suggests that if there is any significant change in the mechanical properties of the metal substrate during LACR, it is restricted to the near surface region (< 70µm). This is consistent with microstructure evolution, as it was observed that LACR did not produce any significant change at greater depths. However, laser surface modification of bare surface (no paint) with a large number of passes (10 passes) was shown to slightly reduce the hardness values in this study.

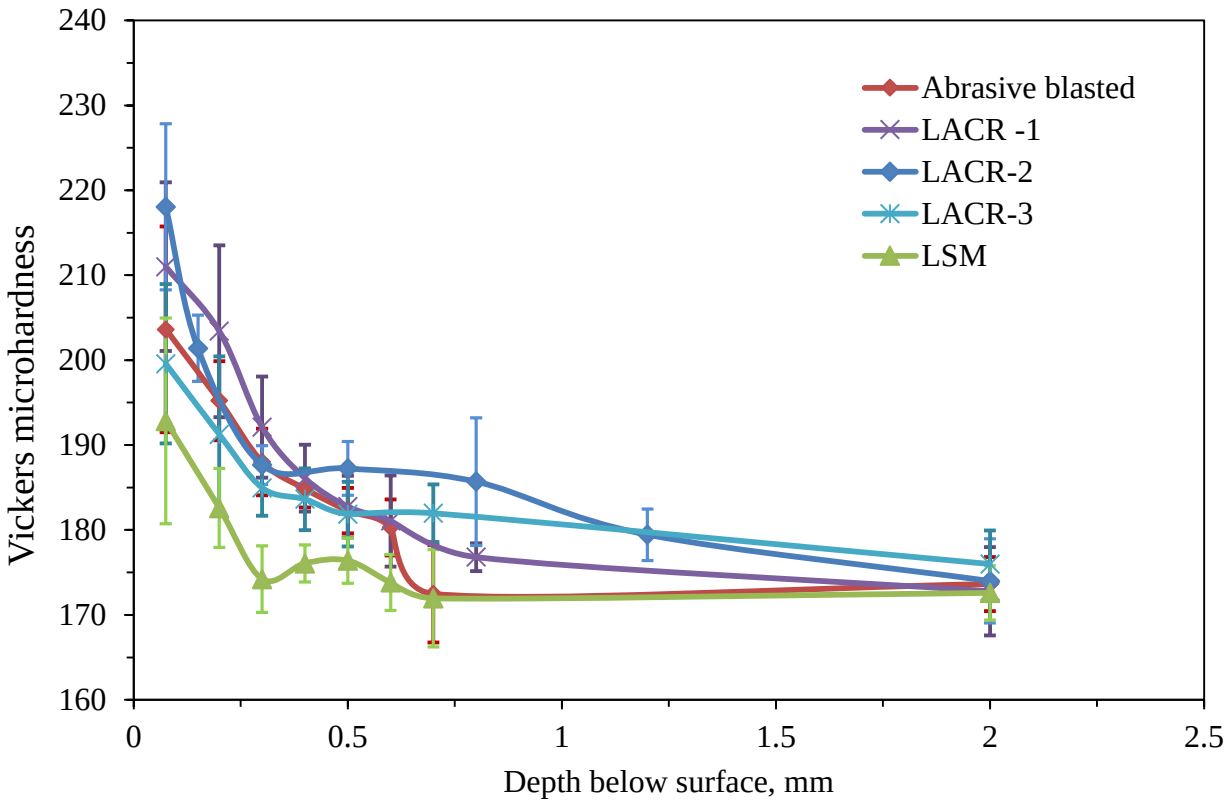


**Figure 2:13: Microhardness depth profile of abrasive blasted and laser treated samples.**

### 2.3.5 Adhesion Testing

The effect of laser ablation coating removal (LACR) on the surface roughness and subsequent coating adhesion was evaluated using a Pneumatic Adhesion Tensile Testing Instrument (PATTI). The mean pull off tensile strength (POTS) value and standard deviations are presented in Table 2.6 (n = 20 / plate). After the four lased sample plates and one control (abrasive blasted) sample were tested, the data revealed no statistically significant difference. In fact, all of the lased samples produced a slightly higher average POTS value than the baseline abrasive blasted sample. It can be stated with 91% confidence that the average adhesion strength of the

LACR samples is above the baseline value of 13.5 MPa (1958 psi) for the grit blasted control sample.

**Table 2.6: Results of Pneumatic Adhesion Tensile Testing Instrument (PATTI) tests performed on painted and LACR plus repainted samples.**

| Laser Conditions | | | | | |
|---|---|---|---|---|---|
| Paint (mils) | 10-10 | 10-10 | 30-10 | 30-10 | 10 |
| Pulse (kHz) | 24 | 24 | 24 | 24 | - |
| Scan (Hz) | 110 | 110 | 110 | 110 | - |
| Sweep (mm/s) | 12.7 | 25.4 | 12.7 | 25.4 | - |
| Passes | 4 | 6 | 8 | 9 | - |
| Mean (MPa) | 14.1 | 14.1 | 14.0 | 13.9 | 13.7 |
| SD (s) | 1.1 | 0.9 | 1.1 | 1.2 | 0.8 |
| Lower 95% Interval | 13.6 | 13.7 | 13.5 | 13.3 | 13.3 |
| Upper 95% Interval | 14.6 | 14.5 | 14.5 | 14.4 | 14.1 |
| p(mean < 13.5) | 0.98 | 0.99 | 0.97 | 0.91 | |
| T-Test, two | 0.24 | 0.13 | 0.48 | 0.79 | 1.00 |
| F Test, two | 0.56 | 0.77 | 0.36 | 0.19 | 1.00 |

It is noted that the surface roughness of both grit blasted and lased surfaces (initially grit blasted) is quantitatively similar using industry standard techniques. However, these measurements do not account for finer scale surface features. In contrast, electron micrographs shown in Figure 2:3 and Figure 2:5 show that a variation in the fine-scale tortuosity

is distinct between the two surface conditions. In general, it has been shown that, adhesion strength scales with increasing surface tortuosity [19-21], however, if the surface features are composed of distinct fine features; i.e. narrow valleys; paints may not completely penetrate into the surface irregularities. This could result in incomplete wetting which has been shown to reduce the POTS [20].

### 2.3.6 Solid-laser interaction modeling

Simulation of laser interaction with materials (SLIM) software [22] was used to model the heat flow during laser-steel surface interaction (only bare metal was considered). Modeling of this system could guide future processing parameter selection and provide additional understanding of the observed microstructure. The thermal and optical properties that were used during this modeling effort are given in Table 2.7. In this modeling approach, input parameters (thermal conductivity, specific heat capacity, reflectivity, and absorption coefficient) were considered independent of temperature change in both solid and liquid phases. Different sources reported different values for the same properties of steel. Therefore, a range of parameters was explored as shown in Table 2.7. The laser pulse assumed in this modeling study had a Gaussian-like spatial energy distribution.

**Table 2.7: Thermal and optical properties utilized in the modeling calculations.**

| | |
|---|---|
| Melting point (K) | 1809 K [23] |
| Boiling point (K) | 3273 K [23] |
| Thermal conductivity (W/cm.K) | $41 \times 10^{-2}$ (solid) [23] |
| | $33 \times 10^{-2}$ (liquid) [24] |
| Latent heat of melting ($J/cm^3$) | 2100 [23] |
| Latent heat of vaporization ($J/cm^3$) | 47840 [25] |
| Specific heat capacity ($J/cm^3 \bullet K$) | 4.5 (solid) [23] |
| | 5.3 (liquid) [26] |
| Reflectivity | 0.7-0.8 (solid) [27] |
| | 0.55-0.6 (liquid) [28] |
| Absorption coefficient ($cm^{-1}$) | $5 \times 10^5$ (solid) [25] |
| | $4 \times 10^5$ (liquid) [28] |

Figure 2:14 shows the steel surface temperature as a function of time for 83 ns laser pulses at different fluences. It is observed that when the laser fluence is less than 2.3 J/cm2, surface temperature does not reach the melting point. At fluences greater than 2.3 J/cm2, the surface temperature is predicted to exceed the melting point of steel. At the melting point, the surface temperature remains constant while latent heat of fusion is absorbed. The surface temperature then rises until the end of the pulse. At 3.7 J/cm2 fluence, surface temperature reaches the vaporization temperature. After the pulse turns off, the liquid cools rapidly until reaching the melting point, at which point the latent heat of fusion is released, and then it cools slowly to room temperature. Finally, melt depth was predicted from the program.

Figure 2:15 shows the melt depth of steel substrate as a function of time for 83 ns laser pulses at a range of fluences. It is also observed that not only the melt depth increased, but also melting occur over a longer period with increasing laser fluences. This is due to the fact that when laser fluence is higher, the absorbed energy is also higher. The maximum predicted melt depth using this software is ~ 0.65 μm at 3.7 J/cm2, which is lower than the experimentally observed melt depth. This may be due to the fact that absorptivity of the baseline abrasive blasted sample is higher than the absorptivity value that has been used as input parameters due to its high surface roughness. Typical values reported in the literature refer to smooth, polished surfaces. Additionally, it should be noted that these predictions do not include the effect of the coating, which could lower the temperature of the substrate due to latent heat of evaporation of the coating and absorption of the incoming beam by the ablation plume.

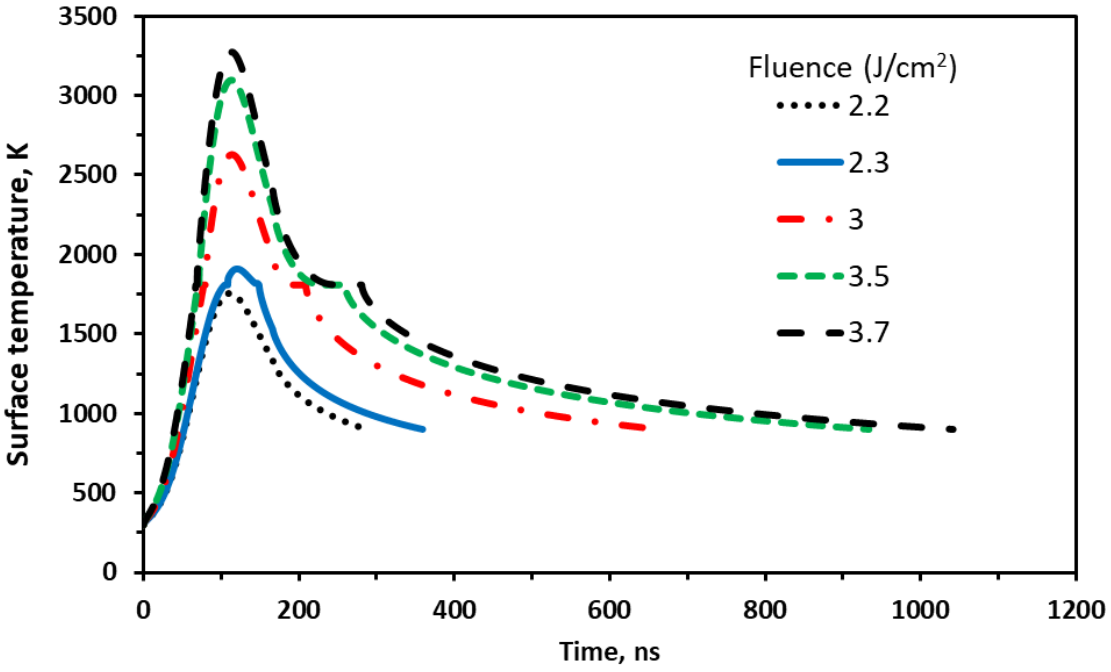


**Figure 2:14: Surface temperature of a steel substrate irradiated by a Nd:YAG laser operating at 1064 nm with a 83 ns pulse duration as a function of fluence.**

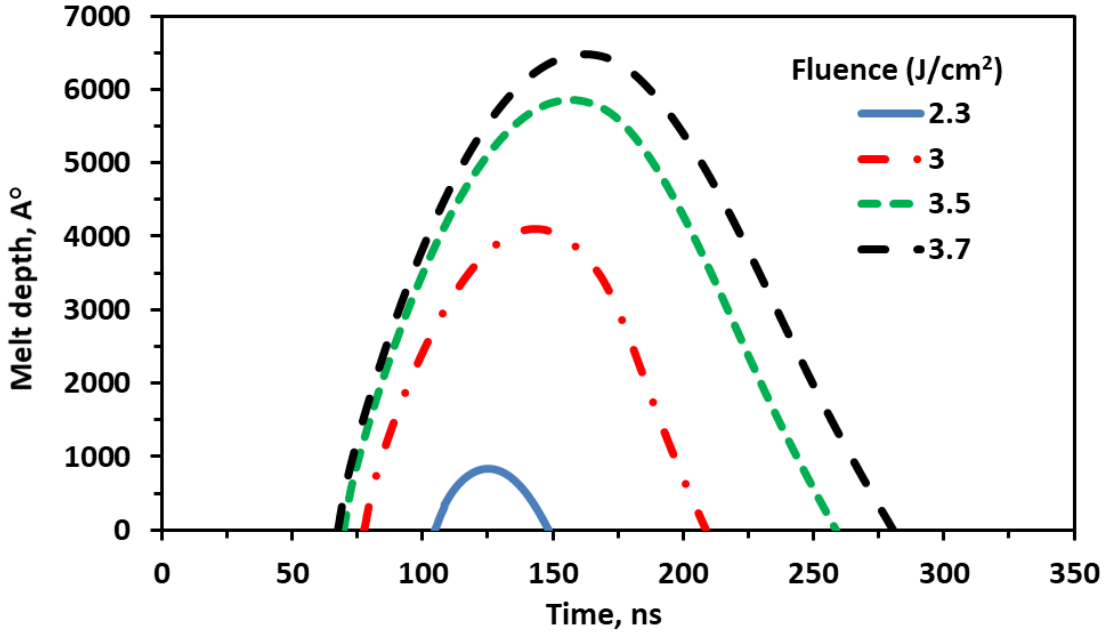


**Figure 2:15: Melt depths of the steel substrate as a function of time and fluence.**

This solid-laser interaction simulation results indicate that there is a fluence threshold below which surface melting of steel substrate will not occur. Therefore, it is claimed that by proper selection of laser processing parameters; i.e. laser power, pulse duration, spot size, pulse frequency one could essentially avoid the surface melting of underlying substrate at the expense of low paint stripping rate. However, all processing parameters explored in this study, where high paint stripping rate was desired, resulted in surface melting. This superficial melting does not appear to adversely affect the adhesion properties or fatigue performance [14].

## 2.4 Summary and Conclusions

Effects of laser ablation coating removal (LACR) from a high strength shipbuilding steel have been assessed. Like any coating removal process, LACR was evaluated relative to the following three overarching issues: effectiveness of material removal, impact on the substrate material, and suitability of affected substrate for subsequent coating application. The following conclusions can be made:

a) The LACR process was effective for the removal of a typical epoxy-based coating. With the laser employed, multiple passes were required to remove the coating, with an increased number of passes required at higher sweep speeds. Between two and four passes were required to remove 0.25 mm(10 mils) of an oxide red epoxy coating from steel at an automated sweep speed of 12.7 mm/ sec (0.5 in/sec), which is considered slow by industry standards. An effective coating removal rate of 45 sq. in. per minute (~19 sq. ft. per hour) was measured using the 7.6 cm laser scan width on 0.25 mm coated samples. This rate was dependent upon the frequency of laser window cleaning and laser focusing conditions.

b) Scanning electron microscope (SEM) imaging of the surface and cross-sections reveals that the underlying metal substrate is melted and re-solidified during LACR. The depth of the observed melted region varied between 1 and 5 μm. No microstructural change was observed at greater depths.

c) The appearance of the surface is clearly changed at the microscopic level. However, conventional surface roughness (profile) measurements using an Elcometer 224 (or stylus profilometry) indicate no statistically significant change in the roughness.

d) Pneumatic Adhesion Tensile Testing Instrument (PATTI) studies performed on samples repainted after LACR confirm equivalent, or superior, performance to the abrasive blasted and painted samples (all samples exhibited >13.5 MPa, 91% confidence).

## Acknowledgements

This work was supported by the Commonwealth Center for Advanced Manufacturing (CCAM), Mr. Matthew Stremler as Program Manager. The authors would also like to thank Vincent Sloan and Christopher A. Calhoun for their help with hardness measurements and implementation of the tip correction algorithm.

## References


[1] J.P. Sylvestre, S. Poulin, A.V. Kabashin, E. Sacher, M. Meunier , J.H.T. Luong, J. Phys. Chem. B. 108 (2004) 16864-16869.

[2] D. Triantafyllidis, L. Li, F. Stott, Mater. Sci. Eng. A. 390 (2005) 271-277.

[3] W. Steen, Laser surface cladding, in: C.W. Draper, P. Mazzoldi (Eds.), Laser surface treatment of metals, NATO Science Series E. Springer Netherlands, 1986, pp. 369-387.

[4] A.C. Tam, H.K. Park, C.P. Grigoropoulos, Appl. Surf. Sci. 127(1998) 721-725.

[5] J.S. Selvan, K. Subramanian, A. Nath, J. Mater. Process.Technol. 91 (1999) 29–36.

[6] J.M. Vitek, A. Dasgupta, S. David, Metall. Trans. A. 14 (1983) 1833-1841.

[7] J.D. Head, J.P. Niedzielski, Laser Paint Stripping, Laser Tech. Inc. MI, 1991.

[8] P. Lovoi, Laser focus world, 30 (1994) 75-82.

[9] G. Schweizer, L. Werner, Industrial 2-kW TEA CO2 laser for paint stripping of aircraft, in: Gas flow and chemical lasers: Tenth International Symposium, 2502 (1995) 57-62.

[10] G.X. Chen, T.J. Kwee, K.P. Tan, Y.S. Choo, Appl. Phys. A, 101(2010) 249-253.

[11] E.D. Oller, Naval application of laser ablation paint removal technology, in: U.S. Navy Corrosion Conference, Norfolk, VA June 2011.

[12] R. Srinivasan, Interaction of laser radiation with organic polymers, in: J.C. Miller (Ed.), Laser Ablation: Principles and Applications, Springer Series of Mater. Sci., 28 (1994) 107–133.

[13] K. Liu, E. Garmire, Appl. opt. 34 (1995) 4409- 4415.

[14] M. Shamsujjoha, S.R. Agnew, J.R. Brooks,T.J. Tyler, J.M. Fitz-Gerald, Surf. Coat.Technol., 281(2015), 206-214.

[15] K. Sampath, J. Mater. Eng. Perform. 15(2006) 32-40.

[16] T.L. Perry, D. Werschmoeller, N.A. Duffie, X. Li, F.E. Pfefferkorn, J. Manuf. Sci. Eng., 131 (2009) 021002.

[17] H. Stamm, U. Holzwarth, D.J. Boerman, F. Dos Santos Marques, A. Olchini, R. Zausch, Fatigue Fract. Eng. Mater. Struct., 19 (1996) 985-995.

[18] D.H. Lee, N.G. Cho, Meas. Sci. Technol., 23 (2010) 105601.

[19] H.J. Roper, R.E.F. Weaver, J. Protect. Coat. Linings, 22 (2005) 52-64.

[20] P.A. Sørensen, S. Kiil, K. Dam-Johansen, C.E. Weinell. Prog. Org. Coat. 64 (2009) 142-149.

[21] B.R.Troconis, G. Frankel, Surf. Coat.Technol. 236 (2013) 531-539.

[22] R. Singh, J. Viatella, JOM 44 (1992) 20-23.

[23] M.F. Ashby, K.E. Easterling, Acta Metall. 32 (1984) 1935-1948.

[24] T. Nishi, H. Shibata, H. Ohta, Y. Waseda, Metall. Mater. Trans. A 34 (2003) 2801-2807.

[25] H. Koch, C. Kägeler, A. Otto, M. Schmidt, Phys. Procedia 12 (2011) 428-436.

[26] R. Urquhart, R. Guthrie, D. Howat, J. S. A. Inst. Min. Met. 74 (1973) 132-139.

[27] J.D. Kim, KSME J. 4 (1990) 32-39.

[28] A. Mahrle, E. Beyer, J. Phys. D: Appl. Phys. 42 (2009) 175507.

# Chapter 3: Effects of Laser Ablation Coating Removal (LACR) on a Steel Substrate: Part 2: residual stress and fatigue


## Abstract

The effects of laser ablation coating removal (LACR), from high strength shipbuilding steel, on fatigue performance have been investigated relative to abrasive blasted specimens. It was shown that the fatigue behavior of the steel subjected to LACR is statistically unchanged from those of the baseline material. Residual stress, surface roughness and fractographic analyses were employed to rationalize the fatigue performance. X-ray measurements revealed that tensile residual stress was induced in the surface by LACR. However, depth-resolved residual stress measurement showed that the tensile residual stress is limited to a shallow depth below which there is a deep case of balancing compressive residual stress. Finally, scanning electron microscopic (SEM) analysis of fracture surfaces showed that cracks initiated from valleys in the roughness profile. Thus, the observed fatigue performance is attributed to the combined effects of residual stress and surface roughness.


## 3.1 Introduction

Laser removal of protective coatings from naval vessels is a promising alternative to traditional paint stripping methods such as grit blasting, chemical paint stripping, needle grinding etc. Over the last few decades, abrasive blasting was the most widely used paint stripping method used for large area marine structures, though smaller repairs may be performed using various handheld tools. Despite the inherent problems associated with abrasive blasting, like noise,

dust, hazardous secondary waste, it possesses an intrinsic benefit of introducing compressive surface residual stress in materials, which can improve fatigue life. In order to substitute for this well-established paint stripping method, the fatigue performance after performing LACR has to be comparable. However, most of the work in this field [1-4] has been focused on the effectiveness of this technology for paint removal, in terms of cleanliness and removal rate, with examination of the effects of laser parameters, like laser power density, to achieve a high degree of cleanliness with a good paint removal rate. Though such studies have a potentially high industrial value, it is also important to understand the effect of this laser paint stripping method on the underlying substrate before one can replace the traditional paint stripping method with this novel technology. A limited number of studies focused on the possible effects of LACR on the underlying substrate [5-7], and these studies raised a number of possibilities related to near surface melting: reduction in surface roughness resulting in reduced subsequent coating adhesion and degradation of fatigue performance due to near surface tensile residual stress introduced during melting and resolidification.

Chapter 1 of this study reported the effect of LACR on surface roughness, microstructure, hardness, and subsequent coating adhesion. Evidence of surface melting during LACR, as observed from surface imaging and cross-sectional microstructure characterization, suggests that tensile residual stresses may develop [8, 9]. Near surface tensile residual stresses are known to reduce the fatigue performance of materials [10, 11]. Thus, the aim of this present work is to investigate the effect of laser ablation coating removal on the residual stress state and fatigue performance of the underlying substrate material (carbon steel). The relative

fatigue resistance of LACR processed, and abrasive blasted (baseline) materials are rationalized in terms of the induced residual stress state and surface asperities (described in Chapter 1).

## 3.2 Materials and Methods

The material used in this investigation was a high strength steel (HSS) used in shipbuilding. The steel plate received in abrasive blasted condition is considered as the baseline material because this is the typical condition prior to painting. The steel plate was coated with different thicknesses of red epoxy, similar to the paint used in marine vessels for corrosion protection. Laser ablation coating removal (LACR) was performed using an adapt Laser Systems model CL1000QNd:YAG, operating at the fundamental wavelength (1064 nm) and pulse duration of 83 ns. Laser processing was performed at a pulse frequency of 24 kHz, scan rate of 110Hz, sweep speed of either 1.3 cm/s or 2.5 cm/s and the number of laser passes was varied between 1 and 14. In order to achieve higher ablation efficiency to meet the industrial requirements of paint stripping rate, nanosecond pulse laser was selected instead of ultrashort pulse laser which causes less thermal damage to underlying materials [13]. More detail concerning the abrasive blasting and laser processing conditions is provided in Chapter 1.

X-ray diffraction residual stress measurements were performed using a Panalytical X'Pert Pro MPD X-ray diffractometer using Bragg-Brentano focusing geometry with a *Cr-*$K_\alpha$ sealed tube source operated at 30 kV and 55 mA. The diffraction angle step size of 0.2-0.3° with counting time of 10-20 seconds per step was used. Both large step size and inadequate time counts per step can both cause error in determining peak position and small changes in peak position will results in considerable changes in the magnitude of the residual stress. Therefore, it is

important to employ a step size which enables us to precisely define the peak position. However, in order to accurately define a peak, FWHM/step size should be 5 to 10% and/or there should be 10-15 points above the FWHM [13]. Even in the worst case scenario of this study (0.3 step size), meets both requirements. In addition, a Gaussian fit to the experimental data showed a very high value of goodness of fit $R^2$ (>96%) in all cases. After considering all these factors, and in order to save experimental time a relatively "large" step size was selected for this study. The measurements were performed according to the NPL Good Practice Guide [14] which describes the $d$ vs. $\sin^2\psi$ method, where $d$ is the lattice spacing of the {211} planes of the steel and $\psi$ is the angle between the diffraction vector and sample surface normal. The tilts were performed on the $\omega$ axis (not the $\chi$). One residual stress measurement typically took 70-80 minutes. The diffraction peak angular positions were determined for negative $\psi$ tilts of 0, -18.43, -26.56, -33.21, -39.23,-45.0, - 50.77 and -56.79 using nonlinear regression of the experimental data with a Gaussian function. The lattice spacing ($d$) for each tilt was calculated using Bragg's law ($\lambda = 2d\sin\vartheta$), where $\lambda(Cr\text{-}K_\alpha) = 2.29$ Å, and then plotted against $sin^2\psi$. The representative data presented in Figure 3:1. Figure 3:1 reveal a linear relation between $d$ vs.$sin^2\psi$, with high goodness of fit $R^2$ values no less than 0.98 for all surface measurements made in the study. However, due to the presence of stress gradient, subsurface residual stress measurement showed a slight curvature in the $d$ vs. $sin^2\psi$ plot, especially in the laser treated samples due to higher stress gradient relative to abrasive blasted samples. Goodness of fit $R^2$ is still high, higher than 95% for most of the measurement. This indicates the applicability of the approach and shows that shear strain components $\varepsilon_{13}$ and $\varepsilon_{23}$ are both close to zero. However, it will be shown that a different level of residual stress is present along the LACR scan and

sweep directions (see Chapter 1). In most of the data present below, only the sweep direction stress is shown since this correlates with the axis of the fatigue samples. The negative slope in the *d* vs. $sin^2\psi$ plot (Figure 3:1(a)) indicates that compressive residual strain is present in the abrasive blasted sample, while the positive slope in the case of the laser treated sample (Figure 3:1(b) is an indicator of tensile residual strain.

Assuming elastic isotropy of the polycrystalline steel and a plane stress condition in the sample surface, the slope of the line of *d* vs. $\sin^2\psi$ plot is proportional to the normal stress within the sample surface along the ø direction according to:

$$\sigma_{ø} = \frac{E}{(1+\nu)sin^2\psi}\left(\frac{d_\psi - d_n}{d_n}\right) \qquad [3.1]$$

where *E* is the Young's modulus, *v* is the Poisson's ratio, and $d_\psi$ is the interplanar spacing measured at each tilt angle; $d_n$ is the spacing for $\psi$ = 0º (i.e. the diffraction vector is parallel to the plate surface normal direction). The magnitudes of the residual stresses were computed employing the following elastic constants typically observed for steel, *E*= 200 GPa and *v* = 0.3.

Finally, the residual stress uncertainties in each sample were calculated by considering the error propagation from uncertainties in the *d* vs. $sin^2\psi$ linear fit [15].

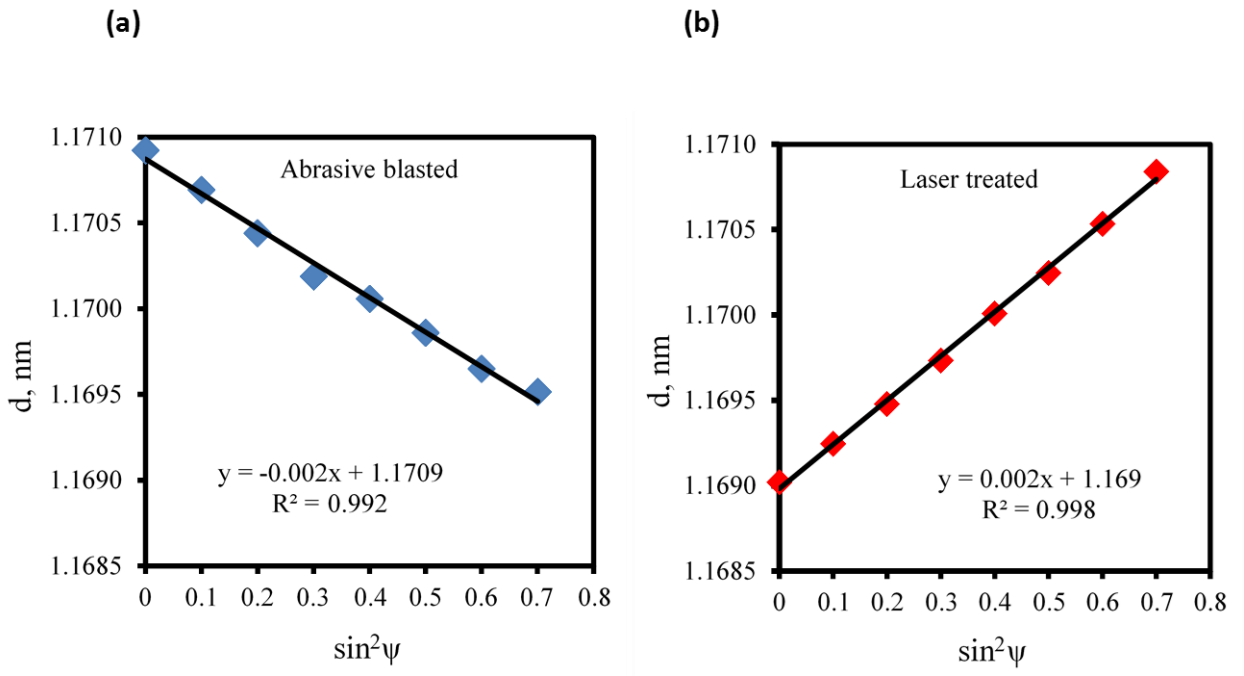


**Figure 3:1: *d* spacing changes linearly with $sin^2\psi$ for both a) abrasive blasted and b) laser treated specimens. A compressive surface residual stress is shown for the abrasive blasted, while a tensile surface stress is shown in the laser treated.**

The variation of the residual stress as a function of depth was determined via progressive layer removal by electropolishing and subsequent residual stress measurement using X-ray diffraction. Electropolishing was performed at 15 V DC in a solution of 6% perchloric acid, 10% butyl cellosolve, 70% ethanol, and 14% water at room temperature. A micrometer was used to measure the thickness of the layer removed. As an example, to remove a 50 µm surface layer from a 25 cm × 20 cm patch required 5 minutes of electropolishing. Correction of the measured residual stress values due to redistribution and relaxation of the stress in the exposed surface was calculated according to the solution proposed by Sikarskie [16], which is based on the original solutions of Moore and Evans [17].

$$\sigma(z_1) = \sigma_m(z_1) + 2\int_{z_1}^{H} \frac{\sigma_m(z)}{z} dz - 6z_1 \int_{z_1}^{H} \frac{\sigma_m(z)}{z^2} dz \quad [3.2]$$

Progressive layer removal was used to a depth of up to 800 µm.

Fatigue tests were performed using an Instron 1320 servo hydraulic load frame with 8500 computer control and data acquisition, aligned according to ASTM E-1012. The fatigue tests were performed according to ASTM E-466, with flat, dog-bone sample geometry. The samples were conventionally machined with an oil-based lubricant to minimize potential corrosion effects. Notably, the backsides of the samples (not painted or laser treated) were surface ground to minimize the chance of crack initiation from that surface, which was not under investigation. Of the thirty-three samples tested in this study, only in two cracks initiated from the surface ground backside of the samples. Similarly, the corners of the gage section and fillet region were rounded (minimum corner radius of 0.8 mm) to avoid initiating at that potential stress concentrator. The fatigue tests were performed under sinusoidal load control, at a stress ratio of $R$= 0.1, and a frequency of 10 Hz. The tests were stopped when specimens broke or after $5\times10^6$ cycles, whichever came first. The fracture surfaces were examined using Scanning Electron Microscopy (SEM) within a JEOL 6700 cold-field emission gun instrument operated at 15 kV, 12 µA probe current and 15-24 mm working distance.

## 3.3 Results and Discussion

### 3.3.1 Residual Stress

In order to understand the effect of LACR on the residual stress state, a wide range of processed samples were investigated and can be divided into five types:

I. Unblasted

II. Unblasted and laser processed

III. Abrasive blasted

IV. Abrasive blasted, and laser processed

V. Abrasive blasted, painted, and laser processed

The residual stress state in the surface of the unblasted (type-I) showed nominally zero residual stress (±40 MPa). Laser surface modification of these unblasted surface (type-II) (using the same laser conditions as LACR) imparts a biaxial tensile residual stress. This is consistent with the microstructural characterization, which reveals that laser processing formed a thin molten and re-solidified layer. During solidification of the molten layer, a high thermal gradient existed. Due to this thermal gradient, contraction of the solidifying metal is constrained by the colder interior, which places the near surface region in tension. In most cases, the magnitude of the surface residual stress in the laser scan (longitudinal) direction was larger than that in the sweep (transverse) direction. Tensile residual stresses up to 505±10 MPa along the laser scan direction and 319±5 MPa along the laser sweep direction were measured after 10 passes of laser scanning over the unblasted surface. It was observed that an increasing number of laser passes increased the level of residual stress. However, the largest single increase in residual

stress occurs with the first pass over bare metal. A single pass of laser scan over the unblasted surface imparted longitudinal and transverse residual stresses of 406±9 MPa and 229±5 MPa, respectively.

Abrasive blasting (type-III) creates a layer of plastic deformation with an elastically deformed region underneath as the material "attempts" to recover its original shape. This places the surface layer in compression. Residual stress measurements of 12 abrasive blasted samples revealed a consistent uniform biaxial compressive surface residual stress of magnitude -264±24 MPa, these values are the arithmatic average of 12 samples measured and the uncertainty value quoted here is the standard deviation of these measurements. Laser surface modifications (LSM) of the abrasive blasted (type-IV) surface causes the residual stress to swing from compressive to strongly tensile. High stresses were observed after 10 passes (395±7 MPa and 279±8 MPa along the scan and sweep directions, respectively). However, as emphasized above, only a single pass was required to impart a large increase in the residual stress (319±3 MPa and 213±12 MPa, scan and sweep, respectively).

The presence of paint actually diminishes the swing in residual stress (from compressive in the abrasive blasted to tensile in the laser treated). Presumably, this is due to less heat being imparted to the steel when there is an ablative/evaporative coating on the surface during laser treatment, in addition to attenuation of the incoming laser beam by ablation products (the plume). It was also observed that LACR of the thickly painted (30 mils) sample imparted lower tensile residual stress compare to thinly painted (10 mils) samples. For example, LACR processing parameters of 1.3 cm/s sweep speed and 7 passes, imparted a tensile residual stress

of 235±9 MPa stress after removing 0.76 mm (30 mils) paint and 314±15 MPa after removing 0.25 mm (10 mils) of paint. However, the typical residual stress level after performing LACR is 242±63 MPa, regardless of paint thickness or laser processing condition. These latter values are the average and standard deviation of 10 distinct samples in condition type-V (abrasive blasted, painted, and laser processed). This range has an upper bound (352±11 MPa) which corresponds to the scan direction after a large number of laser passes and a lower bound (95±8 MPa) which corresponds to the sweep direction after a small number of passes over originally thick (30 mils) paint. It was also noted that the highest residual stresses were observed after a large number of laser passes, as in the LSM of unblasted and abrasive blasted surfaces. Table 3.1 lists the laser processing conditions and magnitudes of surface residual stress measured during this course of study.

Figure 3:2 summarizes the effect of surface treatments on the surface residual stress state of the investigated samples. All the laser processing experiments were carried at 24 kHz pulse frequency, 110 Hz scan rate, and 1.3 cm/s sweep speed.

**Table 3.1: Laser processing conditions of samples and surface residual stress measurement in laser scan and sweep direction. Uncertainty values listed here are calculated by error propagation from the uncertainty of linear fit of *d* vs. $sin^2\psi$.**

| Sample | Paint (mm) | Pulse ( kHz) | Scan (Hz) | Sweep (mm/sec) | Passes | Direction | Magnitude (MPa) |
|---|---|---|---|---|---|---|---|
| LSM -1 ( unblasted) | n/a | 24 | 110 | 1.3 | 1 | Scan | 406±9 |
| | | | | | | Sweep | 229±5 |
| LSM -2 ( unblasted) | n/a | 24 | 110 | 1.3 | 10 | Scan | 505±10 |
| | | | | | | Sweep | 319±5 |
| LSM -3 (blasted) | n/a | 24 | 110 | 1.3 | 10 | Scan | 395±7 |
| | | | | | | Sweep | 279±8 |
| LSM -4 (blasted) | n/a | 24 | 110 | 1.3 | 1 | Scan | 319±3 |
| | | | | | | Sweep | 213±12 |
| LACR -1 | 0.25 | 24 | 110 | 1.3 | 2 | Scan | 218±8 |
| | | | | | | Sweep | 209±8 |
| LACR -2 | 0.25 | 24 | 110 | 1.3 | 3 | Scan | 222±19 |
| LACR -3 | 0.25 | 24 | 110 | 1.3 | 4 | Scan | 341±6 |
| LACR -4 | 0.25 | 24 | 110 | 2.5 | 4 | Scan | 302±5 |
| | | | | | | sweep | 198±12 |
| LACR -5 | 0.25 | 24 | 110 | 1.3 | 4 | Scan | 259±15 |
| LACR -6 | 0.25 | 24 | 110 | 1.3 | 7 | Scan | 314±15 |
| | | | | | 7 | Sweep | 200±7 |
| LACR -7 | 0.25 | 24 | 110 | 2.5 | 14 | Scan | 352±11 |
| | | | | | | Sweep | 258±8 |
| LACR -8 | 0.76 | 24 | 110 | 0.64 | 5 | Scan | 165±16 |
| | | | | | | Sweep | 95±8 |
| LACR -9 | 0.76 | 24 | 110 | 0.64 | 5 | Scan | 187±11 |
| LACR -10 | 0.76 | 24 | 110 | 1.3 | 7 | Scan | 235±9 |
| LACR -11 | 0.76 | 40 | 80 | 1.3 | 8 | Scan | 271±5 |
| | | | | | | Sweep | 248±14 |
| LACR -12 | 0.76 | 24 | 110 | 1.3 | 9 | Scan | 242±13 |
| LACR -13 | 0.76 | 24 | 110 | 1.3 | 9 | Scan | 286±7 |

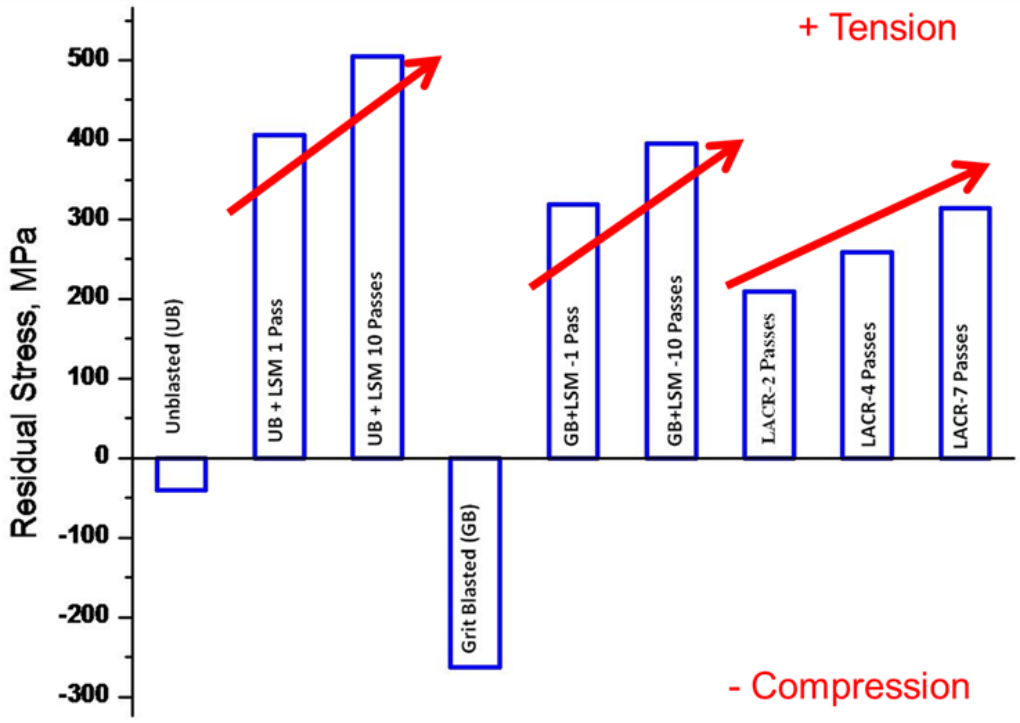


**Figure 3:2: Effect of different surface processing conditions on residual stress. Note the trend of increasing LSM or LACR passes results in higher tensile surface residual stress.**

It is acknowledged that there can be large variations in the residual stress in the near surface region. However, the net section stress must integrate to zero in the unloaded condition. For example, compressive surface stresses imparted by abrasive blasting are balanced by tensile stresses within the plate interior. Because of the strong distinctions noted between the abrasive blasted, and laser treated surface stresses (compressive vs. tensile), it is of interest to determine how deep this change in stress state penetrates into the plate thickness. Based on the fact that melting appears to have been restricted to only a few microns, and the hardness profiles at larger depths are unchanged [see section 2.3.4], it is suggested that the tensile residual stresses imparted by laser processing may be restricted to the near surface region.

Determining the depth to which the residual stress change penetrates would have implications for mechanical properties, like fatigue, as well as part distortion. It has been noted in the literature [18] that variations in subsurface residual stress distribution play an important role in fatigue crack initiation and propagation.

Therefore, the variation of the residual stress as a function of depth of abrasive blasted and laser treated samples was determined. Figure 3:3 shows the depth resolved residual stress of a) unblasted and abrasive blasted samples and b) laser treated samples at different conditions in the sweep direction. Seven sets of laser treated samples (LSM-1, LSM-2, LSM-3, LACR-1, LACR-2, LACR-3, LACR-4, as listed in Table 3.1) were selected for evaluation of residual stress depth profile.

The unblasted material exhibits residual stress amounting to ±40 MPa through the whole thickness measured (~525 µm). The distributions of the residual stresses of the abrasive blasted samples showed typical "U-shape" profile, where compressive residual stress reached its highest magnitude of approximately 400 MPa at a depth of about 40 µm and then it gradually decreased to zero at a significant depth of about 225µm. It should be noted that the solid line represents a fit to the measured and corrected data obtained from four samples. There is observable scatter in the data, as indicated by the data points themselves. In one particular sample (abrasive blasted (LACR-2)), as shown in Figure 3:3(a), a much deeper case of compressive residual stress was observed. It should be noted that the dotted line in the depth profile of abrasive blasted (LACR-2) sample is an indication that there might be depths in between the surface and first measured depth (~150 µm) which will have higher residual stress

values than the residual stress values shown at first measured depth. As discussed in Chapter 1, this variation can result from the variations in abrasive blasting parameters, which were not a focus of this study.

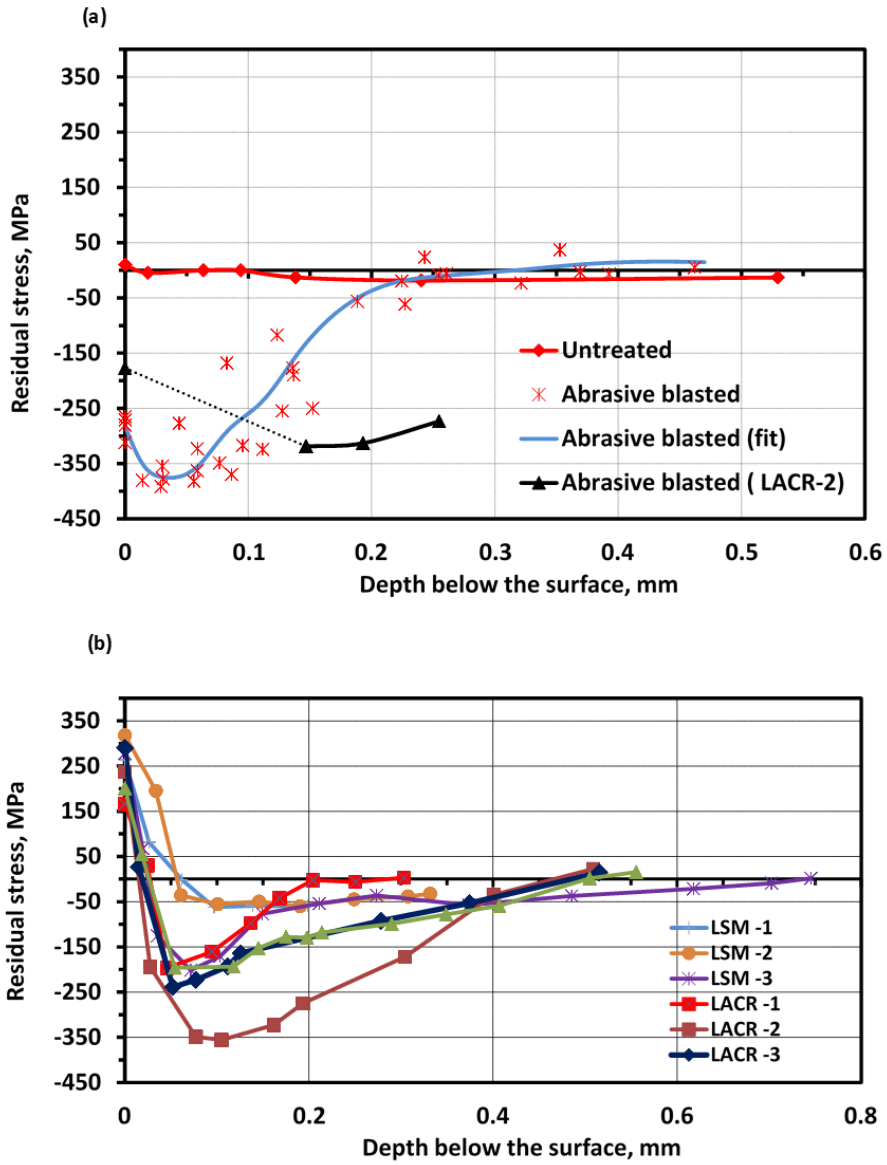


**Figure 3:3: Residual stress as a function of depth of a) unblasted and abrasive blasted samples and b) after performing laser treatment (LSM/LACR).**

The residual stress depth profiles of laser treated samples show that the tensile residual stresses induced were confined to a shallow depth. Tensile residual stress had its peak value at the surface, which decreased to zero just below the surface. This near-surface tensile residual stress case is balanced by the subsurface compressive residual stresses. The sharp swing in residual stress of laser treated samples probably results from the fact that only a thin surface layer is melted and re-solidified.

Depth resolved residual stress measurements on laser treated, unblasted samples (LSM-1 and LSM-2) show that they both have similar depth profiles, irrespective of their laser processing conditions. In both cases, the depth of the tensile region is about 50 μm and the magnitude of the balancing subsurface residual is 50 ±10 MPa throughout the measured thickness.

Laser surface modifications of abrasive blasted samples (with or without paint) showed an even shallower tensile region (~35 μm) relative to LSM of untreated samples. Thermal relaxation of subsurface compressive residual stress was also observed. The magnitude of the maximum compressive residual stress was reduced from about 400 MPa prior to LSM to about half that value (200 MPa) after LSM. It is also noted that a bare, abrasive blasted sample subjected to 10 passes of the laser (LSM-3) developed compressive residual stress to a greater depth.

Note that sample LACR-2 did not undergo the level of relaxation exhibited by other samples. It still has the maximum compressive stress value of about 350 MPa and at a given depth; the stress value is higher relative to other laser treated samples. This is likely due to the initial residual stress state of the baseline abrasive blasted sample rather laser processing conditions. Residual stress distribution of the initial abrasive blasted sample showed that this particular

sample has a deeper case of compressive residual stress relative to other abrasive blasted samples (Figure 3:3(a)). Due to this extended residual stress case of the baseline sample, this particular set exhibits higher subsurface residual stress values even after thermal relaxation. Microhardness measurement of this sample set (LACR-2) also showed that this particular set has slightly higher near surface hardness value (see section 2.3.4).

It should be noted here that the subsurface compressive residual stress "case" of laser treated samples tends to be deeper relative to abrasive blasted samples, except for sample set LACR-1 that shows compressive residual stress case depth of about 225 μm, which is similar to the case depth of abrasive blasted sample. This deep case makes sense, since the tensile near-surface region must be balanced by the subsurface compressive region, especially if one additionally considers the fact that the subsurface compressive stresses are, in general, lower than were observed prior to laser treatment. The shallower case depth of sample LACR-1, where the paint was "just-removed" after only two passes, is likely due to the fact that it has lowest near-surface tensile residual stress, so it does not require the extensive region of balancing compressive stress.

It is clear from the above discussions that there is a noticeable difference in residual stress depth profile among different sets of laser treated materials (Figure 3:3(b)). No simple correlation between laser parameters and residual stress distributions was observed. However, the number of laser passes and initial sample condition seems to affect the residual stress distribution the most. As an example, samples subjected to LACR at two different sweep speeds and the same number of laser passes (LACR-3 and 4) show similar residual stress profiles. In

both cases, depth of the tensile region is about 35µm and highest magnitude of balancing compressive residual is ~220 MPa at a depth of ~50µm. The case depth of the compressive residual stress is about 500 µm, which is more than twice the depth of the compressive case on the abrasive blasted samples. The other feature that has a strong impact on the final residual stress profile is the initial residual stress state, as indicated by the strong differences between the unblasted samples (LSM-1 & 2) and LACR-2 samples, as compared to the greater similarity between samples LSM-3, LACR-1, 3, & 4.

A final aspect related to residual stress profiles that was considered is the possibility of relaxation of residual stress during cyclic loading, especially given the fact that tension-tension tests ($R > 0$) with peak stresses above the yield strength were employed in this study. However, measurements show no significant relaxation of residual stress in either abrasive blasted or laser treated samples after 1000 and 10000 cycles at 183.5 MPa stress amplitude. Figure 3:4 shows the distribution of residual stresses of laser treated sample without any cycle and after 10000 cycles at 183.5 MPa stress amplitude. Considering the experimental error (approximately $\pm$ 25 MPa) associated with x-ray diffraction residual stress measurement, these residual stress depth profiles are indistinguishable.

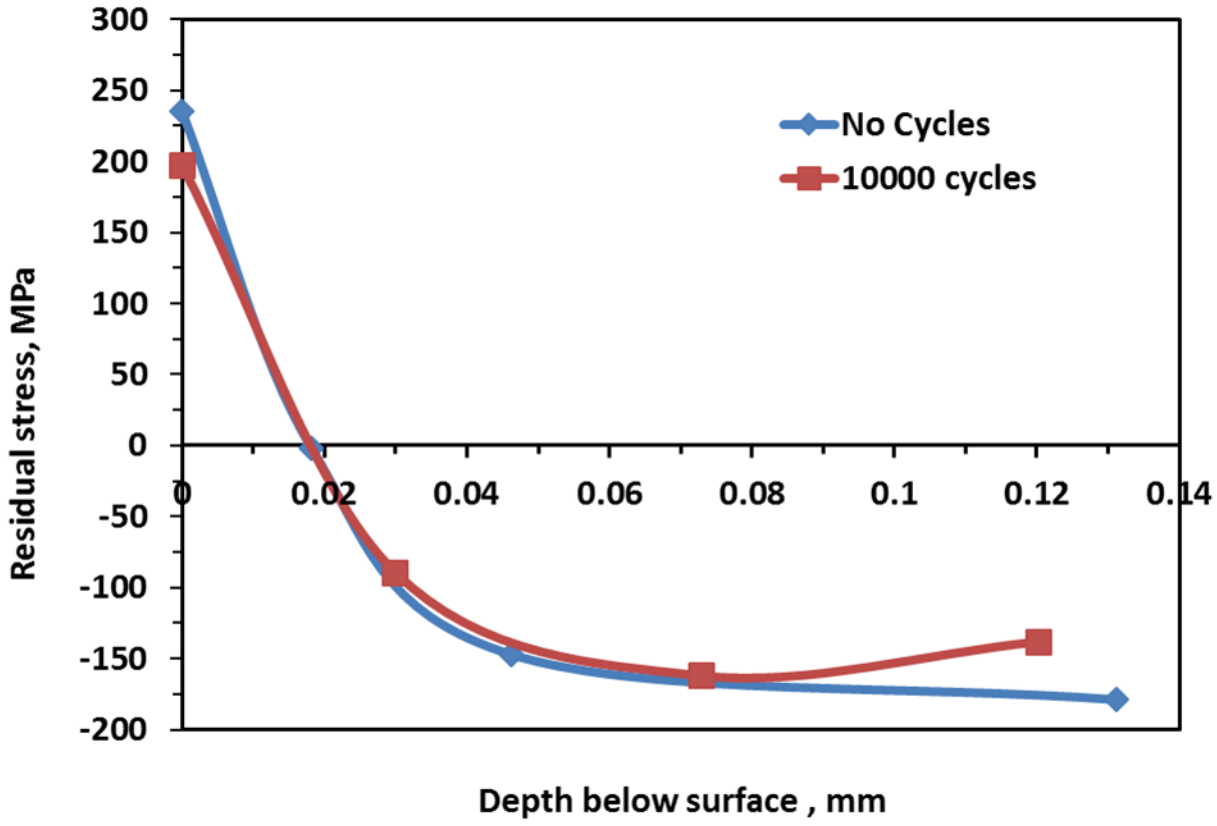


**Figure 3:4: Relaxation of residual stress during fatigue testing.**

### 3.3.2 Fatigue Performance

From standard tensile tests performed on the substrate material in the abrasive blasted condition, a yield strength of 370 MPa and an ultimate tensile strength of 520 MPa were observed. These values were used to determine the range of stress amplitudes (150 to 200 MPa) explored in the fatigue testing. Extensive tensile testing was not performed because prior studies [5, 6] had suggested that LACR induces little change in the bulk mechanical properties of the substrate material. The same five sets of laser treated abrasive blasted samples (with or without coating), which were taken for in-depth residual stress evaluation , were selected for fatigue testing. It should be noted here that LSM-3 was selected to explore the possible

condition where excessive LSM is performed on un-painted material or the case where multiple passes are enforced during LACR, after the paint has been removed, since this condition induced highest level of surface tensile residual stress.

The Wöhler curves of the abrasive blasted and laser treated material (irrespective of the details of laser process parameters) are shown in Figure 3:5. Contrary to prior results [5] laser treated samples showed the same, or slightly longer, fatigue life as compared with the abrasive blasted samples. The curves in the plot are primarily provided as a guide to the eye through the data. However, they are best-fit curves to the experimental data obtained by least squares non-linear regression of the Stromeyer equation [19], which relates $N_f$, the cycles to failure to the stress amplitude, $S$.

$$S = S_L + A\left(N_f\right)^m \qquad [3.3]$$

where $S_L$, $A$, and $m$ are fitting parameters. Employing this relation with an endurance limit, $S_L$, does not represent an endorsement of a particular fatigue design philosophy. Rather, fitting the data to this relation permits a ready comparison between the sets of obtained fatigue data. The bottom curve (blue) is a fit through all of the data obtained from samples in the abrasive blasted condition; the top curve (red) is a fit through all of the data obtained from laser treated samples (irrespective of laser processing conditions); and the dashed curve is a fit through all of the data collectively. Note that only the highest stress amplitude run-out data were included in the regression analysis. The values of the fitting parameters of the Stromeyer equation are listed in Table 3.2.

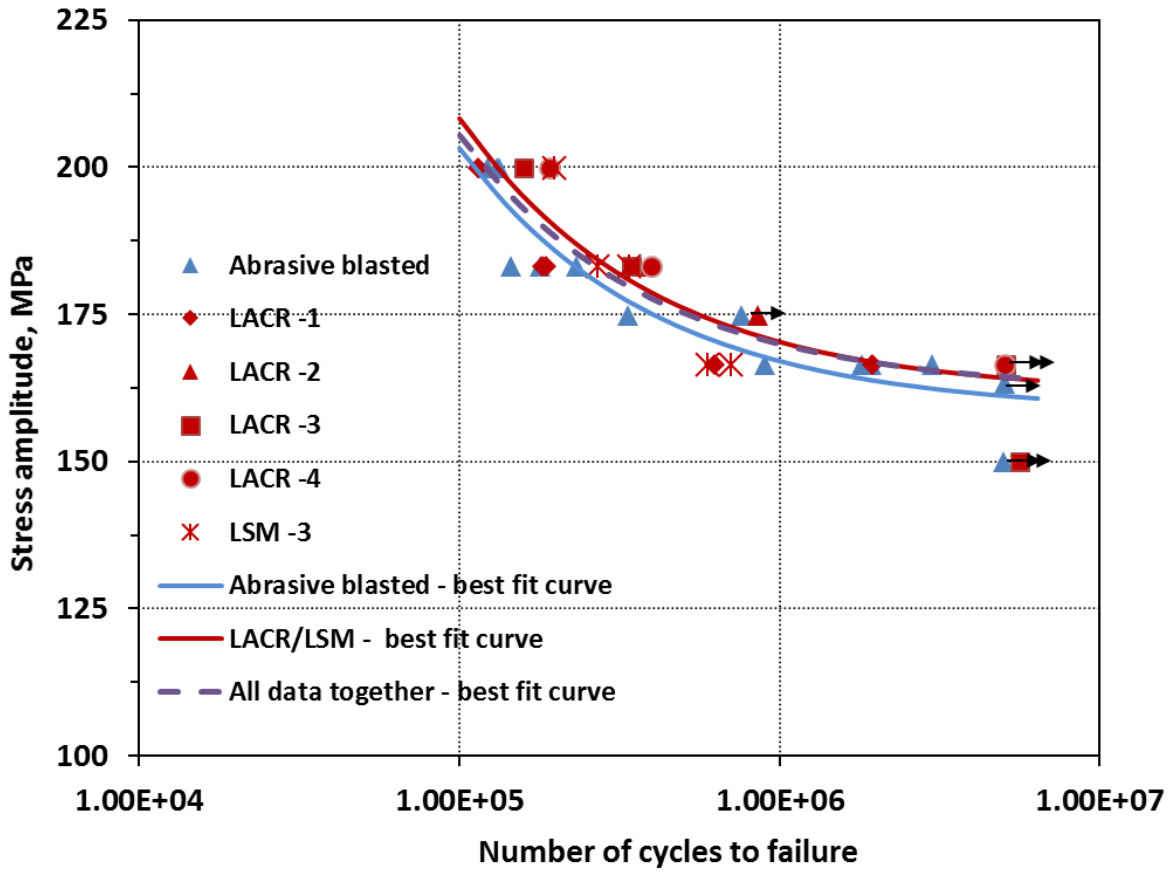


**Figure 3:5: Stress-life (S-N) curves for the abrasive blasted condition compared with LACR samples. Arrows at 5x10$^6$ cycles represent run-out tests. Curves are best fits of the data to the Stromeyer relation.**

**Table 3.2: Fit parameters of the Stromeyer equation from non-linear regression of the S-N data presented in Figure 3:5.**

| Sample condition | Number of samples | $S_L$ | *A* | *m* |
|---|---|---|---|---|
| Abrasive Blasted | 13 | 158.4 $\pm$ 8.2 | 1.7E+05 | -0.72 |
| Laser Treated | 18 | 161.4 $\pm$ 6.6 | 1.9E+05 | -0.72 |
| All Together | 31 | 161.8 $\pm$ 4.2 | 2.0E+05 | -0.73 |

The values presented in Table 3.2 indicate that the fatigue performance of the samples subjected to LACR is same as baseline abrasive blasted samples (within the limits of experimental uncertainty), despite having high surface tensile residual stresses. It is believed that the maintenance of similar fatigue response may be attributed to a compromise between the decreased sharpness of the roughness and the replacement of a compressive residual stress with the one, which is tensile.

### 3.3.3 Fractography

In order to rationalize the experimental fatigue testing results, scanning electron microscopy was used to determine the fatigue crack initiation sites of representative fatigue samples. A thumbnail (half-penny) shaped fatigue crack was observed to emanate from the modified surface prior to final fast fracture irrespective of sample condition (abrasive blasted or laser surface treated). The fast-fracture surfaces were characterized by typical ductile dimple rupture, so no representative micrographs of those features are shown in this paper. Fractographic analysis of the abrasive blasted sample shows that in some cases, the crack seemed to originate at the corner of the sample when examined with the naked eye or by low magnification imaging, as shown in Figure 3:6(a). However, closer inspection of the river marks emanating from the initiation site invariably revealed that the crack actually initiated from a depression on the abrasive blasted surface of the sample (Figure 3:6 (b)).

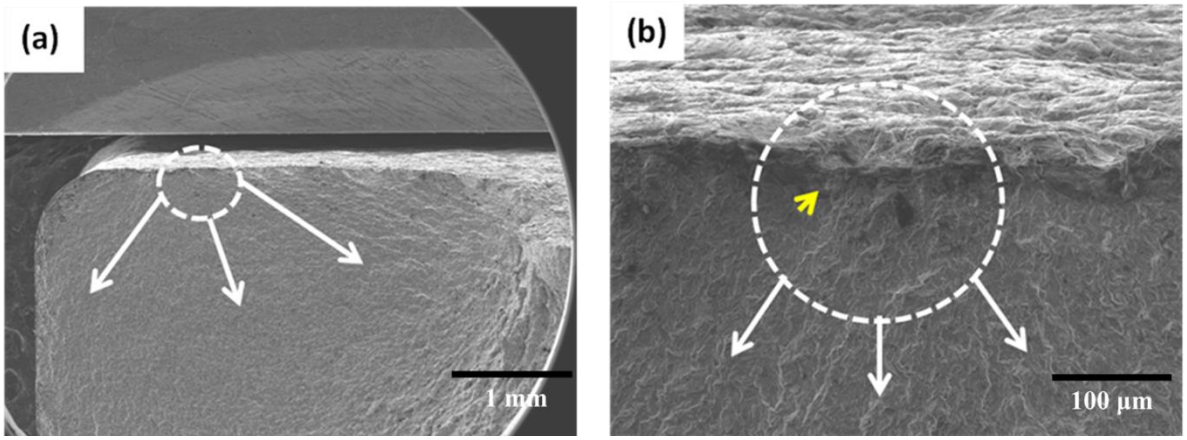


**Figure 3:6: Scanning electron micrographs of a grit blasted sample tested at stress amplitude of 167 MPa, with a fatigue crack that initiated close to a sample corner (a). Higher magnification micrograph (b) of the initiation site, which was a particularly deep valley in the surface profile.**

Fractographs of LACR samples, as shown in Figure 3:7, show that the nature of the fatigue crack initiation is similar to the abrasive blasted samples. In this case, the initiation is located near the center of the laser-processed surface. However, near corner crack initiation of the LACR samples, similar to the one shown in Figure 3:6 for an abrasive blasted sample, was also found some cases. From higher magnification micrographs (Figure 3:7(b-c)), it is clear that the fatigue crack initiated from the surface depression as well, i.e. a valley in the roughness profile. Figure 3:7(d) shows fatigue striations observed at higher magnification just above the initiation site presented in Figure 3:7(c). These observations reinforce the claim that surface roughness is the predominant source of fatigue crack initiation and that surface residual stresses have little effect on fatigue crack initiation.

Multiple cracks initiating from the valleys of the surface roughness were also observed on a single sample, especially at the highest stress level. These small cracks grow independently for some portion of the fatigue life prior to coalescence of two or more of the larger cracks and subsequent growth of a single large crack. The low magnification inset shown in Figure 3:8(a) highlights a couple of distinct initiation sites with the yellow dashed circles. Note the river marks radiating outward from each of them. In between, one can observe a “ledge” where the two simultaneously growing cracks met and linked up into a single crack on its way to final fracture. The dashed white box highlights the corner region of the sample that is enlarged in Figure 3:8(b). However, multiple cracks, as observed in this micrograph, were also observed in some laser treated samples.

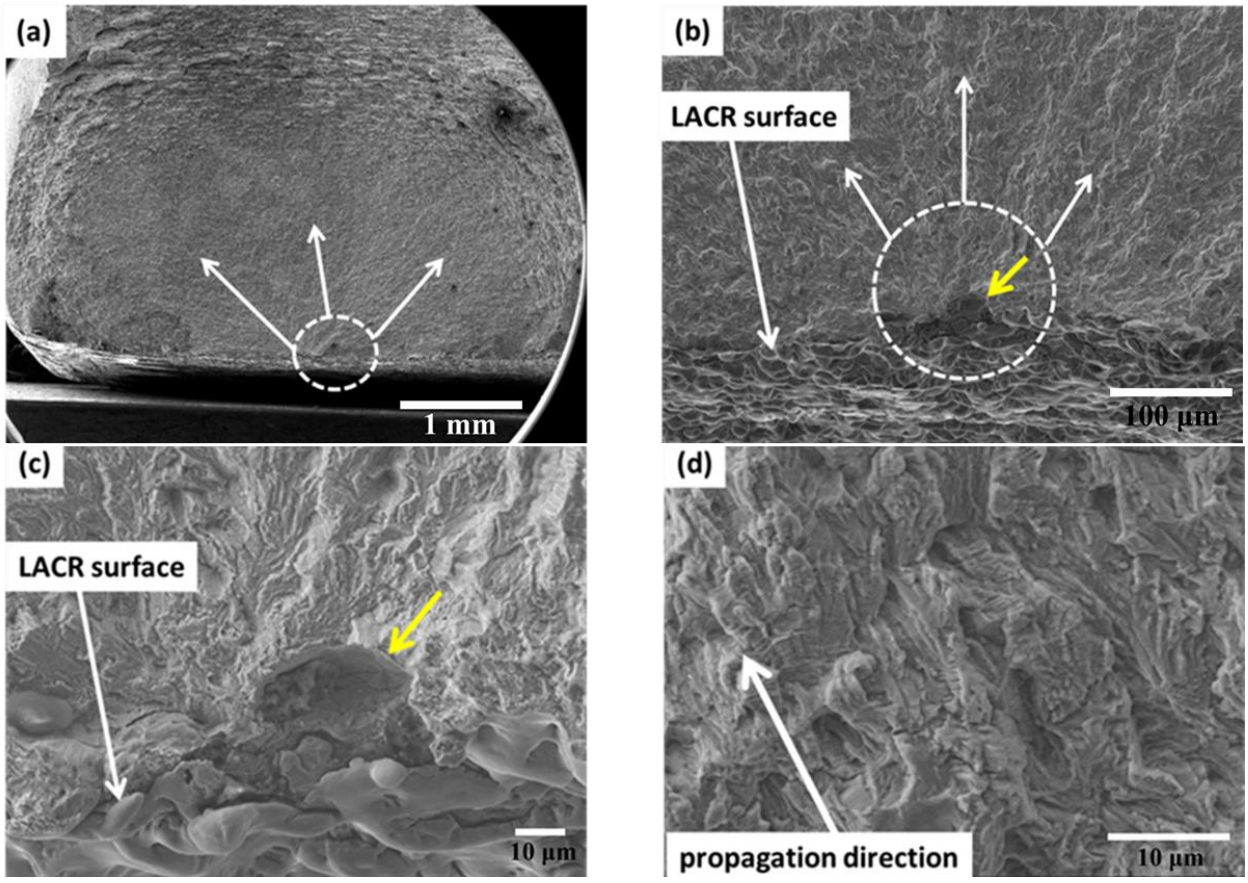


**Figure 3:7: Scanning electron micrographs of a fatigue fracture surface, sample subjected to LACR (LACR -2). Low magnification micrographs show the initiation site (a, b). Higher magnification micrographs (c, d) show the LACR surface and the crack propagation, respectively.**

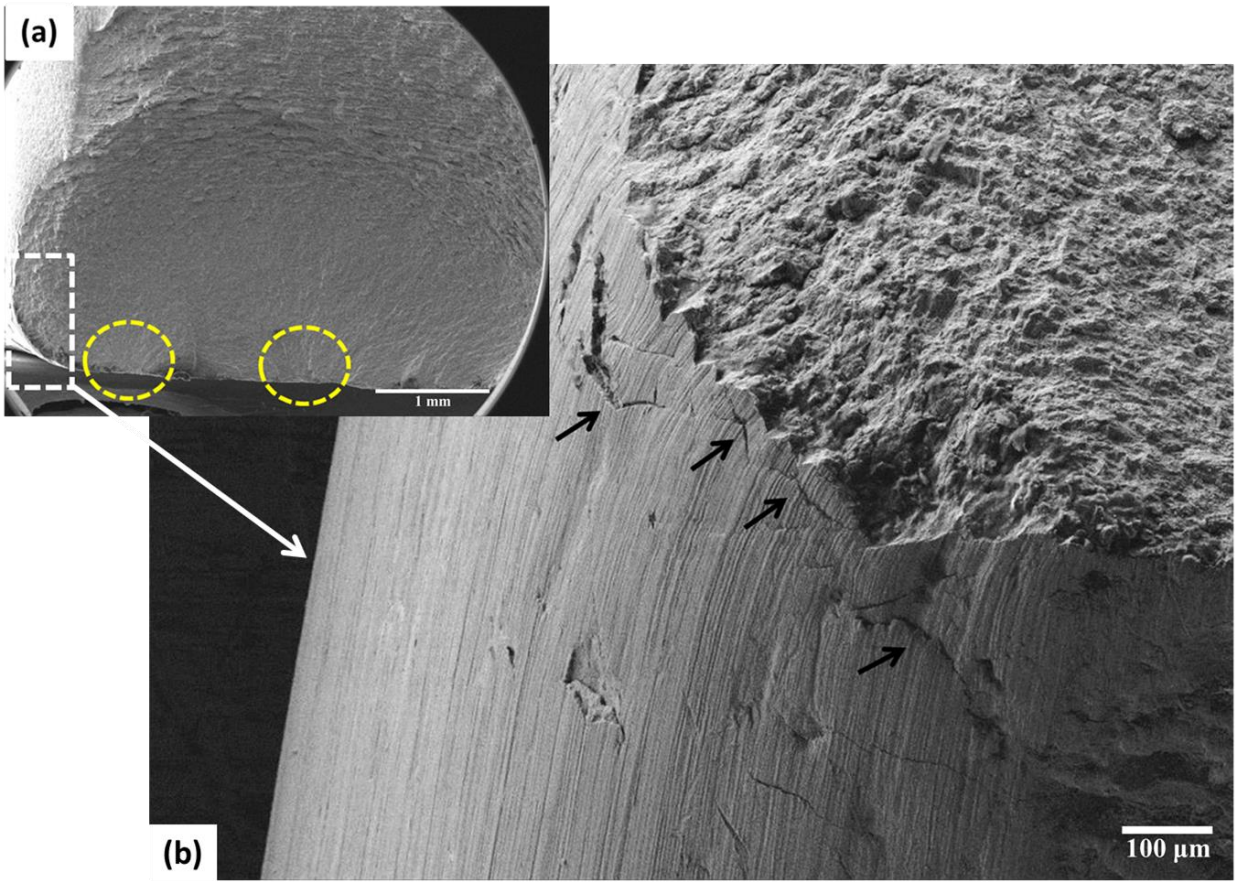


**Figure 3:8**: **Scanning electron micrographs of the fracture surface of an abrasive blasted sample loaded at a stress amplitude of 183 MPa. Multiple initiation sites are shown in (a) indicated by yellow circles, while significant cracking is observed in (b), where the corner regions of an abrasive blasted sample reveal numerous surface cracks (black arrows).**

In addition, abrasive blasting media embedded in the metal surface at the crack initiation site, as shown in Figure 3:9, was also observed in a laser surface modified sample (LSM-3), examined at 167 MPa, which exhibited a low fatigue life relative to the other samples tested at the same stress level. Note the large bright region observed in Figure 3:9(a), which is "charging." Typically charging is indicative of insulating materials that do not allow for an uniform path of

electron flow to ground potential. This particle has the appearance of abrasive media along with a local chemistry (list elements detected) that is also suggestive of garnet, the medium used in this study; see Figure 3:9(b). Ultimately, however, the low fatigue life of this sample appears to be a consequence of a large surface depression associated with embedded abrasive media, not the high surface tensile stress.

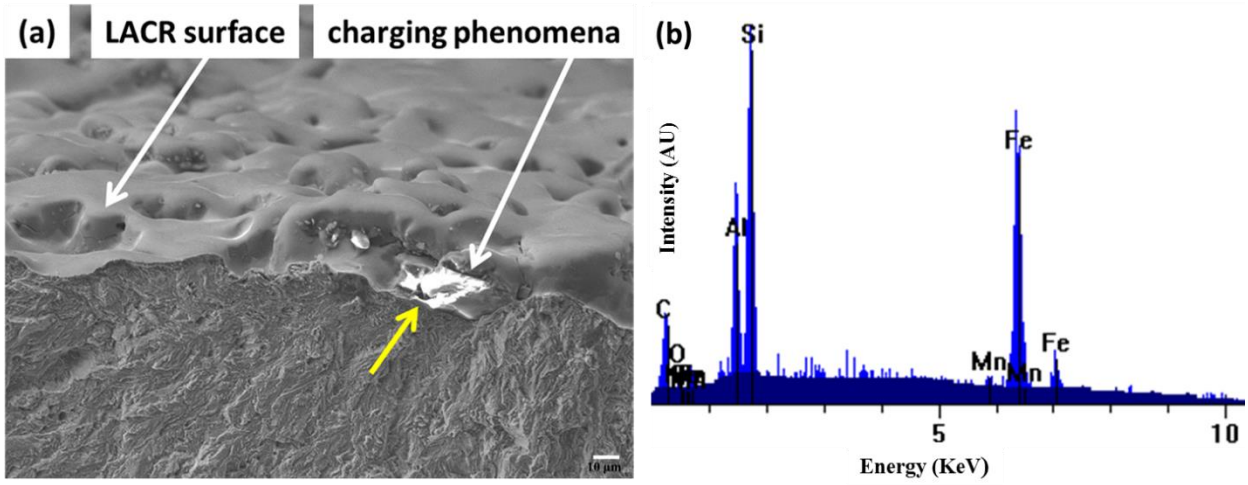


**Figure 3:9: SEM micrograph of laser treated surface (LSM -3) reveals the presence of a large non-conducting particle (note charging in micrograph (a)) at the crack initiation site. The EDS data (b) containing Al and Si are strongly indicative of the abrasive blasting media.**

## 3.4 Modeling and Discussion

Both grit blasting and laser treatment induce significant alterations of the surface roughness and residual stress. Fatigue performance depends on the corporate actions of the surface roughness and residual stress. It is well known that, for the case of a constant surface roughness, a higher tensile residual stress will lead to degradation of the fatigue resistance [20]. Conversely, for similar residual stress field, fatigue performance decreases with increasing

surface roughness [21, 22]. The stress concentration associated with surface roughness increases with increasing roughness and thus, fatigue crack initiation life decreases. Given the fact that the residual stress depth profiles (Figure 3:3 (b)) revealed that tensile residual stresses of the laser treated samples were limited to a shallow depth of about 35 µm, which is less than the typical notch depth (peak-valley height) of ~50 µm, the residual stresses are not considered in the following analysis.

As discussed in Chapter 1 , both LSM on bare surfaces and LACR tend to smooth the surface, even though conventional roughness parameters, ($R_a$, average roughness, $R_y$, *peak-to-valley height*, and $R_z$, ten-point roughness), obtained from a mechanical stylus profilometer, did not show any significant change in roughness values. An imposed change in notch (valley) root radius ($\rho$), due to changes in surface tortuosity from laser treatment, will lower the stress concentration result from the surface irregularities. According to the Neuber rule [23], the stress concentration associated with roughness and hence the fatigue performance, depends on the notch depth (related to $R_z$) and notch root radius rather than average roughness value ($R_a$).

$$k_t = 1 + n\sqrt{\lambda \frac{R_z}{\rho}} \qquad [3.4]$$

Where *n* represents the stress state (*n=1* for shear and *n=2* tension loading). Arola-Ramulu [25] also proposed an expression for stress concentration, in terms of standard roughness parameters and valley radii.

$$k_t = 1 + n\left(\frac{R_a}{\rho}\right)\left(\frac{R_y}{R_z}\right) \qquad [3.5]$$

Stress concentrations based on surface roughness were calculated for both abrasive blasted and laser treated samples using both Neuber and Arola-Ramulu models and listed in Table 3.3. A load factor ($n$ = 2) was used for both models to account for the high value of $R$ = 0.1 (pull-pull fatigue). It should be noted here that the roughness parameters were calculated from roughness profiles corrected for finite tip radius of the profilometer stylus, as described in section 2.3.2.2. To define the effective valley radius, three prominent valleys were chosen from each of the eight measurements for a given sample and all twenty four were averaged. Valley radius was calculated from the first and second derivative of the calculated data by using the following equation:

$$\rho = \frac{\left[1+\left(\frac{dy}{dx}\right)^2\right]^{\frac{3}{2}}}{\left|\frac{d^2y}{d^2x}\right|} \qquad [3.6]$$

It should be mentioned here that actual valley radius could be smaller than the reported value because, even with the adopted tip correction method, it is not possible to detect a valley radius smaller than the tip of the profilometer (determined to be 7 µm using optical microscopy). Note that the computed tip radii are all close to this limiting tip radius.

**Table 3.3: Surface roughness parameters, radius of valley and surface concentration based on Neuber [23] and Aorla-Ramulu [24] models.**

| Sample | $R_a$ (μm) | $R_y$(μm) | $R_z$(μm) | $\rho$(μm) | $k_t$ | |
|---|---|---|---|---|---|---|
| | | | | | Neuber | Arola-Ramulu |
| Abrasive blasted | 6.01 | 47.6 | 36.5 | 10.2 | 4.8 | 2.5 |
| LSM -3 | 5.46 | 43.7 | 33.1 | 12.0 | 4.3 | 2.2 |
| LACR -1 | 6.71 | 51.4 | 39.7 | 9.60 | 5.1 | 2.8 |
| LACR -4 | 6.17 | 45.6 | 37.2 | 10.7 | 4.7 | 2.4 |

There is a significant difference in stress concentration predicted by the two models, but the trends from one sample to another are similar. The lowest stress concentration is predicted for sample set LSM-3, where highest number of laser passes was applied to a bare surface. One should recall that the surface appears increasingly smooth with increasing number of passes (section 2.3.2.1). Sample set LACR-4, with a surface profile similar to sets LACR-2 & 3, shows relatively lower stress concentration compared to abrasive blasted sample. On the other hand, sample set LACR-1 shows the highest stress concentration.

Perhaps due to the lower stress concentration, samples from sets LACR-2, 3 and 4 exhibited fatigue lives on the upper end of the distribution (see Figure 3:5). Nine samples were tested from these sample sets and all them had better fatigue lives than the mean, at a given stress level. Conversely, all of the data points in Figure 3:5 corresponding to sample set LACR-1 have fatigue lives, which are at the low end of the distribution of the LACR samples tested. Although the conclusion is based upon only 4 data points, it does suggest that “just removed” paint is a worst case scenario (with respect to fatigue performance). It is noteworthy that even this worst case is on par with the original abrasive blasted condition. Sample set LSM-3 initially appears to

deviate from the emerging trend. It is predicted to have a lower stress concentration, yet two samples tested at a stress amplitude of 167 MPa performed at the very low end of the range of scatter for all samples tested at this stress level (Figure 3:5). Other LSM-3 samples tested at higher stress amplitudes of 183 MPa and 200 MPa were among the most long-lived samples at those stress levels. Fractographic analysis of the short-lived LSM-3 samples revealed the presence of abrasive blasting media embedded in the metal surface (see Figure 3:9). Thus, it does appear that the rank-order of fatigue lives is correlated with fine details of surface roughness. It is again admitted that the stress concentration model is sensitive to the notch root radius, which approached the value of the stylus tip in every case. It is possible that the actual notch radius is much smaller, particularly in the case of the abrasive blasted. In summary, the fatigue performance of the laser treated samples, irrespective of laser processing conditions, is statistically similar to the fatigue performance of abrasive blasted samples. It is possible that this similarity in responses is due to a compensating effect of the detailed changes in surface roughness and residual stress.

## 3.5 Conclusions

The effects of laser ablation coating removal (LACR) on the residual stress evolution and fatigue performance have been assessed on one type of common shipbuilding steel and compared with base line abrasive blasted substrates. From the experimental results, the following conclusions can be drawn:

1. X-ray diffraction-based measurements of the residual stress have shown that unblasted samples have nominal zero ($\pm 40$ MPa) residual stress throughout the whole thickness.

Abrasive blasting introduced a surface compressive residual stress of -264±24 MPa. Residual stress distributions of abrasive blasted samples show a typical "U-shape" profile, where compressive residual reaches its maximum value (~400 MPa) just below the surface.

2. LACR induces a large shift of the residual stress in the tensile direction. Following LACR, the surface residual stresses were typically 242±63 MPa in tension. Depth resolved residual stress distribution shows that tensile residual stresses are confined to very shallow depth of about 35μm.

3. Fatigue testing confirms that the material subjected to LACR performs as well as abrasive blasted material. Fits to the Stromeyer equation estimate endurance limits of $158.4 \pm 8.2$ MPa for abrasive blasted samples and $161.4 \pm 6.6$ MPa for laser treated samples.

4. Fractographic analyses revealed that cracks initiated from valleys in the surface profile.

5. Models of roughness-based stress concentration correlate with detailed trends in the fatigue lives of samples subjected to LACR. However, it must be admitted that the measure of roughness employed is not sensitive to possible changes in notch root radius, which may have been compensated by changes in surface residual stress state.

**Acknowledgements**

This work was supported by the Commonwealth Center for Advanced Manufacturing (CCAM), Mr. Matthew Stremler as Program Manager.

## References


[1] K. Liu, E. Garmire, Appl. opt. 34 (1995) 4409- 4415.

[2] P. Lovoi, Laser focus world, 30 (1994) 75-82.

[3] A. Tsunemi, K. Hagiwara, N. Saito, K. Nagasaka, Y. Miyamoto, O. Suto, H. Tashiro, Appl. Phys. A 63 (1996) 435-439.

[4] G.X. Chen, T.J. Kwee, K.P. Tan, Y.S. Choo, Appl. Phys. A, 101(2010) 249-253.

[5] E.D. Oller, Naval application of laser ablation paint removal technology, in: U.S. Navy Corrosion Conference, Norfolk, VA June 2011.

[6] S.G. Pantelakis, T.B. Kermanidis, G. Haidemenopoulos, Theor. Appl. Fract. Mech. 25 (1996) 139-146.

[7] S.G. Pantelakis, G. Haidemenopoulos, Surf. Coat. Technol. 106 (1998) 198-204.

[8] Leitz, K. H., Redlingshöfer, B., Reg, Y., Otto, A., & Schmidt, M.R. Kralova, Mater. Sci. Eng. A 174 (1994) L51-L54.

[9] R. Šturm, J. Grum, Mater. Sci. Forum 681 (2011) 188-193.

[10] H. Stamm, U. Holzwarth, D. J. Boerman, F. Marques, A. Olchini, R. Zausch, Fatigue Fract. Eng. Mater. Struct. 19 (1996) 985-995.

[11] M. Heitkemper, M., C. Bohne, A. Pyzalla, A. Fischer, Int. J. Fatigue 25 (2003) 101-106.

[12] K.H. Leitz, B. Redlingshöfer, Y. Reg, A. Otto, M. Schmidt, Phys. Procedia 12 (2011) 230 -238.

[13] H.Wang, J. Appl. Crystallogr. 27 (1994) 716-722.

[14] M.E. Fitzpatrick, A.T. Fry, P. Holdway, F.A. Kandil, J. Shackleton, L. Suominen, Determination of Residual Stresses by X-ray Diffraction—Issue 2, DTI, 2005, Measurement Good Practice Guide No. 52.

[15] J.R. Taylor, An Introduction to Error Analysis - The Study of Uncertainties in Physical Measurements, Second Ed., University Science Books, Sausalito, California, 1997.

[16] D.L. Sikarsie, AIME Trans. 239 (1967) 577-580.

[17] M. Moore, W. Evans, SAE Trans. 66(1958) 340-345.

[18] G. Farrahi, J. Lebrijn, D. Couratin, Fatigue Fract. Eng. Mater. Struct. 18 (1995) 211-220.

[19] C. Stromeyer, Proc. R. Soc. Lond. Ser. A 90 (1914) 411-425.

[20] H. Sasahara, Int. J. Mach. Tool Manuf. 45 ( 2005) 131-136.

[21] L. Wagner, Mater. Sci. Eng., A 263 (1999) 210-216

[22] L. Wagner, M. Mhaede, M. Wollmann, I. Altenberger, Y. Sano, Int. J, Struct. Integ. 2 (2011) 185-199.

[23] H. Neuber, Kerbspannungsleshre (Theory of Notch Stresses), Second Ed., Springer-Verlag, Berlin, 1958.

[24] D. Arola, C. Williams, Int. J. Fatigue 24 (2002) 923-930.

# Chapter 4: Effects of microstructure and abrasive blasting protocol on the fatigue performance of high strength steel after laser ablation coating removal.


## Abstract

The effects of variations in initial microstructure and prior abrasive blasting parameters on the fatigue performance of a high strength steel after laser ablation coating removal (LACR) have been investigated. It is noted that the metal surface is melted and re-solidified during the LACR process. The incumbent abrasive-blasted samples show a slightly better fatigue life compare to LACR samples. SEM fractography reveals that fatigue cracks in LACR processed samples predominately initiated from these embedded particles. A high density of embedded abrasive blasting media was observed before and after performing LACR. Finite element analysis shows that the embedded particles have a high elastic stress concentration factor (which is essentially unchanged by the LACR process). X-ray diffraction-based measurements of the residual stress distributions show that the magnitude of the compressive residual at a depth corresponding to that of the embedded particles is more compressive for abrasive-blasted samples than LACR samples. Thus, the observed detrimental effects of LACR treatment on fatigue performance are attributed to the combined effects of high elastic stress concentration factor and relax residual stress state at the embedded particles.

## 4.1 Introduction

Laser ablation coating removal (LACR) has proven to be an effective method of the removal of epoxy-based coating, as discussed in Chapter 2 and Chapter 3 and in references [1-3]. Furthermore, the performance of an abrasive-blasted high strength shipbuilding steel shows a higher or similar fatigue life after LACR treatment relative to starting abrasive-blasted samples (see Chapter 3). However, different vendors employ different processing routes to meet property specifications, which can result in differences between the microstructures of high strength shipbuilding steels, though they still have chemistries and mechanical properties that fall within the accepted specifications. Questions remain as to how these differences in microstructure would affect the performances of the alloy after laser treatment.

In addition, prior surface processing conditions (abrasive blasting) may have a major impact on the performance of the steel after subsequent LACR treatment. Fatigue performance typically improves when blasting is performed in a controlled manner by the virtue of compressive residual stresses which are imparted by the process [4-7]. However, the beneficial effects of abrasive blasting on fatigue life can become detrimental when blasting process is carried out in an uncontrolled fashion, as surface defects typically increase with increasing blasting pressure/velocity, and the effect of these surface defects can surpass the beneficial effects associated with the imparted compressive residual stress [8-10]. In addition, high-velocity impact results in embedment of the blasting particles [11-13], which act as severe notches and primary fatigue crack initiation sites [5, 8, 14].

Previously, abrasive blasting prior to painting and laser de-painting was conducted in a very controlled manner. However, in order to increase the production rate, abrasive blasting is often conducted at a very high blasting pressure. The main goal of this study to investigate the effects of the changes in initial microstructure and abrasive blasting protocol, prior to coating, on the fatigue performance of a high strength shipbuilding steel after laser ablation coating removal.

## 4.2 Experimental

### 4.2.1 Materials

The microstructure of the high strength steel (HSS-II) under investigation exhibits a combination of distributed pearlite colonies, ferrite, and bainite. In comparison, the microstructures of the materials in Chapter 1 and 2 (HSS-I) show simpler, α-ferrite plus pearlite (α-ferrite + $Fe_3C$ cementite carbides) microstructure, with pearlite colonies arranged in bands parallel to the plane of the plate. Associated with these differences in microstructures, there is also a significant difference in the tensile properties of the two materials investigated. While both materials have a similar ultimate tensile strength (≈520 MPa), the yield strength of the HSS-II (440 MPa) is significantly higher than HSS-I (≈370 MPa). Engineering stress vs. strain plot of the HSS-II is shown in Figure 4:1, for a comparison tensile plot of HSS-I, is also shown.

A 0.25 mm red epoxy coating was applied prior to laser ablation coating removal (LACR). As before (see section 2.2), all the materials are abrasive blasted prior painting. Following coating application, the paint was air dried at ambient temperature and aged for 15 to 20 days prior to laser paint removal application.

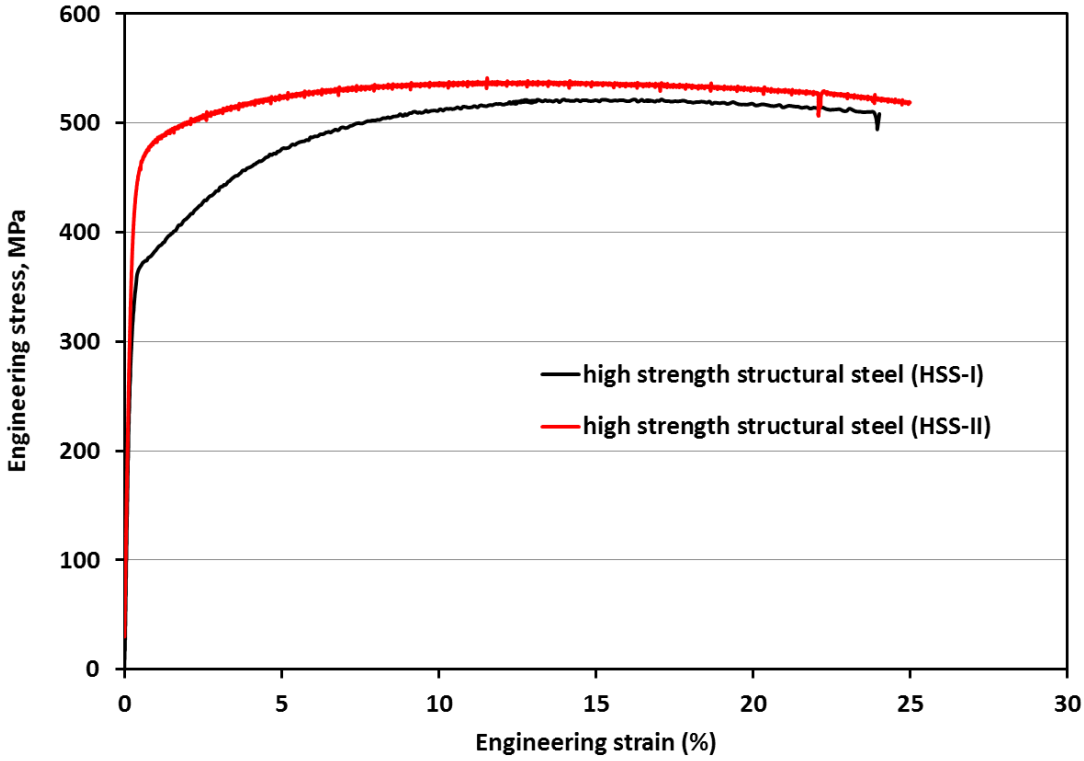


**Figure 4:1: Stress-strain curve shows the difference in tensile properties between high strength shipbuilding steels.**

### 4.2.2 Surface Modifications

A high velocity abrasive blasting utilized garnet grit with a mean diameter of 600 µm as the abrasive blasting medium, a 0.5 inches (12.7 mm) diameter straight bore nozzle at an air pressure of 120 psi (827 kPa) on all samples. The working distance was controlled by the worker. The steel plate received in the abrasive blasted condition is considered as the baseline material because this is the typical condition prior to painting.

All LACR processing was conducted at Norton Sandblasting located in Chesapeake, VA using an Adapt Laser Systems model CL1000Q Nd:YAG laser operating at the fundamental wavelength

(1064 nm) and 1 kW average laser power. To maintain consistency, the laser processing was performed at a pulse frequency of 24 kHz, pulse duration of 83 ns, scan rate of 110 Hz and sweep speed of 1 inch/sec (25.4 mm/s) using “automated sweep”. See section 2.2 for more experimental details of laser processing.

### 4.2.3 Sample preparation

Samples for hardness (micro- and nano-hardness) were prepared using conventional metallographic techniques (see section 2.2). Both the surfaces and cross-sections were examined using optical and FEI Quanta 200 Scanning Electron Microscopy (SEM). Energy Dispersive X-ray Spectroscopy (EDS) was used to determine the chemistry of features of interest during SEM investigations.

### 4.2.4 Hardness

Vickers microhardness measurements were made at various depths using a diamond pyramid indenter with an apical angle of 136°, an indentation load of 0.5 kg, and an indentation duration of 15 seconds. Nanoindentation measurements were performed using Micro Materials NanoTest Vantage equipped with a diamond Berkovich tip. All the nanoindentation tests were performed in a load control mode. In order to obtain hardness as a function of depth, the indenter is loaded to a user-defined depth and then partially unloaded before reloading again to a greater depth at the same location. In this study, the materials were subjected to 10 cycles of loading and unloading to between 10 mN to 75 mN. During each cycle, the load was held at the maximum load for 20 seconds and then 50% unloaded to calculate the hardness value using

Oliver-Pharr method [15]. Finally, an array (12× 9) of hardness measurements was performed on both abrasive blasted and LACR samples at a maximum load of 35 mN with 20 seconds holding time and 90% unloading to obtain nano-hardness values as a function of depth below the processed surface.

### 4.2.5 Roughness

The surface roughness was evaluated quantitatively using a Mitutoyo SJ-210 portable stylus profilometer with a tip radius of 7 µm and using a 3D optical microscope (HiroxTM7700). The average roughness ($R_a$), root mean square roughness ($R_q$) and ten-point height roughness ($R_z$) was calculated from the stylus profilometer using a cutoff length of 0.8 mm and 6 mm traverse length. The areal average roughness ($S_a$) and root mean square roughness ($S_q$) was also calculated from the 3D microscope. More details of each of the roughness measurement techniques are discussed in section 2.2.

### 4.2.6 Residual stress

X-ray diffraction residual stress measurements were performed using a Panalytical X'Pert Pro MPD X-ray diffractometer with Bragg-Brentano focusing geometry and a *Cr-*$K_\alpha$ sealed tube source operated at 30 kV and 55 mA. The measurements were performed using the so-called "*d* vs. $\sin^2\psi$" method, where *d* is the lattice spacing of the {211} planes of the steel and $\psi$ is the angle between the diffraction vector and sample surface normal. A diffraction angle step size of 0.2-0.3° and a counting time of 10-20 seconds per step was used. The variation of the residual stress as a function of depth was determined via progressive layer removal by electropolishing

and subsequent residual stress measurement using X-ray diffraction. See section 3.2 for additional details.

### 4.2.7 Fatigue testing

Fatigue tests of "dog-bone" shape samples were performed using an Instron 1320 servo hydraulic load frame with 8500 computer control and data acquisition, aligned according to ASTM E-1012. The fatigue tests were performed under sinusoidal load control, at a stress ratio of $R$= 0.1, and a frequency of 10 Hz. The tests were stopped when specimens broke or after $5\times10^6$ cycles, whichever came first. The fracture surfaces were subsequently examined using a Scanning Electron Microscope (SEM).

## 4.3 Results

### 4.3.1 Surface morphology

Figure 4:2 shows the Secondary electron (SE) and backscattered electron (BSE) micrographs of abrasive blasting and LACR processed surface. The abrasive blasted surfaces are tortuous, as shown in Figure 4:2(a) where it was observed that abrasive blasting leaves "micro-crater" structures. In addition, it was observed that some of the abrasive blasting media (bright in the SE micrograph (Figure 4:2(a)) and dark in the BSE micrograph (Figure 4:2(b)) are attached to the micro-crater, which they have created.

In contrast with abrasive blasting, LACR produces a surface with a smooth, flowing appearance (Figure 4:2(c, d)). The morphological changes observed are consistent with laser melting and re-

solidification. The blasting particles from the prior abrasive blasting process remain embedded after performing LACR.

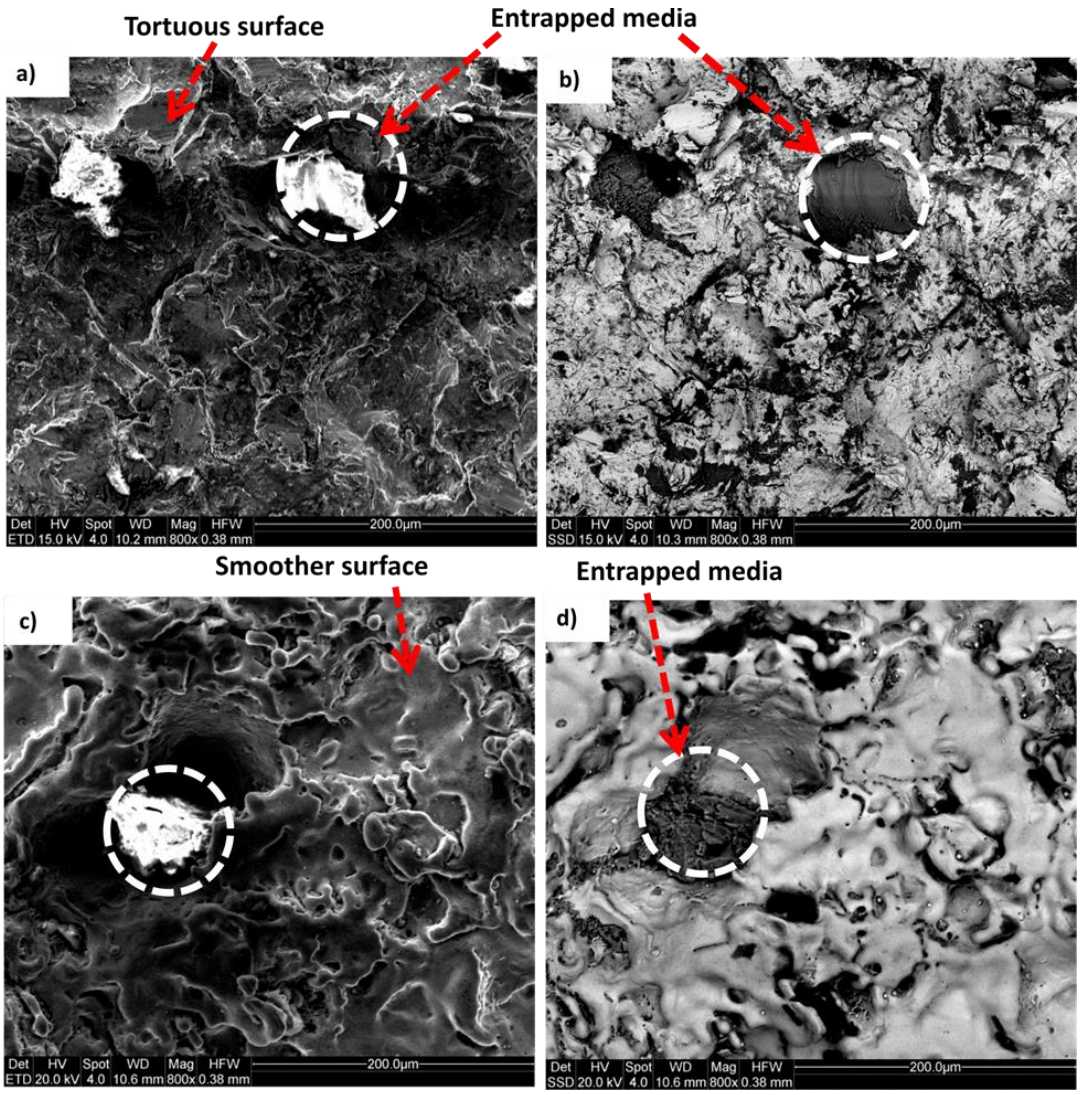


**Figure 4:2: SEM micrographs of high strength steel surfaces after a, b) abrasive blasted and c, d) subsequent LACR treatment.**

The observed surface morphology is similar to the one described in section 2.3.2.1. However, there is a clear distinction observed in terms of density of the embedded blasting media, i.e, a higher density of embedded particles is observed here (where larger media and higher blasting

pressure were employed). This could be the result of the variations in abrasive blasting process parameters like blasting pressure adopted in this study.

### 4.3.2 Roughness

Table 4.1 shows the standard roughness metrics: $R_a$, $R_q$, and $R_z$ measured using a Mitutoyo portable surface profilometer. The profilometry-based roughness results are consistent with surface appearance, as discussed in the previous section. Abrasive blasted samples show a slightly higher roughness value relative to LACR samples.

**Table 4.1: Mean roughness values and standard deviations for abrasive blasted and laser treated samples obtained using a stylus profilometer.**

| Sample | $R_a$ (µm) | $R_q$ (µm) | $R_z$ (µm) |
|---|---|---|---|
| Abrasive Blasted | 9.0±0.6 | 11.4±0.9 | 58.8±4.7 |
| LACR | 7.4±0.7 | 9.2±0.8 | 41.6±4.0 |

Figure 4:3 shows the surface topography of a) abrasive blasted, b) LACR samples obtained via 3D optical microscopy upon a Hirox™ 7700. Contrary to SEM observations, the surface topography observed by 3D optical microscopy do not highlight any significant change in surface morphology between abrasive blasted and LACR samples. This is also reflected in the roughness parameters obtained from these surface topographies, as shown in Table 4.2. Table 4.2 shows that there are no discernible differences in the areal roughness parameters $S_a$ and $S_q$ between abrasive blasted and LACR samples. Regardless, both methods clearly indicate a

higher roughness value of the abrasive blasted and LACR samples relative to roughness value reported in section 2.3.2.2. This observation is consistent with the fact that the samples are blasted at a higher impact velocity.

**a) Abrasive blasted**

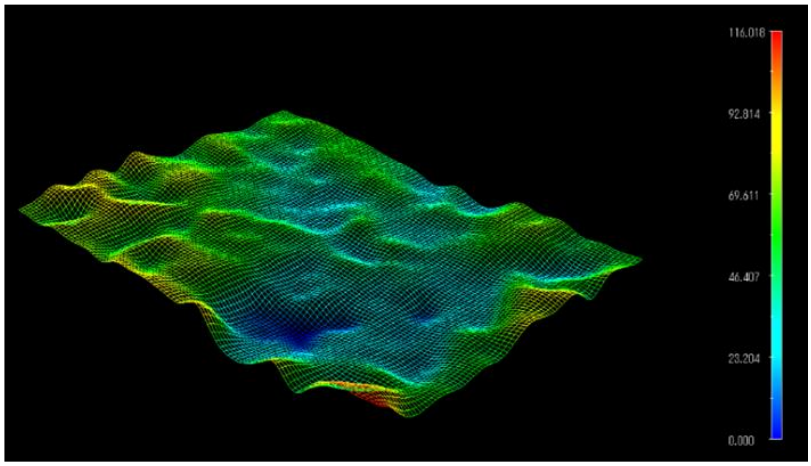


**b) LACR**

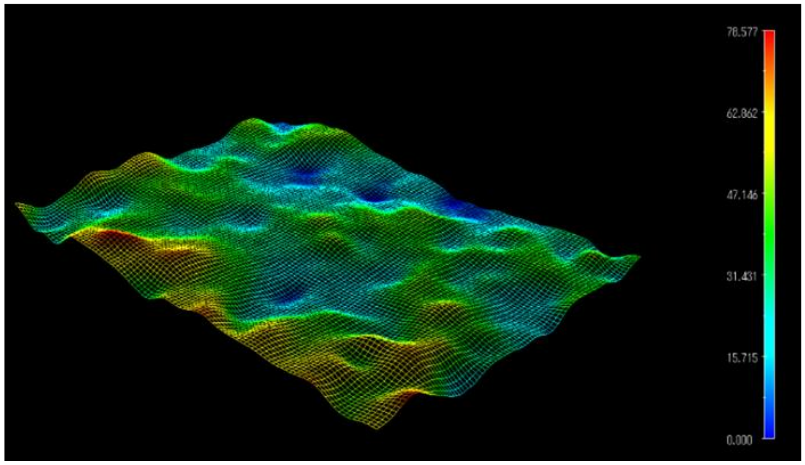


**Figure 4:3: Surface micrographs of a) abrasive blasted, and b) LACR samples obtained using the Hirox$^{TM}$ 7700.**

**Table 4.2: Mean roughness values and standard deviations for abrasive blasted and laser treated surfaces obtained from 3D optical images.**

| Sample | $S_a$ (µm) | $S_q$ (µm) |
|---|---|---|
| Abrasive blasted | 8.0±1.0 | 10.2±1.4 |
| LACR | 8.1±1.0 | 10.2±1.4 |

### 4.3.3 Microstructural Characterization

The microstructure of baseline abrasive blasted sample shows the typical plastically deformed grain structure near the surface, as shown in Figure 4:4. The thickness of the deformed region is about 10 µm. Embedded media are also observed and, in some instances, plastically deformed material flows over the media (Figure 4:4(b). Close observation of the deformed zone indicates the lamellar cementite in the pearlite breaks into granulated cementite, as shown in Figure 4:4 (a) by green arrows. This could occur due to partial dissolution of cementite, due to local heating associated with the large plastic deformation imparted by blasting [16, 17]. This dissolution phenomenon is similar to what occurs to the pearlitic steel during the drawing process [18-20]. According to Languillaume et al. [18], intense plastic deformation results in thinning of the cementite lamellae and the free energy of the cementite phase is increased by the interfacial contribution. At some point, the cementite becomes unstable, dissolving into the supersaturated solid solution of carbon in ferrite. Both the supersaturated ferrite and granular cementite enable a higher degree of surface hardening upon abrasive blasting [17].

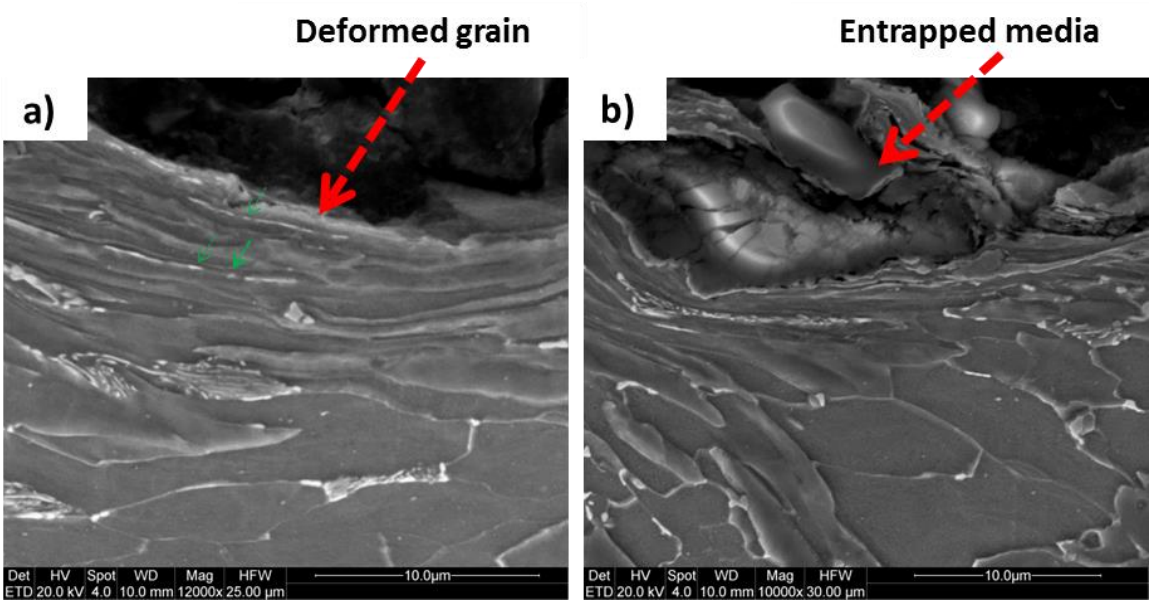


**Figure 4:4: Scanning electron micrograph showing near surface modification after performing abrasive blasting surface treatment.**

Cross-sectional analysis of the metal substrate after LACR confirms melting in the near surface regions. Melt depth varied between 1 and 3 µm. Figure 4:5(b) shows a delineation of the laser-solidified region. The re-solidified zone consists of fine columnar grains. This microstructure is typical for rapid solidification induced by laser surface melting where the unaffected substrate acts as a heat sink and the solidification front moves vertically at a very high velocity. The underlying material still exhibits elongated grains, with a deformed appearance suggesting that they have not recrystallized, consistent with the previous investigation (see section 2.3.3).

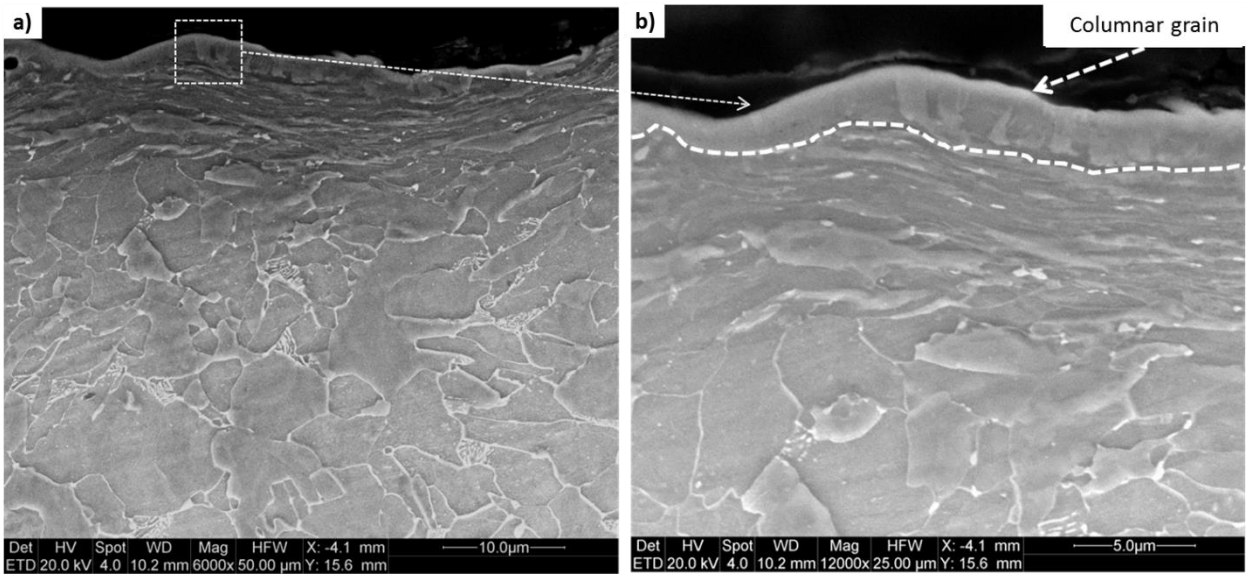


**Figure 4:5: Scanning electron micrographs show delineation of the melted and re-solidified zone. Micrographs show a columnar grain structure in the re-solidified zone.**

A detailed investigation of the re-solidified zone shows that the microstructure varied locally within the zone depending on the pre-existing microstructure. For example, when the laser interacts with the pearlite colonies, the microstructure in the melted zones show a feathery martensitic microstructure (see Figure 4:6(a, b)), in comparison to interaction with the ferrite/bainite microstructure, which results in a fine-grained ferrite (see Figure 4:6(c, d)). Due to high cooling rates of rapid solidification, carbon supersaturated in the austenite can transform into martensitic microstructures. The microstructure of the HAZ shows the coarsening of the cementite precipitates, see the red arrow in Figure 4:6(b, d). In addition, tempering of the bainitic microstructure, where the excess carbon in bainite precipitates as cementite carbide, may take place. Although tempering of bainitic steel is not as sensitive as martensitic steel due to its low excess carbon content, it still can induce substantial softening.

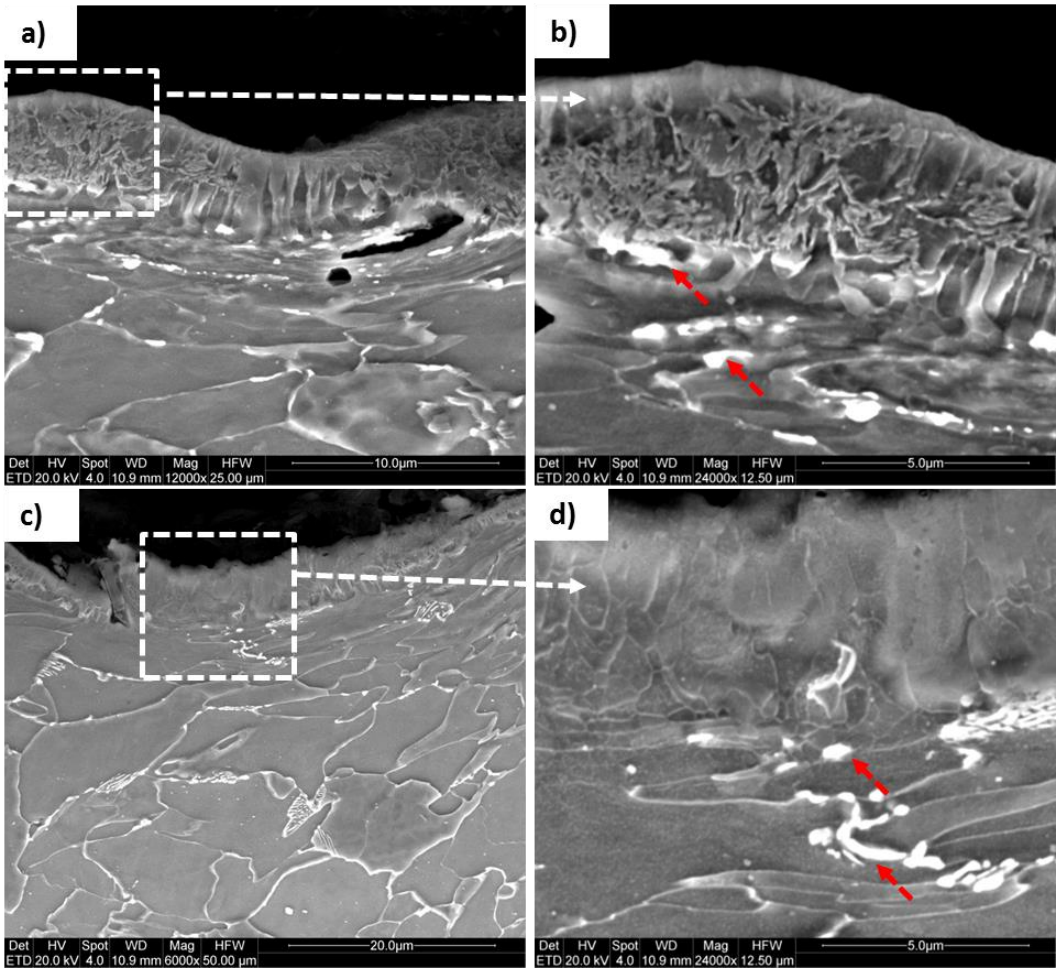


**Figure 4:6: : Higher magnification scanning electron micrographs providing additional details of the re-solidified zone of the laser treated samples: a, b) show "feathery" martensitic type microstructure and c, d) shows fine-grained ferritic microstructure. Red arrow indicates coarsening of the cementite.**

It is critical to note that LACR treatment results in a similar microstructural modification as discussed in Section 2.3.3 for the material HSS-I, with the exception of a high density of grit particles from the prior abrasive blasting treatment remain embedded after LACR process. No

noticeable changes in microstructure underneath these embedded particles are noted, i.e., the microstructure still shows elongated grains (see Figure 4:7).

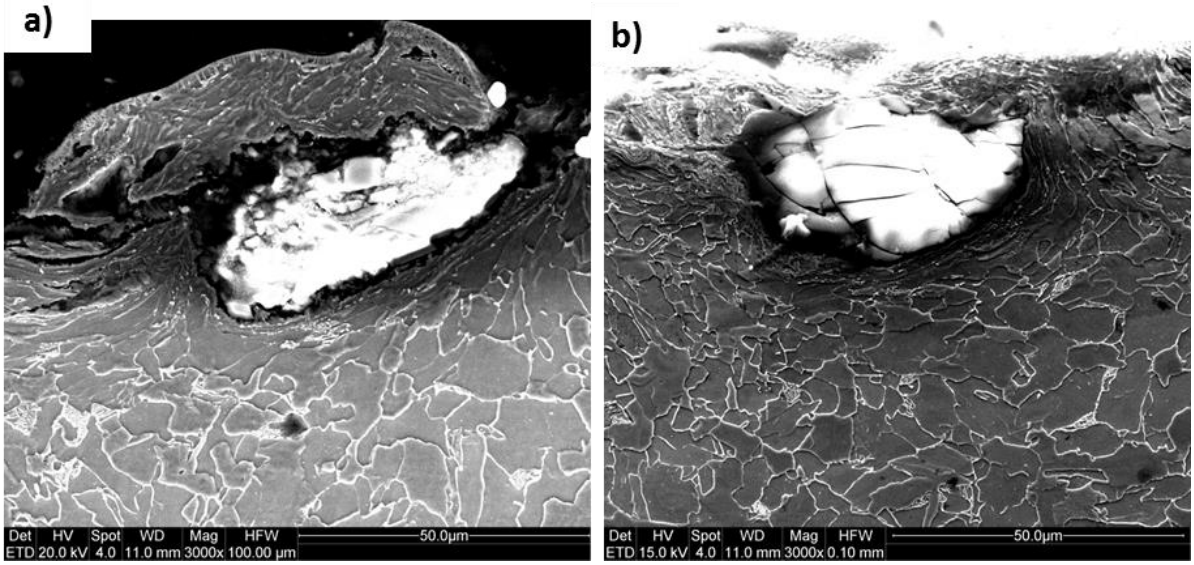


**Figure 4:7: Modifications of microstructure around the embedded particles after LACR treatment.**

### 4.3.4 Analysis of the embedded particles

As it will be discussed later, the embedded particles have a significant influence on the fatigue performance. Therefore, understanding the characteristics of the embedded particles is important. There are two types of embedded blasting particles. In one case, these embedded particles are exposed, i.e., surface embedded particles, and in another case, the particles are partially or totally covered by overlying metal, i.e., sub-surface embedded particles. Researchers have reported that particles already embedded on a surface will be impacted by later incoming particles, causing fractures and deeper embedment [11, 13, 21].

The particle size, i.e., the surface area of the particles, and depth distributions are obtained from the SEM images, such as the one shown in Figure 4:7. SEM images are collected from a sample length of 25.4 mm. The images are then processed using the software image J, developed at the National Institutes of Health (NIH), USA is a Java-based public domain image processing software [22]. A critical part of the digital processing is calibrating it with appropriate physical dimensions (pixel vs. physical dimensions), the area and maximum depth below the surface of the particle is calculated. A number density of 45 particles per $mm^2$ is obtained.

The surface area vs. depth distributions of all the investigated particles is shown in Figure 4:8. The triangular markers in the figure indicate the average depth below the surface of the particles, while the red line indicates the location of the particles, i.e., the minimum of the red line of a particle greater than zero means sub-surface embedded particles while minimum corresponds to zero indicates surface embedded particles. The length of the red line indicates the size of the embedded particles along the depth direction of the sample. Consistent with the previous observations [11, 21], it is noted that most of the sub-surface embedded particles are smaller in size, as shown in Figure 4:8. However, as it will be discussed later, no fatigue crack initiation is observed from these sub-surface embedded particles. Therefore, more focused is given on characterizing the surface embedded particles. Figure 4:9 shows the histogram of surface area (a) and depth (b), i.e., the deepest extent of the particles, distributions of the surface embedded particles obtained from the image analysis. The red solid lines in the Figure 4:9 (a) and (b) correspond to the log-normal distribution fit. An average surface area of 178

µm$^2$, and an average depth of 16 µm with a high standard deviation of 320 µm$^2$ and 10 µm, respectively, for the area and depth distribution of the surface embedded particles, was obtained from this log-normal distribution.

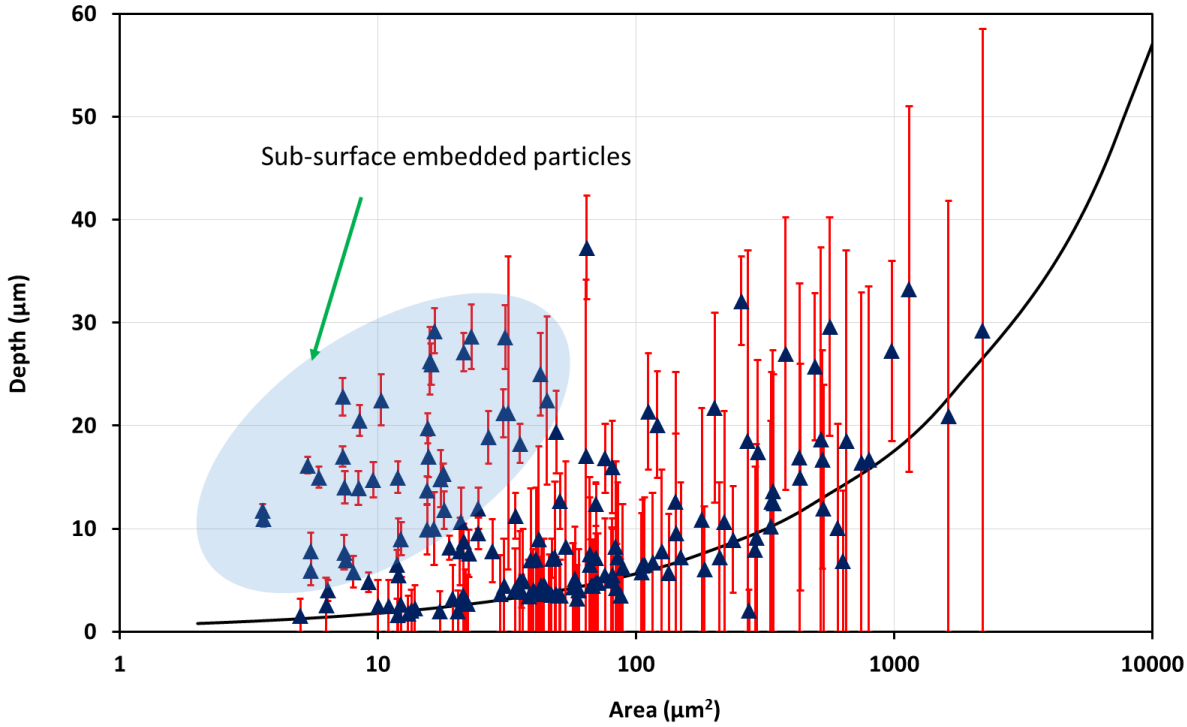


**Figure 4:8: The area vs. depth distributions of the entire investigated embedded particles**

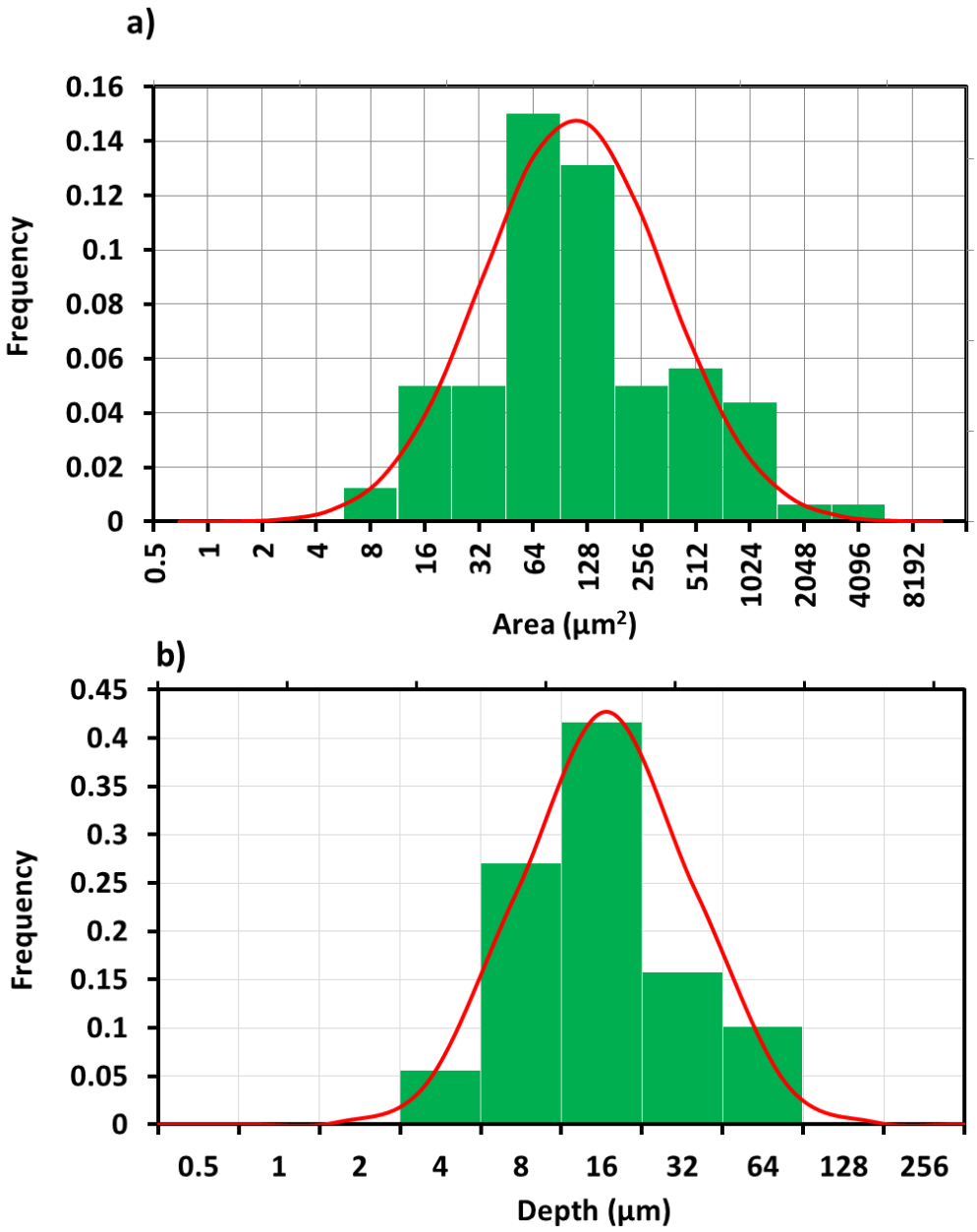


**Figure 4:9: The histogram of area (a) and depth (b) distributions of the surface embedded particles. The red solid line corresponds to the log-normal distribution fit.**

The continuous black line in Figure 4:8 corresponds to the effective depth $\left(d_{eff} = \sqrt{\frac{area}{\pi}}\right)$ of the particles. It is interesting to note that the depths (the deepest extent) of the largest

particles are typically lower than the effective depth, which indicates that these particles have a higher radius of curvature, i.e. they are elongated parallel to the surface plane. A very weak correlation between the surface area and radius of curvature of the particles are observed, however, it again shows that larger particles have a higher radius of curvature (see Figure 4:10). An even weaker correlation between depth (the deepest extent) and radius of the particles are observed, as shown in Figure 4:10. This relatively depth ($t$) independent (random distribution) of radii of curvature ($r$) of the particles indicates that the stress concentration associated with the embedded particles can be highest for the deepest particles, as the elastic stress concentration, $k_t \propto \sqrt{\frac{t}{r}}$. The histogram of t/r distribution is shown in Figure 4:11. Again, the red solid line is the log-normal distribution fit, which gives us an average t/r ratio of 5 and standard deviation of 3.

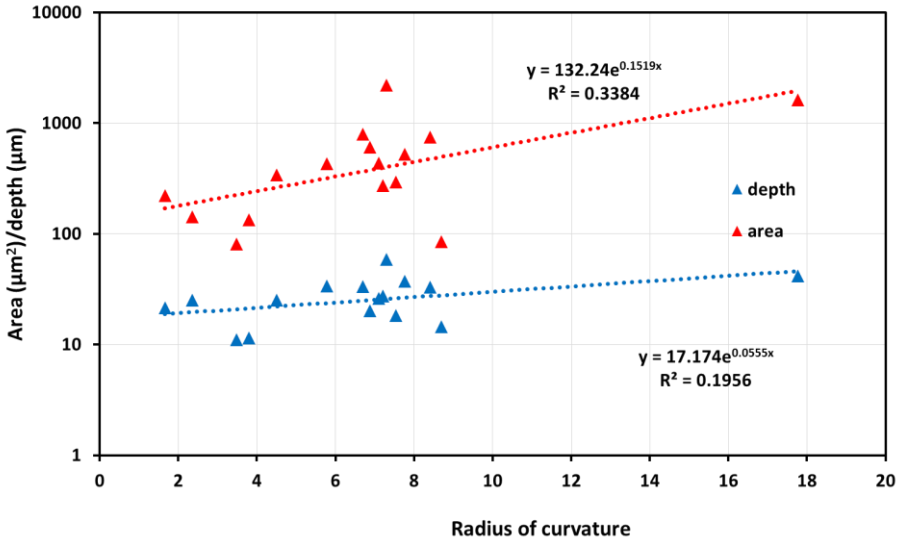


**Figure 4:10: Correlation between the area and depth of the particles with their radius of curvature.**

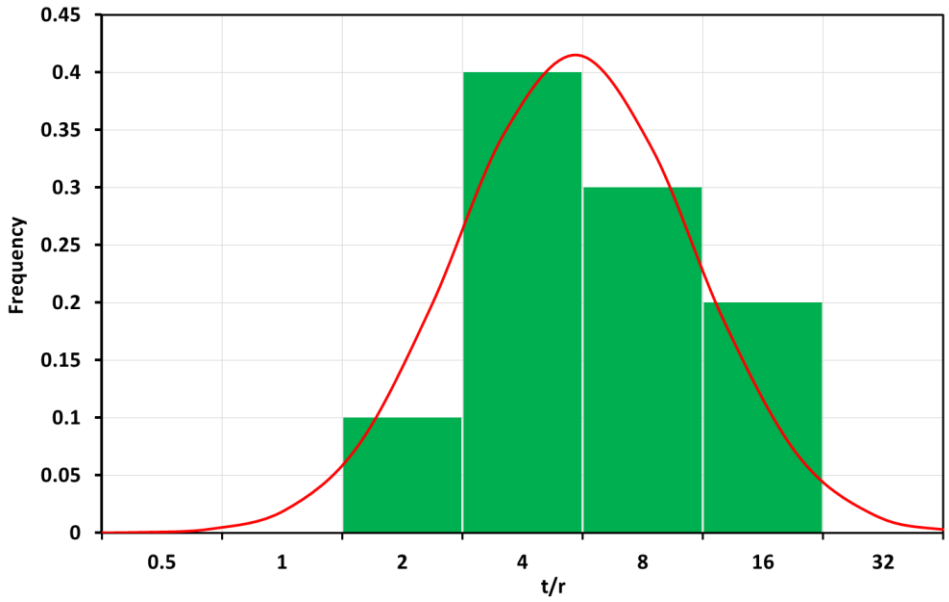


**Figure 4:11: The histogram of distributions of t/r ratio of the surface-embedded particles. Again, the red solid line corresponds to the log-normal distribution fit.**

### 4.3.5 Hardness

#### 4.3.5.1 Microhardness

Figure 4:12 presents the microhardness profile as a function of depth below the surface, taken from the abrasive blasted and LACR samples. As mentioned earlier, due to the size of the microhardness indentations, reliable microhardness measurements were obtained only for depths of 70 µm or more, with at least 10 readings recorded at each depth. Both surface processed samples have high hardness close to the surface and then the values gradually decrease to a depth of ≈200 µm from the sample surface. Given the level of uncertainty, the hardness profiles of the samples are indistinguishable from each other. In order to verify that the variation of hardness is the result of microstructural modifications induced by surface

treatments, a sample is polished 1 mm down from the surface to remove the microstructurally modified zone. Microhardness profile of such a “polished” sample shows that hardness remains constant as a function of depth below the surface, which indicates that hardness variations indeed induced by the abrasive blasting/LACR surface treatments. The microhardness depth profiles are actually consistent with the microstructural observations. The higher hardness of the abrasive blasted samples is related to the deformed zone produced by the high velocity impact of the blasting particles. LACR did not produce any significant change in the microstructure at depths interrogated for microhardness. As a result, both sample types show similar microhardness values at each depth equal to or greater than 70 μm. This indicates that if there is any significant change in the mechanical properties due to different surface treatments, it is restricted to the near surface region, i.e., the affected region is less than 70 μm.

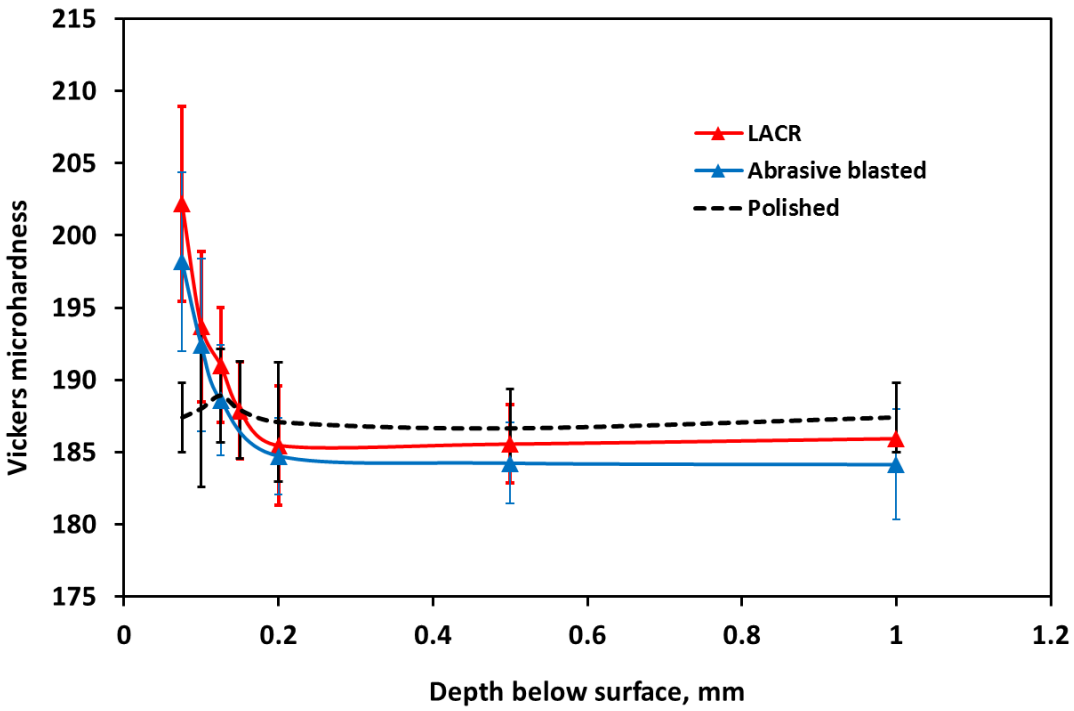


**Figure 4:12: Microhardness depth profile of abrasive blasted, LACR and polished samples. Error bars indicate the standard deviation of hardness values at each depth.**

### 4.3.5.2 Nano-hardness

Figure 4:13 shows the nano-hardness vs. depth plot obtained from loading/partial unloading experiment of a point approximately 20 µm below the abrasive blasted and LACR treated surface and in the mid-plane (base metal). The plots corresponding to abrasive blasted and LACR samples show that hardness value decreases with increasing indentation depth (load), which is not the case for the base metal. The hardness value of the base metal remains constant with increasing depth. The decrease in hardness with increasing depth is typical of many materials, a phenomenon known as the indentation size effect (ISE). Nix and Gao [23], using strain-gradient plasticity (SGP) theory, pointed out that the ISE is the result of the

increasing contribution of geometrically necessary dislocation (GND) over that of statistically stored dislocations at small depth. They proposed the following relationship between hardness and indentation depth based on this SGP theory [23]:

$$\left(\frac{H}{H_0}\right)^2 = 1 + \frac{h^*}{d} \qquad [4.1]$$

Where $H$ and $d_0$ denote hardness and depth, respectively. $H_0$ (the intercept of the $H$ vs. $1/d$ plot) can be defined as the macroscopic hardness value in the limit of infinite depth.

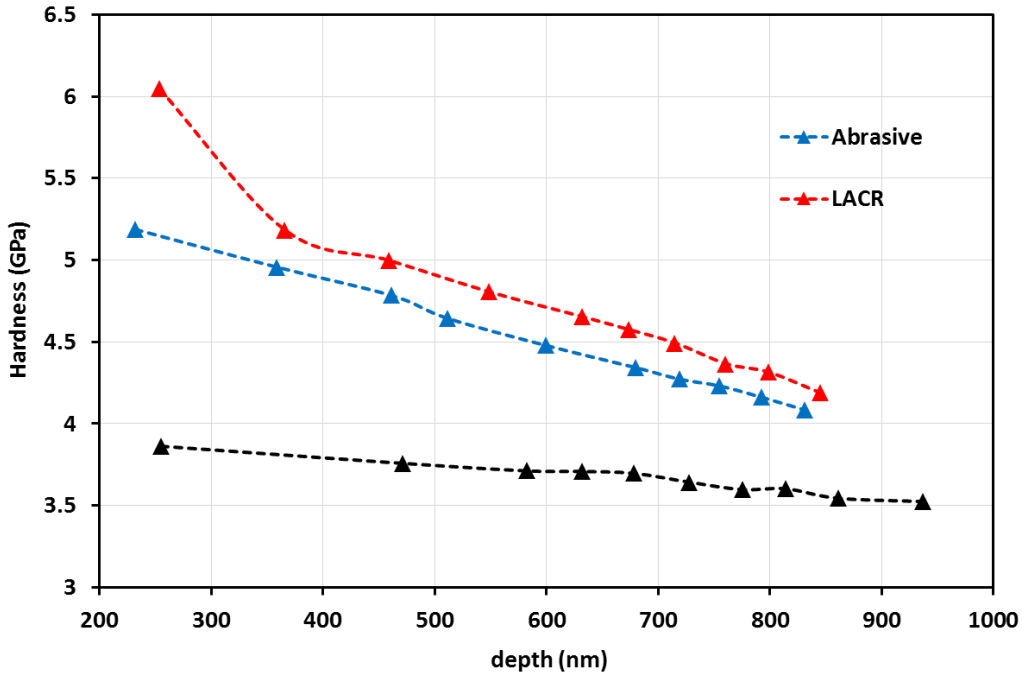


**Figure 4:13: Nano-hardness as a function of the depth for different surface processing conditions.**

In Figure 4:14, the square of nano-hardness ($H$) is plotted against the inverse of the indentation depth for different surface processed steel and one with no surface processing. Figure 4:14

illustrates that the functional dependence between $H^2$ and $1/d$ suggested by equation 4.1 is only valid for depths greater than 350 nm. Ro et al. [24] reported similar observations for aluminum 2024 alloy. They highlighted two related but different reasons for this. The dislocation density may not be high enough at the shallow depths to invoke the functional relationship described in equation 4.1. Secondly, the model also assumes that the deformation is purely plastic. However, at small depths that are comparable to tip radius of the indenter elastic deformation can play a significant role. Therefore, the macroscopic hardness ($H_0$) is determined using the results for depths greater than 350 nm where equation 4.1 accurately describes the dependence of hardness on indentation depth, as shown in Figure 4:14. Depth independent hardness ($H_0$) is determined from the intercept of the linear fit to the $H^2$ vs. $1/d$ data. $H_0$ has thus calculated shows that hardness value close to (≈20 µm below) abrasive blasted and LACR treated surface has a very similar magnitude. $H_0$ determined to be 3.41 GPa and 3.35 GPa for abrasive blasted and LACR samples, respectively, while the data collected from the base metal are slightly lower (~ 3.04 GPa). This is consistent with the Vickers microhardness measurement, as discussed in the previous section. However, conversion of the Vickers hardness value (HV) to GPa (i.e., multiplying with .0098) yields 1.83 GPa, which is significantly lower than the value (3.04 GPa) obtained from nanoindentation. Many other researchers have also reported similar higher hardness value for nanoindentation measurement [25-27].

Nanoindentation hardness ($H$) is calculated by analyzing the load ($P$) vs. displacement curve with Oliver-Pharr method [15]:

$$H = \frac{P_{max}}{A_c} \qquad [4.2]$$

where $A_c$ is the projected contact area. Equation 4.2 clearly indicates that the measurement accuracy of $H$ mainly depends on how well the $A_c$ match with the indent residual projected area $A_r$. Using the finite element method, Bolshakov and Pharr [28] found that when pile-up due to indentation is significant $A_C$ can be as low as 60% of the true contact area, which in turns leads to larger errors in the hardness value. Pile-up typically occurs in the materials with a small value of yield strength ($YS$) over elastic modulus ($E$) ratio [27]. The value of YS/E of the material under investigation is determined to be 0.0022. Therefore, the high nanoindentation hardness of the investigated materials is attributed to the reduced projected contact area due to pile-up.

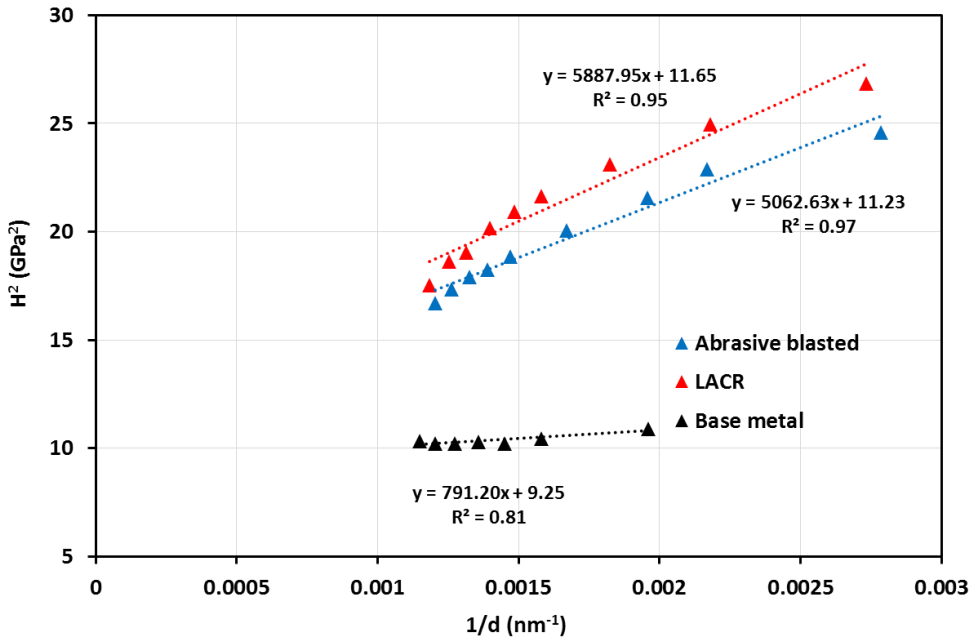


**Figure 4:14: Plots of the square of the nano-hardness value vs. inverse depth show some non-linearity yet still provide high goodness of fit to the Nix & Goa model, especially for the abrasive blasted and laser treated samples.**

Finally, Figure 4:15 shows the mean hardness value (at least 10 indentations per data point), as a function of depth below the surface of the abrasive blasted and LACR samples. Similar to the microhardness depth profile, nano-hardness depth profile also shows that hardness value gradually decreases with increasing depth. Considering the uncertainty associated with the hardness measurement (high error bars), the depth profiles of the abrasive blasted and LACR samples are indistinguishable. This again indicates that the HAZ induced by LACR treatment is shallow and consequently, any significant change in the mechanical properties due to LACR treatment of the baseline abrasive blasted materials appears to be restricted to depth shallower than 10 µm.

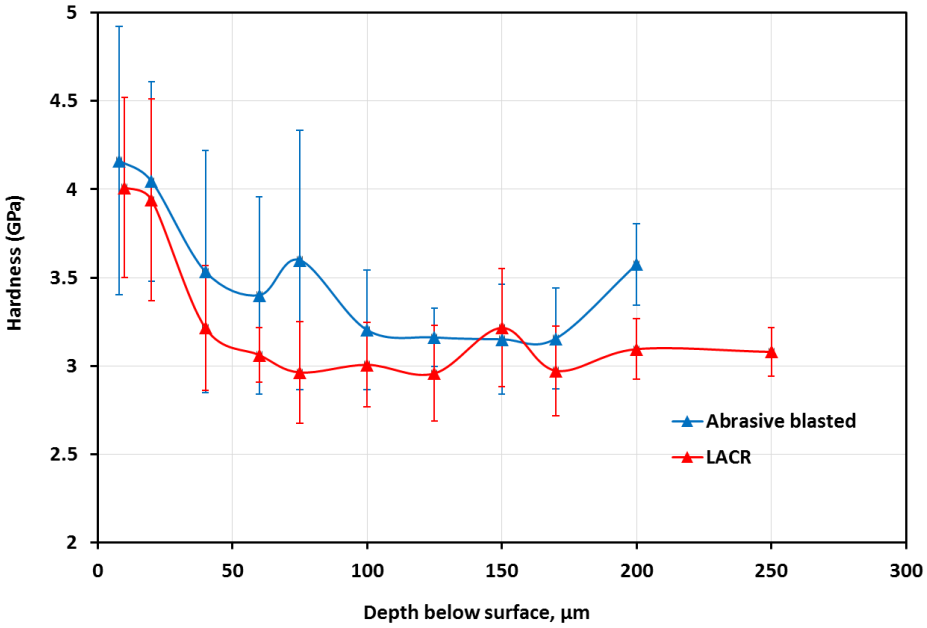


**Figure 4:15: Nano-hardness depth profile of abrasive blasted and LACR samples. Error bars indicate the standard deviation of hardness values at each depth.**

### 4.3.6 Residual stress

Figure 4:16 shows the residual stress as a function of depth from the abrasive blasted and laser treated samples. Abrasive blasting creates a layer of plastic deformation with an elastically deformed region underneath. This places the surface layer in compression. The distributions of the residual stresses of the abrasive blasted samples showed a typical "U-shape" profile, where compressive residual stress reached its highest magnitude of approximately 340 MPa at a depth of about 100 µm and then it gradually decreased to zero at a significant depth of about 325 µm.

The residual stress profile of sample subjected to LACR reveals a tensile surface residual stress, however, the region of tensile residual stress is confined to a shallow depth. The tensile residual stress has its peak value at the surface, and then it decreases to zero just below the surface. This near-surface tensile residual stress “case” is balanced by the subsurface compressive residual stresses. The sharp swing in residual stress of laser treated samples probably results from the fact that only a thin surface layer is melted and re-solidified. The depth of the tensile region is about 30 µm and the highest magnitude of the balancing compressive residual is ≈250 MPa at a depth of ≈120µm. The case depth of the compressive residual stress is about 350 µm, which is similar to the compressive case depth of the abrasive blasted samples.

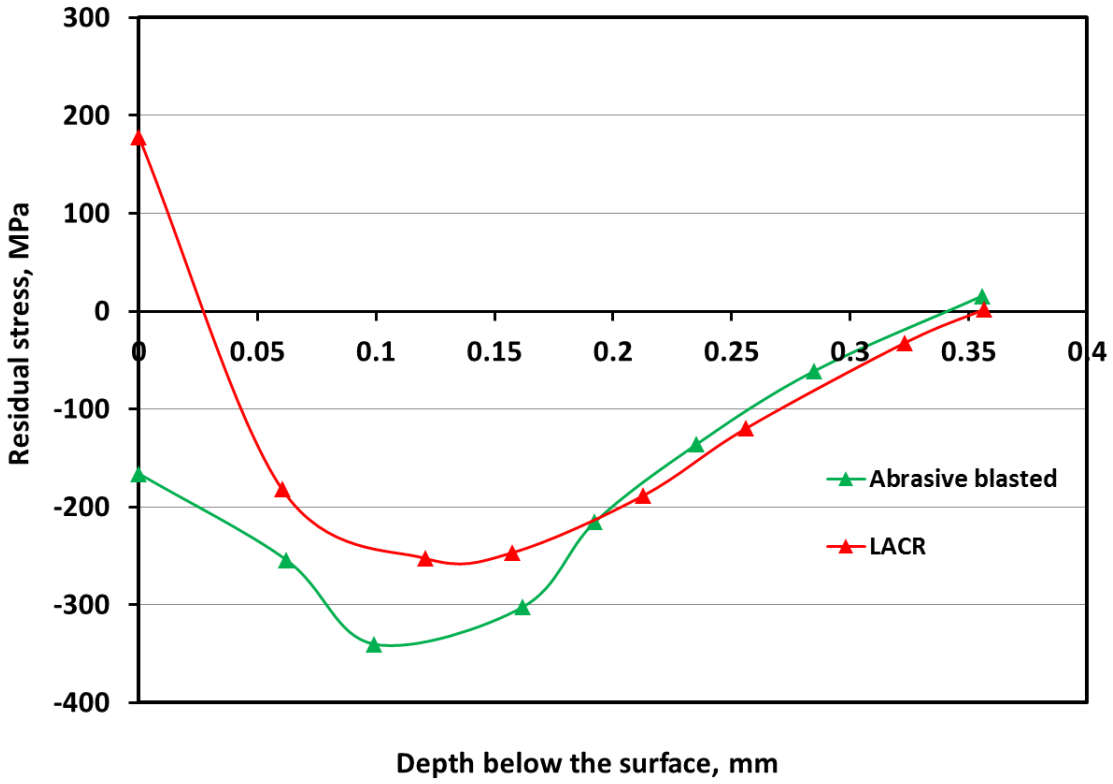


**Figure 4:16: Residual stress depth profile of abrasive blasted and LACR processed steel.**

### 4.3.7 Fatigue performance

The Wöhler (S-N) curves of the abrasive blasted and LACR surface processed steel are shown in Figure 4:17. It should be noted that to differentiate the effect of surface treatment on fatigue performance and to assess the level of scatter of the fatigue life, a number of samples were tested at a single stress amplitude of 208 MPa. The curves in the plot are best-fit to the experimental data obtained by least squares non-linear regression of the Stromeyer equation, which relates $N_f$, the cycles to failure to the stress amplitude, S.

$$S = S_L + A(N_f)^m$$

where $S_L$, $A$, and $m$ are fitting parameters. The fitting parameters are listed in Table 4.3. As before, employing this relation with an endurance limit, $S_L$, does not represent an endorsement of a particular fatigue design philosophy. Rather, fitting the data to this relation permits a ready comparison between the sets of obtained fatigue data. Note that only the highest stress amplitude run-out data were included in the regression analysis.

By comparing the Figure 4:17 with the Figure 3.5 and also, Table 3.2 with Table 4.3, it is shown that the materials in this study have a better fatigue resistance than those in Chapter 1 and 2, irrespective of their surface processing condition, due to their relatively higher yield strength (as shown in Figure 4:1). However, contrary to the fatigue performance of the material HSS-I in which LACR treated samples showed a similar fatigue performance to abrasive blasted samples, LACR processed samples show a modest (< 12%) knock-down of fatigue performance relative to abrasive blasted samples. In order to better understand the root causes of this discrepancy, the fracture surfaces of the failed samples are investigated.

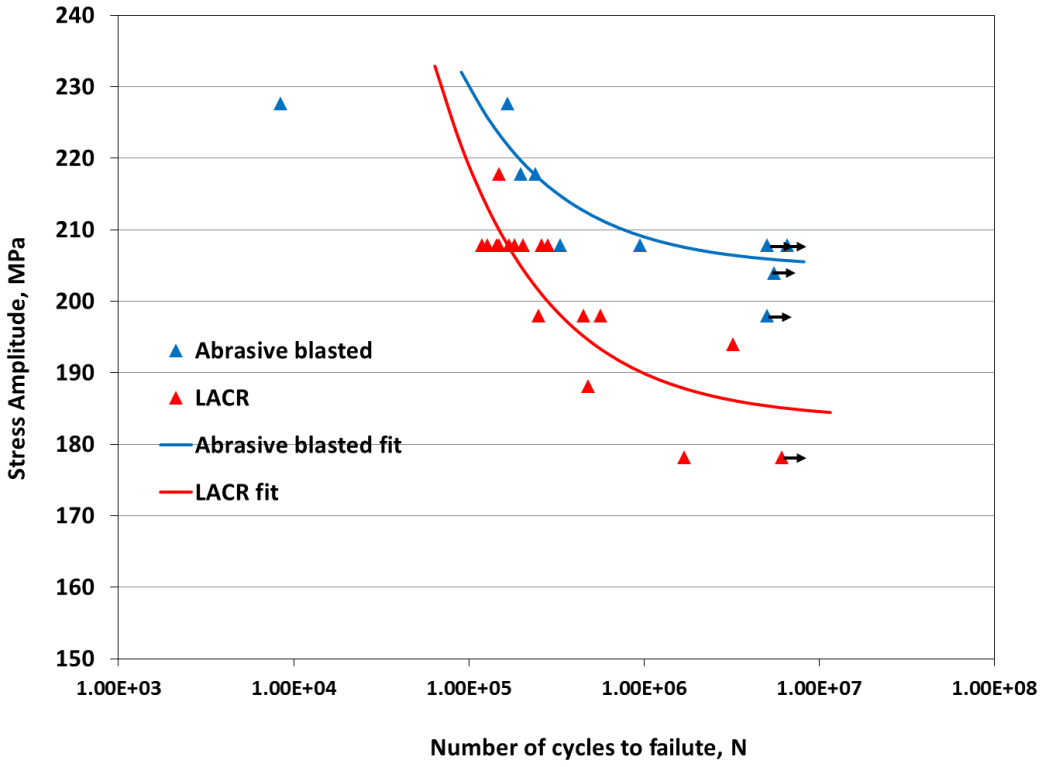


**Figure 4:17: S-N curves for the abrasive blasted and LACR samples. Arrows at $5x10^6$ cycles represent run-out tests and the curves are best fits of the data to the Stromeyer relation.**

**Table 4.3: Fit parameters of the Wöhler-Stromeyer equation from non-linear regression of the S-N data presented in Figure 4:17.**

| Sample condition | $S_L$ | $A$ | $m$ |
|---|---|---|---|
| Abrasive Blasted | 204.5 | 1.7E+05 | -0.72 |
| LACR | 183.4 | 1.7E+05 | -0.72 |

### 4.3.8 Fractography

Fractographic analyses of the abrasive blasted samples show that in most cases, the crack originated from the surface defects, as shown in Figure 4:18. Figure 4:18 shows the

fractographs of the abrasive blasted samples tested at two different stress amplitudes: a, b) 208 MPa, and c, d) 218 MPa. In both cases, cracks initiated from surface depressions, i.e. a valley in the roughness profile, created by abrasive blasting. None of the abrasive blasted samples exhibited corner crack initiation. Multiple cracks initiating from the valleys of the surface roughness were observed on a single sample, especially at high stress levels. These small cracks grow independently for some portion of the fatigue life prior to the coalescence of two or more larger cracks and subsequent growth of a single large crack. The low magnification inset shown in Figure 4:18(c) highlights a couple of distinct initiation sites with the dashed circles. Note the river marks radiating outward from each of them. In between, one can observe a "ledge" where the two simultaneously growing cracks met and linked up to form a single crack on its way to final fracture. Occasional crack initiation from the embedded blasting particles is also observed. 11 abrasive blasted samples were fatigue tested and 6 samples failed. A total number of 31 crack initiation sites are identified from the fractographs of the failed samples. Only 25% of the total crack initiation sites are located at the vicinity of embedded particles.

On the other hand, SEM observation of fracture surface of LACR samples show that crack predominately originated from the vicinity of the embedded media rather than an empty surface depression or valley in the surface profile of laser treated samples (see Figure 4:19). Figure 4:19 shows the crack initiation sites for LACR samples at two different stress amplitudes: a, b) at 198 MPa and c, d) at 208 MPa. Similar to abrasive blasted samples, multiple crack initiation sites are also observed for LACR samples. 12 failed fatigue tested LACR samples were investigated for this analysis and total 33 crack initiation sites are identified. This analysis of the

crack initiation sites shows that 73% of the cracks initiated from embedded particles for LACR samples.

In comparison, SEM observation of fracture surfaces of the HSS-I, in both abrasive blasted and laser treated condition, show that cracks initiated predominately from the surface depressions, i.e. a valley in the roughness profile (see section 3.3.3).

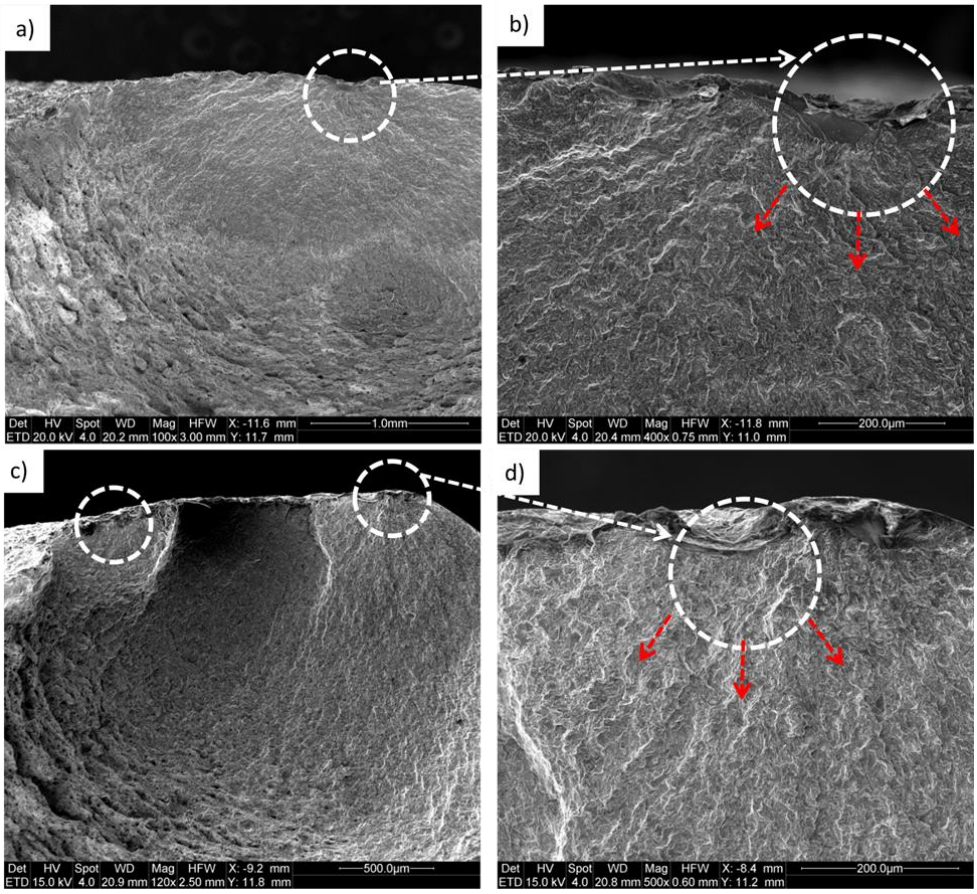


**Figure 4:18: Scanning electron micrographs of the fracture surface of an abrasive blasted sample loaded at a stress amplitude of 208 MPa, showing crack initiation at the surface depression (a, b). Multiple initiation sites are shown in (c) indicated by the circles. Higher magnification micrograph shows crack initiated from the valley of the surface flaw (d).**

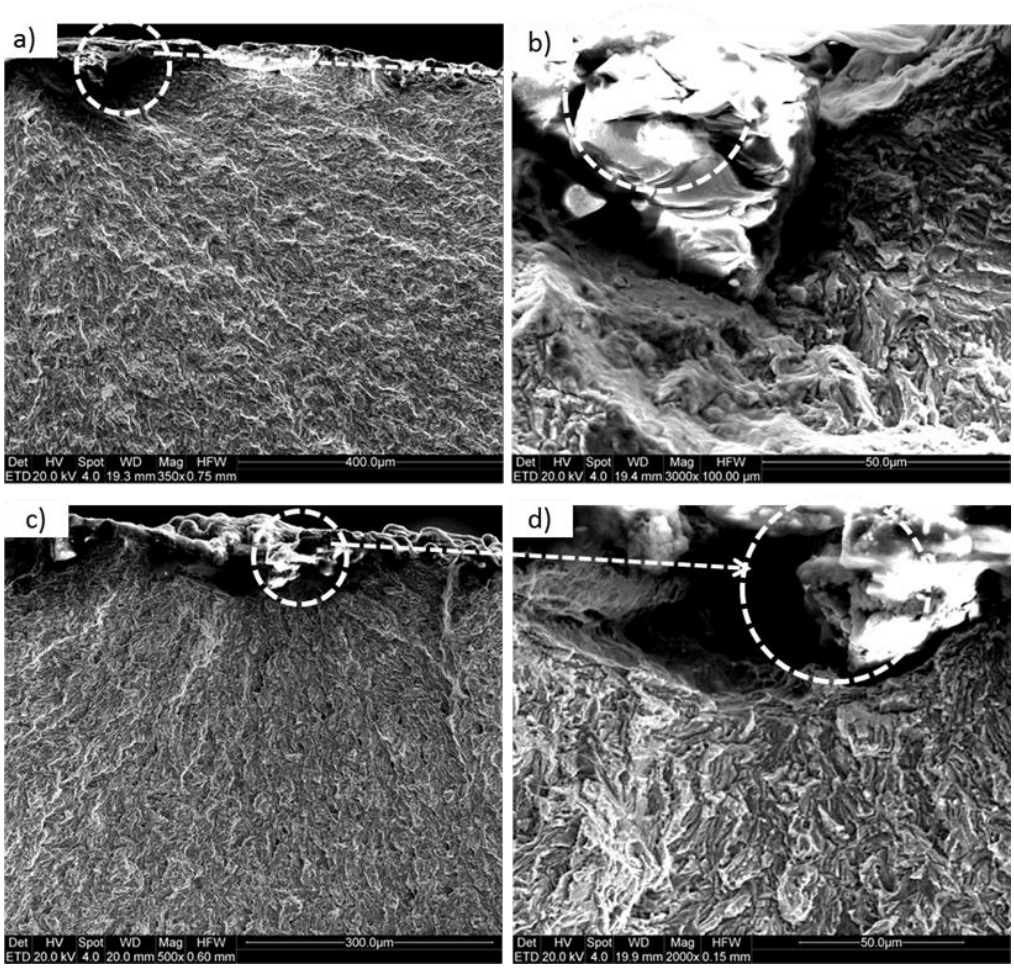


**Figure 4:19: Scanning electron micrographs of the fracture surface of LACR sample loaded at a stress amplitude of a, b) 198 MPa, and c, d) 208 MPa showing crack initiation from the vicinity of the embedded particles.**

Figure 4:20 shows the area vs. depth distributions of the embedded media, which act as crack initiation sites under cyclic loading for abrasive blasted and LACR treated samples. In comparison with Figure 4:8 and Figure 4:9, Figure 4:20 reveals that fatigue cracks typically initiated from the larger surface embedded particles having areas typically in the rage of 500 $\mu m^2$ -3000 $\mu m^2$, which is much higher than the average area of the embedded particles (178 $\mu m^2$). Only 4% of the embedded particles have an area greater than or equal to 500 $\mu m^2$ (see

Figure 4:9). This invokes the well-known facts that fatigue failure occurs from the "weakest" link of the sample. It is also noted here that fatigue cracks in the LACR samples typically initiate from the more deeply embedded particles, as compare to abrasive blasted samples. A cumulative depth distribution of embedded particles which act as crack initiation sites show that 90% of the particles have depths greater than or equal to 40 µm for the abrasive blasted surface condition, and 70 µm for LACR samples (see Figure 4:21). However, this distinction is based on only a small number of sampling data.

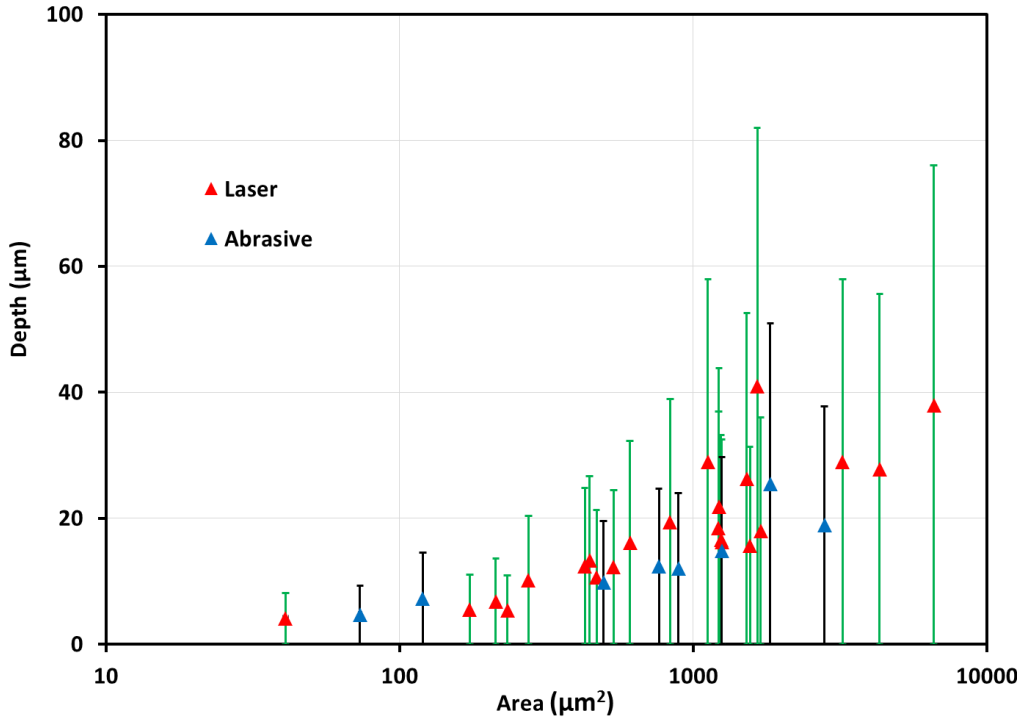


**Figure 4:20: The area vs. depth distributions of the embedded particles from which fatigue crack initiated.**

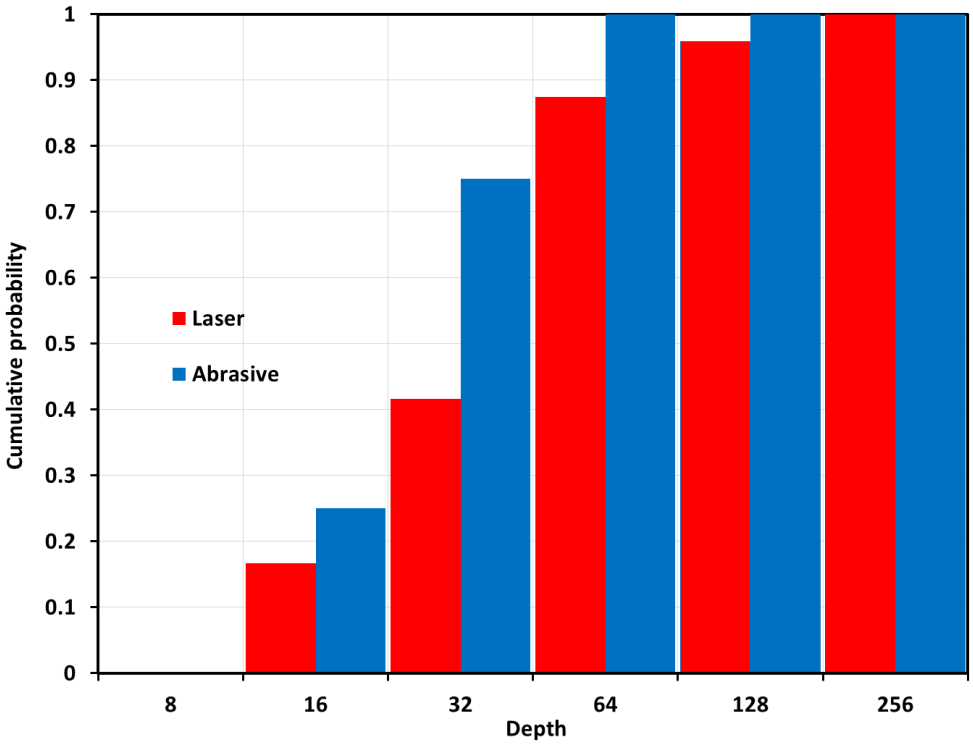


**Figure 4:21: Cumulative distributions of the depth of embedded particles from which fatigue crack initiated.**

## 4.4 Modeling and Discussions

Considering the fact that LACR processing has a similar impact on microstructures, hardness and stress state, as shown by XRD residual stress measurement, for both materials (HSS-I and HSS-II), the distinct fatigue response after LACR treatment is somewhat surprising. As discussed earlier, fatigue performance depends on the corporate actions of the surface damage (e.g. surface roughness, micro-notch in the vicinity of embedded particles) and residual stress. It is well known that, for the case of a constant stress concentration, a higher tensile residual stress will lead to degradation of the fatigue resistance. Conversely, for similar residual stress fields, the fatigue performance decreases with increasing stress concentration. The stress

concentration factor calculation from the roughness parameters shows that (see section 3.4), in the cases where fatigue cracks initiated from valleys in the surface profile, detrimental effects of surface tensile residual stress of laser treated samples are balanced by the beneficial effects of the smoother surface topology and fatigue performance is similar to the abrasive blasted samples. However, laser treated samples of HSS-II show crack initiated predominately from the vicinity of the embedded media, from prior abrasive blasting treatment. Due to the presence of the embedded particles, stress concentration associated with these particles essentially remain the same and compressive residual stresses around these particles may provide an explanation for which the altered behavior is observed. Indeed, XRD based residual stress measurements show that the magnitude of the compressive residual stress below the surface is lower after LACR processing (see Figure 4:16). In addition, because of the initial high surface roughness, the surface smoothing effect after LACR processing is not so evident in this case. Both the high stress concentration factor and detrimental stress state relative to abrasive blasted samples may cause the degradation of the fatigue performance of the LACR samples. In order to verify this hypothesis, the stress concentration associated with the surface defects and temperature distribution in the material are evaluated using finite element analysis.

### 4.4.1 Finite element analysis of the effect of surface topography

In most of the recent approaches [29-31] ( also see section 3.4), the elastic stress concentration factor ($k_t$) is calculated from the averaged geometrical parameters of the surface profile. However, this method clearly depends on the accurate experimental determination of roughness metrics and, as discussed in section 2.3.2.2, it is often associated with the

experimental error. In order to compute $k_t$ more accurately, a new approach using finite element analysis (FEA) is presented here. In this method, 2D surface profiles are created by fitting the surface of scanning electron microscope (SEM) cross-sectional images to the Fourier function. The point clouds obtained from the Fourier function are then imported to SolidWorks software to create a solid surface (see Figure 4:22(a)). The surface is then superimposed on the rectangular part as a surface model in Abaqus to create a 2D deformable part for FEA, as shown in Figure 4:22(b). 2D plane strain FEA is then performed using commercially available Abaqus version 6.14. Materials are considered to be linear elastic with elastic modulus E=200 GPa and Poisson's ratio $\vartheta$ = 0.3. As shown in Figure 4:22(b), the displacement along the x-axis (Uxx) at the boundary x=0 is kept fixed. Also, there is no rotation around the z-axis (UR3 =0) at the boundary x=0. A free boundary condition along the y-axis is imposed. Uniform load is applied as the boundary condition at x=L.

In order to extract meaningful information from the finite element analysis, it is important to determine the sensitivity of the element size on the obtained results. Mesh sensitivity analysis shows that numerical solution converges when the rough surface regions are meshed with an element size of 0.3 μm. Element size is gradually increased with distance away from the rough surface region, in order to increase the computational efficiency (Figure 4:22(c)).

The maximum stress along the loading direction ($\sigma_{xx}$) obtained from FEA analysis is then divided by the nominal applied stress to determine the stress concentration factor ($k_t$). Due to the irregular distributions of the surface grooves, different magnitudes of $k_t$ value are obtained at a different locations and only the maximum value is considered further. For comparison, the

stress concentration factors for the material HSS-I are also computed using the method described above. For each material and surface condition, 3 samples of 25 mm in length were investigated and only maximum value of $k_t$ is reported.

In addition, $k_t$ of the material HSS-I is also computed from the 2D surface topography obtained from the stylus based surface roughness measurement. The FEA-based methodology is similar to the one described above. Here point clouds from the stylus based roughness profile are used instead of those obtained from the SEM cross-sectional images.

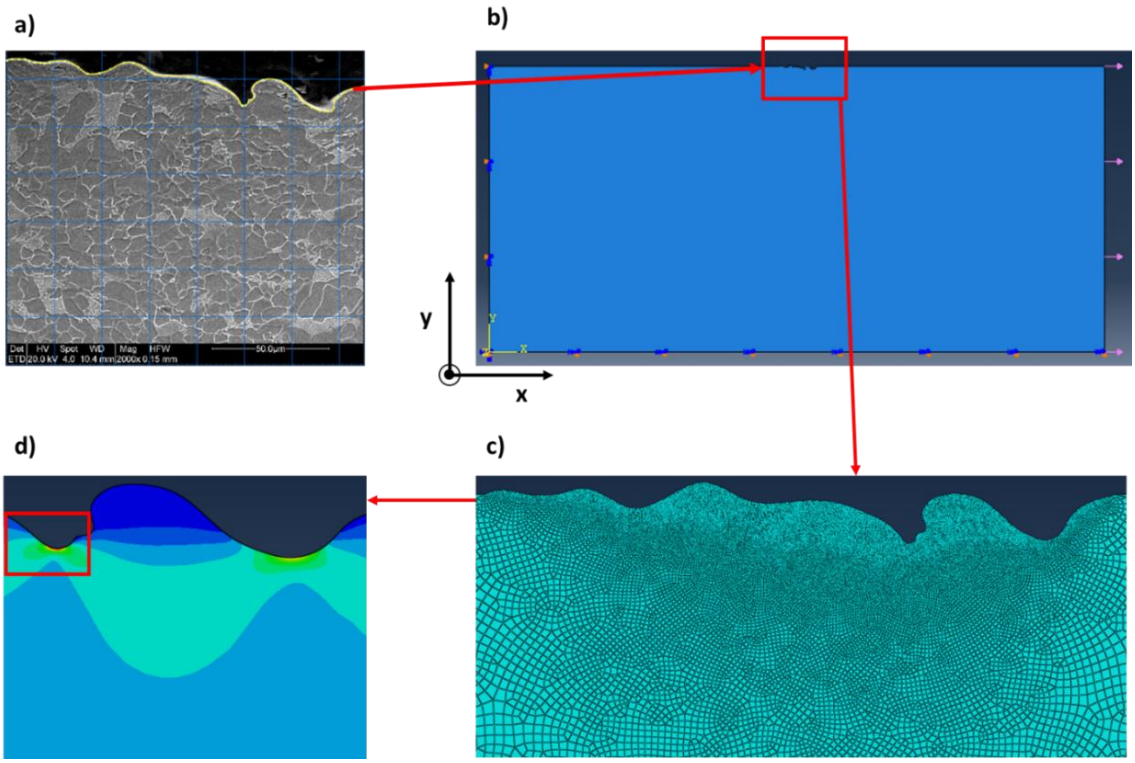


**Figure 4:22: Principle of finite element analysis for determination of stress concentration factor: a) extracting surface profile from SEM cross-sectional image, b) geometry and boundary condition, c) finite element mesh, and d) stress distribution after load applied.**

Figure 4:23 shows the stress concentration factor of the abrasive blasted and LACR samples for both materials HSS-I and HSS-II. Similar to Section 3.4, the maximum value of $k_t$ of the abrasive blasted samples is significantly higher than LACR samples for the material HSS-I, which again reinforces the claim that the similar fatigue performance of the LACR samples relative to abrasive blasted samples indeed the result of the counter balancing effects of lower stress concentration and variations in the residual stress profile. On the other hand, there is no significant difference in the maximum value of $k_t$ between the abrasive blasted and LACR samples of HSS-II sampes. In fact, $k_t$ it is always higher for HSS-II relative to the HSS-I. Both of these observations are due to the fact that the maximum stress concentration is typically associated with the embedded particles in case of the HSS-II material.

It is interesting to note that the maximum value of $k_t$ between the abrasive blasted and LACR samples even for material HSS-I is essentially the same, when $k_t$ is calculated based on the surface profile obtained from the profilometer. This again shows that that profilometer cannot detect the change in fine-scale surface roughness after LACR processing, mainly because the tip of the sylus has a finite radius which precludes detection of the sharpest valleys.

It is also noted that the value of $k_t$ obtained from the FEA analysis is more close to the value of $k_t$ obtained from the Neuber model [30] than the one obtained from Arola-Ramulu model [29].

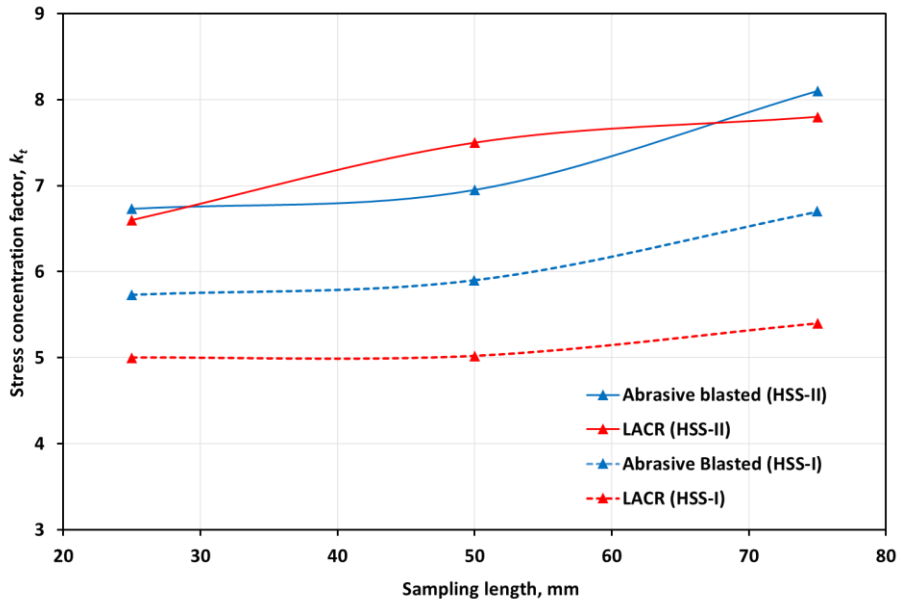


**Figure 4:23: Stress concentration factor of the abrasive blasted and LACR samples based on surface profile obtained from SEM images.**

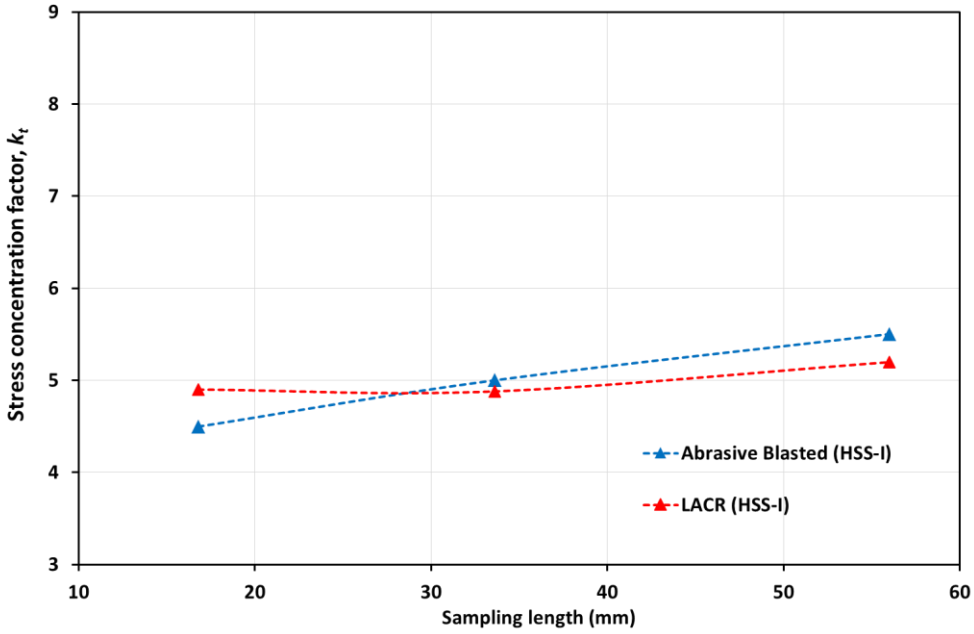


**Figure 4:24: Stress concentration factor of the abrasive blasted and LACR samples of HSS-I based on surface profile obtained from the profilometer.**

Finally, it should be pointed out that the 2D plane strain finite element analysis gives a higher value of $k_t$ than would have been obtained using a 3D finite analysis of a 3D surface topography. As an example, $k_t$ of the elliptical notch with t/r =1 is calculated to be 3.09 from the 2D FEA analysis, while $k_t \approx 2.06$ is obtained from the 3D FEA analysis of corresponding surface depression. Nevertheless, this comparative study based on the 2D FEA provides valuable insights of the stress distributions associated with different surface conditions.

### 4.4.2 Heat transfer analysis

Previously heat flow during laser-steel interaction was modeled using the simulation of laser interaction with materials (SLIM) software (section 2.3.6). Since then, a better understanding of the laser-material interaction and visualization was developed using Abaqus/Standard software.

The mechanisms of heat transfer using a laser source of pulse duration varying within the nanosecond to femtosecond range. In the case of nanosecond pulses, it is a good approximation to use a one-step heating process, since the electron-phonon thermal relaxation is much shorter compared to the laser pulse length and it gets sufficient time to establish local thermal equilibrium with the lattice. Therefore, similar to continuous wave laser, the transient temperature field $T(x, y, t)$ for nanosecond pulsed laser can be obtained by solving the heat conduction equation along with the appropriate initial and boundary conditions.

$$\rho C_p \frac{\partial T}{\partial t} = \frac{\partial}{\partial x}\left(k \frac{\partial T}{\partial x}\right) + \frac{\partial}{\partial y}\left(k \frac{\partial T}{\partial y}\right) + S$$

where $\rho$ is the density, $C_p$ is the specific heat, $k$ is the conductivity and $S$ is the source term. $S$ is considered as a volumetric heat source (W/m$^3$) for pulsed laser while for a continuous wave (CW) laser it was considered as a surface heat source (W/m$^2$).

Temperature dependence of the thermal properties of the steel were taken from the literature [32]. The volumetric heat source *(S)* is a function of laser intensity and the Lambert-Beer law, which can be mathematically expressed as follows:

$$S(x, y, t) = I(x, t)(1 - R)\alpha \exp(-\alpha y)$$

Here $R$ is the reflectivity, $\alpha$ is the absorption coefficient, and $I(x, t)$ is the laser intensity term in the spatial and temporal domain. The absorption coefficient is inversely proportional to laser penetration depth and depends on the wavelength and mathematically it is given by:

$$\alpha = \frac{4\pi k}{\lambda}$$

where $k$ is the extinction coefficient. Extinction coefficient of steel at 1064 nm wavelength is unknown, and 4.5 for iron is used. A Gaussian laser pulse in temporal and spatial domain is usually used to calculate the laser intensity and can be mathematically expressed as:

$$I(x, t) = I_0 \exp\left(-\frac{x^2}{r^2}\right) exp\left(\frac{(t - t_0)^2}{2\sigma^2}\right)$$

Where $I_0$ is the peak intensity (≈ 6× 10$^{11}$ W/m$^2$), $r$ is the laser beam spot radius (≈ 1 mm). In the present case, σ = 35.2 ns (83 ns FWHM), to = 3σ.

Correct discretizations of temporal (pulse duration) and spatial domain (characteristics thermal length) are necessary to obtain realistic results. The characteristic thermal length (thermal diffusion distance) can be expressed as:

$$l = 2\sqrt{\alpha t}$$

where α is the diffusivity of steel and t is the pulse duration. Mesh sensitivity analysis showed that the numerical solution converges for minimum element size of 10 nm. Finally, it is noted that the heat diffusion equation is solved by a backward difference algorithm in Abaqus/standard:

$$\dot{U_{t+\Delta t}} = (U_{t+\Delta t} - U_t)\left(\frac{1}{\Delta t}\right)$$

Figure 4:25 shows the temperature profiles as a function of a) time at the center of the laser beam for different distances below the surface, and b) distance below the surface from the center of the laser beam at the end of single pulse heating period. The modeling result shows a maximum surface (x=0) temperature of ~3800 K at the end of pulse heating period. Melt depth of about 0.8 µm was observed, which is slightly lower than the experimentally observed value (1-3 µm), however, it is consistent with SLIM modeling. The apparent discrepancy could be due to the fact the effects of surface roughness are not considered during FEA analysis. It is well known that surface roughness increases the effective absorption coefficient of the material [33]. The spatial temperature distribution shows that there is essentially no rise in the temperature at a depth of 10 µm. Considering the typical depth of the surface embedded particle (≈16 µm), it can be concluded that heat does not conduct deep enough to relax the residual stress around the embedded particle. Therefore, any change in stress state around the particles would be the result of redistribution of the residual stress due to surface melting. This will be discussed in more detail in Chapter 6. However, this conclusion is solely based on the laser- material interaction analysis of the bare metal, the coating of the base metal and the

presence of embedded blasting media will also affect the temperature distribution. Depending on the thermal properties of the paint, paint can absorb most of the thermal energy and heat diffusion distance in the underlying base material will be even lower than the simulated results. Similarly, the presence of the ceramic particles (garnet abrasive blasting media), which have a very low thermal conductivity, will also the decrease the thermal diffusion distance in the material. Hence, the thermally affected zone calculated from the simulation is expected to higher than what one would experimentally observe. This also correlates well with the microstructural observations, which shows essentially no change in microstructure around the embedded particles (Figure 4:4 and Figure 4:7).

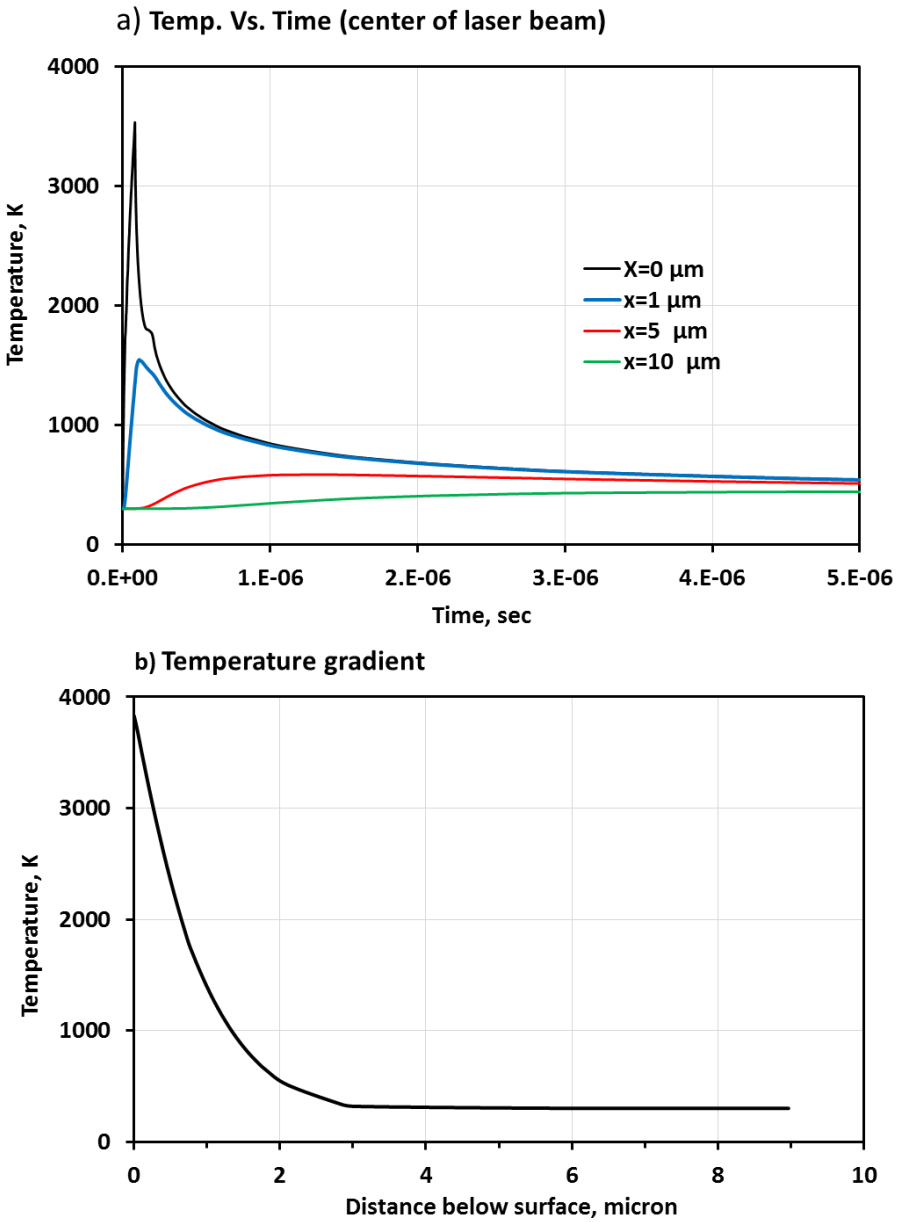


**Figure 4:25: Temperature profile as a function of a) time at the center of laser beam for different distance below the surface and b) distance below the surface from the center of laser beam at the end of pulse heating period.**

## 4.5 Conclusions

The effects of variations of microstructures and abrasive blasting protocol on the fatigue performance of LACR treated high strength shipbuilding structural steel (HSS-II) have been assessed and compared with baseline abrasive blasted substrates. The following conclusions can be drawn from this study:

a) The cross-sectional analyses confirmed that irrespective of initial microstructures, LACR induced similar modifications of the microstructures, i.e., melting and re-solidification of the underlying substrate. The depth of the observed melted region again ranged from 1 µm to 3 µm.
b) No microstructural changes were observed at depths greater than 10 µm after LACR treatment. Also, both micro- and nanohardness measurements show a hardness profile of abrasive blasted and LACR samples which is essentially the same.
c) Changes in abrasive blasting protocol results in a higher density of embedded grit, which remains embedded even after LACR treatment.
d) Roughness parameters calculated from 3D optical micrographs indicate that there is no statistically significant difference in the roughness between LACR and abrasive blasted samples. However, stylus-based roughness measurements show that the LACR samples have a slightly lower roughness values than the abrasive blasted samples.
e) X-ray diffraction-based measurements of the residual stress distributions have shown a typical "U-shape" profile for the abrasive blasted samples, where compressive residual reaches its maximum value (≈340 MPa) just below the surface. On the other hand, the

sub-surface tensile residual stress of LACR samples is confined to a shallow depth of ≈20 μm, followed by balancing sub-surface compressive residual stress.

f) Contrary to fatigue performance reported in Chapter 2 for the material HSS-I, a measureable degradation in the fatigue performance was observed following LACR processing. It is believed this discrepancy is due to differences in the grit blasting protocol (e.g. blasting pressure, velocity). Fractographic analysis confirmed that 73% of the fatigue crack of LACR samples initiated from these embedded grit.

g) Finite element analysis shows that the elastic stress concentration factor decreases significantly after LACR processing due to surface smoothing in case of the materials HSS-I, however, it remains essentially the same for the HSS-II material, where the highest stress concentration data are typically associated with the embedded particles.

The question remains as to why fatigue cracks tended to initiate at embedded abrasive media after LACR treatment but not for abrasive blasted samples, even though this embedded media existed prior to LACR treatment. Finite element heat transfer analysis shows that temperature around these particles may not arise high enough during LACR processing to relax the residual stresses. However, XRD measurement revealed that, at a depth corresponding to embedded particles, the compressive residual stress is higher in abrasive blasted samples than LACR samples. It is thus hypothesized that changes in residual stress state after LACR treatment are responsible for the degradation of the fatigue performance.

**Acknowledgements:** This work was supported by the Commonwealth Center for Advanced Manufacturing (CCAM) and the Virginia Transportation Research Council.

## References


[1] M. Kumar, P. Bhargava, A.K. Biswas, S. Sahu, V. Mandli, M.O. Ittop, B.Q. Khattak, M.K. Tiwari, L.M. Kukreja, *Opt. Laser Technol.*, 46(2013), 29–36.

[2] G. X. Chen, T. J. Kwee, K. P. Tan, Y. S. Choo, M. H. Hong, *Appl. Phys. A Mater. Sci. Process.*, 101(2010), 249–253.

[3] E.D. Oller, Naval application of laser ablation paint removal technology, in: U.S. Navy Corrosion Conference, Norfolk, VA June 2011.

[4] D. Arola, A. E. Alade, W. Weber, Mach. Sci. Technol., 10 (2006), 197-218.

[5] S. Barriuso, J. Chao, J. Jiménez, S. García, J. González-Carrasco, *J. Mech. Behav. Biomed. Mater.*, 30 (2014), 30–40.

[6] L. Pazos, P. Corengia, H. Svoboda, *J. Mech. Behav. Biomed. Mater.*, 3(2010), 416–424.

[7] S. Bagherifard, M. Guagliano, *Eng. Fract. Mech.*, 81(2012), 56–68.

[8] K. Shemtov-Yona, D. Rittel, A. Dorogoy, *J. Mech. Behav. Biomed. Mater.*, 39(2014), 375–390.

[9] M. Lieblich, S. Barriuso, J. Ibáñez, L. Ruiz-de-Lara, M. Díaz, J. L. Ocaña, A. Alberdi, J. L. González-Carrasco, *J. Mech. Behav. Biomed. Mater.*, vol. 63, no. 8, pp. 390–398, 2016.

[10] M. Multigner, E. Frutos, C.L. Mera, J. Chao, J.L. González-Carrasco, *Surf. Coatings Technol.*, 203(2009), 2036–2040.

[11] G. Fowler, P. H. Shipway, I. R. Pashby, *J. Mater. Process. Technol.*, 159(2005), 356–368.

[12] L. Huang, P. Kinnell, P. H. Shipway, *Procedia CIRP*, 6(2013), 594–599.

[13] T. Maruyama, K. Akagi, T. Kobayashi, J. Therm. Spray Technol., 15 (2006), 817-821.

[14] D. Novovic, R. C. Dewes, D. K. Aspinwall, W. Voice, P. Bowen, *Int. J. Mach. Tools Manuf.*, 44(2004), 125–134.

[15] W. C. Oliver, G. M. Pharr, *J. Mater. Res.*, 19(2004), 3–20.

[16] W. B. Lee, K. T. Cho, K. H. Kim, K. I. Moon, Y. Lee, *Mater. Sci. Eng. A*, 527(2010), 5852–5857.

[17] J.Z. Lu, J.W. Zhong, K.Y. Luo, L. Zhang, F.Z. Dai, K.M. Chen, Q.W. Wang, J.S. Zhong, Y.K. Zhang, *Mater. Sci. Eng. A*, 528(2011), 6128–6133.

[18] J. Languillaume, G. Kapelski, B. Baudelet, Acta Mater, 45 (1997), 1201-1212.

[19] W.J. Nam, C.M. Bae, S.J. Oh, S.J. Kwon ,Scr Mater, 42 (2000), 457-463.

[20] M. Zelin, *Acta Mater.*, 50(2002), 4431–4447.

[21] M. Hashish, *J. Eng. Mater. Technol.*, 113(1991), 354-362.

[22] C. A. Schneider, W. S. Rasband, K. W. Eliceiri, *Nat. Methods*, 9(2012), 671–675.

[23] W. D. Nix, H. Gao, *J. Mech. Phys. Solids*, 46(1998), 411–425.

[24] Y. J. Ro, M. R. Begley, R. P. Gangloff, S. R. Agnew, *Mater. Sci. Eng. A*, 435436(2006), 333–342.

[25] R. Rodríguez, I. Gutierrez, *Mater. Sci. Eng. A*, 361(2003), 377–384.

[26] T. Yu, C. Hong, K. Kitamura, K. Tomatsu, A. Taniyama, X. Huang, N. Hansen, *IOP Conf. Ser. Mater. Sci. Eng.*, 219(2017), 12048-12054.

[27] L. Qian, M. Li, Z. Zhou, H. Yang, X. Shi, *Surf. Coatings Technol.*, 195(2005), 264–271.

[28] A. Bolshakov, G. M. Pharr, *J. Mater. Res.*, 13(1998), 1049–1058.

[29] D. Arola, C. L. Williams, *Int. J. Fatigue*, 24(2002), 923–930.

[30] H. Neuber, Theory of notch stresses: principles for exact stress calculation, Edwards, Ann Arbor (MI) (1946).

[31] S. A. Mckelvey, A. Fatemi, *Int. J. Fatigue*, 36(2012), 130–145.

[32] A. Pilipenko, “Computer simulation of residual stress and distortion of thick plates in multi-electrode submerged are welding. Their mitigation techniques,” Doctoral Thesis, Norwegian University of Science and Technology (NTNU), 1992.

[33] L. K. Ang, Y. Y. Lau, R. M. Gilgenbach, H. L. Spindler, Appl. Phys. Lett., 70 (1997), 696-698.

# Chapter 5: The effects of surface roughness on the X-ray diffraction stress measurement


## Abstract

An inhomogeneous stress distribution due to surface roughness was modeled using finite element simulation. This stress distribution was then used to explore the influence of surface roughness on the stress measurements by x-ray diffraction (XRD) technique. Factors that contribute to the deviation from the linearity of the $d\ vs.\ sin^2\psi$ plot are discussed. Although the depth of the x-ray interaction volume is somewhat influenced by the surface profile, the strongest effect of high roughness is one of shadowing the most highly stressed regions of the surface (the valleys). Correlations between the true far-field stress and simulated x-ray diffraction measurements are provided as a function of both a *roughness parameters:* amplitude (a ~ $R_a$), wavelength (b, which may be obtained from Fourier analysis of the profile), the x-ray penetration depth (δ), and the 2θ *diffraction peak position* in the unstressed material.


## 5.1 Introduction

It is well established that surface treatments such as shot peening, abrasive blasting, machining, grinding, laser surface treatment, etc. can introduce significant residual stresses into the surface layers of a component. These residual stresses are known to have a major impact on the component performance, especially fatigue behavior. In order to understand the effects of

the residual stress on the component performance, the accurate determination of residual stress is necessary. X-ray diffraction is the most widely used method for determining surface residual stresses.

The theory underlying the technique is based on continuum elasticity theory and the analysis is only rigorous for smooth, flat samples. Furthermore, the most commonly employed method does not account for stress inhomogeneity below the surface. This assumption is often very reasonable as the penetration depth of x-ray into the materials is usually very shallow [1]. However, the surface treatments like shot peening, abrasive blasting, machining, etc. invariably induce a surface profile as well as residual stress. Although it is well-known that departures from perfectly flat and parallel surfaces will influence the results of diffraction experiments, especially in the commonly employed Bragg-Brentano focusing geometry, the effect on stress measurements has been much less widely explored.

The fact that surface irregularities can have a great influence on the stress value determined by x-ray diffraction method has been established experimentally. Li et al. [2] experimentally examined the effects of surface roughness on x-ray diffraction stress measurement within samples loaded to known stress levels. In their study, steel surfaces were machined to induce roughness and then tempered in vacuum at 600 °C for 15 hours to minimize the effect of machining-induced residual stress. Their investigation showed that there is little influence on XRD determined stress values when the average surface roughness ($R_a$) is less than the x-ray penetration depth in the material. On the other hand, a significant stress relaxation was observed when x-ray penetration depth is lower than the average surface roughness ($R_a$).

However, they fail to explain how surface roughness is actually affecting the stress measurement. Also, $R_a$ is an insufficient measure of the surface profile [3].

In another study, Doig et al. [4] proposed a theoretical model to examine the influence of periodic surface profiles on the stress measured by the x-ray diffraction method. In their study, they assumed that there is a uniform stress state across a machined surface, which is unrealistic. Surface roughness not only affects the details of diffraction geometry, it also causes inhomogeneous stress distribution in the material, stress concentration and relaxation at the valleys and peaks of the roughness profile, respectively. Depending on the roughness profile, the low stress values at the peaks will contribute more to the XRD stress measurement than the highly stress concentrated valleys (i.e. shadowing effect) which results in erroneous interpretation of experimentally measured residual stress.

Despite having a real practical importance, the effects of surface roughness on the x-ray diffraction residual stress measurement are poorly documented in the literature. The main objective of this paper is to theoretically investigate the surface roughness effect on the stress measured using x-ray diffraction method. For this, a model surface profile (a sinusoid) with characteristic ratios of amplitude and wavelength is considered. Finite element method (FEM) analysis is then used to obtain the local strain tensors that arise at all points within the sample volume examined in response to a far-field uniaxial load. The local strain tensors are then used to calculate the average normal strain along the various diffraction vectors within the diffracting volume. Ultimately, empirical relationships which describe the impact of the

roughness (amplitude over wavelength) and Bragg angle are determined, based upon the simulated x-ray diffraction measurements of residual stress.

## 5.2 Methodology

### 5.2.1 Principles of x-ray diffraction stress measurement

The basis of the diffraction based stress measurement is well established, and it depends on the precise determination of interplanar spacing of a given set of crystal planes, for various inclinations, $\psi$, of the diffraction vector from the surface normal direction. The mean lattice plane spacing $d_{hkl}$ for the grains having the diffraction vector normal to the *{hkl}* crystallographic planes are determined from the appropriate $\theta$ value using Bragg's law : $\lambda = 2d_{hkl}\ sin\theta$, where $\lambda$ is the wavelength of the x-ray radiation used. Once the lattice spacing, $d_{hkl}$, is obtained, the strain along the diffraction vector can be obtained from the following formula:

$$\varepsilon_{33}^{'} = \frac{d_{hkl}-d_0}{d_0} \qquad [4.1]$$

where $d_0$ is the unstressed lattice spacing. This strain can be expressed in terms of the strain within the sample coordinate system ($\varepsilon_{ij}$) by the standard tensor transformation of basis:

$$\varepsilon_{33}^{'} = \frac{d_{hkl}-d_0}{d_0} = \varepsilon_{11}cos^2\varphi\ sin^2\psi + \varepsilon_{12}\ sin2\varphi\ sin^2\psi + \ \varepsilon_{22}sin^2\varphi\ sin^2\psi + \varepsilon_{33}cos^2\psi + \varepsilon_{13}\ cos\varphi\ sin2\psi + \ \varepsilon_{23}\ sin\ \varphi\ sin2\psi \qquad [4.2]$$

where $\varphi$ is the angle between the intersection of the diffraction plane with the sample surface plane and a chosen sample direction (e.g., the rolling direction of a sheet). Assuming elastic isotropy of the polycrystalline material and a plane stress condition in the sample surface, the stress can be calculated in a straightforward way, using the following expression:

$$\sigma_{\varphi} = \frac{E}{(1+\vartheta)sin^2\psi}\ \varepsilon'_{33} \qquad [4.3]$$

where *E* is Young's modulus, *v* is Poisson's ratio, $\sigma_{\varphi}$ is the stress component within the sample surface along the $\phi$ direction. $\sigma_{\varphi}$ can be obtained from the slope of a regression line fitted to the calculated $\varepsilon'_{33}$ vs $sin^2\psi$ plot. The detailed explanation of the stress measurement from the x-ray diffraction technique is given in reference [1], along with strategies to account for various departures from the assumptions, such as stress gradients in the surface or elastic anisotropy. One aspect that remains to be accounted for is the potential effect of surface roughness.

### 5.2.2 Application to rough surfaces

The model 1-D surface profile, as shown in Figure 5:1, is represented by the periodic function:

$$y = a\ cos\left(\frac{2\pi x}{b}\right) \qquad [4.4]$$

Note that the normalized roughness ratio (amplitude over wavelength, a/b) is the key variable in what follows. (The absolute roughness amplitude, a, is known to have an effect of diffracted peak breadth [5], but it is generally assumed that it will have little effect on the peak position.) For $\psi$-tilts within the diffraction plane (often denoted as $\omega$-tilts), this type of non-planar surface profile makes an angle $\psi'$ (effective tilt angle) with the diffraction vector ($\overline{k}$, the bisector of the incident and diffracted x-ray beam) which is given by (according to Figure 5:1):

$$\psi' = \psi - \tan^{-1}\left(\frac{dy}{dx}\right) \qquad [4.5]$$

where $\psi$ is the global tilt angle; i.e. angle between the global surface normal and the diffraction vector. (Note: The ω-tilting case explored here is the most commonly employed approach to residual stress measurement, since it does not require special equipment, such as an Eulerian cradle. A similar analysis for out-of-plane ($\chi$) tilts is beyond the scope of the present paper, but similar effects are anticipated given the fact that true surface profiles are 2D in nature.)

Secondly, the surface profile also influences the local x-ray penetration depth, which effect the volume of material that will contribute the diffracted intensity. Figure 5:1 also shows a schematic the x-ray path within the material at a given point B. The incident x-ray beam ($i_0$) penetrates surface at point A and travels a distance AB before diffracting along BC at an angle of 2θ. The total path length of the x-ray beam, *l,* is (AB+BC). Thus, the total diffracted intensity from a volume element at point B can be expressed as:

$$I_{diffracted} = I_{incident} e^{-\mu l} \quad [4.6]$$

where $\mu$ is the linear absorption coefficient. The path length, *l*, depends on the x-ray penetration depth ($\delta$) along the surface normal ($\bar{n}$), tilt angle ($\psi'$), and the Bragg's angular position (θ). From the Figure 5:1, the total x-ray path length can be expressed as:

$$l = AB + BC = \frac{\delta}{sin(\theta+\psi')} + \frac{\delta}{sin(\theta-\psi')} \quad [4.7]$$

The total diffracted intensity from this slab of material is expressed as a fraction of the total diffracted intensity ($G_x = \frac{\int_{x=0}^{\delta} dI_D}{\int_{x=0}^{\infty} dI_D}$) [1]. Assuming that the depth of penetration is small, we

assume that the diffraction from each depth is of equal intensity (contribution to the overall peak position). Hence, combining the $G_x$ relation with equation 4.7 yields:

$$G_x = 1 - exp\left\{-\mu\delta\left[\frac{1}{\sin(\theta-\psi')} + \frac{1}{sin(\theta+\psi')}\right]\right\} \quad [4.8]$$

As it can be seen from this relationship, the x-ray penetration depth ($\delta$) depends on 2θ as well as the effective tilt angle ($\psi'$). As a result, $\delta$ decreases with increasing the ratio of a/b of the surface profile. The x-ray penetration depth profile,$p$, of a rough surface can be expressed as (see Figure 5:1):

$$p = y(x + \delta\ sin\alpha) - (\delta\ cos\alpha) \quad [4.9]$$

where $\alpha$ is the angle between the global and local surface normal at point B. For the examples shown in the present work, equation 4.9 was evaluated using the properties of ferritic steel ($\mu$= 0.089 $\mu m^{-1}$) for Cr-$K_\alpha$ incident radiation [1] for a range (130° -156°) of 2θ positions. Again, for simplicity, every volume element between the surface profile and the x-ray depth of penetration profile was assumed to contribute equally.

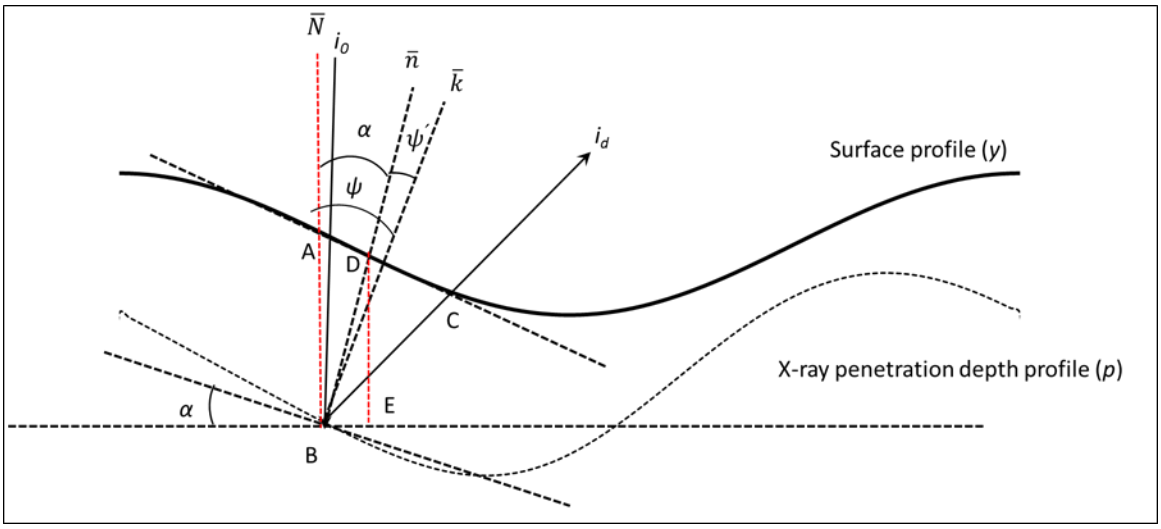


**Figure 5:1: Schematic diagrams showing the geometry of the model surface profile and the detailed x-ray path within the sample. Here $\bar{N}$ is the surface normal of the ideal, smooth surface (global surface normal), $\bar{n}$ surface normal at the x-ray incident point, $\bar{k}$ is the diffraction vector, $\psi$ is the global tilt angle, $\psi'$ is the effective tilt angle due to surface roughness.**

Finally, with increasing surface roughness ratio (a/b = roughness amplitude over wavelength), and/or increasing tilt the angle, $\psi$, stress concentrated areas are partially or fully occluded and only the relaxed peaks contribute to the stress measurement process (as shown in Figure 5:2). The is denoted as a "shadowing" effect. This shadowing effect will take place when the slope of the diffracted line is smaller than the tangent of the roughness profile at point M, as shown in Figure 5:2.

$$\tan(\theta - \omega) = -a\frac{2\pi}{\lambda}sin\left(\frac{2\pi x}{b}\right) \qquad [4.10]$$

Point M and L (see Figure 5:2) can be calculated by solving the equation 4.10. Here equation 4.10 is numerically solved using the Newton-Raphson method. Now, any volume element within the zone LMN will be excluded from the stress calculation for a given surface profile and tilt angle.

### 5.2.3 Finite element simulation

As pointed out by Doig et al. [4], in order to understand the interaction of the surface profile on the x-ray diffraction based stress measurement, prior knowledge of the stress distribution of such a non-planar surface is required. 2-D plane strain finite element simulation was used to analyze the stress distribution on the rough surfaces having a range of a/b values (0 to 0.5). The finite element simulation was performed using the commercial software, ABAQUS. The sample was meshed using 4-node bilinear quadrilateral, reduced integration, and hourglass control elements. A far-field plane strain tension or compression load was applied homogeneously at x=L along the x-direction (see Figure 5:3). The displacement along x-axis (Uxx) at the boundary x=0 was kept fixed. Also, there was no rotation around z-axis (UR3 =0) at the boundary x=0. A free boundary condition along the y –axis was imposed. In this linear elasticity analysis, a material model appropriate for mild steel ($E$ = 200 GPa, and $\nu$ = 0.3) was employed.

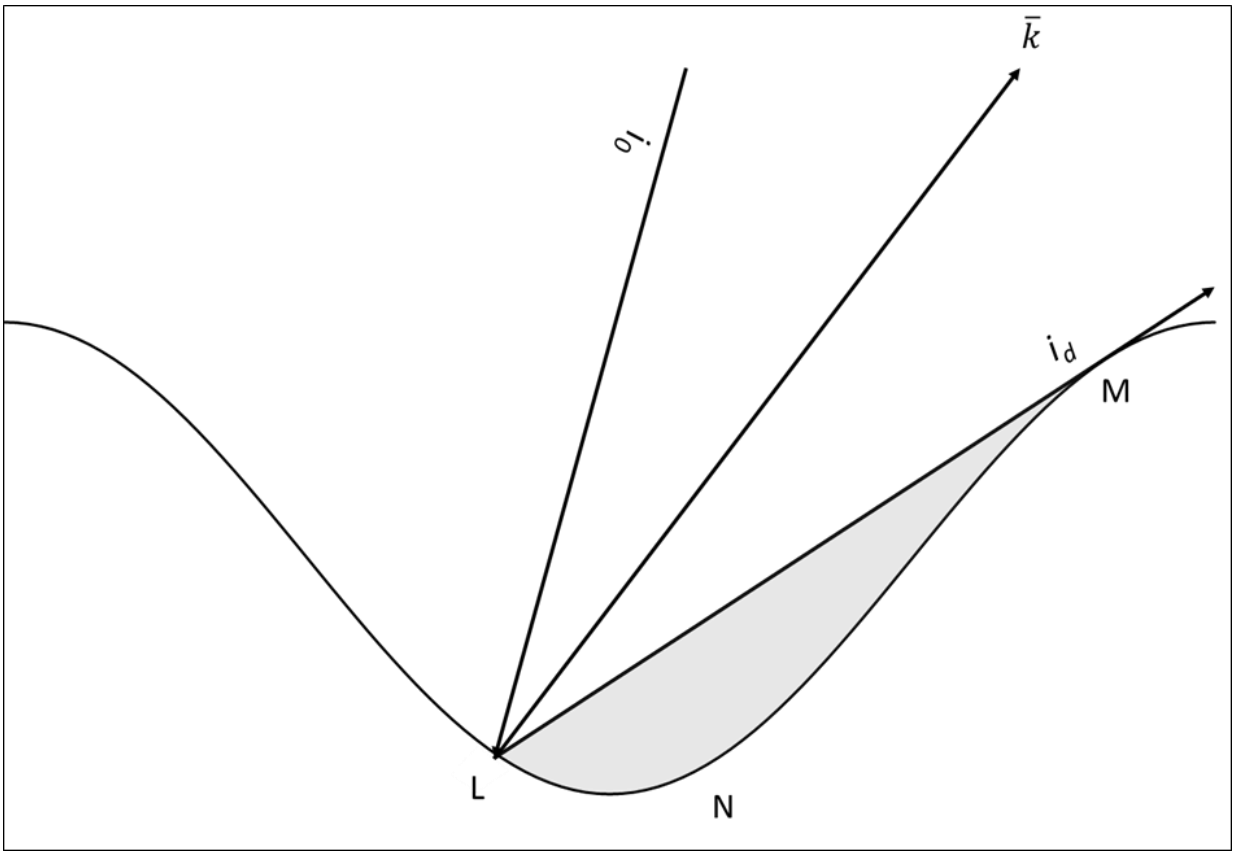


**Figure 5:2: Schematic diagram shows the part of the profile do not contribute in to the average stress measurement due to the "shadowing" effect. Here $i_0$ is the incident x-ray, $i_d$ diffracted x-ray and $\bar{k}$ is the diffraction vector.**

## 5.3 Results and Discussion

The factors that contribute to the erroneous interpretation of the residual stress present in the non-planar surface are: (i) the inhomogeneous stress distribution, which is computed by numerical simulation for a specific surface, and (ii) the x-ray diffraction geometry effects such as the effective x-ray penetration and the shadowing effects. The diffraction geometry is clearly dependent upon the (a) Bragg peak position (2θ), (b) tilt angle, and (c) the penetration depth at

zero roughness ($\delta$), i.e., this due to the specific material's x-ray absorption cross-section. Figure 5:3 shows the stress distribution associated with a mild surface profile of a/b = 0.05. The legend in the Figure 5:3 shows the ratio of the local stress over the applied stress. Obviously, this stress distribution would be perfectly homogeneous for a flat surface. However, stresses vary across the surface profile along the depth and horizontal directions in the presence of roughness. The stresses are concentrated in the valleys and relaxed at the peaks. The level of stress inhomogeneity depends on the surface profile; i.e. a/b ratio.

The FEM solution yields the local stress/strain tensor in the sample coordinates for each integration point. The average strain tensor within the volume confined by x-ray penetration depth and outside the shadowing zone were then calculated in the sample coordinates. Then, the average normal strain resolved along the diffraction vector for a particular global tilt angle ($\psi$) was computed with the help of equation 4.2 using a MATLAB script. The resulting values were plotted against $sin^2\psi$ at discrete values to determine the stress according to equation 4.3.

See Figure 5:4 for the case of 2θ = 156°, b = 100 µm and $\delta$ = 5.6 µm (the effective x-ray penetration depth, i.e. so called 1/e depth, of a flat surface is calculated for a ferritic steel and Cr $K_\alpha$ x-rays. As it is anticipated, the $\varepsilon'_{33}$vs $sin^2\psi$ is perfectly linear for a flat surface. The stress value calculated from the slope is exactly equal to the applied stress value for both tension and compression loading. On the other hand, the $\varepsilon'_{33}$vs $sin^2\psi$ deviates slightly from perfect linearity, even for a relatively shallow surface profile (a/b = 0.05). However, at this low level of roughness, the level of deviation from the actual applied stress (5%) is smaller than the typical level of experimental uncertainty. The linearity of the plot for both positive and negative $\psi$ tilt

indicates that the contribution of the shear strains are inconsequential. It is also noted that the linearity of $\varepsilon_{33}^{'}$vs $sin^2\psi$ plot does not necessarily mean that stress distribution in the diffracted volume is homogeneous. A similar observation was also reported by Chidambarrao et al. [6].

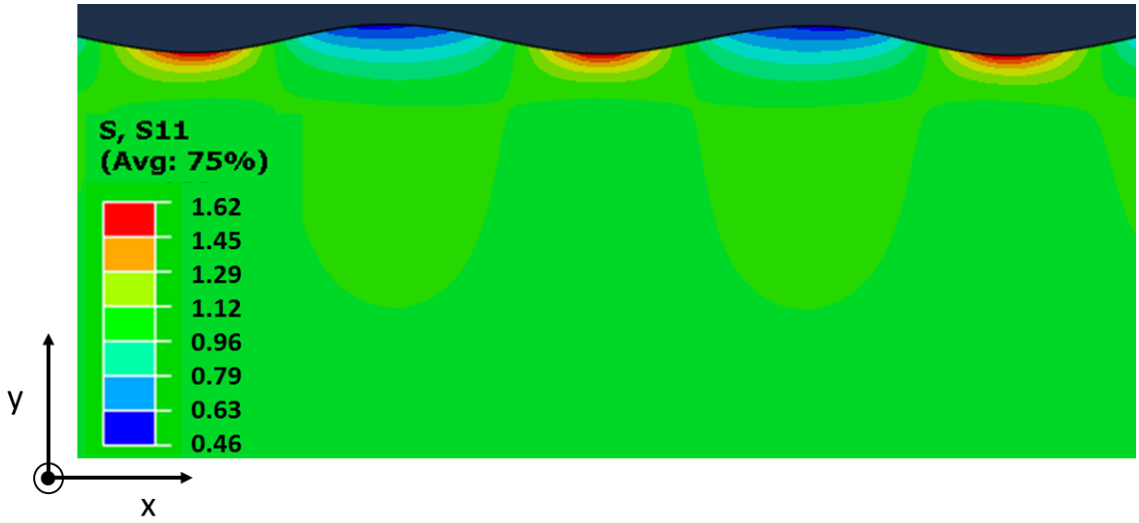


**Figure 5:3: Finite element analysis showing a) homogenous stress distribution in smooth sample, and b) inhomogeneous stress distribution in rough surface.**

The deviation from linearity in the $\varepsilon_{33}^{'}$vs $sin^2\psi$ plots becomes more significant as the a/δ increases for a given wavelength (*b*) of a surface profile, i.e. higher a/b ratio, as shown in Figure 5:5 for a surface profile of aspect ratio (a/b) 0.1. The $\varepsilon_{33}^{'}$vs $sin^2\psi$ plot remains nearly linear up to $\psi$=45° and then the $\varepsilon_{33}^{'}$ drops to a lower value for the subsequent tilt. This non-linearity results from the fact that, as the tilt angle increases, the stress concentrated area is partially or completely occluded. As the roughness ratio, *a/b*, of the surface profile increases, the stress is concentrated into a smaller zone with a higher maximum stress and lower magnitude stresses are distributed over a larger area.

Even if the non-linearity of Figure 5:5 is ignored, the computed stress from the slope of the near-linear portion of the $\varepsilon'_{33}$ vs $sin^2\psi$ plot ($\psi \leq 45°$, in this case) shows a value which is only 54% that of the far-field applied stress. This is due to the fact that the effective x-ray penetration depth is affected by the roughness, i.e. the a/δ increases with increasing roughness. As a result, a large volume fraction of the diffracting material is characterized by a low strain level, which yields a lower average strain for a given tilt and the slope becomes shallower.

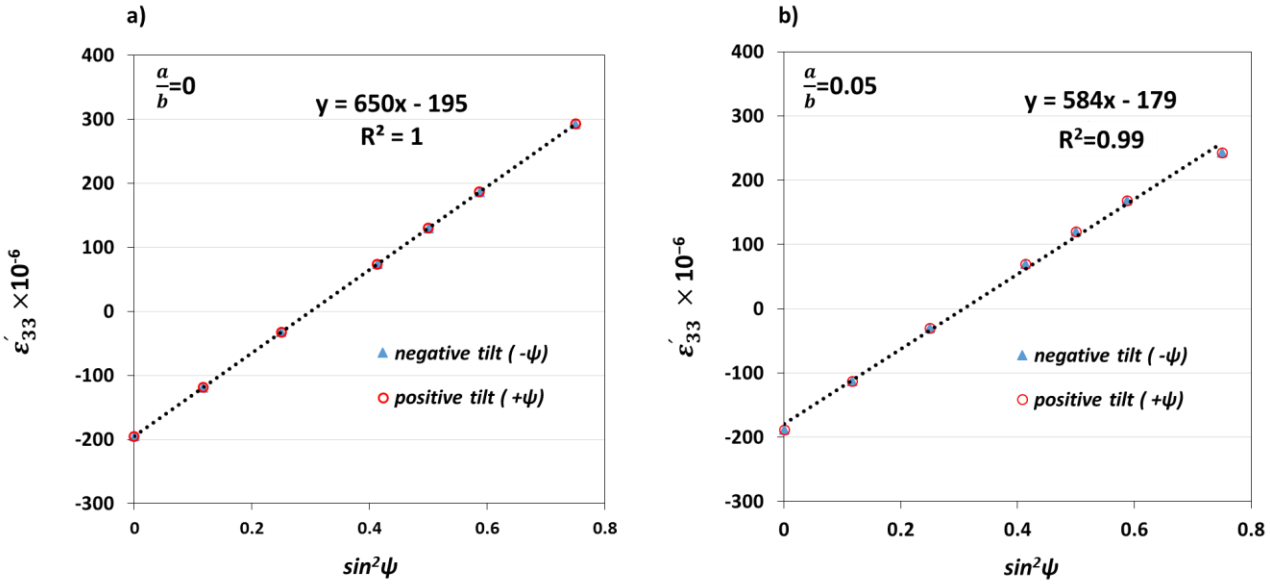


**Figure 5:4: Variation of the strain along the diffraction vector as a function of $sin^2\psi$ for a) a flat surface (a/b = 0) and b) a rough surface (a/b = 0.05).**

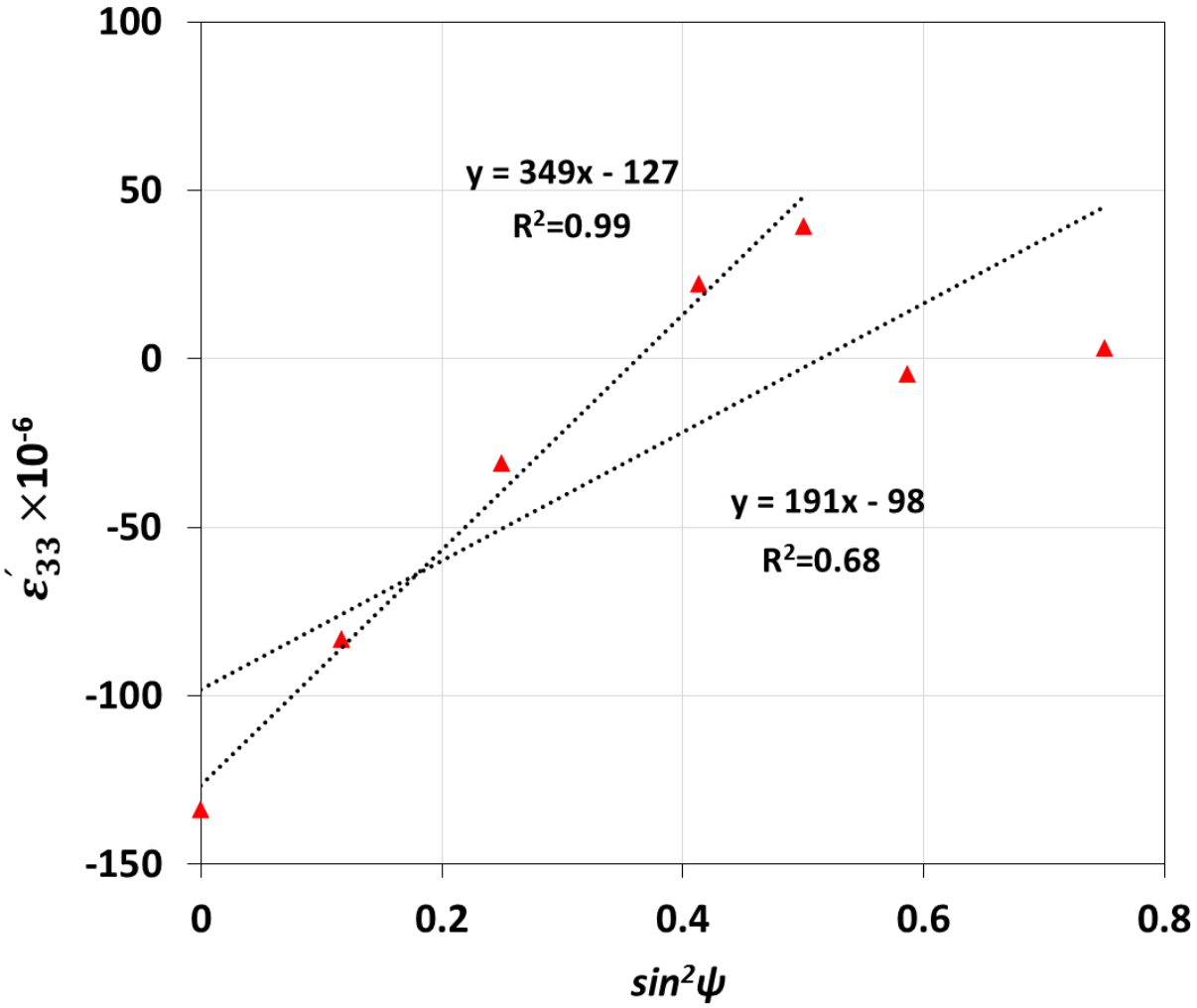


**Figure 5:5: Variation of the strain along the diffraction vector as a function of *a non-planar surface of* a/b =0.1.**

The results clearly indicate the impact of surface profile on residual stress estimates based upon the traditional x-ray diffraction-based *d* vs. $sin^2\psi$ approach. As the a/δ ratio becomes larger for a given wavelength *b*, the effective x-ray penetration depth into the materials becomes smaller, and the shadowing effects take place at smaller tilt angle ($\psi$). Figure 5:6 (a) also shows that for a given surface aspect ratio (a/b), the stress ratio decreases with increasing

wavelength. This is due to the fact that the volume fraction of the low strain region increases in the strain calculation, which yields a lower average strain.

As it discussed earlier, the computed stress data depend on both the a/δ ratio and the surface aspect ratio (a/b) highlighted in the present work as significant because it contributes strongly to the potential for "shadowing." The present simulation results suggest that stress ratio ($\sigma_{calculated}/\sigma_{applied}$) can be described by a functional form as:

$$\frac{\sigma_{calculated}}{\sigma_{applied}} = \left\{1 + \exp(m\frac{a}{b} - n\right\}^{-1} \quad [11]$$

where *m* and *n* are fitting parameters determined by fitting to the simulation data. Figure 5:6(a) and (b) show the variations of the simulated measurement stress, as a function of the *a/b* and the *a/δ* for different wavelength of the roughness (b), respectively. From these data, it is revealed that *n* can be described by a power law relationship with *b/δ*.

$$n = A\left(\frac{b}{\delta}\right)^{B} \quad [12]$$

where *A* and *B* are the fitting parameters. In short, use of just three fitting parameters m, A, and B can describe all possible combinations of roughness and X-ray absorption depth. Fitting of the data in Figure 5:6 shows that the values of m, A and B are 51.05, 9.1 and -0.182, respectively.

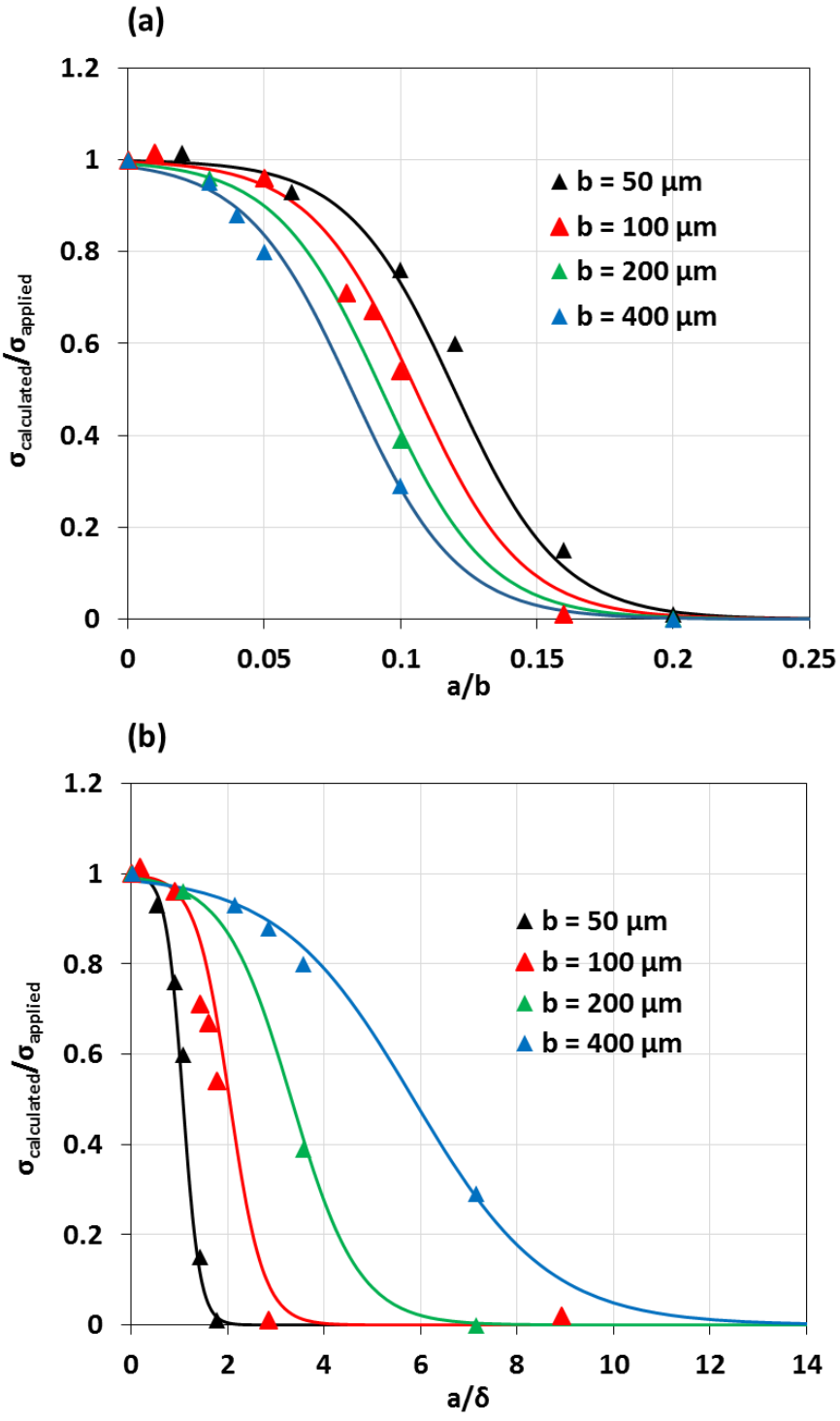


**Figure 5:6: Ratio of the calculated stress applied stress as a function of surface a) amplitude (a) over wavelength (b) and b) amplitude (a) over x-ray penetration depth (δ).**

The Bragg peak position 2θ also plays an important role in evaluating and applying stress correction. As the diffraction angle θ becomes smaller, the x-ray penetration depth into the materials becomes smaller and shadowing effects take place for a surface with relatively smaller aspect ratio and at a smaller tilt angle ($\psi$). Figure 5:7(a) shows the variations of the ratio of calculated and applied stress as a function of the a/δ ratio of the surface profile of wavelength b = 100 μm for different 2θ positions. The calculated stress can also be represented using equation 4.11. It is interesting to note that the 2θ dependence on the computed stress can be described as a linear variation of fitting parameters m with 2θ position (see Figure 5:7(b)).

It is usually recommended to use reflections with 2θ angles greater than 125° [7]. However, the selection of peaks around lower bound of the recommended 2θ position will introduce a large error in the stress measurement. Figure 5:6(a) shows that, for a surface profile with an a/δ ratio of 0.9, the measured stress can be as low as 84% of the actual stress, if 2θ = 130° is selected for stress measurement. Although the Figure 5:6 and Figure 5:7 are explicitly calculated for ferritic steel, equation 4.11 can be generalized for any x-ray source and any material of known x-ray penetration depth (δ) as x-ray penetration depth is the is the only material parameter used in equation 4.11.

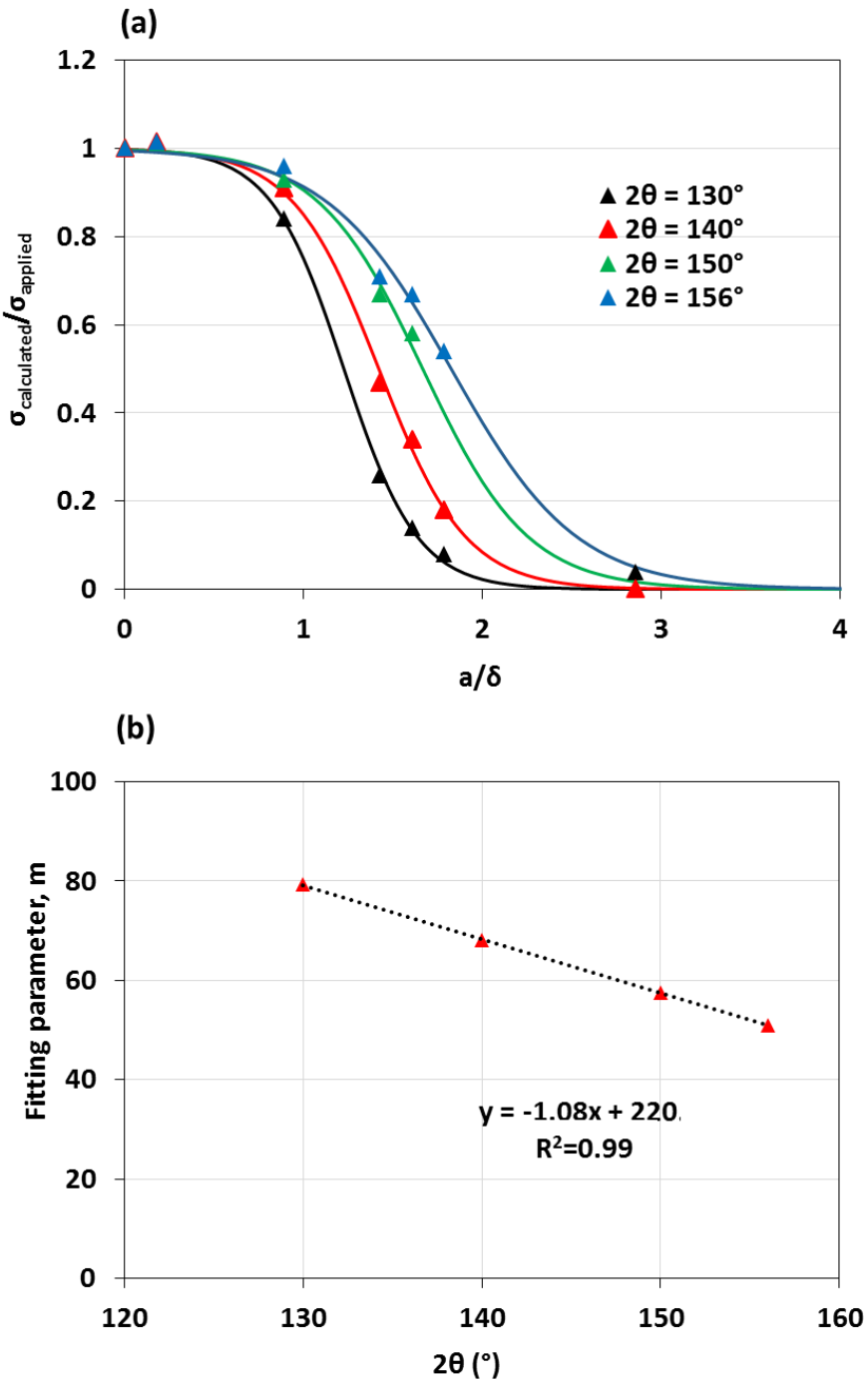


**Figure 5:7: a) Ratio of the calculated stress applied stress as a function of a/δ for a surface profile with wavelength, b= 100 µm for different 2θ position and b) variations of fitting parameter, m as a function of 2θ position.**

In the interest of generalizing the findings, it is noted that the surface finish is usually experimentally measured and generally expressed by parameters such as average ($R_a$), root mean squared ($R_q$), or the 10-point average peak to valley ($R_z$) roughness. These parameters are dependent only on the amplitude of the surface profile and do not include the wavelength effects. Therefore, as an example, surfaces with equivalent $R_a$ values could have a different roughness ratio, *a/b*. Ignoring the effects of wavelength, b, could generate inaccurate results (see Figure 5:6). As such, the surface roughness effect on the stress measurement based on the ratio between average roughness parameter ($R_a$) and x-ray penetration depth (δ) of the flat sample surface, as reported in reference [2], without considering the wavelength of the surface profile is insufficient. The authors in reference [2] used different machining techniques (grinding, 4 teeth drill, 60 ° triangular plate drill) to introduce a different level of surface roughness into ferritic steel and showed that for *Ra*/ δ close to 1 surface roughness did not significantly affect the stress measurement using Cr x-ray source. $\delta$ was calculated to be 9 µm for 75% absorption of the diffracted beam. The present analysis showed that this could only be true if the wavelength is greater than 200 µm. The stress ratio could be as small as 65 %, if the wavelength is 100 µm.

It is recommended that users employ both a measure of roughness amplitude (e.g., $R_a$, which is equivalent to $\frac{2a}{\pi}$ for the simple profile of equation 4.4 together with a measure of the wavelength of the roughness, which can be obtained from the Fourier transformation of the roughness profile. The present authors investigated the effects of different abrasive blasting

parameters on the evaluation surface roughness of a high strength ferritic steel, as reported in reference [8]. The average roughness parameter, $R_a$, for a blasted surface can be up to 7 μm (corresponding to $a_{eff} \approx$ 11 μm and a/δ as high as 2.0). Fourier analysis reveals that b is in the range of 200 to 500 μm. The present analysis shows that this will result in stress ratio (measured/applied) as low as 86% for b= 200 μm and 95 % for b=400 μm. Doig et al.[4] also reported that the a/δ ratios can be as high as ≈2.68 and wavelength (b) can be in the rage of 50 μm to 200 μm for a turned finish steel surface. Under these conditions, the present analysis shows that the stress ratio could be as low as 70% for the maximum value of b ≈200 μm and the actual stress distribution could be completely obscured by the surface geometry for b≈ 50 μm, this is consistent with their observation [4].

While the present analysis is based on an ideal periodic surface profile (sinusoidal wave), which is not characteristic of all surface profiles, it is a reasonable estimate of surfaces generated by shot peening, machining, and laser treatment. Furthermore, other surface profiles can be represented using Fourier series, such that the present analysis may be generalized. Finally, the present analysis, which assumes all the elements within the x-ray penetration depth contributed equally to the diffraction signal, provides a conservative estimate of the systematic error associated with roughness. The actual average strain obtained from the x-ray diffraction will have a larger contribution from the elements in the shallower depths.

## 5.4 Conclusions

The stress distributions of non-planar surfaces with a range of profiles (amplitude over wavelength ratios) were modeled using the ABAQUS finite element code. The average normal

strain along the diffraction vector was computed from the nodal strain from the finite element simulation. Stress calculated from the average $\varepsilon_{33}^{'}$ $(\text{or } d)$ vs *sin²ψ plot* (a simulated x-ray stress measurement) confirms that the value of applied and measured stress are the same, for a smooth surface profile (i.e., roughness amplitude/wavelength ratio ≈ 0). However, as the roughness increases, it introduces a systematic error into the stress measurement. In fact, roughness ratios (a/b) as low as 0.05 for a surface of wavelength b=100 μm and 2θ = 156° would induce about ≈5% error into the stress calculations. The dependence of the error on the absolute wavelength (b) of the surface profile and Bragg peak position is also shown to play an important role in error determination. For a fixed value of a/b ratio, the error increases with increasing the wavelength (b) (because the a/δ parameter is increasing, and this has been previously demonstrated experimentally). The error also increases with decreasing 2θ position, which provides additional guidance regarding the lowest acceptable scattering angle to employ on samples with measurable roughness. Relationships are proposed which permit estimation of the actual far-field stress, given a known roughness and surface stress value experimentally measured using xrd.

**Acknowledgements:** Financial support for this work was provided by by the Virginia Transportation Research Council (VTRC). The authors would like to thank Prof. Peidong Wu, McMaster University, for the helpful tip suggesting the use of finite element analysis for determining the stress distribution in the vicinity of rough surfaces. James M. Fitz-Gerald (University of Virginia) is gratefully acknowledged for valuable discussions.

## References


[1] I.C. Noyan, J.B. Cohen, *Residual stress: measurement by diffraction and interpretation*, Springer-Verlag, New York, USA (1987).

[2] A. Li, V. Ji, J.L. Leburn, G. Ingelbert, *Exp. Tech.,* 19(1995), 9–11.

[3] M. Shamsujjoha, S.R. Agnew, J.R. Brooks, T.J. Tyler, J.M. Fitz-Gerald, *Surf. Coatings Technol.* 281(2015), 206–214.

[4] P. Doig, P.E.J.J. Flewitt, Appl. Cryst., 14(1981), 321-325.

[5] T.C.J. Sparks, R. Kumar, E.D. Specht, P. Zschack, G.E. Ice, T. Shiraishi, K. Hisatsune, *Adv. X-ray Anal.,* 35A (1991), 57–62.

[6] D. Chidambarrao, Y.C. Song, I.C. Noyan, *Adv. X-ray Anal.* 44 (2001), 122–127.

[7] M.E. Fitzpatrick, A.T. Fry, P. Holdway, F.A. Kandil, J. Shackleton, L. Suominen "Determination of Residual Stresses by X-ray Diffraction - Issue 2, *Meas. Good Pract. Guid.*, no. 52", National Physical Laboratory (2005).

[8] M. Shamsujjoha, S.R. Agnew, M.A. Melia, J.R. Brooks, T.J. Tyler, J.M. Fitz-Gerald, Surf. Coatings *Surf. Coatings Technol.* 281(2015),193–205.

# Chapter 6: Finite element modeling of the interaction of stress concentration and residual stress with applied load


## Abstract

The effects of surface roughness and embedded particles on fatigue crack initiation after abrasive blasting and subsequent laser ablation coating removal (LACR) are investigated using 2D plane strain finite element analysis (FEA). The FEA models are constructed using real surface profiles from scanning electron microscope (SEM) cross-sectional images. The stress concentration associated with the combination of roughness, embedded particles, and the local residual stress distribution are computed using elasto-plastic modeling. It is observed that compressive and tensile residual stresses are concentrated at the surface valleys for abrasive blasting and LACR processes, respectively. The highest magnitude of compressive residual stress is observed in the proximity of the deepest and sharpest particles, for the abrasive blasting condition, which ameliorates the potentially adverse effect of these particles on the fatigue performance. The compressive residual stress state, at this critical location, is relaxed by subsequent LACR treatment. As such, the simulations reveal a strong propensity for fatigue crack nucleation at the particles after LACR, which correlates well with the experimental observation.


## 6.1 Introduction

Laser ablation coating removal (LACR) is a technique used to remove paint from a substrate. Like many other surface modification techniques, LACR results in modification of the surface

profile (e.g. due to laser surface melting) and residual stress state in ways that can affect the fatigue performance [1-3]. In addition, the near-surface material properties, i.e. surface roughness, residual stress, microstructure, phase fractions etc., prior to LACR, have a strong influence on the subsequent fatigue performance upon LACR. Abrasive blasting is one of the most common surface treatments used by shipbuilding and bridge construction industries prior painting because the imparted surface roughness has been shown to improve paint adhesion.

As discussed in Chapter 4, the fatigue performance of the underlying steel substrate remains the same after LACR processing when abrasive blasting is conducted in a controlled fashion, using low pressure blasting, and LACR leads to degradation of the fatigue performance when prior blasting is performed with a high blasting pressure. The high-pressure blasting results in embedment of the blasting particles. While the high-velocity impact can result in a higher magnitude of local compressive residual stress at the vicinity of the embedded particles, the embedded particles can also act as micro-notch and nuclei for the fatigue crack initiation [4]. Experimental results show that this embedded media rarely serves as the primary initiation site for abrasive blasting samples, but acts as the predominant crack initiation sites after LACR treatment. 75% of the fatigue crack initiated from the surface depression for abrasive blasted surface treated samples while 73% of the crack originated from the embedded particles after LACR surface treatment of the initial abrasive blasted surface (see Figure 6:1). Therefore, questions of “when” and “to what extent” the changes in stress concentration (associated with surface topology and embedded media) and residual stress state affect the fatigue performance still need to be clarified.

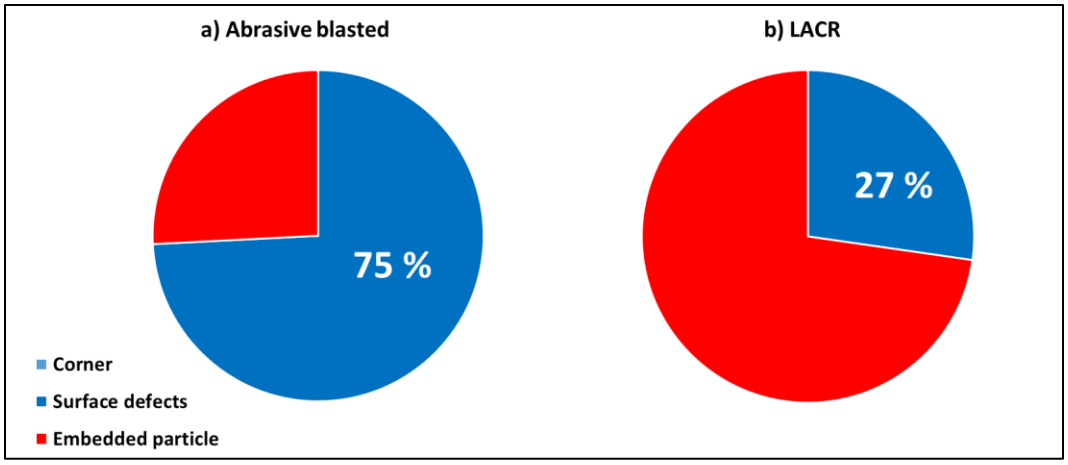


**Figure 6:1: Pie chart of the fatigue crack initiation sites of the a) abrasive blasted and b) LACR samples.**

Informed by experimental assessments of the residual stresses, finite element analysis (FEA) is employed to evaluate the local stress state, in the vicinity of the surface and around the particles after abrasive blasting and LACR processing. The method is attractive because geometries with complex surface profiles, elasto-plastic constitutive behavior, and embedded (elastic) particles can be analyzed in a detailed fashion.

In this study, realistic shapes and sizes of the embedded particles are considered. Two surface profiles having relatively “low” and “high” levels of roughness are examined. Two dimensional (2D), plane strain elastic-plastic finite element analysis is employed to examine the driving force for the crack initiation either in the vicinity of the embedded particles or at the valleys of the surface profile.

In addition to affecting crack initiation, the residual stress field ahead of the crack tip can also influence the fatigue crack growth rate. In general, residual stress generates a stress intensity

contribution, $K_{res}$, to the effective minimum and maximum stress intensity factor, which is expected to be $K_{max} + K_{res}$ and $K_{min} + K_{res}$. Here $K_{max}$ and $K_{min}$ are the stress intensity factors for external loading. While $\Delta K_{eff}$ ($K_{max} + K_{res} - K_{min} - K_{res}$) remains the same as applied stress intensity rage ($\Delta K$), residual stress affects the fatigue life by changing the nominal stress ratio, $R = (K_{max} + K_{res})/ (K_{min} + K_{res})$. If compressive residual stress value is high enough to results in negative value of $R_{app}$, it might induce crack closure effect, which will further retard the crack propagation rate [5-7]. However, examining the residual stress field (see Figure 4.16) it is noted that that the stress field become similar within 100 µm deep into the material for both surface condition and it is hypothesized that the difference in fatigue life between two surface conditions is mainly related to difference in fatigue crack initiation life.

It should be noted here that the goal of this 2D finite element based study is not to develop a new modeling paradigm for fatigue life prediction. Rather, it is to use the model to understand and interpret the experimental results. The consequences of the analysis are considered in the discussion section.

## 6.2 Finite element modeling

### 6.2.1 2D FE models for realistic surface profile and embedded particles

The commercially FE code, Abaqus version 6.14 [8], is used to develop the model, perform the FE calculations, and visualize the results. 2D deformable parts for the FEA are created from SEM cross-sectional images. 108 SEM cross-sectional images were collected from abrasive blasted and LACR treated samples corresponding to 75 mm along the surfae. 30 images were randomly

selected for elastic stress concentration factor ($k_t$) analysis. The details of the methods are described in section 4.4.1. The normal distribution of the maximum value of $k_{t,max}$ associated with surface profile of each image is shown in Figure 6:2. Two surface profiles were then selected for more detailed study: i) profile-1 ($k_{t,max}$ value corresponds to 37th percentile) and ii) profile-2 ($k_{t,max}$ value corresponds to 94th percentile). The profile-1 has "typical" roughness metrics observed in this study: $R_a \approx 7.0$ µm, $R_z \approx 20$ µm. On the other hand, $R_a$ and $R_z$ values computed for profile-2 are relatively "high" for values for this study at 13 µm and 52 µm, respectively. Selection of these two surface profiles will aid in investigating the relative effects of surface profile, embedded particles, and residual stress state on the fatigue performance. The shapes of the selected surface profiles are shown in Figure 6:3.

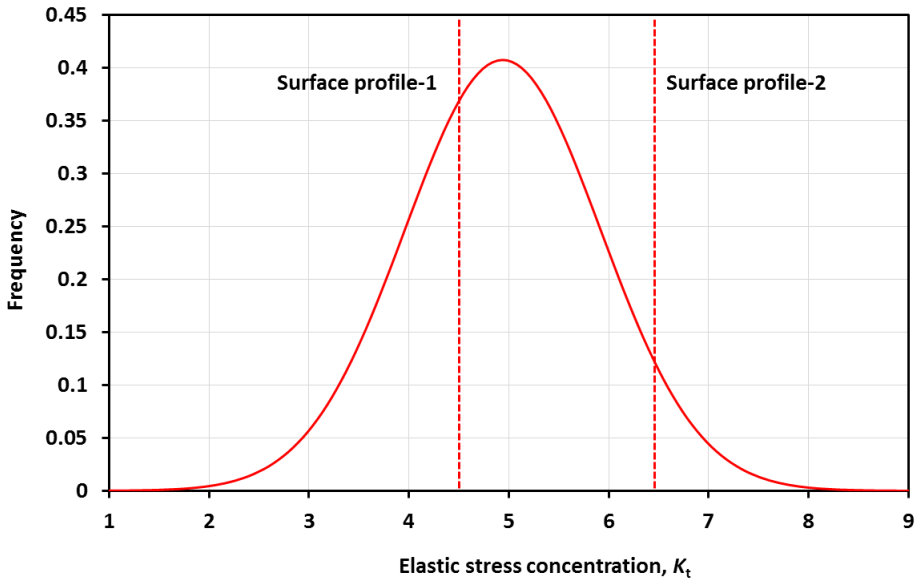


**Figure 6:2: The normal distributions of elastic stress concentration factor of the surface profiles obtained from SEM images.**

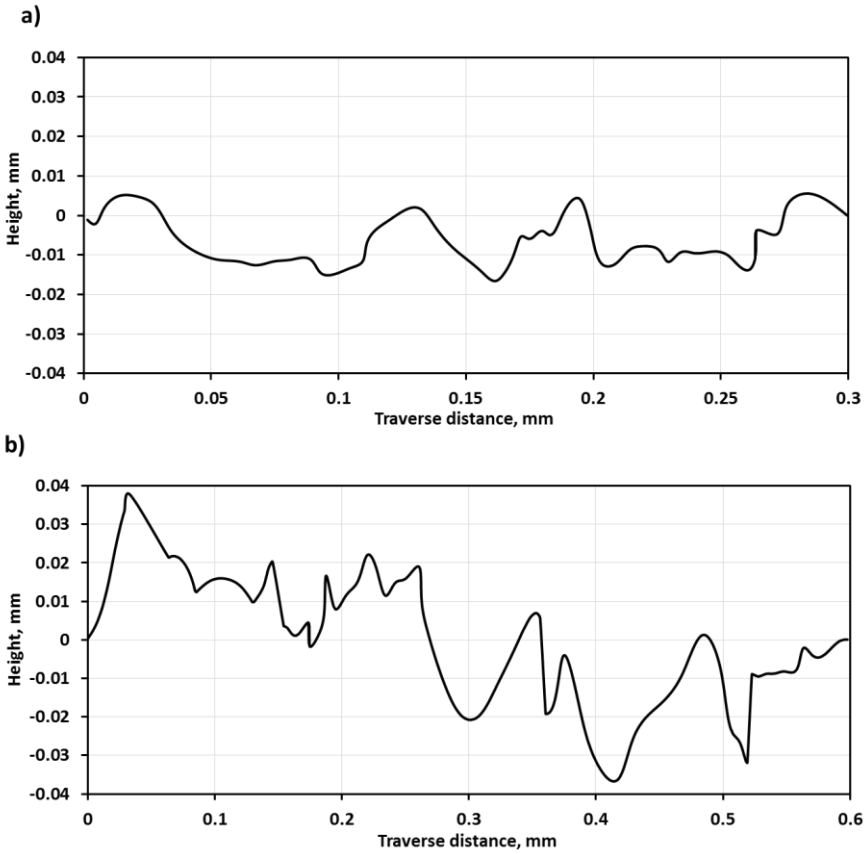


**Figure 6:3: The representative surface roughness profiles used for the detailed, elasto-plastic finite element analysis.: a) profile-1 (low roughness and $k_{t,max}$ values) and b) profile-2 (relatively higher roughness and $k_{t,max}$ values).**

Once the part is created, it is partitioned to accommodate the shape of the embedded particle. As discussed in Chapter 4, the fatigue cracks initiated from the surface embedded particles having a typical surface area of 500-3000 $\mu m^2$ and depth in the range of 25-85 µm. Particles having similar size and depth distributions with a range of local radii of curvature at the deepest point are incorporated in the FEA to assess the influence of realistic particles shape and size on the local stress-strain behavior.

A 2D plane strain assumption is adopted to improve the computational efficiency of the analysis. The impact of this simplifying assumption will be considered in the discussion section. The sample was meshed using 4-node bilinear quadrilateral, reduced integration, and hourglass control elements. Regions close to the rough surface and embedded particles are meshed with an element size of 0.3 μm, as it has been shown in Chapter 4 that this mesh size leads to convergence of the numerical solutions. Similar to that simpler elasticity study, a mesh gradient is applied, i.e., element size increases away from the rough surface and embedded particle. A far-field plane strain tension load is applied at x=L along the x-direction. The displacement along the x-axis (Uxx) at the boundary x=0 is kept fixed. In addition, there is no rotation around the z-axis (UR3 =0) at the boundary x=0. A free boundary condition is imposed along the y-axis. Figure 6:4 presents the geometry and boundary conditions used during the simulation.

The interface between the particles and the matrix is modeled as a hard contact pair, where the particle and matrix function as master and slave surface. During this hard contact analysis, no penetration of the slave nodes into the master surface is allowed. The surfaces transmit no contact pressure unless nodes of master and slave surfaces come in contact. The Coulomb friction relationship is employed in the contact model:

$$F_f = \mu F_n$$

where $F_f$ is the friction force, $F_n$ is the normal force and $\mu$ is the friction coefficient. The value $\mu$ is taken as 0.5 for friction between the steel matrix and ceramic particles [9, 10].

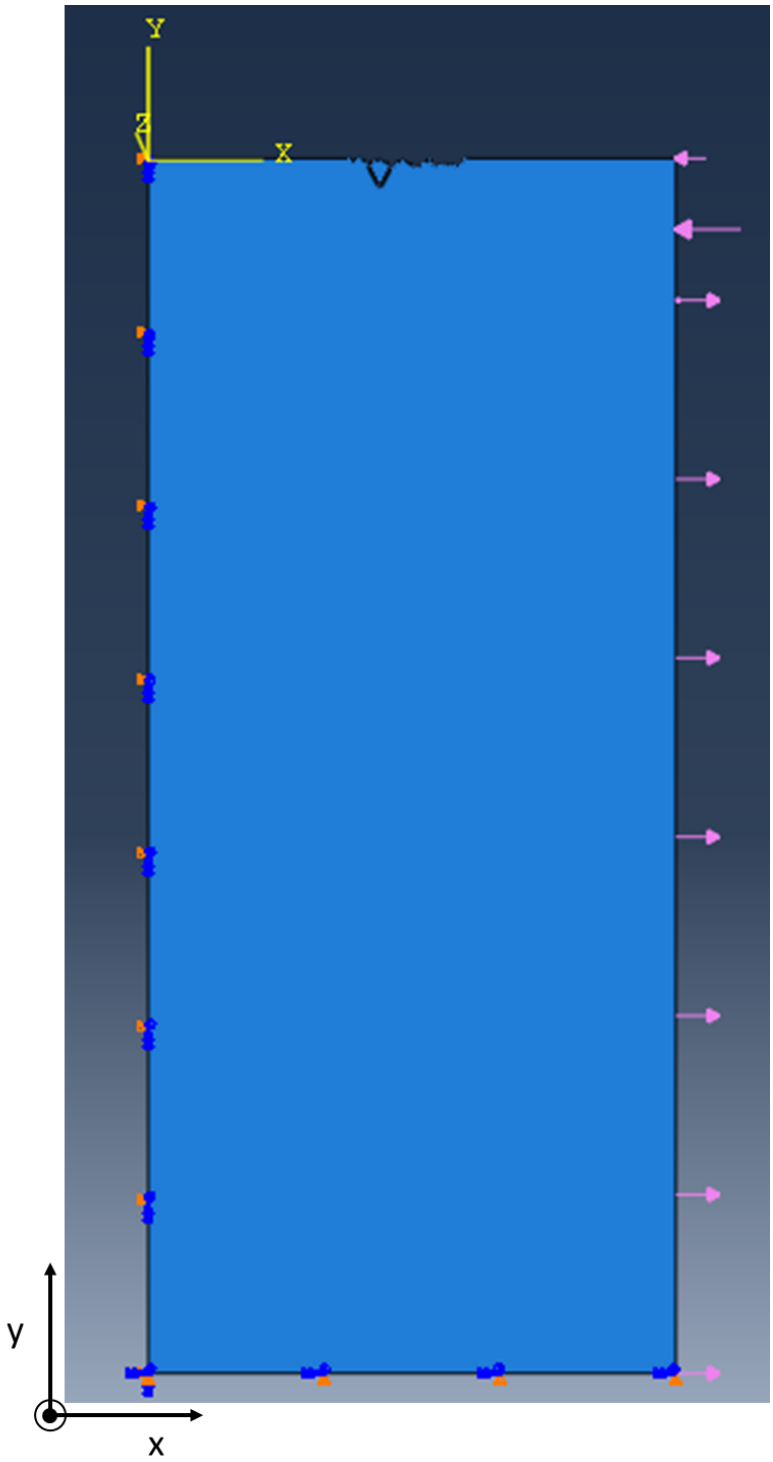


**Figure 6:4: Representative geometry (includes surface profile and an embedded particle) and boundary condition of the finite element analysis.**

### 6.2.2 Material Models

The elastic stress-strain relationship is governed by Hooke's law as:

$$\sigma_{ij} = C_{ijkl}\varepsilon_{ij}^{E}$$

where $\sigma_{ij}$ are the components of the Cauchy stress, $\varepsilon_{ij}^{E}$ the elastic strain tensor, and $C_{ijkl}$ is the elastic stiffness tensor, which can be related to the Young's modulus $E$ and Poisson's ratio $\vartheta$, for the case of elastic isotropy:

$$C_{ijkl} = \frac{E}{1+\nu}\left[\frac{1}{2}\left(\delta_{ik}\delta_{jl}\right) + \frac{\vartheta}{1+\vartheta}\delta_{ij}\delta_{kl}\right]$$

The embedded garnet particles are considered to be linear elastic with elastic modulus $E$ = 240 GPa and the Poisson's ratio $\nu$ = 0.28 [11]. The steel matrix is modeled as a rate independent elastic-plastic material with an isotropic hardening [12]. The elastic modulus of steel E=200 GPa and the Poisson's ratio $\nu$ = 0.3. A basic assumption of the infinitesimal strain, elastic-plastic models is that the deformation can be additively decomposed into elastic and plastic parts. Thus, the total strain, $\varepsilon_{ij}$, can be represented generally as:

$$\varepsilon_{ij} = \varepsilon_{ij}^{E} + \varepsilon_{ij}^{P}$$

where $\varepsilon_{ij}^{P}$ is the plastic strain. The yield function ($f$) that limits the purely elastic response of the materials can be defined as:

$$f = \sqrt{\frac{3}{2}\, S_{ij} : S_{ij}} - \sigma_{YS} = 0$$

where $\sigma_{YS}$ is the yield strength and $\sqrt{\frac{3}{2}\, S_{ij} : S_{ij}}$ is the equivalent Von-Mises stress and $S_{ij}$ is the deviatoric stress tensor defined by [8]:

$$S_{ij} = \left(\sigma_{ij} - \tfrac{1}{3}\sigma_{ij}\delta_{ij}\right).$$

The plastic stress-strain relationship for isotropic material can be expressed as:

$$d\varepsilon_{ij}^{p} = \lambda\, S_{ij}$$

where $d\varepsilon_{ij}^{p}$ is the plastic strain increment, λ is the plastic multiplier, which is incrementally solved according to the strain hardening behavior of the material. The properties of the matrix (steel) are computed from the experimental stress-strain plot, as shown in Figure 4:1.

### 6.2.3 Imposition of initial residual stress

Imposing residual stress in the model is critical; especially in order to capture the variations in the local stress distributions, which arise due to the surface inhomogeneity and embedded particles. In this study, the residual stresses are directly read into the model as the "INITIAL CONDITION" using SIGINI FORTRAN subroutine [13]. A similar approach also has been adopted in reverences [14-16]. Experimentally it was observed that both abrasive blasting and LACR induce equal in-plane residual stress, therefore, equibiaxial residual stress within the specimen is assumed for both cases:

$$\sigma_{xx}^{res} = \sigma_{zz}^{res} = \sigma_{res}$$

$$\sigma_{yy}^{res} = \sigma_{xy}^{res} = \sigma_{xz}^{res} = \sigma_{yz}^{res} = 0$$

The depth-resolved spatial distribution of the residual stress, as obtained from the X-ray measurements corrected for successive layer removal using electropolishing (see Figure 4.16), are fitted with a cubic polynomial function:

$$\sigma_{res} = Ay^3 + By^2 + Cy + D$$

Coefficient A, B, C, and D of the cubic function for the residual stress distribution of the abrasive blasted and LACR samples are given in Table 6.1.

**Table 6.1: Coefficients of the cubic polynomial function fitted to experimentally measured residual stress distributions of abrasive blasted and LACR samples.**

| Sample | A | B | C | D |
|---|---|---|---|---|
| Abrasive blasted | 32451 | 23062 | 3612 | -154 |
| LACR | 52468 | 38124 | 7417 | 167 |

Therefore, all the elements at a specific depth below the surface are initially assigned the same magnitude of the residual stress. It is assumed that the interior balancing residual stress has a uniform magnitude of tensile residual stress and its magnitude is calculated by equating the area under the curve of the compressive and tensile residual stress zone. The stress thus induced in the model, which only has variations along the depth direction is called here as "global" residual stress. Once the initial residual stress distribution is incorporated in the FE model, it is followed by re-equilibration of the initial stress field subject to the principle of the virtual work (PVW). The PVW states that the external work must be equal to the internal work.

This step is particularly important considering the surface inhomogeneity present in the model, which will result in variations of stress component along x-direction. This type of varying stress is called the "local" stress in this study. During the stress redistribution step, the following boundary condition is applied. The displacement along the x-axis (Uxx=0) and rotation around z-axis (UR3 =0) at the boundary x=0 is kept fixed. A distributed load, equivalent to residual stress distribution in the sample, is applied at x=L. Once the equilibrium step is finished, external loads (i.e. those associated with fatigue testing) are applied at x=L along the x-direction.

## 6.3 Results

### 6.3.1 Residual stress redistribution

Figure 6:5 (a) shows the initial stress distribution ($\sigma_{xx}^{res}$) of the abrasive blasted sample with surface profile-1, based on the global residual stress measured using X-ray diffraction and containing a particle with cross-sectional of area 2370 μm$^2$, depth of 65 μm and radius of curvature 5 μm. During the stress redistribution step, the rough surface profile, the presence of the inclusion, and the associated interface condition between the inclusions and the matrix alter the local residual stress distributions. Figure 6:5(b) shows that the redistributed stresses are concentrated around the valleys of the surface profile and also at the vicinity of the embedded particles, while the peak regions of the surface profile are relaxed. The contours of the $\sigma_{xx}$ component of the stress distribution reveal that the maximum value of the compressive residual stress approached to 730 MPa in the proximity of the particle. The maximum value of compressive residual stress ($\sigma_{xx}$ component of the stress distribution) in the valley of the surface profile is calculated to be 550 MPa. For LACR samples, however, the maximum

compressive residual stress in the vicinity of the particles reduced to ~450 MPa, due to lower magnitude of the global residual stress at the maximum depth of the embedded particles (see Figure 6:5 (b)). The figure also shows that the tensile residual stresses are concentrated around the valleys of the surface profile with maximum tensile residual stress computed to be 320 MPa.

This distinction in global vs. local residual stress can also be realized from the finite element analysis of the abrasive blasting or related process like shot peening, foreign object damage or any other impact process. Researchers have shown that residual stresses are indeed concentrated underneath the impacted zone while rims of the impact are either very relaxed or tensile depending on the impacting process [17-24]. Generally, a high-velocity single impact process, e.g., foreign object damage, results in tensile residual stress at the rim of the impact [17, 18]. However, when impact coverage of the surface is high, e.g. shot peening; stresses are typically zero at this region[21, 24](also, see in Appendix-I). These inhomogeneous stress distributions due to surface roughness also discussed in Chapter 5. In fact, the stress correction method proposed in Chapter 5 is also applied here to more carefully assess the effect of the surface residual stress state of LACR samples on the stress concentrations which occur during fatigue loading. It is found that global residual stress calculated based on the correction method provides a similar magnitude of tensile residual stress (≈172 MPa) at the surface as measured using XRD method (≈178 MPa).

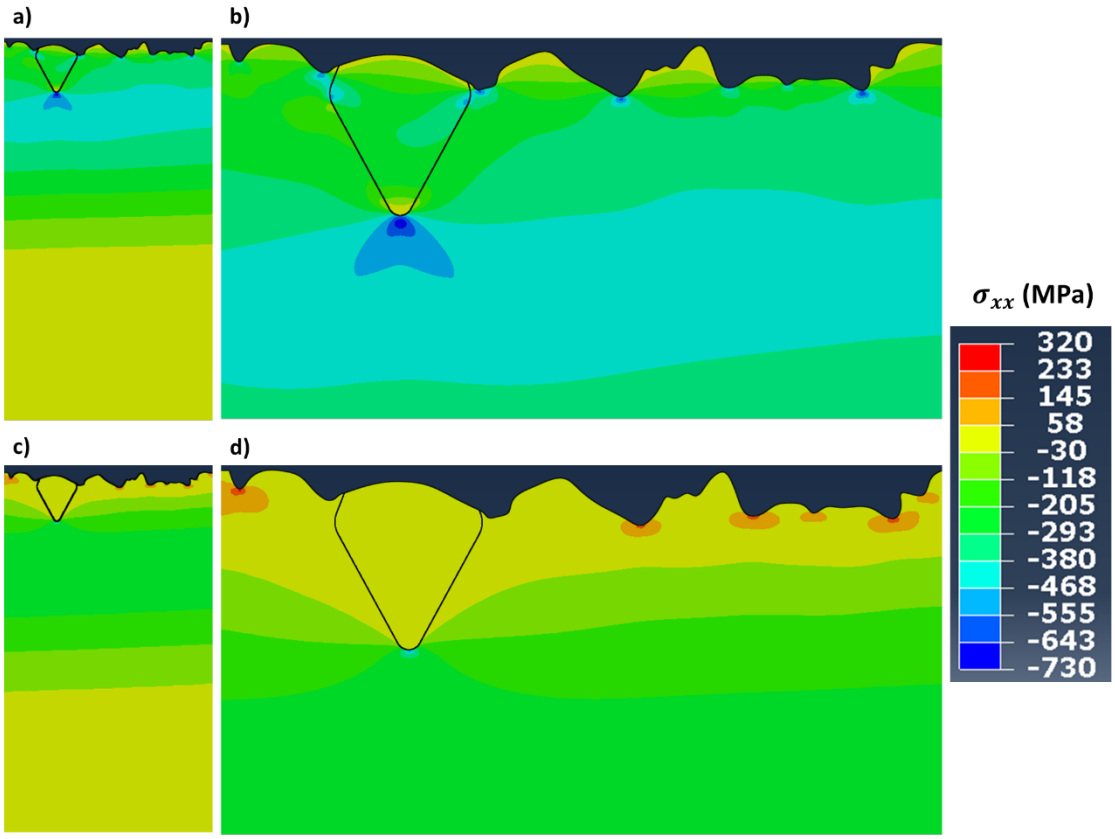


**Figure 6:5: The local residual stress state after re-equilibration of a) an abrasive blasted sample (magnified version of the same in (b)), c) a LACR sample (magnified version of the same in (d)).**

In addition to the global initial stress distribution, i.e., measured residual stress distribution of the abrasive blasted and LACR samples, the surface profile, the area, depth, and radius of the curvature of the embedded particles play a critical role in local stress distribution. The effects of these factors are systematically investigated and the results are summarized in Figure 6:6, which show the local residual stress distributions of the particles investigated for both surface profile-1 and profile-2 and for both abrasive blasted and LACR samples. The maximum residual stress associated with the surface profiles for both surface conditions are also presented in the

figures for reference. Due to the higher roughness value of profile-2, the maximum concentrated compressive residual stress of the abrasive blasted samples at the valley of surface profile-2 (-677 ± 16 MPa) is much higher than the concentrated stress at the valley of profile-1 (-552 ±22 MPa). The magnitude of the maximum concentrated tensile residual stress at the surface depression is calculated to be ~194 ± 16 MPa and ~300 ± 27 MPa for surface profile-1 and profile-2, respectively. Figure 6:6 (a) also shows that the absolute magnitude of the local compressive residual stress in the proximity of each group of particles for both abrasive blasted increases with aspect ratio of the particles, i.e., increasing t/r ratio of the particles, for surface profile-1, as the $k_t$ increases with increasing t/r ratio, for surface profile-1. However, when the local compressive stress around the particles as a whole this simple correlation between the residual stress *vs. t/r* ratio breaks down. For example, local stress around the shallower particles (depth ≈35 µm) having t/r ≈ 7 show much lower compressive stress (-565 MPa) than relatively deeper particles (depth ≈65 µm) having t/r ≈ 6.5. The residual stress around 65 µm having t/r ≈ 6.5 is computed to be -650 MPa . This, indicates the importance of the global residual stress distribution on the local residual stress, e.g., the magnitude of the compressive residual stress is higher at a depth 65 µm than at 35 µm, as shown in Figure 4.16. Similar to the abrasive blasted samples, compressive residual stress around the particles associated with surface profile-1 increase with increasing t/r ratio for LACR samples. However, the absolute magnitude of the compressive residual stress is much lower compared to abrasive blasted samples. The local residual stress around the 65 µm and 85 µm deep particles is quite similar, while the stress around 35 µm particles are much lower.

Figure 6:6 (b) shows that the compressive residual stress around the particles of the abrasive blasted samples with surface profile-2 has the similar characteristics as it was observed for surface profile-1, i.e., local residual stress distribution decreases with increasing t/r ratio. However, residual stress around the particles of the LACR samples with surface profile-2 show a different trend. The deepest particles (depth ≈85 µm) still show that local residual stress in the proximity of the particles increases with decreasing radius of curvature of the particles, however, relatively shallower particles (depth ≈35 and 65 µm) show a slight or no decrease in residual stress value with increasing t/r ratio. The residual stress values around 35 µm and 65 µm deep particles are computed to be 57 ± 9 MPa and -36 ± 16 MPa, respectively.

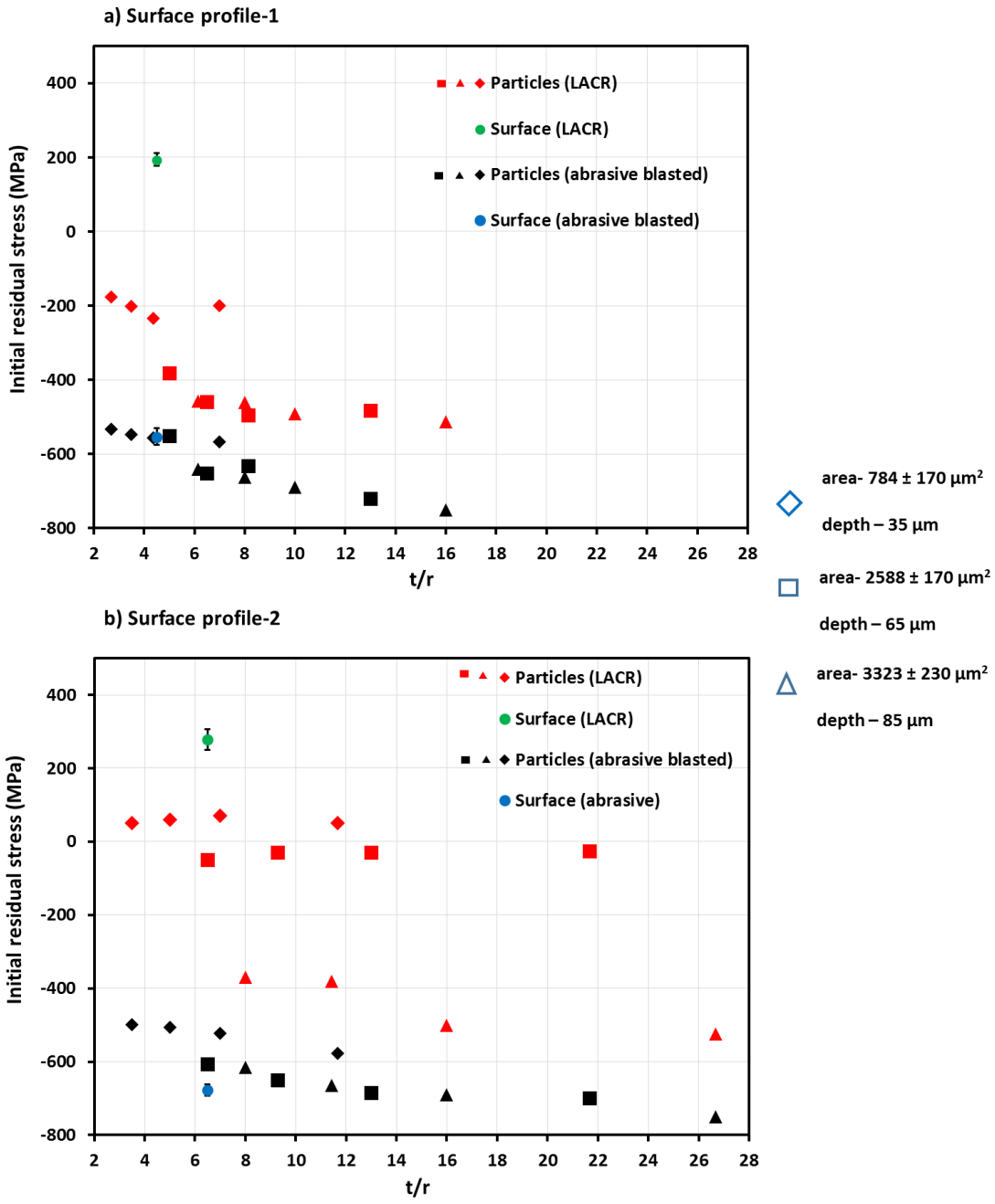


**Figure 6:6: Initial residual stress distributions around all the examined particles as a function of t/r ratio for the surface a) profile-1 and b) profile-2. Highest stress level at the surface is also reported for comparison. Each shape of markers in the plot corresponds to the dimensions of the particle.**

### 6.3.2 Elastic-plastic analysis

In order to determine the "hot spots" for fatigue crack initiation, the deformation behavior at the surface valleys and around the particles is examined under an applied load of 440 MPa along $\sigma_{xx}$ direction. The hot spots are highlighted by the circles where the stress component along the loading direction ($\sigma_{xx}$) is concentrated for abrasive blasted and LACR samples and for both surface profiles containing a particle of area 2370 $\mu m^2$,depth of 65 μm and radius of curvature 5 μm. Figure 6:7 and Figure 6:8 reveal multiple hot spots at the surface, for both surface conditions and surface profiles. Stress distributions ahead of these micro-notches are monitored and only the one with maximum stress concentration ($k_{t\text{-}ep,max} = \sigma_{xx}/\sigma_{applied}$) is reported. As expected, the maximum stress concentrations (within surface valleys) are higher for surface profile-2 than the profile-1. The maximum stress concentration for the abrasive blasted surface condition is computed to be 1.35 and 1.82, and for LACR samples it is computed to be 1.76 and 2.04, respectively, for the surface profile-1 and profile-2.

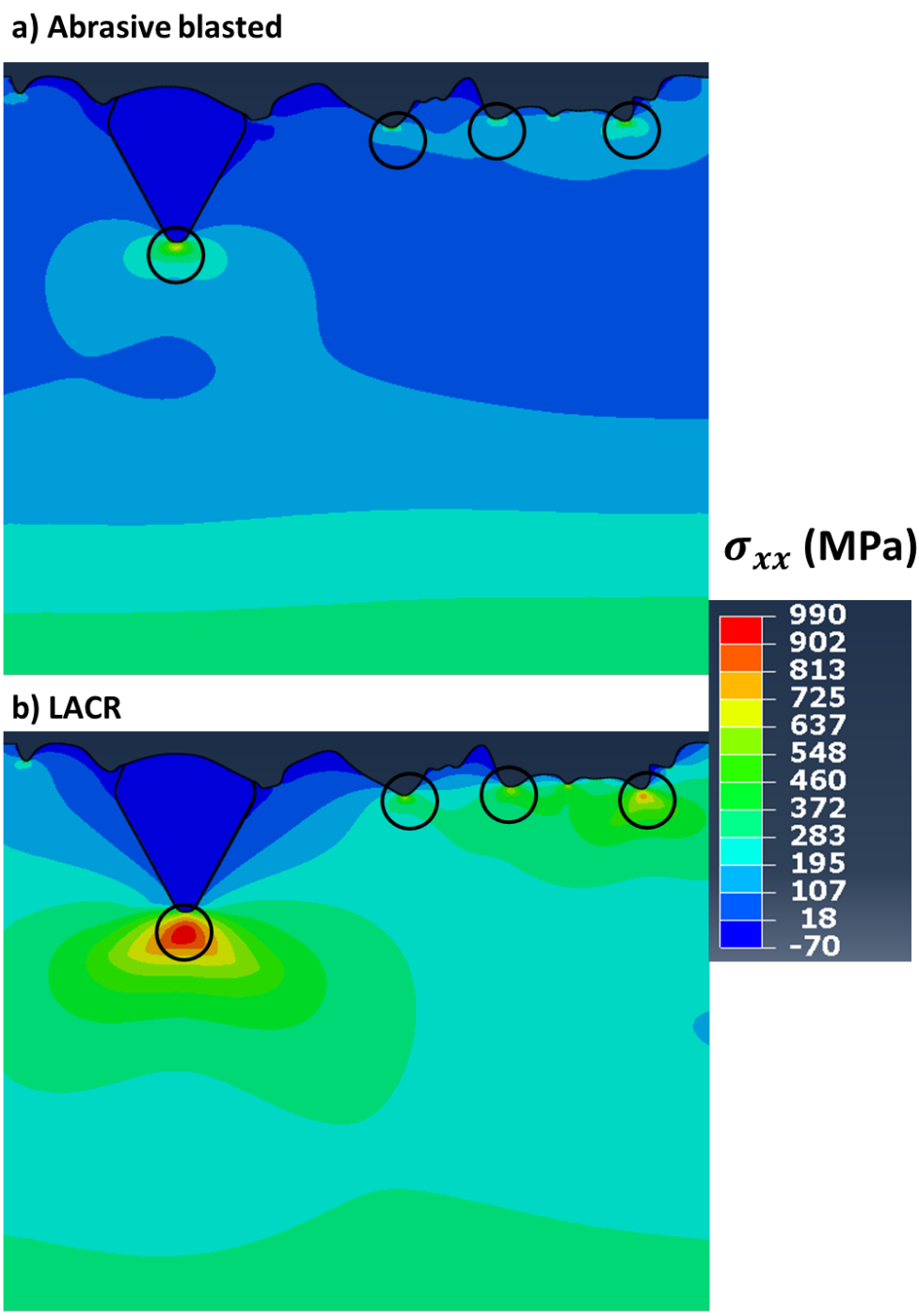


**Figure 6:7: Isostress contours of the $\sigma_{xx}$ component for a) abrasive blasted and b) LACR samples having surface profile-1 for applied load of 440 MPa.**

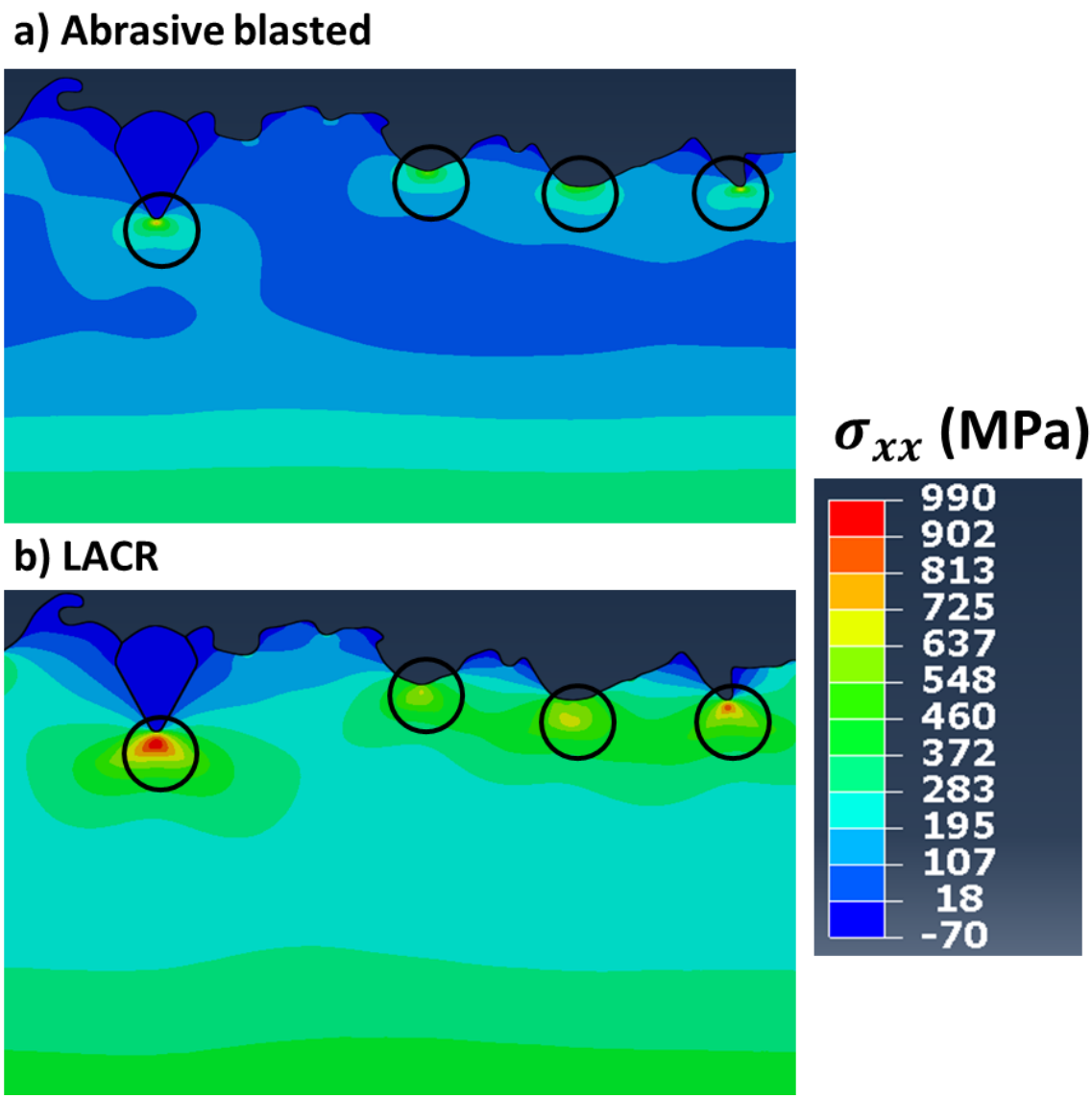


**Figure 6:8: Isostress contours of the $\sigma_{xx}$ component for a) abrasive blasted and b) LACR samples having surface profile-2 for applied load of 440 MPa.**

Figure 6:9(a) shows the variations of the stress ahead of the embedded particles as a function of their t/r ratio for abrasive blasted and LACR samples having surface profile-1. For both surface conditions, stresses around the particles increase with increasing t/r ratio. However, no definite correlation between stress concentrations vs. t/r ratio is observed, as the local residual

stress field does not hold a strong correlation with t/r ratio. Figure 6:9 (a) shows that stresses around the investigated particles with radii of curvature higher than 10 µm are either same or lower than the computed maximum surface stress, for abrasive blasted surface conditions. After a holistic consideration of the all the particles, it is noted that the the maximum of the elastic-plastic stress concentration factor is higher around the particles with t/r value greater 10. On the other hand, irrespective of a particle's depth and dimensions, the stresses around the particles are always higher than the maximum surface stress for LACR samples, as shown in Figure 6:9 (a) .

A different trend is observed for the component having a rougher surface profile corresponds to the profile-2. FE simulations show that the local stress distributions around the particles for abrasive blasting surface conditions are always lower than the calculated maximum stress associated with surface roughness. On the other hand, one observes the highest stress level at the particles or at the surface valleys depending on the surface geometry or the dimension of the particles for LACR samples. Figure 6:9 (b) shows that only the local stress distributions around the smallest, shallowest (35 µm deep) particles having radii of curvature greater than 7 µm (t/r = 5.0) is lower than the highest stress level at the surface valleys. It is interesting to note that the stress level is always higher around the deeply embedded particles relative to stress at the surface valleys for LACR samples, which corresponds well with the experimental observation that shows that fatigue crack typically initiated from the deeply embedded particles after LACR surface treatment.

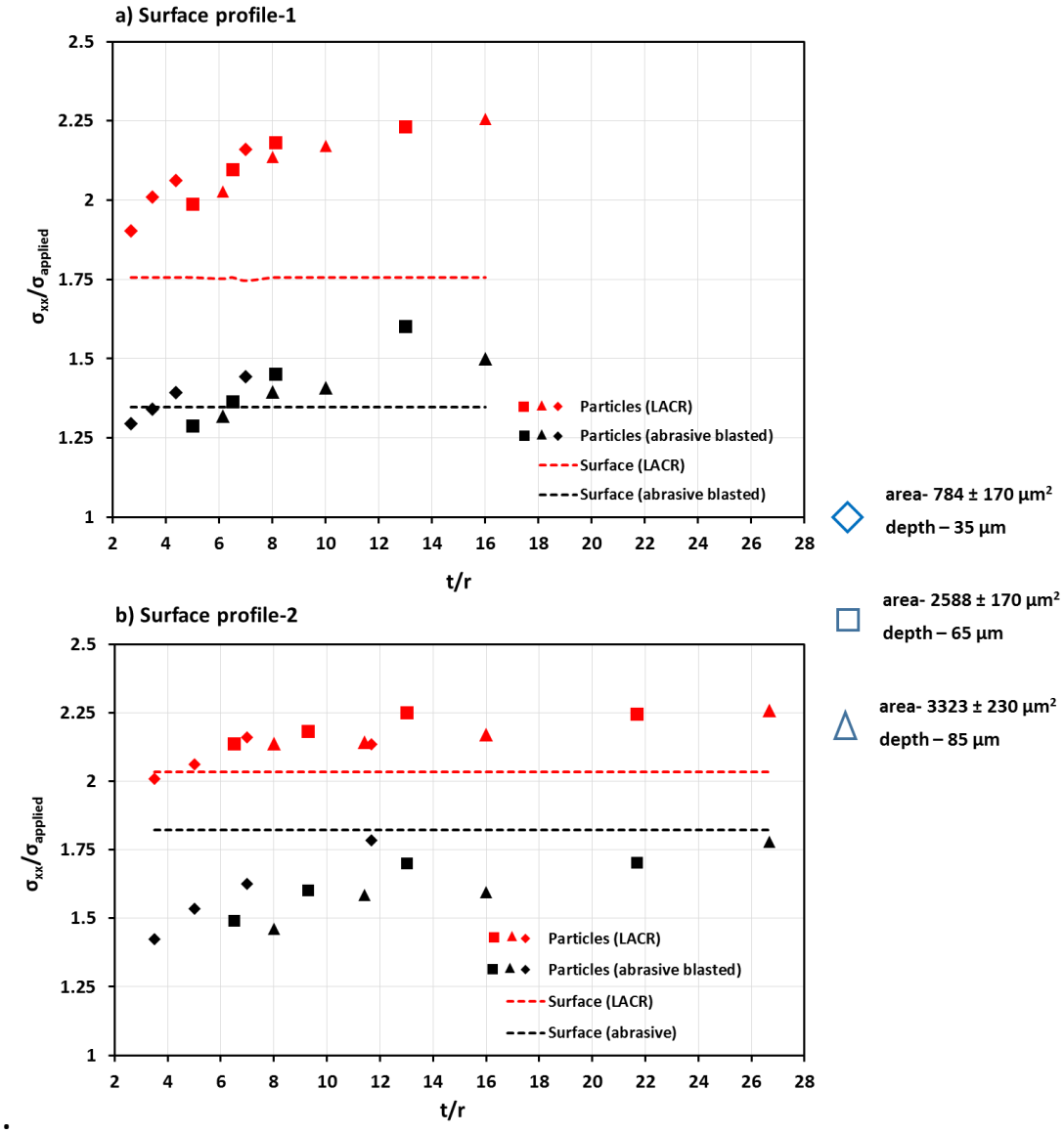


**Figure 6:9: Stress distributions around all the examined particles as a function of t/r ratio for the surface a) profile-1 and b) profile-2. Highest stress level at the surface is also reported for comparison. Each shape of markers in the plot corresponds to the dimensions of the particle.**

Depth distributions of the residual stress field ahead of these surface defects show a quite similar behavior. As an example, the residual stress field ahead of the surface defects as a function of distance from the surface defect is shown in Figure 6:10 for surface profile-2

containing a particle of area 2370 µm$^2$,depth of 65 µm and radius of curvature 5 µm. It shows that the stress levels at distances greater than 50 µm ahead of the particles and surface valleys become similar for both LACR and abrasive blasted samples. It is also noted that, similar to XRD measured residual stress, for both surface condition the stress field become similar beyond 100 µm depth into the material. Therefore, growth rates of a crack of a length above 100 µm would be similar for both materials. This reassures that the difference in fatigue life between two surface conditions is mainly related to differences in fatigue crack initiation life.

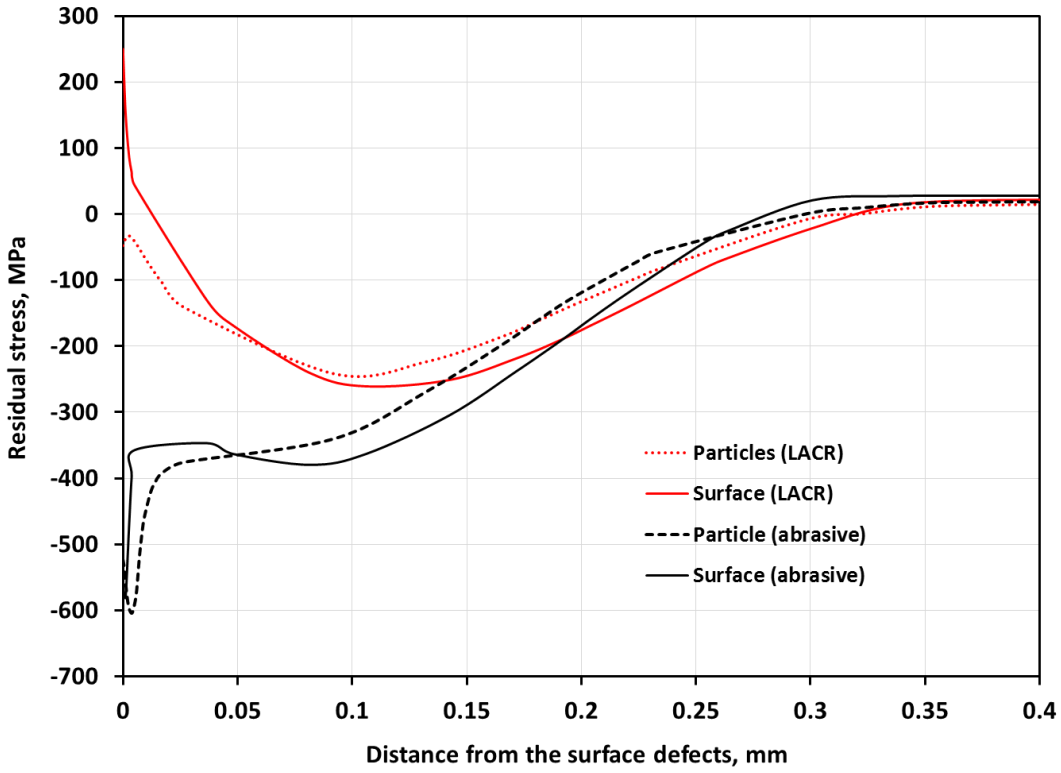


**Figure 6:10: Residual stress distributions ahead of the surface defects.**

## 6.4 Discussion

The interaction between the stress concentrations associated with the surface roughness and embedded blasting media particles, the residual stress field associated with different surface treatments, and the applied loading conditions were analyzed using the finite element method to understand their influence on the fatigue performance.

Fatigue crack nucleation is a localized process and any defects in the component facilitate the crack nucleation process. Abrasive blasting-induced surface roughness and embedded blasting particles are strong stress raisers and act as primary crack initiation sites. As discussed earlier, the location of the crack initiation sites vary, depending on the surface conditions (see Figure 6:1). This clearly indicates that considering only the stress concentration associated with these defects is insufficient to evaluate the driving force for crack formation and propagation. The residual stress distribution imparted by abrasive blasting and its alternation by subsequent LACR treatment also play a key role in fatigue life determination.

FE analysis reveals that the local residual stress depends on the particles size, depth and their radius of curvature and, of course, the surface treatment. For abrasive blasting surface treatment, high compressive stresses always observed around the particles and it increases with the “severity” of the particles, i.e., t/r ratio. This observation correlates well with the nature of the abrasive blasting process. The very fact that these blasting particles remained embedded in the surface indicates that the material has been aggressively impacted [4]. Researchers using both experimentation and finite element analysis have shown that both the depth of the surface depression and local residual stresses around this depth are function of

abrasive blasting parameters and both simultaneously increases with increasing impact velocity [4, 21, 25, 26].

Laser-material interaction during LACR process results in melting and resolidification, which leads to changes in surface residual stress state. The residual stress shift from compressive to tensile upon LACR treatment, redistribution of the subsurface residual stress also occurs, as it can be seen from the depth-resolved global residual stress distribution (see Figure 4.16). This is also reflected in FE analysis. While the residual stress in the vicinity of the particle is still compressive, the absolute magnitude of the stress is significantly lower. In addition, when the depth (~ 35 μm) of the particles is similar to the surface depression (surface profile-2), a strong pull on the particles from surrounding tensile stress may completely relax the initially strong compressive stress. This relatively relaxed residual stress renders the embedded particles as the primary crack nucleation sites upon LACR treatment. However, the relative location of the maximum of the concentrated stress will depend on the stress concentrations and initial residual stress state of the surface. However, invoking the “weak link” approach in fatigue life analysis, it can be claimed that crack initiation at surface will more likely to occur which has the similar characteristics as surface profile-2 ($k_t \approx 6.5$, which lies at the tail of the distributions of $k_t$). For this surface profile, the magnitude of the concentrated stress at the surface valleys are always higher than the local stress at the particles for abrasive blasting surface condition. Contrary to this observation, thes concentrated stress around only the shallowest particles examined here is lower than the surface stress.

It should be noted here that the local maximum stress, on which the present study focused, is not the only factor which influences crack initiation. Other approaches emphasize the roles of mean stress, stress amplitude, accumulated plastic strain, and combinations of these values into so-called fatigue indicator paramters (FIPs) [27]. Exploration of these parameters in the present context would be an excellent direction for future research. However, it has also been suggested that crack nucleation from the notches occur when stress intensity factor *(ΔK*) for equivalent crack is greater than or equal to threshold intensity factor ($K_{th}$) for crack growth, i.e., $\Delta K \geq K_{th}$. From the fatigue threshold criteria [28, 29]:

$$\Delta K_{th} = F\ k_t \Delta\sigma\sqrt{\pi a}$$

where *F* is the geometric factor, *a* is the short crack length and $k_t\sigma$ is the local stress field. Considering the fact that the geometric factor and $k_t$ are the expected to remain unchanged at the candidate initiation sites, the local stress field is the only factor which changes due to residual stress applied load interaction, and it is propotional to the driving force for crack nucleation in this type of analysis.

Finally, it should be noted here the driving force for fatigue crack initiation calculated based on the 2D plane strain FEA was performed in order to increase the computational efficiciency. As shown in section 4.4.1, this results in a more severe stress concentration state than would have been obtained using a 3D finite analysis of a 3D surface topography. As mentioned in section 4.41, $k_t$ of the elliptical notch with t/r =1 is calculated to be 3.09 from the 2D FEA analysis, while $k_t \approx 2.06$ is obtained from the 3D FEA analysis of an ellipsoidal surface depression with t/r = 1. 100% of the investigated particles have a lower driving force for crack initiation than surface

valleys, for abrasive blasting conditions, and it is reduced to only 15% ,after LACR surface processing for component with surface profile-2. In reality, particles were responsible for 25% of the crack initiations in the abrasive blasting condition, and 73 % of the crack initations after LACR. This qualitative agreement between the model and experiment, provides insight regarding the complicated interaction between residual stress, stress concentration, and applied load.

## 6.5 Conclusions

Finite element modeling is used to study the effects of surface modification techniques, i.e., abrasive blasting and laser ablation coating removal (LACR), on the fatigue performance of a high strength steel. Significant findings of this work are as follows:

a) A methodology has been developed to construct FE models with a real surface profile from SEM cross-sectional images and with embedded blasting particles.

b) A simplified algorithm is presented to simulate the local residual stress distribution at the surface and at the particles induced by abrasive blasting and LACR processes.

c) The dependence of local residual stress distributions on the size, depth, and radius of the curvature of embedded particles was determined. The compressive residual stress at the particles is relatively relaxed for LACR process conditions.

d) Counteracting effects of the very compressive residual stress and high stress concentration associated with particles makes these embedded particles less susceptible to fatigue cracking for abrasive blasting surface condition.

e) The driving force for fatigue crack nucleation at the particles is higher for the LACR samples due to relaxed residual stress states and a high stress concentration factor. Among the particles examined (for both surface profiles), 91% of the particles show higher driving force for crack nucleation than the surface after LACR.

f) On the other hand, prior to LACR only 29% of particles show a higher level of concentrated stress as compared to the surface.

g) This correlates well with the observation that 73% of fatigue cracks initiate at embedded particles after LACR, whereas 75% of fatigue cracks initiate at the surface valleys for abrasive blasting conditions.

## References


[1] J. T. Coleman, P. Sjoblom, "Design Engineering and Support Program (DESP), Delivery Order RZ16: Effects On Mechanical Properties From Laser Paint Stripping." Dayton Univeristy (2005).

[2] M.L. Klingenberg, J.J. Valencia, G.A. Price, J.R. Adams, T.P. Blair, Transitioning laser technology to support air force depot transformation needs: Final Report, Navy Metalworking Center, Johnstown (2010) .

[3] S. Pantelakis, G. Haidemenopoulos, *Surf. Coatings Technol.*, 106(1998), 198–204.

[4] K. Shemtov-Yona, D. Rittel, A. Dorogoy, *J. Mech. Behav. Biomed. Mater.*, 39(2014), 375–390.

[5] J. E. LaRue, S. R. Daniewicz, *Int. J. Fatigue*, 29(2007), 508–515.

[6] M. Dorman, M. B. Toparli, N. Smyth, A. Cini, M. E. Fitzpatrick, P. E. Irving, *Mater. Sci. Eng. A*, 548(2012), 142–151.

[7] M. Achintha, D. Nowell, D. Fufari, E. E. Sackett, M. R. Bache, *Int. J. Fatigue*, 62(2014), 171–179.

[8] *Abaqus User's Manual, Version 6.14, Dassault Systèmes Simulia Corp., Providence, RI. 2014.* .

[9] D. H. Hwang, K. H. Zum Gahr, *Wear*, 255(2003), 365–375.

[10] K.H.Z. Gahr, *Wear*, 133(1989), 1–22.

[11] I. Suzuki, O.L. Anderson, *J. Phys. Earth*, 31(1983), 125–138.

[12] F. Dunne, N. Petrinic, *Introduction to Computational Plasticity*, Oxford University Press, New York (2005).

[13] *Abaqus 6.14: User Subroutines Reference Manual.* .

[14] M. R. Hill, "Modeling of residual stress effects using eigenstrain," *In: Proceedings of 10th International Conference on Fracture,* Oahu, Hawaii (December 2001).

[15] D.J. Smith, G. H. Farrahi, W. X. Zhu, C. A. Mcmahon, *Int. J. Fatigue*, 23(2001), 293–302.

[16] D.J. Buchanan, R. John, *Mater. Sci. Eng. A*, 615(2014), 70–78.

[17] X. Chen, J. W. Hutchinson, J. Mech. Phys. Solids, 50 (2002), 2669-2690.

[18] X. Chen, *Trans. Famena*, 37(2013), 57–66.

[19] B. Lin, S. Zabeen, J. Tong, M. Preuss, P. J. Withers, *Int. J. Mech. Mater.*, 82(2015), 78–90.

[20] H.Y. Miao, S. Larose, C. Perron, M. Lévesque, *Adv. Eng. Softw.*, 40(2009), 1023–1038.

[21] S.A. Meguid, G. Shagal, J. C. Stranart, J. Daly, *Finite Elem. Anal. Des.*, 31(1999), 179–191.

[22] M. Frija, T. Hassine, R. Fathallah, C. Bouraoui, A. Dogui, *Mater. Sci. Eng. A*, 426(2006), 173–180.

[23] S.A. Meguid, G. Shagal, J. C. Stranart, *Int. J. Impact Eng.*, 27(2002), 119–134.

[24] S.M H. Gangaraj, M. Guagliano, G.H. Farrahi, *Surf. Coatings Technol.*, 243(2014), 39–45.

[25] M. S. Eltobgy, E. Ng, M. a Elbestawi, *Proc. Inst. Mech. Eng. Part B J. Eng. Manuf.*, 218(2004), 1471–1481.

[26] S. Wang, Y. Li, M. Yao, R. Wang, *J. Mater. Process. Technol.*, 73(1998), 64–73.

[27] D.L. McDowell, F.P E. Dunne, "*Int. J. Fatigue*, 32(2010), 1521–1542.

[28] S. Suresh, R.O. Ritchie, *Int. Met. Rev.*, 29(1984), 445–475.

[29] G. S. Chen, K.C. Wan, M. Gao, R.P. Wei, T.H. Flournoy, *Mater. Sci. Eng. A*, 219(1996), 126–132.

# Chapter 7: Conclusions and Future work

## 7.1 Conclusions

The effects of the laser ablation coating removal on the fatigue performance of the high strength shipbuilding structural steel obtained from two different lots having distinct microstructures and tensile properties have been investigated. Both materials were abrasive blasted as this is the typical condition used in industry prior painting and any subsequent LACR treatment. This also provides an opportunity to compare the performance of the LACR with abrasive blasting, a well-established coating removal technique. Two different abrasive blasting techniques were employed: i) the material HSS-I was abrasive blasted in a controlled laboratory setting, and ii) the material HSS-II was blasted in the typical industrial fashion, with higher pressure and size of the abrasive medium. The following conclusions can be drawn from this study:

i) The LACR process has been proven to be an effective method for the removal of a typical epoxy-based coating from the steel substrate. However, multiple passes were typically required to remove the coating, with an increased number of passes required at higher sweep speeds. An effective coating removal rate of 45 sq. in. per minute (~1.8 $m^2$/hr) was measured using the 7.6 cm laser scan width on 0.25 mm coated samples, which is considered slow by industry standards. It is possible that the removal rate can be improved using improved laser focusing conditions and parameters.

ii) The cross-sectional analyses confirmed that, irrespective of surface conditions and microstructures, for the selected laser processing parameters, the underlying substrate experienced melting and re-solidification after LACR treatment. The depth of the observed melted region ranged from 1 μm to 5 μm and the heat affected zone (HAZ) after LACR treatment only about XX μm. No microstructural changes were observed at greater depths. Heat transfer analysis shows that thermally affected zone is confined to a depth less than 10 μm. In addition, micro- and nano-hardness-based depth profiles show that hardness values between abrasive blasted and LACR samples are essentially same for a depth greater than 10 μm. Notably, employment of the Nix and Gao strain gradient plasticity-based approach to nanohardness assessment was required to obtain this conclusion.

iii) Blasting the surface with a higher impact velocity result in a higher surface roughness for the abrasive blasted samples of the material HSS-II. In addition to higher roughness, this blasting protocol induced a high density of surface-embedded particles, which remain embedded even after LACR processing. Although the appearance of the surface is clearly changed at the microscopic level, especially for the material HSS-I, the conventional surface roughness (profile) measurements indicate no statistically significant change in the roughness, even for HSS-I.

iv) XRD measurements of the depth-resolved residual stress show that both the abrasive blasting protocols result in a similar “U-shaped” residual stress distributions, where compressive residual stress reaches its maximum value at

about ~100 µm below the surface. LACR induces a large shift of the residual stress, with significant tensile stress at the surface. However, depth-resolved residual stress measurement shows that the tensile residual stresses are confined to a shallow depth of about 35µm for both the material HSS-I and HSS-II.

v) The stress correction method developed in this study shows that the roughness of the materials under investigation will have no measureable effect on the residual stress assessed using XRD method.

vi) Fatigue testing of the samples shows that, depending on the blasting protocol, the fatigue response can either i) remain the same (HSS-I) or ii) be degraded by LACR (HSS-II), relative to abrasive blasting. In cases where the fatigue response remains unchanged by LACR, it is believed that the effects of tensile residual stress and surface topology are counteracting. Finite element analysis shows that the maximum stress concentration $k_t$ , associated with surface roughness, decreases significantly after LACR processing due to surface smoothing in this case.

vii) In cases where the fatigue strength decreased, the fatigue crack initiation sites shifted from surface regions of stress concentration to embedded abrasive media, as such $k_t$ remains the same after both surface treatments.

viii) Finite element examination of the residual stress field reveals concentrated compressive residual stress in the proximity of the embedded particles for abrasive blasting surface treatment. The local compressive residual stress is highest for the

largest and deepest particles having the smallest radius of curvature. This local compressive residual stress relaxes significantly after LACR treatment.

ix) Elastic-plastic finite element analysis under monotonic tensile loading reveals that the combination of high stress concentration and relaxed residual stress provides an explanation for why the embedded particles become the primary crack initiation sites after LACR treatment.

## 7.2 Future Work

The work undertaken in this study has highlighted some key issues related to the LACR process, which warrant further investigation. Some suggestions follow:

i) The results of the study have shown that fatigue performance of laser treated samples highly depends on the prior surface treatment condition. Examining the fatigue performance of the laser treated samples without any prior treatment (i.e., which may induce residual stress or surface roughness) will help to single out the effects of laser treatment on fatigue performance. Based on the obtained results, a standard experimental protocol should be developed to parameterize the prior surface conditions that can be used before LACR treatment.

ii) The experimental residual stress field data obtained from XRD measurement were incorporated and redistributed using a FE model to compute the stress field around the valleys of the profile and embedded particle. An experimental strategy should be

developed for a complete residual stress field measurement around these surface defects. During the research no current method for residual stress measurement was capable of accurately measuring the residual stress field around such defects. However, future advances may make this possible with the Focused Ion Beam-Scanning Electron Microscope- Digital Image Correlation (FIB-SEM-DIC) based micro mechanical stress relaxation methods looks most promising. The method involves micro-hole drilling using the FIB of a dual beam focused ion beam-field emission gun scanning electron microscopes (FEBSEM/FIB). DIC of SEM images recorded during drilling records the resulting surface displacements. Finally, the residual stress fields are reconstructed from the recorded displacement field as a function of depth [1, 2].

iii) It is clear from this study that any thermal damage induced by the laser ablation coating removal would have a significant effect on the performance of the component. Therefore, a study should be designed to evaluate the effects of laser intensity, fluence, peak power, pulse duration, etc. on the efficiency and extent of the thermal damage (melt depth) of the underlying substrate. Due to the larger number of variables is involved in LACR process, experimental determination of their effects would be prohibitively costly and time-consuming. Therefore, a complementary approach is to use computational simulation methods based on suitable experimentally validated computational models. Finite element simulation can be used this for this purpose. However, one of the main difficulties in simulating laser ablation process using the FE method is in deleting the element to simulate the

ablation process. In recent years, a number of researchers have adopted so called element “birth and death” technique to incorporate or delete the elements in desired time step of the finite element solution [3, 4]. The same technique can be used for the laser ablation process too.

iv) Finally, a range of paint-material (aluminum, composites, etc.) combinations should be used to expand the understanding of the implications of wider application of the laser ablation coating removal (LACR) method.

## References


[1] B. Winiarski, M. Benedetti, V. Fontanari, & M. Allahkarami, J. C. Hanan, P. J. Withers, *Exp. Mech., 56 (2016)*, 1449-1463.

[2] B. Winiarski, P. J. Withers, *Exp. Mech.,* 52 (2012)*,* 417-428.

[3] I.A. Roberts, C.J. Wang, R. Esterlein, M. Stanford, D.J. Mynors, *Int. J. Mach. Tools Manuf*., 49 (2009), 916-923.

[4] S. Marimuthu, A.M. Kamara, H.K. Sezer, L. Li, G.K.L. Ng, *Comput. Mater.* Sci., 88 (2014), 131-138.

# Appendix

## Appendix-I: Finite element modeling of abrasive blasting induced residual stress

### Model description

Finite element simulation of shot peening typically uses an explicit time integration scheme. This scheme advances the solution with a large number of small time increments and is well suited for analyzing a dynamic response over a short time period. The analysis employs a Lagrangian formulation [1, 2]. The momentum equation can be expressed as:

$$M\ddot{U} = F^{ext} - F^{int}$$

where *M* is the lumped mass matrix, $\ddot{U}$ is the nodal acceleration at each time step, $F^{ext}$ is the externally applied load for each node and $F^{int}$ is the internal forces. These sets of equations are solved using explicit time integration with the central difference method employing a lumped mass matrix.

$$\dot{U}^{(i+\frac{1}{2})} = \dot{U}^{(i-\frac{1}{2})} + \frac{\Delta t^{(i+1)} + \Delta t^{(i)}}{2}\dot{U}^{(i+\frac{1}{2})}$$

For an isotropic material, the minimum stable time increment Δt depends on the mesh size and material properties and can be evaluated as:

$$\Delta t \propto L_{min}\sqrt{\frac{\rho}{E}}$$

where $L_{min}$ is the minimum dimension in the FE mesh, $\rho$ is the density *E* is the elastic of material.

Simulations typically consist of projecting one or many particles towards the target surface with a given initial velocity and determining the response of the material during and after the impact(s). Shots are usually are modeled as rigid, however, EItobgy [2] had shown that the choice of modeling shots as rigid, elastic or elastic-plastic has an influence on the resulting stress state. In Abaqus/Explicit, the contact between the shots and the target surface function as as master and slave surface. During this hard contact analysis, no penetration of the slave nodes into the master surface is allowed. The surfaces transmit no contact pressure unless nodes of master and slave surfaces come in contact. The Coulomb friction relationship is employed in the contact model:

$$F_f = \mu F_n$$

where $F_f$ is the friction force, $F_n$ is the normal force and $\mu$ is the friction coefficient.

The material constitutive theory a key element for shot peening simulations. Shot peening creates large plastic strains and high strain-rate loading with strain rates up to $10^6$ $s^{-1}$ [3]. The Johnson-Cook material model is usually used to describe the flow stress behavior of the target material [2, 3].

$$\sigma = [A + B\varepsilon^n]\left[1 + Cln\left(\frac{\dot{\varepsilon}}{\dot{\varepsilon_0}}\right)\right]\left[1 - \left(\frac{T - T_r}{T_m - T_r}\right)^m\right]$$

where $\sigma$ is the von Mises effective stress, A,B,C and m are material constant, $\varepsilon$ is the effective plastic strain, $\dot{\varepsilon}$ is the effective strain rate, $\dot{\varepsilon_0}$ is a reference strain rate, *T* is the workpiece temperature, $T_m$ is the melting temperature and $T_r$ is the reference temperature.

## Results

A 2D dynamic elastoplastic model finite element model has been created. 3 uniformly spaced rigid sphere of radius 0.08 mm was considered as shots. A shot velocity of 55 m/sec was used. A 4-node bilinear plane strain quadrilateral, reduced integration, hourglass control was used to mesh the target. Johnson-Cook material model for low carbon steel was used [4].

This preliminary effort shows a high concentrated compressive stress underneath the impact, while residual stress are at relax state at the peaks of the surface (see Figure 1). The depth – resolved residual stress distribution matches well with the experimental results, as shown in Figure 2. However, the effects of the process parameter, multiple impacts on the same area or peening coverage on the stress distribution have not been investigated.

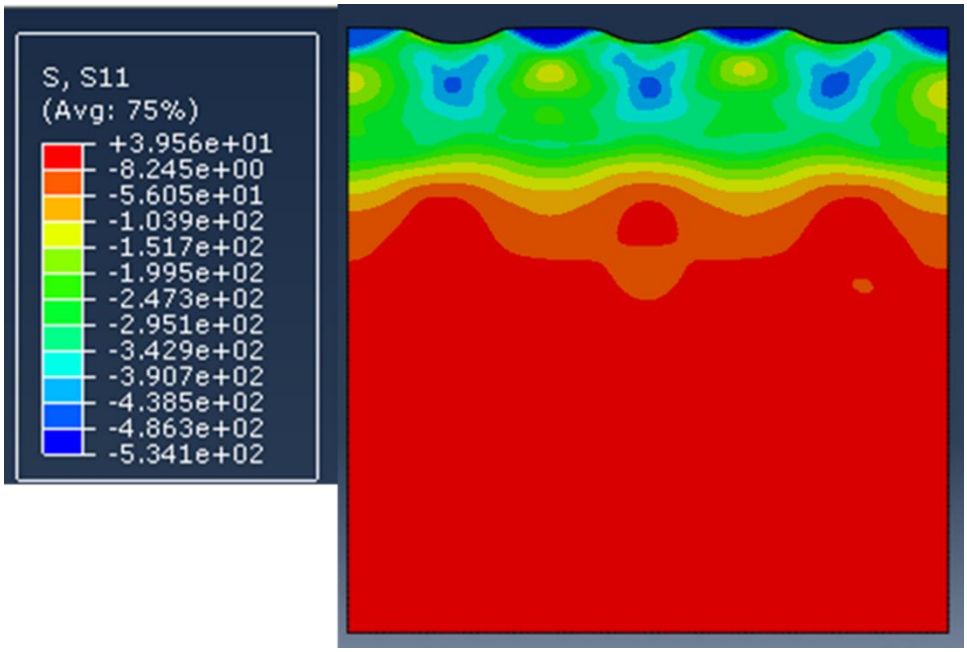


**Figure 1: Local residual stress distribution due to abrasive blasting.**

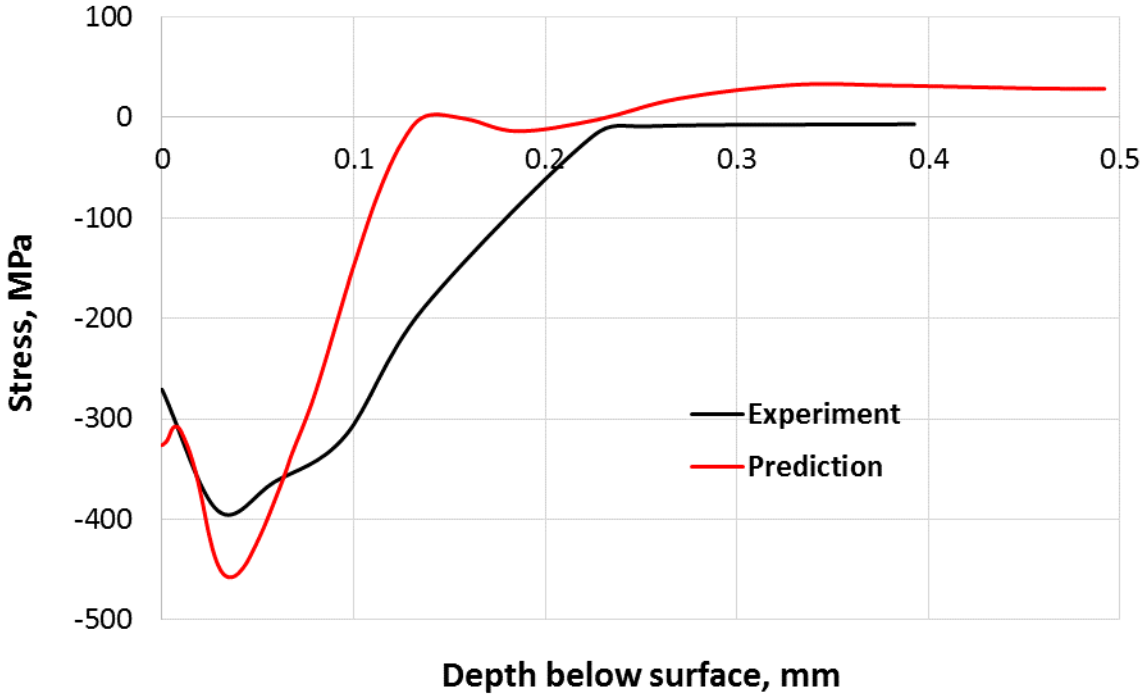


**Figure 2: Residual as a function of depth below surface of abrasive blasted samples**

## References

[1] M.S. Eltobgy, E. Ng, M.A. Elbestawi, *Proceedings of the Institution of Mechanical Engineers, Part B: Journal of Engineering Manufacture*, *218*(2004), 1471-1481.

[2] S.A. Meguid, G. Shagal, J.C. Stranart, J. Daly, *Finite elements in analysis and design*, *31*(1999), 179-191.

[3] X.K. Zhu, Y.J. Chao, *Computers & Structures*, *80*(2002), 967-976.

[4] K. Vedantam, D. Bajaj, N.S. Brar, S. Hill, *AIP conference proceedings,* 845(2006), IOP Institute of Physics Publishing Ltd.

## Appendix-II: High strength and ductility of additively manufactured 316L stainless steel explained

**Abstract**

Structure-property relationships of an additively manufactured 316L stainless steel were explored. A scanning electron microscope (SEM) and electron backscattered diffraction (EBSD) analysis revealed a fine cellular dendritic (0.5-2μm) substructure inside large irregularly shaped grains (~100 μm). The cellular structure grows along the <100> crystallographic directions. However, texture analysis revealed that the main <100> texture component is inclined by ~15° from the build direction. X-ray diffraction line profile analysis indicated a high dislocation density of ~$1 \times 10^{15}$ $m^{-2}$ in the as-built material, which correlates well with the observed EBSD microstructure and high-yield strength, via the traditional Taylor hardening equation. A significant variation in strain hardening behavior and ductility was observed for horizontal (HB) and vertical (VB) built samples. Ductility of HB and VB samples measured 49% and 77%, respectively. The initial growth texture and subsequent texture evolution during tensile deformation are held responsible for the observed anisotropy. Notably, EBSD analysis of deformed samples showed deformation twins, which predominately form in the grains with <111> aligned parallel to the loading direction. The VB samples showed higher twinning activity, higher strain hardening rates at high strain, and therefore, higher ductility. Analysis of annealed samples revealed that the observed microstructure and properties are thermally stable, with

only a moderate decrease in strength and very similar level of ductility and anisotropy, as compared to the as-built condition.

**Keywords**

Additive manufacturing, selective laser melting, dislocation density, twinning-induced plasticity.

## 1 Introduction

Laser powder bed fusion is a type of laser-based additive manufacturing (AM) process during which metallic parts are fabricated from a 3D computer aided drawing (CAD) file by selective melting of successive layers of powder using a sharply focused laser beam, e.g., selective laser melting (SLM), direct metal laser melting (DMLM). This “freeform” manufacturing method can produce extremely complex shapes relative to a traditional subtractive manufacturing method (machining) [1]. The density, microstructures and, consequently, the mechanical properties of the additively manufactured material are sensitive to laser processing parameters such as laser power, scanning speed, and scanning strategies. Indeed, it has been reported that with proper selection of laser processing parameters and scanning strategies, it is possible to obtain near fully dense parts [2–4]. The microstructure development in AM materials is complex because of the complicated thermal distribution. Each location in the component first undergoes rapid solidification, and then undergoes repeated reheating and cooling with an additional deposited layer. This complicated thermal history can result in microstructural heterogeneity in the as-built part [5].

316L stainless steel is one of the most widely investigated materials for AM. This is because 316L has a wide range of applications in marine, biomedical, nuclear reactor, chemical, and petrochemical industries owing to its high strength, good ductility, and high corrosion resistance [6–8]. Several studies have been performed to optimize the process parameters to fabricate near fully dense 316L SS parts [4, 9–11]. These studies reported that the average strength of the optimized parts are much higher than the counterpart as-cast, hot pressed (HP) or hot isostatic pressed (HIP) 316L stainless steel parts, while the ductility has been reported to be slightly lower [7, 8, 12]. The microstructure in the as-built 316L stainless steel materials is reported to be a sub-micron cellular-dendritic solidification structure, resulting from the high cooling rate inherent to AM process [8, 13, 14]. Many researchers have attributed the higher strength of as-built 316L stainless steel to the refined microstructure and high dislocation density. However, a quantitative connection between the dislocation density and observed strength is yet to be made.

Anisotropy of the mechanical properties, especially the ductility, with respect to as-built directions is still a matter of controversy. For example, some researchers [15–18] reported a higher ductility of the built material when the sample is tested perpendicular to the build direction relative to the samples tested along the build direction. They attributed this low ductility to the presence of defects along the melt pool boundary. Carlton *et al*. [19] reported that even a very low level of porosity can significantly reduce the ductility of as-built parts. On the other hand, other authors [20–22] showed a higher ductility of samples tested along the build direction. Tomus *et al*. [21] reasoned that the higher number of grain boundaries results

in lower ductility of the samples deformed perpendicular to the build direction. This apparent controversy will be examined by taking account of the specific preferred crystallographic orientation (texture) that results from AM processing [23]. The effects of the initial texture and its evolution during deformation need to be considered.

The main objective of this study is to examine the microstructure and crystallographic texture that develops during AM and correlate the observed microstructure with mechanical properties determined by tensile testing perpendicular and parallel to the build direction.

## 2 Experimental and Methods

### 2.1 Laser powder bed fusion (LPF) and heat treatment

The nitrogen atomized spherical pre-alloyed 316L stainless steel powders acquired from the EOS® product specification [24] were used as a starting material. Table 1 lists the chemical composition of the EOS powders [24].

**Table 2: Chemical composition of starting 316L stainless steel powders and as-built parts**

| | Cr | Ni | Mo | C | Mn | Cu | S | Si | N | Fe |
|---|---|---|---|---|---|---|---|---|---|---|
| Powders [24] | 17.00 - 19.00 | 13.00 - 15.00 | 2.25 -3.00 | 0.03 | 2.00 | 0.50 | 0.010 | 0.75 | 0.10 | Bal. |
| As-built | 20 | 16 | 2-3 | 0.006 | 1.00 | | 0.005 | 0.4 | 0.049 | Bal. |

Bulk material was fabricated using an EOS EOSINT® M280 AM system at the Naval Surface Warfare Center, Dahlgren Division, Virginia, equipped with a 400 W continuous wave Nd:YAG fiber laser. EOS-recommended laser processing parameters (e.g., power, scanning speed, spot diameter) were used. To minimize oxidation, laser-melting operations were conducted in a nitrogen environment. A stainless steel base plate and layer thickness of 20 µm were maintained throughout the process. A bidirectional scanning strategy, scanning vector is rotated by 70° between each layer, was used for all samples. Figure 11 shows the component built on a based plate for this study: (a) illustrates how the tensile samples, in accordance with ASTM E8 [25], were directly fabricated; (b) and (c) show the X axis of the specimen is defined as the long transverse direction (TD) and the Y axis is parallel to the building direction (BD). Selected AM samples were annealed in a vacuum furnace at 1100° C for 1 (HT1) and 13 hours (HT13) and cooled at a rate of 100° C/min.

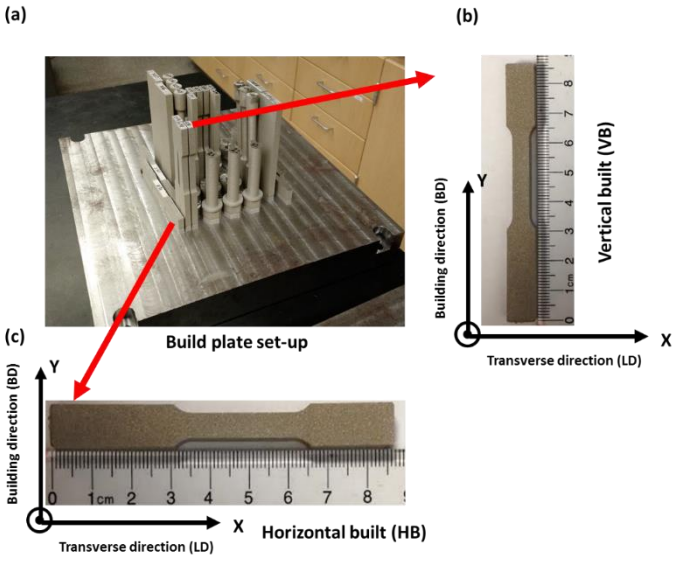


**Figure 11: a) shows the built components. The vertical and horizontal build samples are shown in (b), (c), respectively.**

## 2.2 Microstructure characterization and chemical analysis

Samples were observed with a Leica™ light optical microscope and an FEI Quanta™ 200 SEM equipped with an AZtec energy dispersive spectrometer (EDS). For microstructural analysis, the samples were sectioned using conventional band saw and slow-speed diamond saw methods, mounted in Konductomet® and mechanically ground up to 1200 grit silicon carbide paper, polished with a diamond pastes of 3 and 1 µm, and final polished using 0.05 µm colloidal silica. Finally, the samples were electro-etched at a room temperature in a solution of 10 g oxalic acid and 90 ml distilled water at 6 VDC for 60 seconds. EDS analysis measured the chemical composition of the material; however, EDS is only a semi-quantitative measure of the chemical composition and cannot yield compositional data for light elements with high precision. Therefore, the composition of light elements, such as carbon and nitrogen, was measured using EXTR Leco TCH600 according to ASTM E1019-11 [26].

Electron backscattered diffraction (EBSD) was performed using an FEI Company™ Quanta™ 650 scanning microscope equipped with an Oxford Instruments' AztecHKL® system, NordlysNano EBSD detector, and HKL Channel 5.0 EBSD post-processing software. The microscopes were operated at 20 kV, at a working distance of 15-20 mm. The EBSD scans were performed at a step size of 0.1-0.7 µm. The fraction of points successfully indexed was always greater than 95%. The kernel average misorientation (KAM) obtained from the EBSD analysis was used to estimate the geometrically necessary dislocation (GND) calculation. In this analysis, KAM was determined up to the second-nearest neighbor. The misorientation values exceeding a threshold value of 2° were excluded from the KAM calculation, since they were most likely from

adjacent grains. The KAM magnitude is affected by the step size of an EBSD scan and, therefore, only the scan performed at a step size of 0.1 μm was used in the final analysis.

### 2.3 Hardness and tensile tests

Vickers microhardness measurements were made using a diamond pyramid indenter with an apical angle of 136°, an indentation load of 0.5 kg, and an indentation duration of 15 seconds. The measurement was performed on a face perpendicular to the build direction and the reported results are an average of at least 10 indentation measurements per sample. Uniaxial tensile tests were performed using an MTS 318.1 system with a nominal strain rate of 1×10-3 $s^{-1}$ at ambient temperature. A contactless MTS® LX 500 laser extensometer was used to measure axial strain in the sample gage upon loading. As mentioned above, these flat dog-bone samples were directly fabricated by AM and only machined to remove the support structure.

### 2.4 X-ray diffraction

X-ray diffraction (XRD) was used to characterize the phase content, dislocation density, and crystallographic texture of the as-built, annealed, and deformed samples. All XRD measurements were performed using a conventional PANalytical® X'Pert Pro MPD [multipurpose diffractometer] X-ray diffractometer with a Cu-Kα sealed tube source operated at 45 kV and 40 mA. Similar sample surface preparation methods were used for the X-ray diffraction analysis as for microstructural characterization.

### 2.4.1 Phase identification and Dislocation density

The Bragg-Brentano focusing geometry was employed to collect diffraction pattern over the 2θ range of 30°-110° with a step size of 0.004° and counting time of 50 seconds per step for phase quantification and dislocation density measurement. The PANalytical X'Celerator linear position sensitive detector was used to collect the diffracted beam during this θ:2θ scans. A programmable divergence slit of 0.5° was used for both the incident and diffracted beams. A sample spinner programmed to a revolution time of 2 seconds was used to obtain better grain-sampling statistics. Instrumental broadening effects were evaluated and corrected using a silicon standard [27]. Both the modified Williamson-Hall (mWH) [28] and the more sophisticated Convolutional Multiple Whole Profile (CMWP) [29, 30] methods were employed to investigate the dislocation density present in the as-built and annealed samples.

In the modified Williamson-Hall (mWH) method, the full-width-half maximum (FWHM) obtained from single peak fitting of the diffraction data can be represented by the following equation:

$$(\Delta K)^2 = \left(\frac{0.9}{D}\right)^2 + \left(\pi \frac{M^2\, b^2}{2}\right) \rho (K^2 C\,) \qquad [1]$$

where *K* is the diffraction vector defined by $K = \frac{2sin\theta}{\lambda}$, *D* is the coherent domain size, *b* is the burgers vector (0.255 nm for FCC [face-centered cubic] iron), $\overline{C}$ is the average contrast factor and *M* is a dimensionless parameter related to the dislocation density and outer cut-off radius $R_e$ by $M = R_e\sqrt{\rho}$. The parameter *M* is sensitive to the dislocations arrangement in the material. *M* > 1 indicates that dislocations are randomly distributed to form a screening strain field while

*M* < 1 indicates that dislocations are arranged into low-energy dislocation structures (LEDS). The values of the average contrast factor for cubic crystals can be defined as:

$$\bar{C} = \bar{C}_{h00}\left(1 - q\left(\frac{h^2k^2+h^2l^2+k^2l^2}{(h^2+k^2+l^2)^2}\right)\right) \quad [2]$$

where $\bar{C}_{h00}$ is the average contrast factor of h00 reflection. $\bar{C}_{h00}$ can be calculated from the elastic constant of the crystal. The anisotropic elastic constants of face centered cubic (FCC) austenite are: $C_{11}$=210 GPa, $C_{12}$=130 GPa and $C_{44}$=120 GPa [31, 32]. These values were used to calculate the value of $\bar{C}_{h00}$ using ANIZC computer program [29] for both edge (0.281) and screw dislocations (0.289). However, the average value of 0.285 for the mixed (i.e. equal proportion of edge and screw type) dislocations were used, since variations in contrast factor are small and the consequences of this simplifying approximation are small. The *q* parameter was calculated by minimizing the difference of $\Delta K$ values between the measured and calculated one from the linear fitting of the equation [2]. Additional detail describing the method used can be found in reference [28]. The collected diffraction patterns were analyzed for determining the lattice constant, *a*, and FWHM using X'Pert High Score Plus software, assuming pseudo-Voigt peak shapes. It should be noted here that the slope of the mWH plot is related to both the *M* parameter and the square root of dislocation density, and therefore, dislocation density cannot be directly calculated from this method.

For the quantitative analysis of the dislocation density, the X-ray diffraction patterns were evaluated by the CMWP fitting procedure. In CMWP, the peak profile functions are calculated as the convolution of the size, strain, and instrumental broadening. The measured diffraction

pattern is then fitted with the calculated profile function using a nonlinear least squares method [29, 30]. Though CMWP is one of the most sophisticated methods available for line broadening analysis, it does involve a large number of fitting parameters, and different combinations of initial values can yield different solutions associated with local minima in the sum of the squared residuals. Therefore, the parameters obtained from mWH were used as a guide for quantitative analysis using the CMWP fitting procedure. Note that the same average contrast factor value was used in both the CMWP and mWH methods.

#### 2.4.2.2 Texture measurement

Texture measurements were performed with the X-ray sealed tube source oriented in point focus mode. A 2 mm × 1 mm cross slit was used to minimize defocusing at higher $\chi$ tilts. A graphite monochromator was placed in front of the point detector in order to block fluorescence and $K_\beta$ radiation. The (1 1 1), (2 0 0) and (2 2 0) incomplete ($\chi$= 0° to 80°) pole figures were measured on a 5° × 5° grid of azimuth (Ø) and tilt ($\chi$) angles. An experimental defocusing curve was obtained from a randomly textured Ni powder sample. The background subtraction, defocusing correction, calculation of the complete orientation distribution function (ODF), and recalculation of complete pole figures were performed using the MATLAB® MTEX library.

## 3 Results

### 3.1 Chemical composition and phase identification

The EDS and Leco analyses, which were used to measure the chemical composition of heavy and light elements (C,N,S,P) respectively, revealed that no significant compositional changes occurred during AM, in agreement with other recent studies [8, 13] where no loss of metallic elements was detected. The chemical composition of the 316L stainless steel AM parts and the starting powder, per suppliers' specification, are listed in Table 1. Contrary to several studies [34–36], where they reported the possibility of increasing the nitrogen content when parts were made in a nitrogen environment, the current as-built parts did not show any increase in N content.

The X-ray diffraction analysis revealed that both the as-built and annealed parts were fully austenitic. No trace of second phases (δ-ferrite, α-ferrite or martensite) were observed within the detection limit of X-ray diffraction (See Figure 12). Saeidi *et al*. [37] also reported the formation of single phase austenite during selective laser melting of 316 L stainless steel. However, they reported the formation of ferrite after δ-annealing heat treatment at 1100° C for one hour followed by furnace cooling and cited solute partitioning as responsible. Similar to the current results, Sistiaga *et al.* [38] reported a single phase austenite after a similar annealing heat treatment at 1095°C for 2 hours followed by water cooling. Finally, it is noted that due to a high initial dislocation density, the as-built samples have significantly broader diffraction peaks, as compared to annealed samples (Figure 12).

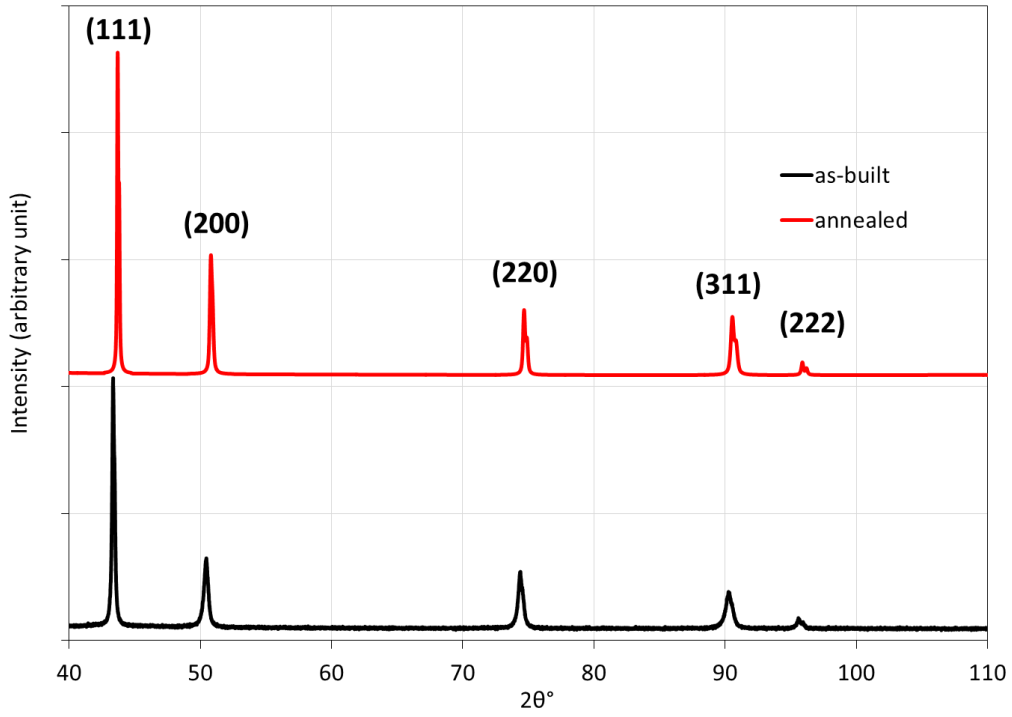


**Figure 12: XRD patterns of the as-built and annealed samples confirming single-phase austenite.**

### 3.2 Microstructure and crystallographic texture

Figure 13 (a) shows an optical micrograph of the as-built 316L stainless steel, constructed out of sections to create a 3D view. The as-built samples exhibit a typical layered microstructure, characterized by melt pool boundaries generated along the laser scanning paths. It should be noted that the differently oriented melt pool boundaries are the result of the bidirectional scanning strategy, i.e., 70° rotation between successive layers. However, in general arc-shaped melt pool morphology was observed. Optical images show that coarse grains are growing inside these melt pool boundaries. Since the previous layers are partially re-melted, heterogeneous

nucleation on the metallurgical solid/liquid interface occurs easily and new grains grow epitaxially in the direction of the maximum temperature gradient.

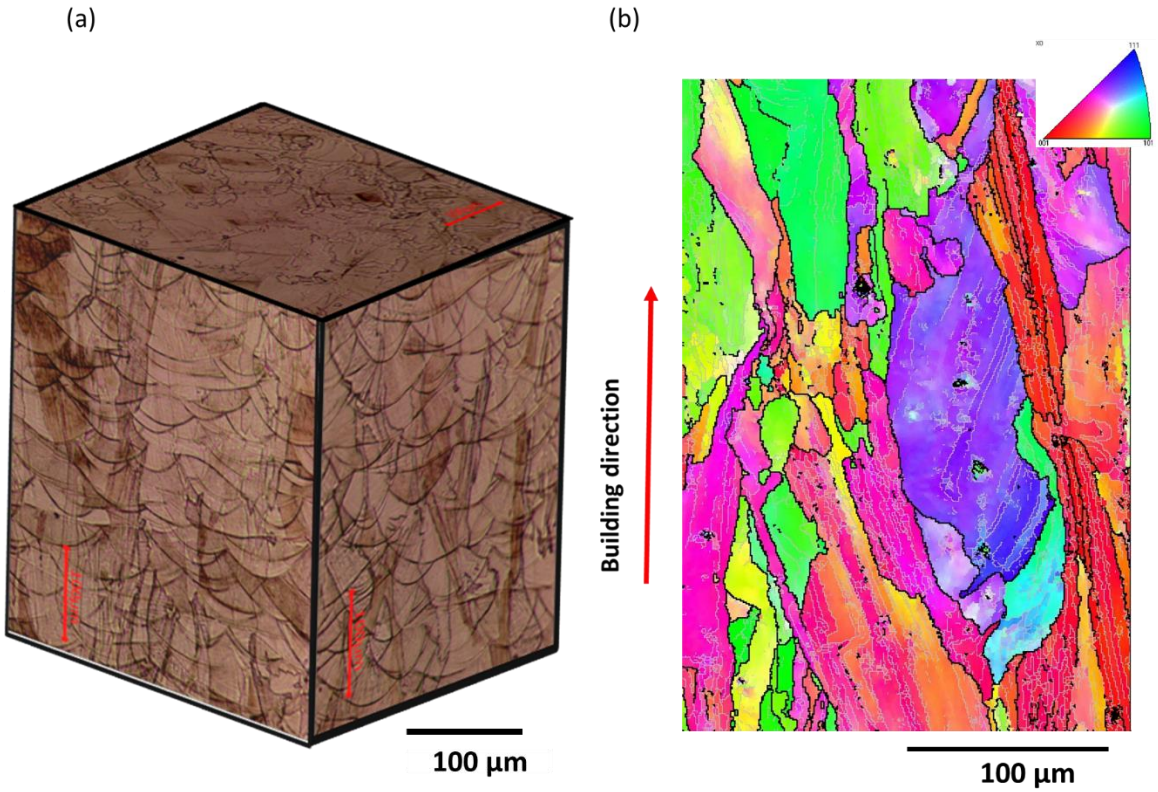


**Figure 13: a) The 3-D optical micrograph of as-built 316L stainless steel shows the laser tracks along the building direction, and b) shows the cellular microstructure within the irregularly shaped grains, as indicated by the faint gray low angle boundaries.**

EBSD analysis confirms the presence of coarse grains of up to 200 µm along the building direction, as shown in Figure 13(b). No melt pool boundaries are noticeable in the orientation image maps, which confirms the epitaxial nature of resolidification. The dark black line in Figure 13(b) outlines the grain boundary (misorientation angle is greater than 15°). The gradient in color inside these coarse grains suggests the presence of significant dislocation substructure.

Closer SEM inspection of the microstructure reveals the formation of cellular dendritic solidification microstructure inside the grain, as shown in Figure 14.

Figure 14(a) shows the cellular-dendrite structure with varying morphology and growth direction inside the laser track (marked by red outlines) due to the variation in local solidification condition. AM is a dynamic process because the heat source is continuously moving. As the laser beam moves away, the maximum temperature gradients change direction. The growing columnar crystals seek to follow the maximum temperature gradients while maintaining their preferred growth direction, <100>. The morphological difference in cell structures depends on their growth direction with respect to metallographic section. A higher magnification image reveals that the cross-sectional dimensions of the elongated intergranular cells are about 0.5- 1 μm, as shown in Figure 14(b). Colonies of these cells have the same crystallographic orientation and belong to the same coarse grain, as revealed by the EBSD analysis. Prior studies [8, 13] have shown Mo enrichment at the cell boundaries using transmission electron microscopy (TEM).

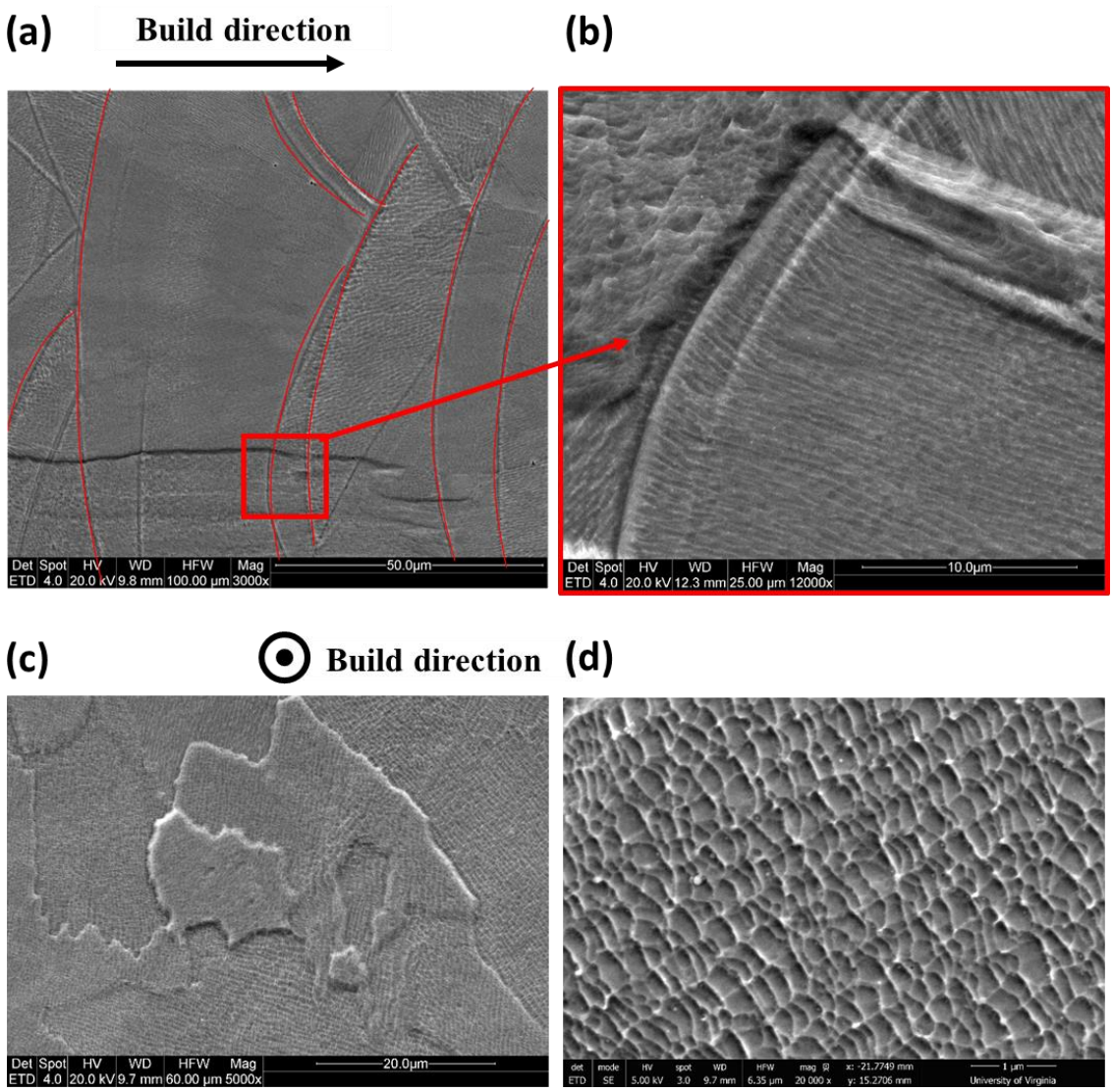


**Figure 14: SEM micrographs of the a, b) front views and c, d) top views of the as-built samples. The red solid lines outline the melt pool boundaries.**

Due to the preferred growth direction, the AM built part usually exhibit a so-called "growth texture," i.e., <100> direction is parallel to build direction [39]. Figure 15 (a) shows the (100) pole figure of as-built 316L stainless steel, where BD is at the center of the pole figure and TD of the sample is vertical. The observed texture is distinct from that published or other AM processes. There is a <100> fiber tilted ~15° away from the BD, with a peak intensity of 2.8

times random, and there is another <100> || TD texture component. The inverse pole figures (IPFs) show that the <100> intensity is stronger along the TD than the BD, as shown in Figure 15 (b) and Figure 15 (c), respectively. The type and strength of the texture developed during AM largely depend on the scanning strategy [23, 39] . The bidirectional scanning strategy used in this study changes the heat flow direction between layers, which inhibits the growth of very large columnar grains. This is why the observed texture is not very strong.

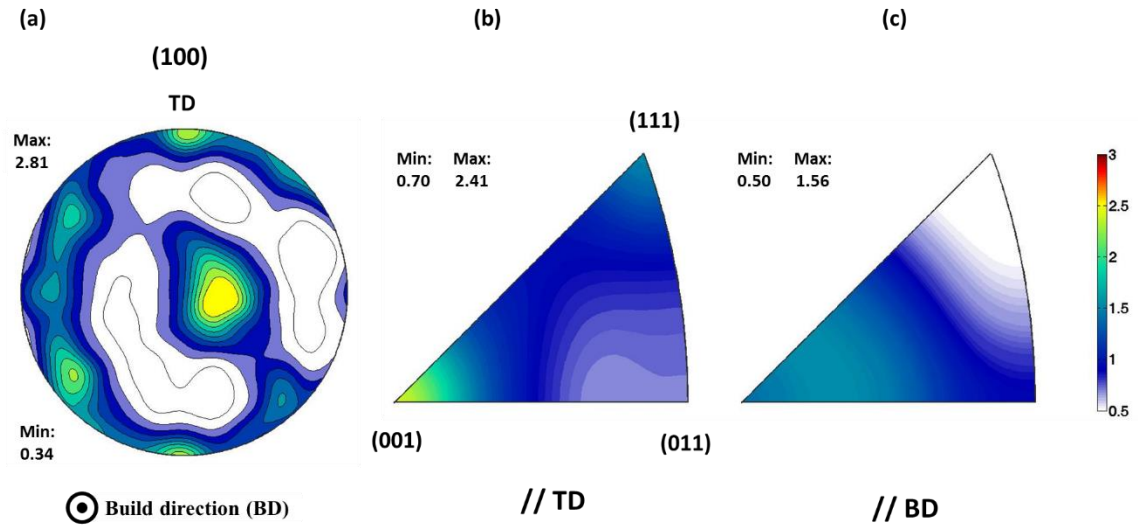


**Figure 15: Figure shows the macrotexture a) (100) pole and b, c) IPF parallel to TD and BD obtained from the XRD measurement of as-built sample.**

Figure 16 shows the microstructures of the samples annealed at 1100°C for a, b) one hour (denoted HT1) and c, d) 13 hours. After annealing for one hour, the laser tracks and cellular dendritic structures are no longer apparent (see Figure 16(b)). The EBSD analysis also reveals that there is still misorientation present inside these large grains, which suggests that recrystallization is not complete. However, the average misorientation inside the grains is

smaller relative to the as-built samples, an indication that dislocation recovery processes have occurred. Furthermore, a few misorientation-free small grains were also observed, indicating partial recrystallization has occurred. The macrotexture of the one-hour annealed (HT1) samples show no significant change. It still shows the near <100> fiber texture, where (100) pole is about ~15° tilted with respect to the building direction (see Figure 17), which is another indication that little recrystallization has occurred. This is consistent with the observation made by Sistiaga *et al*. [38]. Evidence of recrystallization and grain growth was observed after annealing for 13 hours, as is shown in Figure 16 (c, d). Note the presence of larger, more equiaxed grains and twin boundaries, Σ3 (60° about <111>), indicated in red, which highlight the formation of annealing twins after the 13-hour anneal.

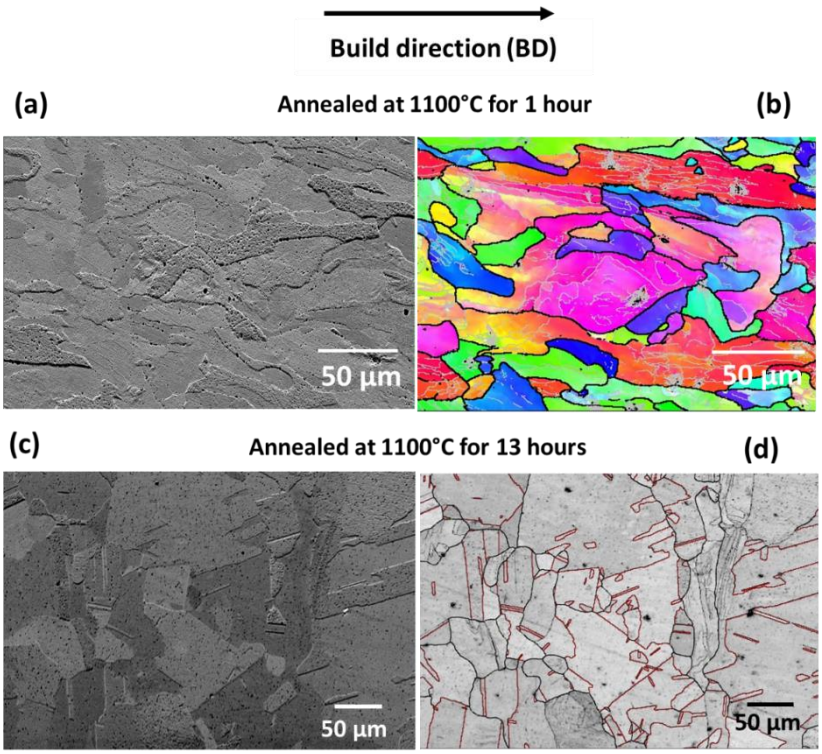


**Figure 16: Microstructure of heat-treated AM parts annealed at 1100°C for a, b) one hour and c, d) 13 hours.**

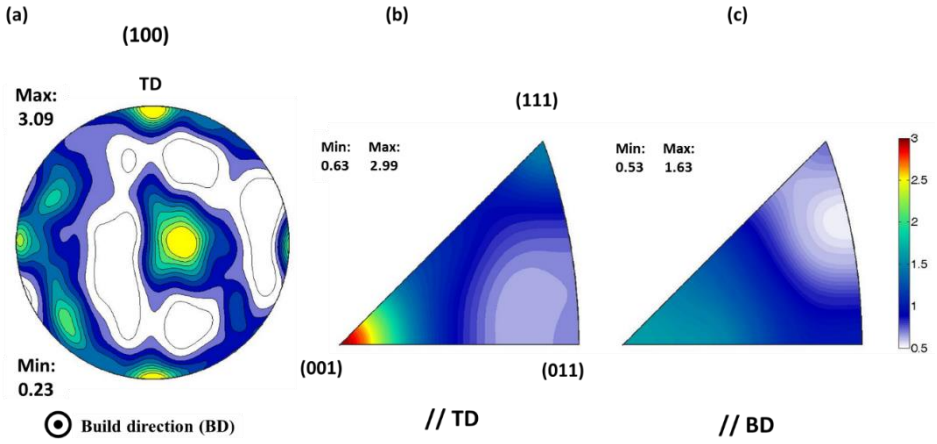


**Figure 17: Figure shows the macrotexture a) (100) pole and b) IPF parallel to TD and BD obtained from the XRD measurement of the samples annealed at 1100°C for one hour.**

### 3.3 Dislocation density

Figure 18 shows the mWH plot of the as-built and HT1 samples, in which the FWHM of each peak is peak is plotted as a function of $K^2C$, where $K = \frac{2sin\theta}{\lambda}$ and C is the average contrast factor. Namely, the FWHM is plotted as $\Delta K = \Delta\theta \frac{2cos\theta}{\lambda}$, where $\Delta\theta$ is the FWHM of the diffraction peak. As it can be seen from the equation [1], the mWH plot gives two important microstructural parameters. The slope $\left(\pi \frac{M^2 b^2}{2} \rho\right)$ is related to the microstrain and dislocation density, whereas the intercept of the line ($\left(\frac{0.9}{D}\right)^2$) provides the size of the coherent scattering domain (*D*). The larger slope and intercept of the as-built samples indicates that these samples have higher microstrain owing to higher dislocation density and smaller sub-grain (coherent scattering domain) size relative to the annealed samples, as listed in 2. It should be noted here that the dislocation density present in the samples annealed at 1100°C for 13 hours is below the detection limit of XRD-based line broadening analysis.

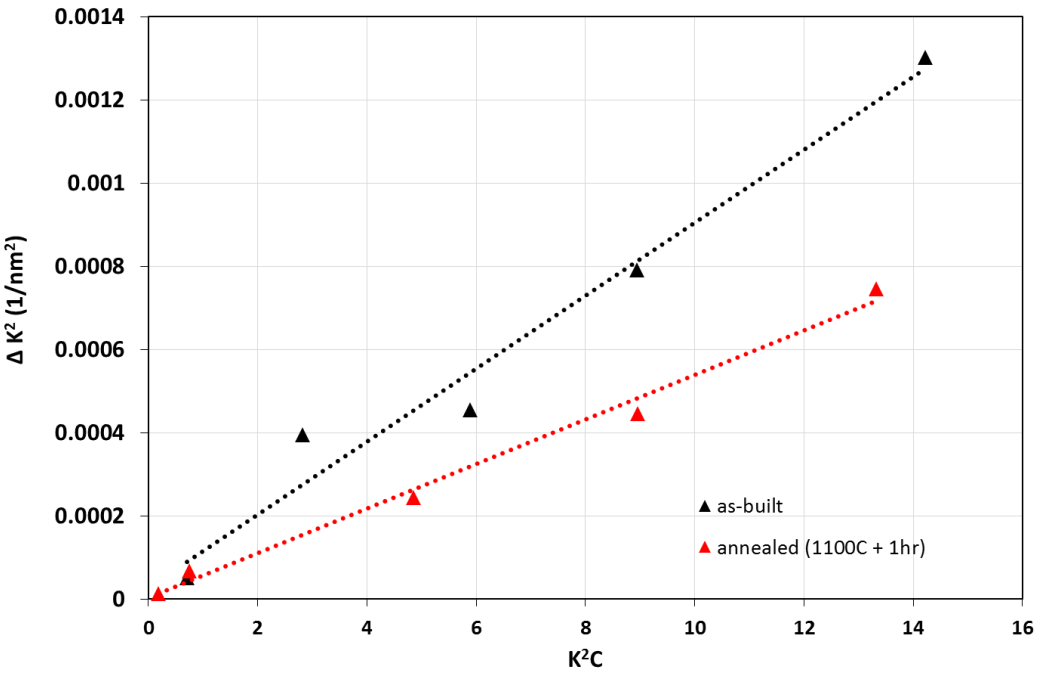


**Figure 18: Modified Williamson-Hall plot of an as-built sample as well as a sample annealed at 1100 °C for one hour. The FWHM of each peak plotted as a function of $K^2C$ shows a higher dislocation density in the as-built material.**

The line broadening analysis performed using the CMWP procedure is shown in Figure 19 for HT1 sample. The green and red lines show the measured and fitted data, respectively, with the residual shown at the bottom of the figure.

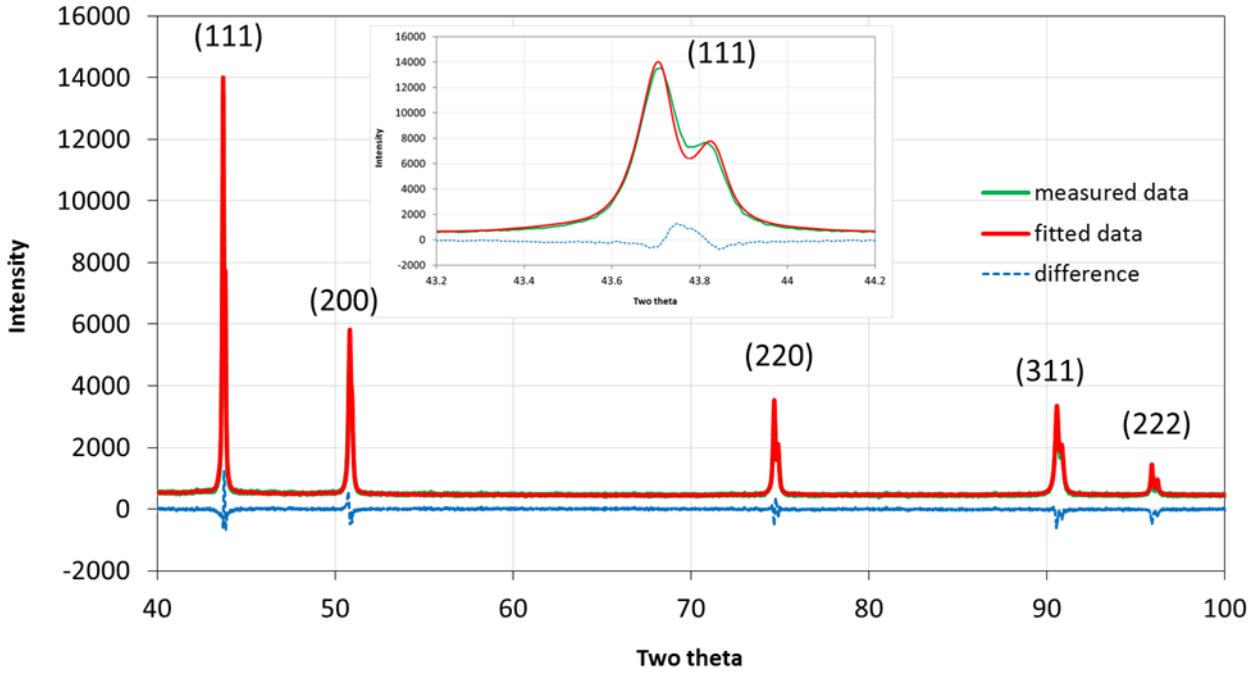


**Figure 19: The measured and fitted diffraction pattern obtained using CMWP of the as-built samples. The magnified view of the (111) peak shows a good matching between the measured and simulated profile.**

As it can be seen from the inset (magnified (111) peaks), a good fit is obtained. The area-weighted mean sub-grain size ($\langle X \rangle_{area} = m \exp(2.5\sigma^2)$, where $m$ is the median and $\sigma^2$ is the log-normal variance of the crystalline size) and dislocation density ($\rho$) are the two microstructural parameters obtained from the CMWP procedures and values are listed in Table 2.

**Table 3: Sub-grain size and dislocation density estimated from the modified Williamson-Hall (mWH) and CMWP methods, along with the geometrically necessary dislocation (GND) density estimated using the Kernel Averaged Misorientation (KAM) data obtained using EBSD.**

| Specimen | Sub-grain size (nm), mWH | Microstrain, mWH | Sub-grain size (nm), CMWP | Dislocation density ($10^{14}$ $m^{-2}$), CMWP | Parameter (M), CMWP | GND density ($10^{14}$ $m^{-2}$) |
|---|---|---|---|---|---|---|
| As-built | 180 | 90 | 190 ± 28 | 11.8 ± 1.1 | 0.17 ± 0.03 | 5.3 |
| HT1 | 500 | 50 | 296 ± 80 | 2.40 ± 0.19 | 0.56 ± 0.12 | 2.2 |

Similar to the mWH method, a higher dislocation density and smaller sub-grain size was observed for as-built samples relative to HT1 sample. As Table 2 indicates, the dislocation density of (1.18 ± 0.11) × $10^{15}$ $m^{-2}$ of as-built materials decreased to (2.4 ± 0.2) × $10^{14}$ $m^{-2}$, and the sub-grain size of 190 ± 28 nm increased to 296 ± 80nm after annealing heat treatment for one hour. The dislocation arrangement can be inferred from the parameter *M*. Both as-built and annealed material show $M < 1$, i.e., *M* is 0.17 ± 0.03 and 0.56 ± 0.12, respectively, indicating that the dislocations are arranged into low energy dislocation structures (LEDS). The high dislocation density of the as-built materials correlates well with microstructural observations of other researchers, who reported that a high concentration of dislocations exists at the cellular-dendritic boundaries [14, 37, 40, 41]. That short-term annealing results in a reduction in dislocation density without changing the sub-grain structure at the micron scale were also reported by Saeidi *et al.* [37]. As usual, use of the coherent scattering domain-size determined using line broadening techniques as a proxy for the average sub-grain size yields a somewhat

lower value than the sub-grain size observed in the SEM and EBSD images (see Figure 14). (In short, though the two quantities are related, they are not the same thing.)

In order to complement XRD-based dislocation density calculation, the geometrically necessary dislocations (GND) density also studied from the EBSD analysis using the KAM method. By this approach, the dislocation density can be estimated from the following formula [42]:

$$\rho_{GND} \cong \frac{2\,\theta_{KAM}}{bd} \qquad [3]$$

where *b* is the Burgers vector magnitude (0.255 nm for FCC iron) and *d* is the step size. Figure 20 shows the KAM maps for as-built and HT1 samples. A significant increase in sub-grain size (or decrease in the density of sub-grain boundaries) can be visually observed, in the KAM maps obtained from the HT1, which lends support to the notion that smaller sub-grains merge into larger sub-grains within the bigger grain [43]. Table 2 presents the GND density of as-built and HT1 samples calculated from the equation [3] revealing a 58% reduction in GND density. Comparing the estimated GND values with total dislocation density calculated from XRD line profile analysis, which accounts for both GND's and statistically stored dislocations, it appears that GNDs account for about 50% and 90% of the total dislocation density of as-built and HT1 samples, respectively.

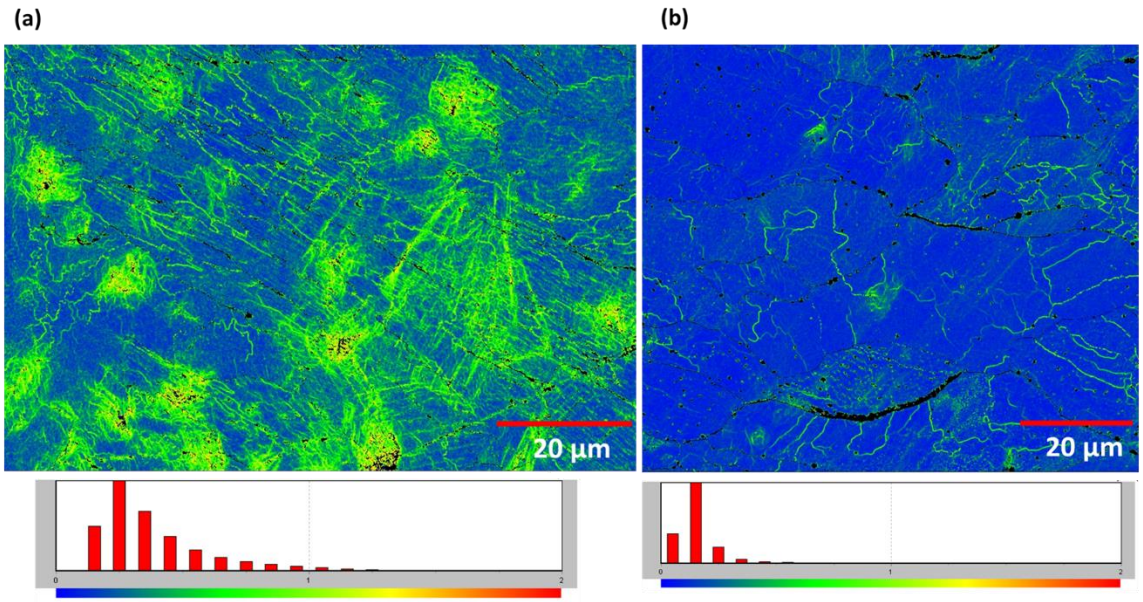


**Figure 20: Kernel average misorientation map of a) AS-built and b) HT1 samples**

### 3.4 Mechanical properties and deformation behavior

Figure 21 shows representative a) engineering stress-strain and b) true stress-strain of the both AS-built and HT1 samples tested along the build direction (vertical built) and the scanning direction (horizontal built), and the respective work hardening rates ($\theta = \frac{d\sigma}{d\varepsilon}$) as a function of true strain are shown in Figure 21. Eight vertical and four horizontal as-built samples were tested during this study, and the single curve presented should be taken as representative of those multiple tests. However, only one vertical and one horizontal sample from the HT1 material was tested. Average tensile properties such as yield strength, ultimate tensile strength, uniform strain, and strain to failure were calculated from these plots are listed in Table 3, along with the Vickers microhardness and the properties of an as-cast 316L stainless, obtained from reference [7]. Each as-built sample condition exhibited low scatter in the mechanical

properties, as shown by the small standard deviation listed in Table 3. This indicates that the processing conditions adopted in this study are capable of producing 316L stainless with highly reproducible properties.

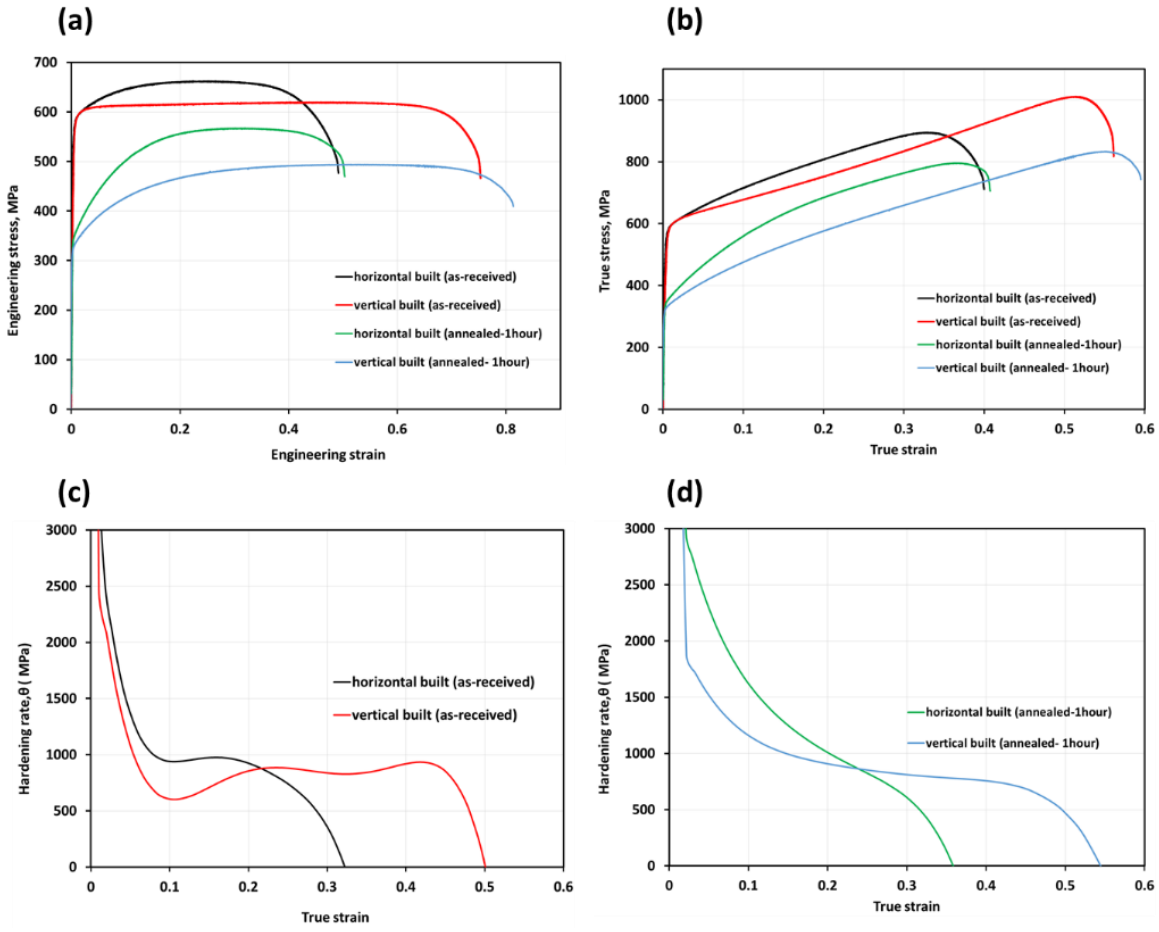


**Figure 21: Representative a) engineering stress-strain, and b) true stress-strain plot of the as-built and one-hour annealed samples. c, d) show the work hardening rate (θ)-true strain plot of the as-built and one-hour annealed samples, respectively.**

**Table 4: Mechanical properties, e.g., yield strength, ultimate tensile strength, total elongation, uniform elongation and microhardness, of the investigated as-built and one-hour annealed materials are listed. For comparison, mechanical properties of an as-cast reference material are also listed.**

| Samples | Yield strength (MPa) | Ultimate tensile strength (MPa) | Engineering strain to failure | Uniform true strain | Uniform true strain (Considère analysis) | Vickers microhardness |
|---|---|---|---|---|---|---|
| As-built (horizontal) | 584±11 | 667±15 | 0.49±0.03 | 0.23±.03 | 0.22 | 199 |
| As-built (vertical) | 588±20 | 622±27 | 0.77±0.03 | 0.37±0.02 | 0.41 | |
| Annealed 1hour (horizontal) | 339 | 568 | 0.50 | 0.29 | 0.28 | 184 |
| Annealed 1hour (vertical) | 322 | 495 | 0.81 | 0.43 | 0.42 | |
| As-cast [7] | 200 | 450 | 0.45 | | | 165 |

As-built samples have higher hardness, strength, and ductility relative to the as-cast 316L stainless steel. Both horizontal (HB) and vertical (VB) as-built samples show a similar yield strength. However, the HB samples show a higher tensile strength and lower ductility (49%) relative to VB samples. The high hardness and strength of the AS-built materials are in good agreement with the result reported in [7, 8, 15, 17, 20]. However, the ductility of AM 316L observed presently is significantly higher than the reference [7] as-cast material as well as that reported in other studies of AM material, with the exception of reference [20], in which they

also reported 70% elongation at failure for the vertical build samples. However, no explanation for this high ductility was provided. Annealing heat treatment at 1100°C for one hour reduced the hardness value of as-built samples by only about 8%. A more significant reduction (23%) in hardness value was observed for samples annealed for 13 hours (HT13) in which recrystallization is observed to have made significantly greater progress. HT1 samples show a significant decrease in yield and tensile strength, but the strain hardening behavior and ductility remain largely unchanged.

In addition to the difference in tensile strength and ductility, the vertical and horizontal samples show a distinct work hardening behavior ($\theta\ vs\ \varepsilon$) (see Figure 21(c)). The $\theta\ vs\ \varepsilon$ plot of the HB samples can be characterized by three distinct stages. Stage-I ($(\varepsilon < 0.09)$, a sharp decrease in θ value was observed, typical of materials in which the plastic deformation proceeds by slip. With an increasing strain, a nearly constant θ value (linear hardening) was observed up to a strain level of 0.17 (Stage-II) followed by a final decrease in hardening rate (Stage-III).

This multistage behavior is typical of materials that exhibit deformation twinning-induced plasticity (i.e., the TWIP effect). Indeed, $\theta\ vs\ \varepsilon$ plot of the vertical samples show the typical hardening behavior observed in the twin-induced plasticity (TWIP) steel [44-46] and can also be characterized by three distinct stages. Stage-I of VB samples again shows a rapid decrease in the hardening rate up to a strain value of 0.09. Stage-II ($\varepsilon < 0.23$) shows a sharp abrupt increase of the θ value (i.e., primary twining stage). With progress in deformation (Stage-III), θ remains essentially constant in the strain range of 0.23 to 0.41. Above this strain level, the sample has undergone plastic instability. Therefore, the stress and strain levels reported at higher strains are

only approximate, and the intrinsic strain hardening response cannot be readily ascertained. Note that the onset of necking is well-predicted by the conventional plastic instability analysis based on Considère's criterion $\left(\frac{d\sigma}{d\varepsilon} = \sigma\right)$. Mechanistically, stages II and III are understood to result from the dynamic refinement of the microstructure by fine twins, which continually introduce new barriers to dislocation motion, as explained by Bouaziz *et al*. [46].

EBSD analysis of the sample deformed to a true strain value of 0.18 revealed deformation twins ({111} <112>) in both HB and VB samples (dark black features interior to grains in Figure 22). At this strain level, twins usually appear as bundles, and therefore, it was possible to index these nanoscale twins even with a relatively large step size of 0.4 µm. Figure 22 (a, b) shows the IPF for the crystal direction along the tensile loading direction (LD) for VB and HB samples, respectively. The deformation texture is characterized by a weak <111> || LD and a strong <100> ||LD fiber. This texture evolution is atypical of TWIP steel, which usually shows a strong <111> || LD and a weak <100> || LD [44].

Initial grain orientation has a strong effect on the activity of twinning. Deformation twinning mainly occurs in the grains that are closely orientated to the <111>||LD direction and only a small fraction of grains with other orientations contain twins. This is true for both VB and HB samples. Several authors employed Schmid's law to explain the dependence of twinning on crystal orientation [45, 48]. In a similar way, consideration of the Taylor factor values of the investigated grains of the HB and VB can be insightful (Figure 22 (c, d)). The grains with favorable orientation for twining (<111> || LD) have the highest Taylor factor (*M*) value of ~3.65. However, twining is also observed in the grains having a value of *M* as low as 3.06. On

the other hand, no twin activity was observed in the grains with a value of $M$ < 2.6 (<100> || LD).

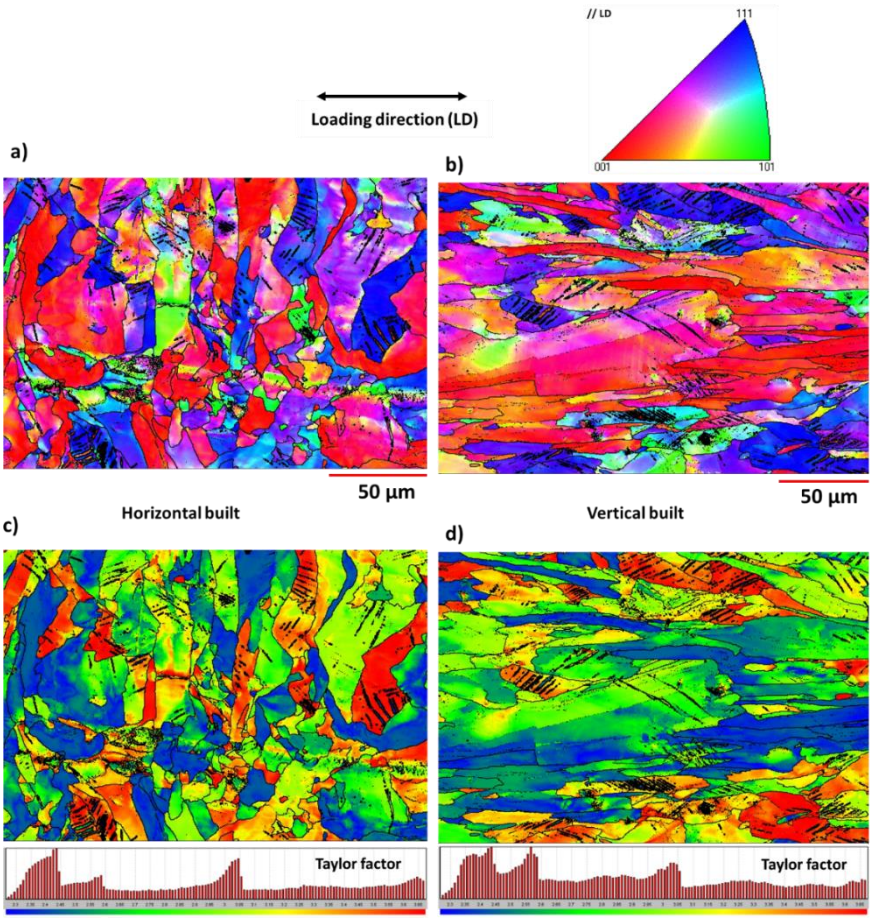


**Figure 22: a, b) LD-IPF maps and c, d) calculated Taylor factor of the horizontal and vertical built samples strained to 0.18 true strain. Loading direction is horizontal.**

The macrotexture obtained from X-ray diffraction measurement is consistent with the EBSD analysis. Figure 23 shows the inverse pole figures (IPFs) of HB and VB samples strained to different levels. After straining to $\varepsilon$ =0.18, HB samples show a relatively stronger <100>||LD fiber and weaker <111>||LD fiber. No significant strengthening in texture was observed beyond this strain level. Texture measurement of the HB samples strained at $\varepsilon$ =0.40 (true strain at

failure) exhibits a weaker <111>||LD and stronger <100>||LD fiber texture. On the other hand, the texture evolution of VB samples shows a distinct behavior. The initial texture does not show any preferred crystal orientation along the sample loading direction. The texture evolution up to $\varepsilon$ =0.18 is modest, only about two times random. However, samples deformed to $\varepsilon$ =0.57 (true strain at failure) show a stronger <111>||LD relative to <100>||LD fiber, which is typical for TWIP steel. Still, the texture evolution is rather weak (peak intensity of only 2.5 times random), which is also typical for TWIP steel [45, 46]. Based upon these observations, it appears that there was more twinning in the case of the VB sample than the HB sample.

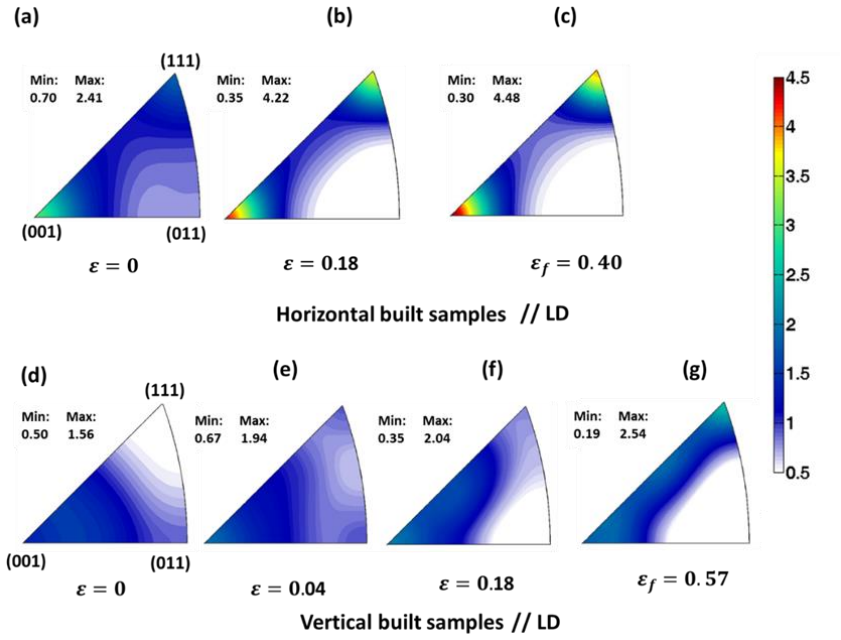


**Figure 23: Shows the IPFs parallel to tensile loading direction (LD) of initial (a), after deformed at $\varepsilon$ =0.18 (b), and $\varepsilon$ =0.40 (failed samples) (c) for horizontal built samples. IPF of Initial (d), after deformed at $\varepsilon$ =0.04 (e), $\varepsilon$ =0.18 (f) and $\varepsilon$ =0.57 (failed samples) (g) of VB samples are also shown.**

# 4 Discussion

## 4.1 Microstructure, dislocation density and thermal stability

The observed complex microstructure is rather typical of additive manufacturing. This is because the inherent high cooling rate of the AM process, where the material in the melt pool undergoes rapid solidification, at typical cooling rates in the range of $10^3$ to $10^8$ K/sec [7]. Evolution of cellular solidification morphology can be understood using classical solidification theory. According to this theory, the solute will pile up ahead of the interface owing to the smaller solubility in the solid when the equilibrium partition coefficient ($k^E$) is less than one. Under these so-called constitutional undercooling conditions, the stability of the planar interface will break down and a cellular structure will form. The interface stability theory proposed by Mullins and Sekerka [49] additionally takes capillarity effects into consideration and can explain the evolution of cellular substructure observed in AM parts. The perturbation tip radius ($R$) decreases with increasing solidification velocity. At very high growth velocity, as observed in AM process, the capillary force becomes important because of the smaller value of tip radius. The magnitude of the solute diffusion length in the interdendritic region and capillarity effects govern the formation of cellular structures during rapid solidification [50].

Rapid solidification also results in high dislocation density substructures [51]. However, the exact mechanism of dislocations generation during solidification is yet to be understood, though several mechanisms of dislocations formation have been proposed including the following [52]:

a) Steep solute concentration gradients at the cell boundary will result in coherency strains. In order to dissipate the associated strain energy, dislocations could be formed.

b) Very high thermal stresses could nucleate and drive dislocation motion, again, in order to dissipate strain energy.

c) Quenched-in clusters of vacancies could form prismatic dislocation loops.

d) The misorientation of the neighboring cells could result in interfacial dislocations upon collision of the cells.

Saeidi *et al.* [37] qualitatively revealed a high density of dislocations at the cell boundaries in SLM 316L stainless steel. Similar qualitative observations also reported for other AM-built materials [8, 14, 41, 53, 54]. The present quantitative investigation using XRD-based line profile analysis revealed a dislocation density on the order of ~$10^{15}m^{-2}$. This dislocation density is typical of 20% cold work austenitic stainless steel [55]. However, SLM-built materials are in a lower energy state compared to cold work material due to the low energy configuration of the dislocations in the former, as indicated by a low value of dislocations arrangement parameter ($M$ < 1) in line broadening analysis. LEDS based on TEM analysis have also been reported [8, 14]. Owing to this relatively low stored energy in the material, the present AM-built materials are thermally stable up to a very high temperature. Annealing of the AM samples at a very high temperature of 1100°C for one hour was insufficient to drive complete recrystallization or grain coarsening (see Figure 16). For comparison, note that Herrera *et al*. [56] reported recrystallization in cold-rolled 316L stainless steel T ~600°C after one hour.

### 4.2 Higher yield strength

It is already well accepted that the higher yield strength of the AM-built material relative to conventional as-cast materials is the consequence of the refined microstructure and high density of dislocations resulting from the rapid solidification. Several researchers have invoked the Hall-Petch relation, i.e., the macroscopic yield strength is inversely proportional to square root of grain size ($D^{-1/2}$), to account for the cell size effects on the yield strength [13, 40, 57]. However, for materials with well-defined dislocation cell structures as observed in AM materials, it has long been known that the macroscopic yield strength depends on the inverse of the dislocation cell size ($d^{-1}$) [58–60]. Furthermore, the cell size ($d$) can be related to dislocation density ($\rho$) by the following equation [59]:

$$d = K\rho^{-\frac{1}{2}} \quad [4]$$

where $K$ is an arbitrary constant. Therefore, the higher yield strength of AM-built materials should be correlated with the dislocation density. According to Taylor's equation, the yield strength can be expressed as:

$$\sigma_y = \sigma_0 + M\alpha Gb\sqrt{\rho} \quad [5]$$

Where $\sigma_0$ is the friction stress, $M$ is the Taylor factor, $\alpha$ is the proportionality constant, $G$ is the shear modulus (77 GPa for 316 stainless steel), $b$ is the Burger's vector of dislocations, and $\rho$ is the dislocation density. The value of constant $\alpha$ depends on the type, density, and interaction of dislocations at different strain levels [61, 62]. Here, a value of 0.26 ± 0.015 for $\alpha$, obtained from references [63–65], was used. These authors empirically assessed the value of $\alpha$ for high manganese and 304L stainless steels, which show similar TWIP behavior as the material being

studied. Several authors have investigated the grain size effects on the yield strength, i.e., the Hall-Petch relationship, of 316L stainless and reported friction stress to be 100 ± 20 MPa [62, 66]. This high value of friction stress corresponds to the high concentration of solute in the iron matrix.

On the other hand, the Taylor factor value of polycrystalline material depends on texture. Here, the viscoplastic self-consistent (VPSC) model [67] was used to calculate the an effective value of *M* for both the HB and VB samples in as-built and annealed conditions. The material was idealized as 1000 discrete "grain" features with orientations and volume fractions selected to match the texture. Details of the Taylor factor calculation from the initial texture can be found in reference [68]. The initial value of *M* for the HB and VB samples was calculated to be 2.6 for both the as-built and annealed conditions, which is consistent with the observed isotropy in yield strength.

Table 4 shows the comparison between calculated and experimentally measured yield strength. The calculated yield strength of as-built and annealed samples shows a good agreement with the experimentally measured yield strength. It should be noted here that the yield strength uncertainties in each sample were calculated by considering the error propagation from uncertainties in the Taylor's equation resulting from uncertainties in $\sigma_0$, $\alpha$ and dislocation density ($\rho$).

**Table 5: Comparison between yield strength calculated using Taylor's equation (complete with uncertainty propagation) and experimentally measured values.**

| Samples | α | Taylor factor, M | Dislocation density, $\rho$ ($m^{-2}$) | Yield strength, MPa (predicted) | Yield strength, MPa (experimental) |
|---|---|---|---|---|---|
| As-built (horizontal) | 0.26 ± 0.015 | 2.6 | $11.8 \pm 1.1 \times 10^{14}$ | 573±35 | 584±11 |
| As-built (vertical) | | | | | 588±20 |
| Annealed 1hour (horizontal) | | | $(2.40 \pm 0.19) \times 10^{14}$ | 313±15 | 339 |
| Annealed 1hour (vertical) | | | | | 322 |

### 4.3 Deformation behavior and higher ductility

Austenitic stainless steels deform either by dislocation slip, mechanical twining and/or martensitic transformation. Often, these deformation mechanisms co-exist [69]. The stacking fault energy (SFE) of the material, which depends on the chemical composition, is a controlling factor in determining which mechanism(s) will be operative. Frommeyer *et al.* [70] suggested that at the SFE lower than the 16 mJ/m$^2$ martensitic transformation ($\gamma$ *to* $\varepsilon$) dominates, while twinning occurs for SFE higher than 25 mJ/m$^2$. Based on the empirical relationship proposed by Pickering *et al*. [71], and the alloy chemistry listed in Table 1, the SFE value of 316L stainless is estimated to be 32 mJ/m$^2$, suggesting that twinning will be favored over martensitic transformation. The analysis of the deformed samples at different strain level using EBSD at $\varepsilon =$

$0.18$ (see Figure 22) and XRD at $\varepsilon = 0.05, 0.18, \varepsilon_f$ (not shown in the interest of space, though the data appears so in Figure 2) confirms the absence of martensitic phase.

Twinning activity is one of the main factors contributing to the high ductility of AM built materials, particularly for the VB samples. Twin boundaries, similar to the grain boundaries, act as obstacles to dislocation movement. As twins are introduced, they decrease the mean free path of the dislocations on the slip planes intersecting the twinning planes. This dynamic refinement of the microstructure enhances the work hardening behavior of the material during plastic deformation, which in turn delays the onset of plastic instability.

**4.4 Texture evolution and anisotropic behavior**

Considering the presence of a very low density of porosity, or lack of fusion defects in the material being studied (density > 99%), it is suggested that variation in texture is responsible for the observed anisotropic mechanical behavior. FCC polycrystals with high stacking fault energy develop a pronounced <111> ||LD fiber texture during straining [72]. However, low SFE FCC materials deformed by mechanical twinning result in a <100>||LD fiber. The initial grain size and grain orientation have strong effects on twin formation and twin activity. In general, <111>||LD oriented grains favor twinning due to their high Taylor factor. Formation of twins within <111>||LD grains reinforce the <100>||LD fiber. A limited number of twins form within the <100>||LD orientation reinforce the <111>||LD fiber. Crystallographic texture analysis of

as-built samples (see Figure 23) shows a preferred orientation of (100) grains along TD (see Figure 15). The texture evolution observed during loading along the TD direction, i.e., horizontal built samples is indicative of primarily slip-based strain accommodation. On the other hand, no preferred orientation was observed along the built direction (Figures 7 and 13). At low strain level of $\varepsilon$ =0.04, a <100>||LD fiber is beginning to developed. No significant intensification was observed of this fiber was observed at the strain level of $\varepsilon$ =0.18, i.e., no <111>||LD was observed even at this intermediate level of strain. This indicates a higher activity of twining for VB material. The reinforcement of <111>||LD fiber only observed for samples strained at $\varepsilon$ =0.57. Depending on initial texture, twinning and slip appear to have been activated to different. Future work will seek to quantify the relative contributions of the slip and twinning modes.

## 5 Conclusions

The microstructure and mechanical properties of an additively manufactured (AM) 316L stainless steel were investigated. The following conclusions can be drawn from this study:

a) AM of 316L stainless steel results in a single-phase, austenitic microstructure that remains stable during tensile deformation, i.e., no stress-induced martensitic phase transformation was observed.

b) An elongated, cellular microstructure resulting from the AM process is characterized by walls of high dislocation density $1.2 \times 10^{15}\ \mathrm{m}^{-2}$ measured by XRD line profile, which is consistent with EBSD-based estimates of the geometrically necessary dislocation density.

c) The observed high dislocation density is shown to be responsible for the relatively high yield strength (~588 MPa) of the as-built AM material.

d) Preferred growth during the solidification process and bi-directional laser scan pattern results in a relatively weak texture with <100>||transverse direction and <010> inclined ~15° from the build direction.

e) Although the yield strength is relatively isotropic, the initial texture contributes to anisotropic strain hardening and ductility (49% and 77% elongations observed for horizontal (HB) and vertical build (VB) samples, respectively).

f) EBSD analysis confirms the formation of twins during tensile deformation. Previous research has shown that twinning results in a dynamic Hall-Petch relationship, which contributes significantly to strain hardening. The texture evolutions for the tensile-deformed HB and VB samples indicate a higher degree of twinning activity in the VB samples, consistent with the observed higher resistance to plastic instability (and hence enhanced ductility) in those samples. Annealing at 1100°C reveals that AM-316L stainless steel is thermally stable, shows only moderate decrease in dislocation density and strength, and displays very similar strain hardening response, level of ductility and anisotropy as compared to the as-built condition.

**Acknowledgements:**

The authors acknowledge and thank the Naval Sea Systems Command and the Office of Naval Research for sponsoring the research discussed in this paper. The work was mentored by Naval

Surface Warfare Center, Dahlgren Division, as a project through the Naval Engineering Education Consortium Program.

## References

[1] N. Shamsaei, A. Yadollahi, L. Bian, and S. Thompson : *Addit. Manuf.*, 2015, vol. 8, pp. 12-35.

[2] J. P. Kruth, P. Mercelis, J. Van Vaerenbergh, L. Froyen, and M. Rombouts: *Rap. Prototyp. J.,* 2005, vol. 11, pp. 26-36.

[3] Q. Jia and D. Gu: *J. Alloys Compd.*, 2014, vol. 585, pp. 713–721.

[4] J. A. Cherry, H. M. Davies, S. Mehmood, N. P. Lavery, S. G. R. Brown, and J. Sienz: *Int. J. Adv. Manuf. Technol.*, 2015, vol. 76, pp. 869–879.

[5] L. Thijs, K. Kempen, J. Kruth, and J. Van Humbeeck: *Acta Mater.*, 2013, vol. 61, pp. 1809-1819.

[6] Harry Bhadeshia and Robert Honeycombe: *Steels: microstructure and properties*, 4th ed., Cambridge, MA : Butterworth-Heinemann, and imprint of Elsevier, 2017, p. 488.

[7] F. Bartolomeu, M. Buciumeanu, E. Pinto, N. Alves, O. Carvalho, F.S. Silva, and G. Miranda: *Addit. Manuf.*, 2017, vol. 16, pp. 81-89.

[8] K. Saeidi, X. Gao, Y. Zhong, and Z. J. Shen: *Mater. Sci. Eng. A*, 2015, vol. 625, pp. 221–229.

[9] R. Li, Y. Shi, Z. Wang, L. Wang, J. Liu, and W. Jiang: *Appl. Surf. Sci.*, 2010, vol. 256, pp.

4350-4356.

[10] S. Dadbakhsh, L. Hao, and N. Sewell: *Rapid Prototyp. J.*, 2012, vol. 18, no. 3, pp. 241–249.

[11] B. Zhang, L. Dembinski, and C. Coddet: *Mater. Sci. Eng. A*, 2013, vol. 584, pp. 21–31.

[12] D. Wang, C. Song, Y. Yang, and Y. Bai: *Mater. Des.*, 2016, vol. 100, pp. 291–299.

[13] Y. Zhong, L. Liu, S. Wikman, D. Cui, and Z. Shen: *J. Nucl. Mater.*, 2016, pp. 170-178.

[14] Z. Sun, X. Tan, S. Tor, and W. Yeong: *Mater. Des.*, 2016, vol. 104, pp. 197-204.

[15] J. Suryawanshi, K. Prashanth, and U. Ramamurty: *Mater. Sci. Eng. A*, 2017, vol. 696, pp. 113-121.

[16] C. Haase, J. Bültmann, J. Hof, S. Ziegler, S. Bremen, C. Hinke, A. Schwedt, U. Prahl, and W. Bleck: *Materials*, 2017, vol. 10, p. 56.

[17] A. Röttger, K. Geenen, M. Windmann, F. Binner, and W. Theisen: *Mater. Sci. Eng. A*, 2016, vol. 678, pp. 365-376.

[18] W. Shifeng, L. Shuai, W. Qingsong, C. Yan, Z. Sheng, and S. Yusheng: *J. Mater. Process. Technol.*, 2014, vol. 214, pp. 2660–2667.

[19] H. D. Carlton, A. Haboub, G. F. Gallegos, D. Y. Parkinson, and A. A. MacDowell: *Mater. Sci. Eng. A*, 2016, vol. 651, pp. 406–414.

[20] E. Liverani, S. Toschi, L. Ceschini, and A. Fortunato, “,” *J. Mater. Process.Tech.*, 2017, vol. 249, pp. 255-263.

[21] D. Tomus, Y. Tian, P. Rometsch, M. Heilmaier, M. Heilmaier and X. Wu: *Mater. Sci. Eng. A*, 2016, vol. 667, pp. 42-53.

[22] I. Tolosa, F. Garciandía, F. Zubiri, and F. Zapirain: *Int. J.Adv. Manu. Tech.,* 2010, vol. 51, pp. 639-647.

[23] X. Zhou, K. Li, D. Zhang, X. Liu, J. Ma, W. Liu, and Z. Shen: *J. Alloys Compd.*, 2015, vol. 631, pp. 153–164.

[24] EOS GmbH. EOS Stainless Steel 316L material data sheet. [Online] [Cited: August 21, 2017.] https://cdn1.scrvt.com/eos/77d285f20ed6ae89/dd6850c010d3/EOSStainlessSteel316L.pdf.

[25] ASTM E8/E8M-16a: *Standard Test Methods for Tension Testing of Metallic Materials. West Conshohocken, Pennsylvania : American Society for Testing and Materials, 2016.*

[26] ASTM E1019-11: Standard Test Methods for Determination of Carbon, Sulfur, Nitrogen, and Oxygen in Steel, Iron, Nickel, and Cobalt Alloys by Various Combustion and Fusion Techniques. West Conshohocken, Pennsylvania : American Society for Testing and Materi.

[27] D. Black, D. Windover, A. Henins, D. Gil, J. Filliben, and J.P. Cline : *Adv. X-ray Anal.*, 2009, vol. 53, pp. 172-179.

[28] T. Ungár and A. Borbély: *Appl. Phys. Lett.*, 1996, vol. 69, pp. 3173–3175.

[29] G. Ribárik, J. Gubicza, and T. Ungár: *Mater. Sci. Eng. A*, 2004, vol. 387, pp. 343-347.

[30] G. Ribárik, T. Ungár and J. Gubicza: *J. Appl. Crystallogr.*, 2001, vol. 34, pp. 669–676.

[31] M. El-Tahawy, Y. Huang, T. Um, H. Choe, J. Lábár, T.G. Langdon and J. Gubicza: *J. Mater. Res. Technol.*, 2017 (In Press).

[32] M. Mangalick and N. Fiore, *Trans Metall. Soc. AIME*, 1968, vol. 242, p. 2363.

[33] A. Borbély, J. Dragomir-Cernatescu, G. Ribárik and T. Ungár: *J. Appl.Crystallogr.*, 2003, vol. 36, pp. 160-162.

[34] T. LeBrun, T. Nakamoto, K. Horikawa, and H. Kobayashi, "*Mater. Des.*, 2015, vol. 81, pp. 44-53.

[35] L.E. Murr, E. Martinez, J. Hernandez, S. Collins, K.N. Amato, S.M. Gaytan and P.W. Shindo: *J. Mater. Res. Technol.*, 2012, vol. 1, pp. 167–177.

[36] L. Facchini, N. Vicente Jr., I. Lonardelli, E. Magalini, P. Robotti, and A. Molinari: *Adv. Eng. Mater.,* 2010, vol. 12, pp. 184-188.

[37] K. Saeidi, X. Gao, F. Lofaj, L. Kvetková, and Z. J. Shen: *Alloys Compd.*, 2015, vol. 633, pp. 463–469.

[38] M. L. . Sistiaga, S. Nardone, C. Hautfenne, and J. Van Humbeeck: *Annual International Solid Freeform Fabrication Symposium,* 2016, pp. 558–565, Austin, TX, USA.

[39] F. Geiger, K. Kunze, and T. Etter: *Mater. Sci. Eng. A*, 2016, vol. 661, pp. 240-246.

[40] D. Zhang, W. Niu, X. Cao, and Z. Liu: *Mater. Sci. Eng. A*, 2015, vol. 644, pp. 32–40.

[41] W.M. Tucho, P. Cuvillier, A. Sjolyst-Kverneland, and V. Hansen: *Mater. Sci. Eng. A*, 2017, vol. 689, pp. 220–232.

[42] M. Calcagnotto, D. Ponge, E. Demir, and D. Raabe: *Mater. Sci. Eng. A*, 2010, vol. 527, pp. 2738–2746.

[43] J.C. Li: *J. Appl. Phys.*, 1962, vol. 33, pp. 2958-2965.

[44] I. Gutierrez-Urrutia and D. Raabe: *Acta Mater.*, 2011, vol. 59, pp. 6449–6462.

[45] B.C. De Cooman, Y. Estrin, and S.K. Kim: *Acta Mater.*, 2017 (In Press).

[46] O. Bouaziz, S. Allain, and C. Scott: *Scr. Mater.*, 2008, vol. 58, pp. 484–487.

[47] I. Gutierrez-Urrutia, S. Zaefferer, and D. Raabe: *Mater. Sci. Eng. A*, 2010, vol. 527, pp. 3552–3560.

[48] H. Beladi, I. B. Timokhina, Y. Estrin, J. Kim, B. C. De Cooman, and S. K. Kim: *Acta Mater.*, 2011, vol. 59, pp. 7787–7799.

[49] W. Mullins and R. Sekerka: *J. Appl. Phys.*, 1964, vol. 35, pp. 444-451.

[50] R. Trivedi and W. Kurz: *Int. Mater. Rev.,* 1994, vol. 39, pp. 49-74.

[51] A. Glezer, and I. Permyakova: *Melt-Quenched Nanocrystals*. Boca Raton : CRC Press (Taylor & Francis Group imprint), 2013. p. 369.

[52] V. Zolotorevsky, N. Belov, and M. Glazoff: *Casting aluminum alloys*. First. Amsterdam :

Elsevier Science, 2007.

[53] D. Tomus, Y. Tian, P. A. Rometsch, M. Heilmaier, and X. Wu: *Mater. Sci. Eng. A*, 2016, vol. 667, pp. 42–53.

[54] J. Walker, K. Berggreen, A. Jones, and C. Sutcliffe: *Adv. Eng. Mater.*, 2009, vol. 11, pp. 541-546.

[55] S. Murugesan, P. Kuppusami, E. Mohandas, and M. Vijayalakshmi: *Mater. Lett.*, 2012, vol. 67, pp. 173–176.

[56] C. Herrera, R. L. Plaut, and A. F. Padilha: *Mater. Sci. Forum*, 2007, vol. 550, pp. 423–428.

[57] K. Saeidi: *Stainless steel fabricated by laser melting: Scaled-down structural hierarchies and microstructural heterogeneities*, Stockholm University, Stockholm, Sweden, 2016.

[58] G. Langford and M. Cohen, *Metall. Mater. Trans.*, 1970, vol. 1, pp. 1478-1480.

[59] M. Staker and D. Holt: *Acta Metall.*, 1972, vol. 20, pp. 569-579.

[60] D. Kuhlmann-Wilsdorf: *Metall. Trans.*, 1970, vol. 1, pp. 3173-3179.

[61] F. Lavrentev: *Mater. Sci. Eng.*, 1980, vol. 46, pp. 191-208.

[62] X. Feaugas and H. Haddou: *Metall. Mater. Trans. A*, 2003, vol. 34, pp. 2329-2340.

[63] G. Dini, R. Ueji, A. Najafizadeh, and S. M. Monir-Vaghefi: *Mater. Sci. Eng. A*, 2010, vol. 527, pp. 2759–2763.

[64] B. Hutchinson and N. Ridley: *Scr. Mater.*, 2006, vol. 55, pp. 299-302.

[65] M. Kassner: *Acta Mater.*, 2004, vol. 52, pp. 1-9.

[66] B. Kashyap and K. Tangri: *Acta Metall. Mater.*, 1995, vol. 43, pp. 3971-3981.

[67] J. W. Hutchinson: *Proc. R. Soc. London A Math. Phys. Eng. Sci.*,1976, vol. 348, pp. 101-127.

[68] C.N. Tome, C.R. Canova, and U.F. Kocks: *Acta Mater.*, 1984, vol. 32, pp. 1637-1653.

[69] Y. F. Shen, X. X. Li, X. Sun, Y. D. Wang, and L. Zuo: *Mater. Sci. Eng. A*, 2012, vol. 552, pp. 514–522.

[70] G. Frommeyer, U. Brüx, and P. Neumann: *ISIJ Int.*, 2003, vol. 43, pp. 438-446.

[71] F. Pickering: *Physical metallurgy and the design of steels*, App. sci. pub. Ltd., 1978.

[72] C. Haase, C. Zehnder, T. Ingendahl, A. Bikar, F. Tang, B. Hallstedt, W. Hu, W. Bleck, and D.A. Molodov, *Acta Mater.*, 2017, vol. 122, pp. 332–343.